LOCKHEED MARTIN ENERGY RESEARCH LIBRARIES
3 4456 0513259 4

CENTRAL RESEARCH LIBRARY
DOCUMENT COLLECTION

OAK RI[illegible]BORATORY

operated by

UNION CARBIDE CORPORATION
NUCLEAR DIVISION

for the

U.S. ATOMIC ENERGY COMMISSION

ORNL-TM-2090

cy. 2

DECLASSIFIED

CLASSIFICATION CHANGED TO:
BY AUTHORITY OF: AECM 2104 a2 B6
BY: C. Kachurmesh 10/10/74

# FUELS AND MATERIALS DEVELOPMENT PROGRAM QUARTERLY PROGRESS REPORT FOR PERIOD ENDING DECEMBER 31, 1967

Compiled by
P. Patriarca

OAK RIDGE NATIONAL LABORATORY
CENTRAL RESEARCH LIBRARY
DOCUMENT COLLECTION
LIBRARY LOAN COPY
DO NOT TRANSFER TO ANOTHER PERSON
If you wish someone else to see this document, send in name with document and the library will arrange a loan.

**NOTICE** This document contains information of a preliminary nature and was prepared primarily for internal use at the Oak Ridge National Laboratory. It is subject to revision or correction and therefore does not represent a final report.

[redacted]

LEGAL NOTICE

This report was prepared as an account of Government sponsored work. Neither the United States, nor the Commission, nor any person acting on behalf of the Commission:

A. Makes any warranty or representation, expressed or implied, with respect to the accuracy, completeness, or usefulness of the information contained in this report, or that the use of any information, apparatus, method, or process disclosed in this report may not infringe privately owned rights; or

B. Assumes any liabilities with respect to the use of, or for damages resulting from the use of any information, apparatus, method, or process disclosed in this report.

As used in the above, "person acting on behalf of the Commission" includes any employee or contractor of the Commission, or employee of such contractor, to the extent that such employee or contractor of the Commission, or employee of such contractor prepares, disseminates, or provides access to, any information pursuant to his employment or contract with the Commission, or his employment with such contractor.

[redacted]

ORNL-TM-2090

Contract No. W-7405-eng-26

# FUELS AND MATERIALS DEVELOPMENT PROGRAM QUARTERLY PROGRESS REPORT FOR PERIOD ENDING DECEMBER 31, 1967

Compiled by

P. Patriarca

APRIL 1968

OAK RIDGE NATIONAL LABORATORY
Oak Ridge, Tennessee
operated by
UNION CARBIDE CORPORATION
for the
U.S. ATOMIC ENERGY COMMISSION

[redacted]

LOCKHEED MARTIN ENERGY RESEARCH LIBRARIES

3 4456 0513259 4

[redacted]

[redacted]

[redacted]



# FOREWORD

This is the fifteenth quarterly progress report describing work performed at the Oak Ridge National Laboratory for the Fuels and Materials Branch, Division of Reactor Development and Technology, U.S. Atomic Energy Commission. The specific programs covered are as follows:

| Program Title | Person in Charge | Principal Investigator(s) |
|---|---|---|
| **Part I. Metals and Ceramics Division** | | |
| Fuel Element Fabrication Development | G. M. Adamson, Jr. | W. R. Martin |
| Mechanical Properties | C. J. McHargue | J. R. Weir, Jr. |
| Mixed Nitride Fuels Development | W. O. Harms | J. L. Scott |
| Nondestructive Test Development | W. O. Harms | R. W. McClung |
| Sintered Aluminum Products Development | G. M. Adamson, Jr. | W. R. Martin<br>D. G. Harman |
| Sol-Gel Fast Reactor Fuels | P. Patriarca | A. L. Lotts<br>J. L. Scott<br>R. G. Wymer* |
| Weldability of Nickel-Bearing Alloys | G. M. Adamson, Jr. | G. M. Slaughter |
| Zirconium Metallurgy | C. J. McHargue | P. L. Rittenhouse |
| **Part II. Reactor Chemistry Division** | | |
| Fission-Gas Release and Physical Properties of Fuel Materials During Irradiation | O. Sisman | R. M. Carroll<br>J. G. Morgan |

*Chemical Technology Division.

[redacted]

[redacted]

[redacted]

[redacted]



CONTENTS

Page

Summary . . . . . ix

Part I. Metals and Ceramics Division

1. Fuel Element Fabrication Development . . . . . 3

Dispersion Plate Fabrication . . . . . 3

Testing of Blending Homogeneity by X-Ray Attenuation . . . 7

Characterization of $U_3O_8$ Fuel Powders . . . . . 8

Irradiation Testing of Miniature Fuel Plates . . . . . 9

Aluminum Surface Film Studies . . . . . 11

Conversion of $UF_6$ to Uranium Oxides in a Flame Reactor . . . . . 14

Economic Analysis of the Flame Reaction Process for Converting $UF_6$ to $UO_2$ Powder . . . . . 17

Preparation of $PuO_2$ Powder from $PuF_6$ by Chemical Vapor Deposition . . . . . 19

2. Mechanical Properties . . . . . 20

Effects of Neutron Irradiation on the Elevated-Temperature Mechanical Properties of Type 316 Stainless Steel . . . . 20

Development of Titanium-Modified Type 304L Stainless Steel . . . . . 25

The Effects of Prestrain on the Tensile and Creep Properties of Irradiated and Unirradiated Type 304L Modified Stainless Steel . . . . . 26

Comparison of Postirradiation Properties of Six High-Temperature Alloys at 760°C . . . . . 29

Development of a Modified Hastelloy N with Improved Resistance to Radiation Damage . . . . . 39

EBR-II Gamma Heat Experiment . . . . . 45

3. Mixed Nitride Fuels Development . . . . . 50

Fabrication of Mixed Nitrides . . . . . 51

Hot-Press Design . . . . . 51

Survey on Theory of Hot Pressing . . . . . 53

Analog Computer Simulation of Hot Pressing . . . . . 57

Phase Behavior and Thermodynamic Properties of the Plutonium-Nitrogen System . . . . . 60

Phase Behavior . . . . . 60

Thermodynamic Properties . . . . . 61

[redacted]

[redacted]




Conclusions . . . . . 61

Fuel Cycle Sol Gel . . . . . 62

Synthesis and Fabrication of UN and U(C,N) . . . . . 63

Fuel-Cladding Thermal Conductance . . . . . 64

Fundamental Studies on Uranium Nitride . . . . . 71

Band-Theory Calculations . . . . . 71

Low-Temperature Specific Heat . . . . . 72

Elastic Constants . . . . . 74

Uranium Self-Diffusion in UN . . . . . 74

Ternary Systems Containing Thorium and Uranium . . . . . 77

Helium Bubble Migration in UN in a Temperature Gradient . . . . . 78

Transport Properties . . . . . 78

Studies in the U-C-N System . . . . . 87

4. Nondestructive Test Development . . . . . 99

Electromagnetic Test Methods . . . . . 99

Analytical Studies . . . . . 99

Phase-Sensitive Eddy-Current Instrument . . . . . 101

Temperature-Compensated Probes . . . . . 101

Ultrasonic Test Methods . . . . . 102

Fabrication of Reference Notches . . . . . 102

Ultrasonic Frequency Analysis . . . . . 103

Optical Visualization of Ultrasound . . . . . 104

Penetrating Radiation Methods . . . . . 105

Holography . . . . . 105

Fuel Homogeneity . . . . . 105

5. Sintered Aluminum Products Development . . . . . 106

Dispersion Preparation . . . . . 106

Powder Consolidation . . . . . 106

Effects of Reduction During Extrusion . . . . . 113

Effects of Transverse Extrusion . . . . . 115

Thin Foil Preparation of High-Oxide SAP . . . . . 121

Development of Advanced SAP Materials . . . . . 121

Anisotropy of Extruded SAP 895 . . . . . 124


[redacted]

[redacted]



6. Sol-Gel Fast Reactor Fuels . . . . . 130
Plutonium Ceramic Facilities . . . . . 131
Building 3019 Facilities . . . . . 131
Building 4508 Facilities . . . . . 134
Preparation of $(U,Pu)O_2$ Sol-Gel Material . . . . . 138
Development of $(U,Pu)O_2$ Fabrication Techniques . . . . . 138
Sphere-Pac Development . . . . . 138
Pellet Development . . . . . 140
Irradiation Testing of Sol-Gel $(U,Pu)O_2$ Fuels . . . . . 143
Uninstrumented Screening Irradiation Tests . . . . . 143
ORR Instrumented Tests . . . . . 147
Transient Testing of Sol-Gel-Derived $(U,Pu)O_2$ Fuel . . . 149
Short-Term Irradiations (Rabbit Tests) . . . . . 153
Fast Flux Irradiation Tests of Sol-Gel $(U,Pu)O_2$ Fuels . . . . . 153
Gas-Cooled Fast Reactor Program . . . . . 153
Comparison of Neutron Cross Sections of Cladding Materials . . . . . 154
Irradiation Test Calculations . . . . . 154
7. Weldability of Nickel-Bearing Alloys . . . . . 157
Metallographic Study . . . . . 157
Aluminum and Titanium . . . . . 158
Influence of Sulfur and Phosphorus . . . . . 158
Microprobe Studies . . . . . 162
8. Zirconium Metallurgy . . . . . 165
Tubing Test Program . . . . . 165
Knoop Microhardness Analysis of Texture Changes During Tubing Fabrication . . . . . 165
Tubing Fabrication Study . . . . . 169
Circumferential Texture Variations in Zircaloy Tubing . . 171
Texture Development in Single-Crystal Zirconium . . . . . 174
Corrosion of Zirconium Alloys . . . . . 178

[redacted]

[redacted]



Part II. Reactor Chemistry Division

9. Fission-Gas Release and Physical Properties of Fuel Materials During Irradiation . . . . . 181

Steady-State Fission-Gas Release from $UO_2$ at High Temperature . . . . . 182

Specimens for High-Burnup Studies . . . . . 184

Fission-Gas Release from Enriched Specimens (C1-21) . . . 188

In-Reactor Thermal Conductivity of Uranium Dioxide . . . . 190

[redacted]

[redacted]



# SUMMARY

## PART I. METALS AND CERAMICS DIVISION

### 1. Fuel Element Fabrication Development

We showed that the void volume found in either oxide or intermetallic dispersion fuel plates depends on the type and amount of fuel as well as plate size. Of the materials tested to date, a low-fired $U_3O_8$ produced the highest void fraction. Procedures were developed that will yield a more stable and uniform $U_3O_8$ by elimination of the delta phase. To aid blending studies, we designed and built a special device that permits removal of complete layers from within a blend. The sample is then examined by x-ray attenuation techniques to determine its uranium content and distribution and, by comparison with other samples, the blend homogeneity.

A series of miniature fuel plate samples was fabricated for irradiation in the G-12 facility of the ETR. We are comparing present and increased fuel loading of two grades each of $U_3O_8$ and uranium-aluminum intermetallics as well as the effects of particle size distribution in the original blends. After only a short exposure, a failure in another experimenter's sample shut the loop down, and excessive bowing was found in two of the three tiers of ORNL samples. The cause of the bowing has not yet been determined.

In the flame reactor being developed for producing $UO_2$ directly from $UF_6$, we showed that once a stable flame has been established, the fluorine may be turned off and sufficient heat will result from the reaction. This results in a considerable cost saving and makes this process competitive with sol gel. While high fluorine contents were found in the as-deposited powder, they were removed by a subsequent hydrogen treatment. Such powders were fabricated into pellets with densities ranging from 75 to 97%.

The apparatus for producing $PuO_2$ by vapor fabrication was operated successfully. The resulting powders are now being studied. Converting the $PuF_4$ into $PuF_6$ appears to be a bigger problem than the deposition of the $PuO_2$.

[redacted]

[redacted]



## 2. Mechanical Properties

Our program investigating the high-temperature irradiation embrittlement of fuel cladding materials includes studies of types 316 and 304 stainless steel and the titanium modification of these steels, Incoloy 800, and Hastelloy N.

After high-temperature irradiation of type 316 stainless steel, the tensile ductility was independent of irradiation temperature over the range 550 to 750°C. However, the creep ductility at 650°C was lower for lower irradiation temperatures.

We have received 1500-lb heats of both the high- and low-carbon versions of the 0.2% Ti-modified type 304 stainless steel. Specimens of the high-carbon heat are being irradiated in the ORR.

Tentative results indicate that prestrain up to about 5% has only a small effect on the postirradiation ductility of type 304 stainless steel. Larger prestrain decreases the postirradiation elongations and creep rates.

The properties of various alloys at 760°C were compared directly after irradiation at 760°C. The properties of Hastelloy X, Hastelloy N, Hastelloy N-titanium, type 304 stainless steel, type 304 stainless steel-titanium, and Incoloy 800 containing various amounts of titanium and carbon were very sensitive to strain rate. Selection of alloys must be based upon the results of a wide range of testing conditions, since the ductility of some alloys varies by a factor of 5 as the strain rate is changed.

The development of an improved Hastelloy N has involved decreasing the molybdenum content and the addition of titanium. Postirradiation properties of this alloy at 650°C show considerable improvement in both strength and ductility over that exhibited by the standard Hastelloy N.

Some results of the gamma heating measurements in EBR-II are available. These data are currently being analyzed.

## 3. Mixed Nitride Fuels Development

We have chosen hot pressing as one method for forming high-density mixed-nitride fuel (U,Pu)N and designed a hot press for a glove box.

[redacted]

[redacted]



An analog computer circuit was formulated in accordance with theories of hot pressing to predict end-point density.

The phase behavior and thermodynamic properties of PuN have been reviewed and analyzed. Results of the various investigations are in good agreement, and areas of needed research are pointed out.

A mixed-nitride fuel cycle with a sol-gel conversion scheme shows considerable promise. We are investigating the kinetics of the reactions and the possible intermediate compounds.

We extended our capability for the preparation of high-quality pressed-and-sintered specimens of UN by developing isostatic-pressing techniques to supplement conventional cold pressing. Synthesis and fabrication techniques for U(C,N) compositions are also being developed.

An apparatus was modified to study thermal contact resistance and to find ways to decrease the resistance. Our first objective is to determine the relative importance of the many variables involved.

Our program of fundamental studies on UN is proving fruitful and progress is reported on band-theory calculations, low-temperature specific heat measurements, elastic constants, diffusion, and transport properties.

Studies on the U-C-N system have largely centered on solving problems in chemical analysis. Previous conclusions that the UC-UN system is thermodynamically ideal, based on x-ray data, are confirmed at 1500°C. Free carbon can be determined successfully.

## 4. Nondestructive Test Development

We are developing new techniques and equipment for the nondestructive examination of materials and components. Major emphasis has been on eddy-current, ultrasonic, and penetrating radiation methods.

Our analytical work on electromagnetic phenomena has included preparation of computer programs for calculation of several parameters using the newly derived integrals for closed form solutions and issuance of a report on this work. A paper was presented on the portable phase-sensitive instrument. Studies have begun on the use of wire materials other than copper to obtain higher temperature operation with less temperature drift.

[redacted]

In our work on electrodischarge machining of reference discontinuities, we have developed capabilities for making notches in tube bores as small as 0.050 in. Cracking is being encountered during the making of notches in tungsten. Improved replication techniques have been developed for transverse notches. Frequency analysis techniques are being studied to improve reproducibility of response of transducers and instruments. Work has begun on the optical visualization of ultrasound in several selected transparent solids.

Work has begun with laser holography to gain sufficient familiarity for development of advanced holographic techniques of benefit to nondestructive testing. Electronic circuitry has been developed and installed to allow automatic averaging and print-out of x-ray attenuation data during the scanning of a specimen such as a fuel plate.

### 5. Sintered Aluminum Products Development

Our program has been to investigate the problems and parameters related to primary billet fabrication of SAP. After the preparation of specifications for atomized powder, ball milling of these powders to produce flake, and selection of a billet consolidation process, we have fabricated several large billets using the selected parameters. The conclusion of our program will be the evaluation of these billets. Since the properties of the end product are influenced by the manner in which the consolidated billet is reduced, we have examined some aspects of the secondary metalworking of SAP.

We have concluded our work on permissible hydrogen impurity levels, duration of vacuum treatments for billets, and comparison of vacuum annealing before and after vacuum hot pressing. Our remaining tasks involve the final analysis of mechanical property reproducibility in large-scale billets produced by Process B. The effects of reduction during extrusion, transverse extrusion, and anisotropy of SAP have been studied.

### 6. Sol-Gel Fast Reactor Fuels

We continued the preparation, development, and testing of sol-gel-derived fuels for fast reactors. Equipment for the fabrication and

[redacted]



out-of-reactor characterization of plutonium-bearing materials is now either in operation or in the final stage of installation. Approximately 1 kg of $UO_2$–25% $PuO_2$ sol-gel microspheres was prepared for fabrication studies and irradiation test capsules, and 280 g of $PuO_2$ was prepared for pelletizing studies.

Pellets were made from sol-gel $(U,Pu)O_2$ microspheres to densities as high as 93% of theoretical. The best results were obtained by grinding the microspheres to −325 mesh. Preliminary studies have been conducted on tray drying sols, which offers a simpler route than microsphere production for making pellets. The Sphere-Pac development emphasized increasing packing densities above the 83 to 85% obtained from two-size fractions. If a coarse fraction with a range of particle sizes is used, the coarse-bed density can be increased from 62.5 to 72.5%, and infiltration with a single-size fine fraction produced densities greater than 88%.

Three capsules containing $(U,Pu)O_2$ have been removed from the ETR. One capsule operated at a heat rating of 50 kw/ft to a burnup of approximately 2% FIMA. A second achieved 29 kw/ft and approximately 1% FIMA. Examination of the third capsule is just beginning. The radiochemical burnup analyses correlate very well with computer results. The design of instrumented capsules to be used in the ORR was completed, and all parts are on hand for the construction of the first capsule. A program was formulated to investigate the sol-gel $(U,Pu)O_2$ under conditions simulating accidental power excursions in the TREAT facility. We outlined a preliminary program for testing fuel fabricated by both pelletizing and Sphere-Pac techniques in the EBR-II. Cross-section data for proposed LMFBR and GCFR cladding materials were collected. Calculational procedures were developed for irradiation tests. The preirradiation procedure consists of developing a flux-energy spectrum for the irradiation facility unperturbed, solving the Boltzmann transport equation to get the fission rate as a function of radius, and calculating radial temperature distribution from the fission rate. Postirradiation procedures include calculation of burnup from analytical data and comparing observed microstructural changes with a calculated temperature profile.

[redacted]

## 7. Weldability of Nickel-Bearing Alloys

We are accumulating data on the effects of minor elements, individually and combined, upon the weld cracking behavior and mechanical properties of welds in several special heats of Incoloy 800. Microstructural studies have been conducted on the samples tested in the hot-ductility investigations reported last quarter. Additions of aluminum and titanium to the basic iron-nickel-chromium ternary resulted in laminations in the wrought structure; the nature of failure in synthetic weld heat-affected zones varied with titanium and aluminum contents. In the pure ternary alloy, failure appeared to be due to liquation, whereas the aluminum- and titanium-containing heats failed intergranularly with much secondary cracking.

The addition of sulfur to titanium- and aluminum-containing alloys resulted in precipitates that tended to align themselves in the original rolling direction. Failures in the synthetic heat-affected zones were all intergranular. Over the ranges studied, phosphorus additions to the same basic alloys did not result in increased grain-boundary embrittlement. Microprobe studies on a sulfur-containing alloy indicated that the grain-boundary precipitate was enriched in titanium and sulfur. We propose that the association of titanium and/or aluminum with the sulfur prevents the usual deterioration of properties that accompanies sulfur additions to nickel-containing alloys.

## 8. Zirconium Metallurgy

We have developed a simple and rapid qualitative method of following the effect of various tubing fabrication procedures on the crystallographic texture formed in the tubing. The method involves Knoop microhardness measurements taken on sections perpendicular to the tubing axis at several degrees of reduction.

We initiated a study of the fabrication of zirconium alloy tubing to: (1) show in detail how fabrication events affect texture; (2) allow control of texture in the finished product; and (3) demonstrate the most economical and efficient method of tube production.

Basal and prism pole figures were determined for nine specimens from a single cross section of a forged 4-in.-diam Zircaloy-4 bar. The position and intensity of the texture peaks for the individual specimens varied considerably. This variation may be the cause of the circumferential texture gradients found in Zircaloy tubing.

Our study of texture development in zirconium single crystals has shown that all major textural changes occur quite rapidly, mainly by twinning, and are completed very early in the deformation process. The final perfecting of the texture occurs rather slowly during the later higher reductions.

## PART II. REACTOR CHEMISTRY DIVISION

### 9. Fission-Gas Release and Physical Properties of Fuel Materials During Irradiation

Postirradiation examination of a fine-grain $UO_2$ specimen, irradiated at 1700°C, shows equiaxed grain growth, which, from the fission-gas release rates, occurred between 1630 and 1700°C. Fission-gas bubbles were located on the grain boundaries.

Enriched single-crystal spheres are being irradiated to test the effect of burnup. At 1.8% U burnup no effect has been noted. The fission-gas release does not conform to our defect-trap model, and we believe the high fission density in these specimens has exceeded the limits of application of the model.

A new mathematical method of dealing with the in-reactor thermal conductivity data has been developed. This method promises an increased precision in measurements of thermal diffusivity by the step perturbation method.

[redacted]

[redacted]

[redacted]

# PART I.

# METALS AND CERAMICS DIVISION

[redacted]

[redacted]

[redacted]

[redacted]



# 1. FUEL ELEMENT FABRICATION DEVELOPMENT

G. M. Adamson, Jr.

Factors affecting plate fabrication and irradiation performance for research reactor fuel elements are being investigated. These studies should lead to the fabrication of plates with increased fuel loadings, permit the use of cheaper fuels, provide assurance that a given fabrication practice will produce satisfactory plates, permit predictions of the effects on plate quality of changes in production equipment and processes, reduce the development work and lead time necessary for long-range new-generation fuels, generate data that will improve the quality of specifications, and permit rapid solution to the problems that continually arise in the shops of the industrial fabricators. Other efforts are being devoted to improving the reliability and reducing the cost of the nondestructive inspection techniques for the fuel plates.

We have continued at a reduced effort the direct conversion of fissionable halides to refractory fuel compounds by chemical vapor deposition. Emphasis is gradually being shifted from the uranium to the plutonium system.

## Dispersion Plate Fabrication

M. M. Martin W. R. Martin

The concept of reducing swelling in fuel dispersions by the introduction of fabrication voids has been used by several investigators to explain variations in irradiation performance. If this concept is real, then we must understand the factors controlling the final void volume in order to obtain consistent and improved irradiation performance.

Full-size and miniature fuel plates were fabricated to test two grades of $U_3O_8$ and two grades of aluminum intermetallic at various uranium loadings. The pressing and rolling conditions were identical for the plates, regardless of the type and quantity of fuel. The void volume data for the miniatures, as compacts and final plates, are given

[redacted]

in Fig. 1.1. From these data, one can conclude that the void volume depends on the type and amount of fuel. Most importantly, one can note that the void volumes obtained in the plates containing arc-cast intermetallic were slightly higher than were those obtained for the hi-fired[1] $U_3O_8$ and significantly greater than those for the $UAl_3$ prepared by the hydride method. However, the void volume obtained for plates containing the burned $U_3O_8$ is much greater than for any other fuel examined. In general, it appears that increasing the void volume of compacts results in more void volume in the final plates. However, we emphasize that this relationship is general and further testing is needed. From void volume alone, we conclude that the irradiation performance of burned $U_3O_8$ should be better than that of the other hi-fired $U_3O_8$ or the intermetallics.

The void volume data on the full-size plates are compared in Table 1.1 with data from the miniature plates. The same conclusions seem to apply; however, the void volume is less in the miniature plates by about 2%.

The present specifications for ATR and HFIR call for an acceptable fuel particle size to be the following:

| | | |
|---|---|---|
| HFIR | −170 +325 mesh | < 10 wt % fines |
| ATR | −100 +325 mesh | < 25 wt % fines |

The role of fuel fines is of interest from several points of view. Fines generated during fuel production are expensive to recycle and should be used at the highest acceptable rate. However, increasing the tolerable level of fines may affect the fabricability and, most importantly, the irradiation performance of the plate.

Our initial studies on $UAl_3$ indicate that fuel fines up to 10 wt % and a particle-size variation from 63 to 105 μ have only secondary effects on the void volumes of miniature fuel plates. However, fuel homogeneity based on HFIR inspection techniques was affected to a

[1]The term "hi-fired" is used to designate the $U_3O_8$ currently used in fuel elements. It is prepared by a process that culminates in firing at high temperatures.

[redacted]



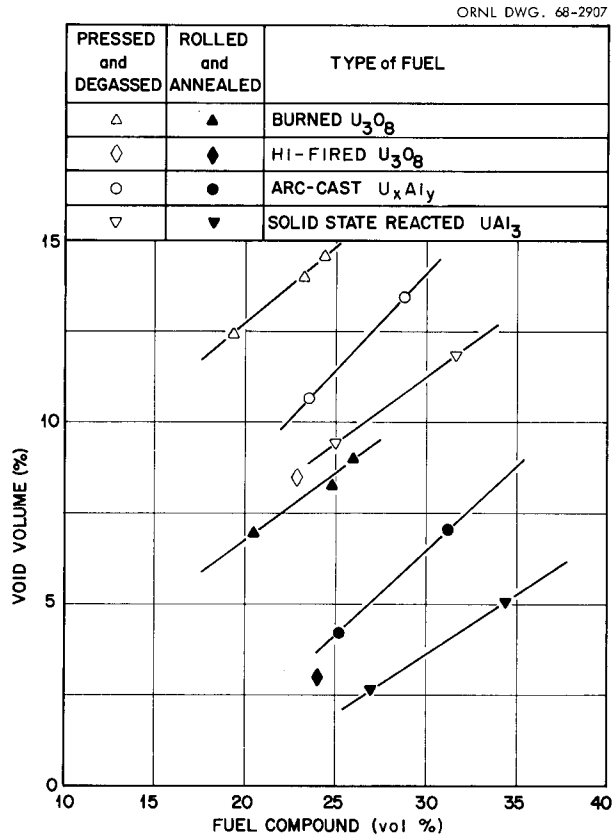


Fig. 1.1. Void Volume in Compacts and Miniature Plates for Various Fabrication Variables.

Table 1.1. Comparison of Void Volume in Miniature and Full-Size Plates

| Uranium (wt %) | Void Volume in Final Plates, % | |
|---|---|---|
| | Miniature | Full Size |
| | $UAl_3$ (hydride) plates | |
| 27 | < 1.0 | 3 |
| 32 | 2.0 | 4 |
| 36 | 2.5 | 4.8 |
| 43 | 5.2 | 7 |
| | $U_3O_8$ (hi-fired) plates | |
| 27 | | 2.7 |
| 32 | | 3.5 |
| 36 | | 4.3 |
| 43 | 3.0 | 5.1 |

[redacted]

[redacted]



greater degree. The data for $UAl_3$ fuel (made by the hydride method) are given in Table 1.2. Increasing both the primary particle size and the size range increased the average void volume in the final rolled plate and also improved fuel homogeneity. Introduction of powder fines lowered the void volume and improved fuel homogeneity of some but not all of the plates. However, this indication is based on a total of ten fuel plates and the trend may not be statistically significant.

Table 1.2. Particle-Size Variations in $UAl_3$-Bearing Miniature Fuel Plates

| Primary Particle Size Range (μ) | Fines Content < 44 μ (wt %) | Void Volume, % | | Fuel Homogeneity |
|---|---|---|---|---|
| | | Range | Average | |
| 44–63 | 0 | 4.8–5.2 | 5.0 | Poor |
| 44–88 | 0 | 5.0–5.4 | 5.2 | Fair |
| 44–103 | 0 | 5.8 | 5.8 | Excellent |
| 44–88 | 10 | 4.3–5.3 | 4.9 | Fair to excellent |

The effect of particle size and hence fines on irradiation must either be based on irradiation experience with plates having excellent fuel homogeneity or predicted on the basis of a model. Failure models of fuel dispersions can be found in the literature.[2,3] If we assume that the limiting criterion is to prevent the intersection of the recoil damage zones surrounding each particle, we can calculate the minimum particle size to satisfy that criterion as a function of fuel volume. The effect of powder fines can then be estimated from those data. We have completed our initial calculations and hope to fabricate fuel

[2]D. W. White, A. P. Beard, and A. H. Willis, "Irradiation Behavior of Dispersion Fuels," p. 717 in Fuel Elements Conference, Paris, November 18–23, 1957, TID-7546, Book 2 (March 1958).

[3]J. H. Gittus, The Mechanism of Failure in $UO_2$/Stainless Steel Cermets, TRG Report 1278 (July 1966).

[redacted]

plates having fines at levels of 3, 10, 20, and 30 wt %. These plates will be irradiated, and the irradiation performance will be compared to the predictions based on our calculations.

## Testing of Blending Homogeneity by X-Ray Attenuation

A. K. Chakraborty B. E. Foster
S. D. Snyder W. R. Martin

We studied the application of x-ray attenuation for the determination of green density, segregation, and homogeneity of powder blends. The purpose is to develop greater homogeneity of aluminum–$U_3O_8$ powders during blending and to relate the results with those of the compact and fuel-plate stages.

To achieve these results, a mechanical device was designed and fabricated such that the powders can be blended and samples from individual layers removed. This device consists of an open aluminum cylinder 9 1/2 in. high and 4 in. in diameter, with a tight-fitting cylindrical lid. The whole cylinder with the lid can be inserted into the oblique blender, and the powder in different proportions can be blended for different periods of time.

To collect the powder mixtures from different layers after different blending times and without disturbing the blend, special trays were constructed. For these trays, aluminum was used as a frame and 7.4-mil beryllium foils were used as the lids. The beryllium foils were glued on aluminum. Beryllium was chosen because of its low absorption of x rays.

This device was first tested with aluminum having 80% fines (i.e., 80% less than 44 μ). The x-ray attenuation of the aluminum powder was fairly uniform from scoop to scoop.

Before work with the Al–40 wt % $U_3O_8$ binary system, other experiments were carried out with Al–40 wt % Fe powders. Iron powder with the same particle size as $U_3O_8$ powder was used because it has nearly the same theoretical density as $U_3O_8$, although the particle shapes of the two powders are different. These binary powders were blended for

[redacted]



4, 8, 16, and 32 min. Then, with the help of four different trays, the x-ray attenuations of the four layers were determined. The x-ray attenuations of the powders at different layers were different at low blending times, but the deviation became minimal after 32 min of blending. A run of 64 min will indicate the probable blending time for maximum homogeneity.

Segregation of a powder can be affected by the concentration of the powder and by the differences in density, size, and shape of different particles. It is also a function of blending time. Segregation of iron-aluminum powders was followed by observing the deviation from average green density of the small sample slices.

Powders from different trays were collected to make particle size analyses by sieving and television microscopy.

We plan to determine the homogeneity of aluminum–$U_3O_8$ powders using differently heat-treated $U_3O_8$ powders and varying the volume of the powder in the cylinder, the blending time, and the particle size of the powders.

## Characterization of $U_3O_8$ Fuel Powders

J. T. Venard W. R. Martin

Several annealing and firing experiments have been completed on Y-12-produced $U_3O_8$ taken from various stages in the process. Low-temperature (800 to 1000°C) anneals do not improve the hi-fired or refired product and may increase the amount of delta or beta phase present. Based on the factors of surface area, density, yield of −170 +325 mesh fraction, and presence of delta or beta phase, an optimized firing schedule has been determined. This proposed firing schedule consists of 5 hr at 1400°C, followed by a furnace cool and an additional 5 hr at 1400°C. We also suggest that no sizing be done between firings and that all material that screens larger than 170 mesh and smaller than 325 mesh be redissolved. These process modifications are expected to give a more consistent "dead-burned" $U_3O_8$. Once the modified process product is available, we will roll test plates for nondestructive and destructive evaluation.

[redacted]

[redacted]



## Irradiation Testing of Miniature Fuel Plates

M. M. Martin W. R. Martin

Miniature fuel plates have been fabricated to be irradiated in the G-12 loop at the ETR. We are sharing the loop for these irradiations with Idaho Nuclear Corporation. For ETR cycle 93, the loading of ORNL samples is shown in Table 1.3. Two levels of fuel loading are given; the lower value is comparable to that of HFIR and the higher fuel loading represents a 25% increase.

In tiers 1 and 5 of the loop, various types of fuels are being compared. Two grades of $U_3O_8$ include the hi-fired oxide now being used successfully in HFIR and a burned oxide, which would be much cheaper to produce. Two grades of aluminum intermetallic were also included in these tests. The more conventionally prepared arc-cast $U_xAl_y$ fuel is similar to that used by commercial fabricators in ETR and ATR fuel plates. It is important to note, however, that we found no metallographic or radiographic evidence of free uranium metal in this fuel, which had been cast at ORNL. The second grade of intermetallic, $UAl_3$, was prepared by the hydride process and powder-metallurgy procedures. The samples in tier 3 were designed to test the effect of particle size for intermetallic fuels having good fuel homogeneity.

The irradiation of the samples in cycle 93 began on December 8, and after 567-Mwd exposure a fission-product release in the loop shut the reactor down. Both ORNL and Idaho Nuclear miniature plates were removed from the loop. The fission release observed came from an Idaho Nuclear sample located in tier 4. ORNL plates in tiers 1 and 3 were bowed, whereas no bowing was noted for the ORNL plates in tier 5. An Idaho Nuclear Corporation estimate of the average burnup of the ORNL specimens is as follows.

| Tier | Fission/cm$^3$ of Core ±20% |
|---|---|
| 1 | $8 \times 10^{19}$ |
| 3 | $2 \times 10^{20}$ |
| 5 | $1.6 \times 10^{20}$ |

[redacted]

Table 1.3. Miniature Test Plates for ETR G-12 Loop Irradiations

| Tier in G-12 Loop | Reference Plate Number | Fuel Type | Method of Fuel Preparation | Maximum Size (μ) | Fines < 44 μ (wt %) | Uranium Loading (g/plate) | Instrumented Plate Temperature (°F) |
|---|---|---|---|---|---|---|---|
| | | | Cycle 93 | | | | |
| 5-2 | 0-3-893 | $U_3O_8$ | Burning | 88 | 3.0 | 2.205 | 375–370 |
| -1[a] | 0-3-886 | $U_3O_8$ | Hi-firing | 88 | 3.1 | 2.205 | |
| -3 | 0-24-965 | $U_xAl_y$ | Arc casting | 88 | 10.0 | 2.205 | |
| -4 | 0-24-959 | $UAl_3$ | Solid-state reaction | 88 | 10.0 | 2.205 | |
| 1-2 | 0-56-895 | $U_3O_8$ | Burning | 88 | 3.0 | 2.756 | 250–230 |
| -1[a] | 0-56-891 | $U_3O_8$ | Hi-firing | 88 | 3.1 | 2.756 | |
| -3 | 0-57-973 | $U_xAl_y$ | Arc casting | 88 | 10.0 | 2.756 | |
| -4 | 0-57-961 | $UAl_3$ | Solid-state reaction | 88 | 10.0 | 2.756 | |
| 3-1[a] | 0-57-956 | $UAl_3$ | Solid-state reaction | 88 | 10.0 | 2.756 | 342–340 |
| -2 | 0-57-963 | $UAl_3$ | Solid-state reaction | 63 | None | 2.756 | |
| -3 | 0-57-967 | $UAl_3$ | Solid-state reaction | 88 | None | 2.756 | |
| -4 | 0-57-968 | $UAl_3$ | Solid-state reaction | 105 | None | 2.756 | |
| | | | Cycle 94[b] | | | | |
| 1-1[a] | 0-56-891 | $U_3O_8$ | Hi-firing | 88 | 3.1 | 2.756 | |
| -3 | 0-56-899 | $U_3O_8$ | Hi-firing | 88 | 3.1 | 2.756 | |
| 3-1[a] | 0-57-956 | $UAl_3$ | Solid-state reaction | 88 | 10.0 | 2.756 | |
| 4-2 | 0-24-959 | $UAl_3$ | Solid-state reaction | 88 | 10.0 | 2.205 | |
| -4 | 0-24-965 | $U_xAl_y$ | Arc casting | 88 | 10.0 | 2.205 | |
| 5-1 | 0-3-886 | $U_3O_8$ | Hi-firing | 88 | 3.1 | 2.205 | |
| -2 | 0-3-893 | $U_3O_8$ | Burning | 88 | 3.0 | 2.205 | |
| -4 | 0-24-964 | $U_xAl_y$ | Arc casting | 88 | 10.0 | 2.205 | |
| 6-2 | 0-56-894 | $U_3O_8$ | Burning | 88 | 3.0 | 2.756 | |
| -4 | 0-56-957 | $U_3O_8$ | Hi-firing | 88 | 3.1 | 2.756 | |

[a]Instrumented plate.

[b]Tier 5 (plates 5–1, etc.) reinserted in cycle 94.

We have no information yet as to the cause of the fission break in the Idaho Nuclear sample or the bowing of the ORNL samples in tiers 1 and 3. Thermal-cycling tests on unirradiated plates similar to those irradiated indicate that the plates are thermally stable and that exposure to the loop temperatures should not have caused the bowing. We will investigate the possibility of bowing due to hydraulic forces. All plates will be returned to ORNL at the earliest possible date for further examination.

A second array of samples also described in Table 1.3 was selected for irradiation to begin in cycle 94, on or about January 15. Duplicate samples of the bowed ORNL plates were not all available in time for this reactor cycle. The ORNL plates from tier 5 of the abbreviated cycle 93 have been reinserted for irradiation in this cycle. Samples in positions 2 and 4 of tier 6 are similar to those that bowed in cycle 93. From this irradiation, we will collect irradiation performance data on two grades of oxide and intermetallic fuels. The particle-size experiment, not completed in cycle 93, will be rescheduled for loop irradiations this summer.

## Aluminum Surface Film Studies

J. V. Cathcart

A substantial buildup of corrosion product occurs on the aluminum fuel element cladding during the operation of such reactors as the HFIR and the ATR. The extent of corrosion is not sufficiently severe to threaten the structural integrity of the fuel elements; however, the layer of corrosion products, principally boehmite, acts as a barrier to heat flow from the fuel element and limits the permissible fuel loading. Given the relatively short length of a fuel cycle in a HFIR-type reactor, even a small improvement in the corrosion resistance of the cladding would be highly beneficial. The purpose of our research is to find means to reduce the corrosion rate of aluminum and its alloys in a reactor environment or to reduce the thickness of the resulting corrosion products.

Our present approach involves applying a protective coating to the aluminum in the form of an anodic film. Anodic films having widely varying morphology, structure, and composition may be formed on aluminum, depending on the bath composition and anodizing conditions. We hope to find a film with the toughness, mechanical strength, and adherence to provide the desired degree of protectiveness.

Screening tests were performed on samples of 99.999% Al and on the 6061 aluminum alloy used in the HFIR fuel elements. The samples were in the form of coupons, 0.5 × 0.75 × 0.025 in., and the tests were conducted under static conditions in water at 200°C.

Pure aluminum is readily attacked by water at 200°C; for example, one of our test specimens was completely converted to boehmite in a 24-hr test. Coating the aluminum with anodic films formed in dilute solutions of $Na_3PO_4$ and boric acid produced little change in the corrosion rate; however, an aluminum specimen coated with 0.001-in.-thick film formed in an oxalic acid bath experienced very little attack in 336 hr at 200°C. There was no metallographic evidence of hydrogen penetration of the specimen grain boundaries, and the surface appearance of the specimen changed very little.

The details of the reaction that did occur are revealed in the electron micrograph shown in Fig. 1.2. The specimen was replicated in cross section. A thin layer of a crystalline reaction product (boehmite) is visible at the outer surface of the anodic film. The weight change that occurred during corrosion suggests that at least a part of the boehmite was formed by the reaction of water directly with the anodic film. A columnar structure is evident in the anodic film itself and is probably associated with the well-known pore structure that the film develops during anodization in oxalic acid.

The 6061 aluminum is much less subject to attack in static water at 200°C than pure aluminum; however, it does corrode severely at that temperature when a large heat flux exists across the water-specimen interface.[4] Reasoning that the effect of the heat flux must be related

[4] J. C. Griess, H. C. Savage, and J. L. English, Effect of Heat Flux on the Corrosion of Aluminum by Water. Part IV. Tests Relative to the Advanced Test Reactor and Correlation with Previous Results, ORNL-3541 (February 1964).

[redacted]



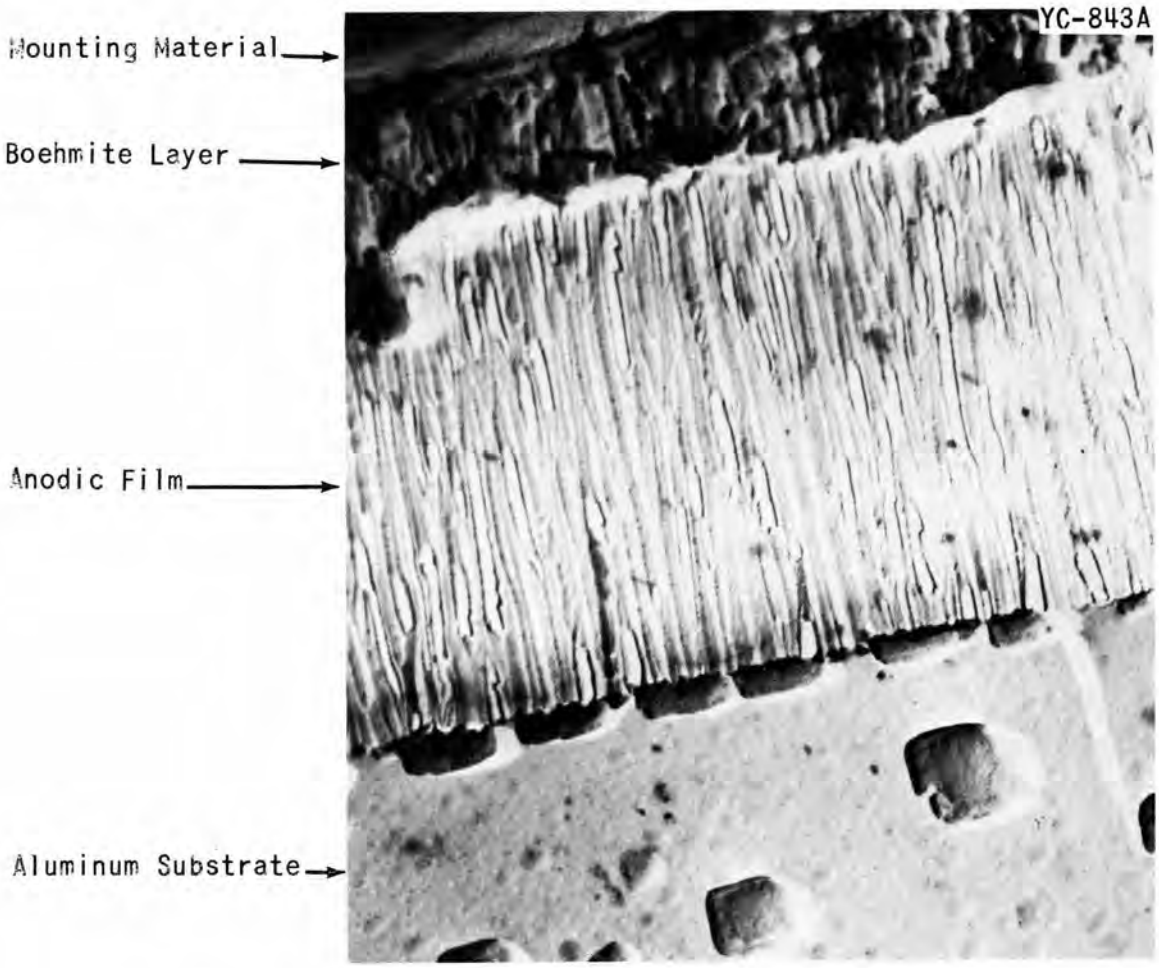


Fig. 1.2. Indirect Carbon Replica, Shadowed with Chromium, of the Cross Section of a 99.999% Al Specimen Anodized in Dilute Oxalic Acid and Corroded in Static Water at 200°C for 336 hr. Specimen etched in HF prior to replication. 12,000×.

to the existence of a strain gradient in the oxide film, we attempted to simulate such test conditions by corroding 6061 aluminum specimens mounted under elastic stress. Such specimens exhibited twice the corrosion rate of unstrained 6061 aluminum.

Adequate investigation of the effect of an anodic film on the 6061 alloy will require more severe test conditions. Therefore, in cooperation with the Reactor Division we are planning a test in a flowing loop under conditions of high heat flux. The test specimen will itself be a part of the loop, and its interior is in the form of

[redacted]

a slot 1 × 6.5 × 0.050 in. We have developed a suitable technique for anodizing the interior of such a specimen, and the test will be carried out as soon as the fabrication of the specimen is completed.

## Conversion of $UF_6$ to Uranium Oxides in a Flame Reactor

J. I. Federer W. R. Martin

Direct conversion of $UF_6$ to uranium oxides in a flame reactor has been demonstrated and reported.[5] The reactants, which produced a submicron size powder in a hydrogen-fluorine flame, were hydrogen, oxygen, and $UF_6$. Process optimization and characterization of the product have continued.

Chemical analyses showed 5 to 10% F in as-prepared powder.[5] The fluorine could be derived from two sources: the free fluorine used to form a flame and the fluorine contained in $UF_6$. If the process were used commercially, free fluorine would significantly increase the cost of the product. Uranium oxides were subsequently produced, therefore, in a flame having no free fluorine added, except for ignition. A stable flame was established with 2100, 700, and 25 $cm^3$/min of hydrogen, oxygen, and $UF_6$, respectively. The fluorine content and x-ray analysis of the product prepared with these flow rates at 15 and 50 torr are presented in Table 1.4. The fluorine content was comparable to that of powder prepared with no free fluorine added to the flame, showing that the fluorine contamination is derived from $UF_6$. The presence of $UF_4$ in the powder from the dry traps in experiment 14 accounts for the relatively high fluorine content of the sample.

During flame stabilization studies, the intensity and size of the flame were found to be sensitive to pressure changes of 5 torr or less. The flame is still being characterized in terms of flow rates and pressure.

Chemical and x-ray analyses of as-prepared powder do not agree on the phases present. Chemical analysis of some samples shows that $UO_2$,

[5] J. I. Federer, Fuels and Materials Development Program Quart. Progr. Rept. Sept. 30, 1967, ORNL-TM-2020, p. 41.

Table 1.4. Composition of Oxides from Flame Reactor Experiments

| Experiment | Sample Location | Reaction Pressure (torr) | Fluorine Content (wt %) | X-Ray Analysis[a] | | | |
|---|---|---|---|---|---|---|---|
| | | | | $UO_2$ | $U_3O_8$ | $UF_4$ | Other[b] |
| 14 | Reaction tube | 50 | 4.81 | S | NF | NF | NF |
| | Dry traps | | 19.8 | S | NF | S | W |
| 15 | Reaction tube | 15 | 7.62 | S | W | NF | W |
| | Dry traps | | 8.33 | S | W | NF | W |

[a]Amount of phase estimated from intensities of lines on x-ray powder patterns. S — strong, W — weak, NF — sought, not found.

[b]Unidentified compounds.

$UO_3$, $UF_4$, $U(OH)_4$, $UO_2F_2$, and $H_2O$ are present, but x-ray diffraction shows only $UO_2$ and a small amount of unidentified compounds. The compound $U(OH)_4$, being amorphous, would not be shown by x-ray diffraction, nor would water. The compounds $UO_3$, $UF_4$, and $UO_2F_2$, if actually present, may be too finely divided or not sufficiently crystalline to diffract x rays. Nevertheless, heat treatment in hydrogen at 1000°C produces $UO_2$ having a greatly reduced fluorine content.[5] The compound $UO_3$ is reduced to $UO_2$; $U(OH)_4$ is decomposed to $UO_2$ and water, while $UF_4$, $UO_2F_2$, and other fluoride or oxyfluoride compounds react with water to form $UO_2$ and HF.

The effect of heat-treating temperature on fluorine removal was studied. Samples of as-prepared powder containing 4.65% F were heated in dry hydrogen at 600, 800, and 1000°C for 16 hr. The results are:

| Temperature (°C) | Fluorine Content (wt %) | Oxygen-to-Uranium Ratio |
|---|---|---|
| 600 | 0.22 | 2.116 |
| 800 | 0.091 | 2.281 |
| 1000 | 0.032 | 2.358 |

The highest temperature, 1000°C, yielded the lowest fluorine content, but the value is much higher than the 5 to 10 ppm F obtained in other samples by a similar treatment.[5] In addition, the oxygen-to-uranium ratio increased with increasing temperature, which is the reverse of

the expected behavior. The particle size of the powder was independent of temperature and about ten times larger than the as-prepared powder.

The sinterability of the powder is presently being investigated. Two batches of powder, each containing about 10 wt % F, were heat treated in dry hydrogen at 1000°C for 16 hr before pressing and sintering. The analysis of this material is shown below:

| Batch Number | Fluorine Content (ppm) | Oxygen-to-Uranium Ratio |
|---|---|---|
| 3A | 33 | < 2.001 |
| 4-3A | 29 | < 2.001 |

The material was subsequently treated as follows:

1. uniaxially pressed at 10,000 psi into 1/4-in.-diam × 1/4-in.-long pellets having a bulk density about 45% of theoretical,
2. isostatically pressed at 10,000, 30,000 or 50,000 psi, which increased the bulk density slightly,
3. sintered at 1200, 1400, 1600, or 1800°C for 4 hr. A hydrogen atmosphere was used for pellets sintered at 1200°C, but due to a furnace heating limitation sintering at higher temperatures was performed in a vacuum of $10^{-5}$ torr or less.

The relative bulk densities are shown for one batch as a function of pressing pressure and sintering temperature in Fig. 1.3; the other batch behaved similarly. The pellets sintered at 1200°C have surface-connected porosity; therefore, the bulk densities are higher than the true values. The pellets are being examined metallographically to determine the void distribution. The highest density obtained in both batches of powder was 97% of the theoretical value. Higher densities might be obtained if the as-prepared submicron powder were pelletized and the fluorine were removed during the sintering heat treatment; this procedure would take advantage of the greater compaction possible with very fine powder.

[redacted]



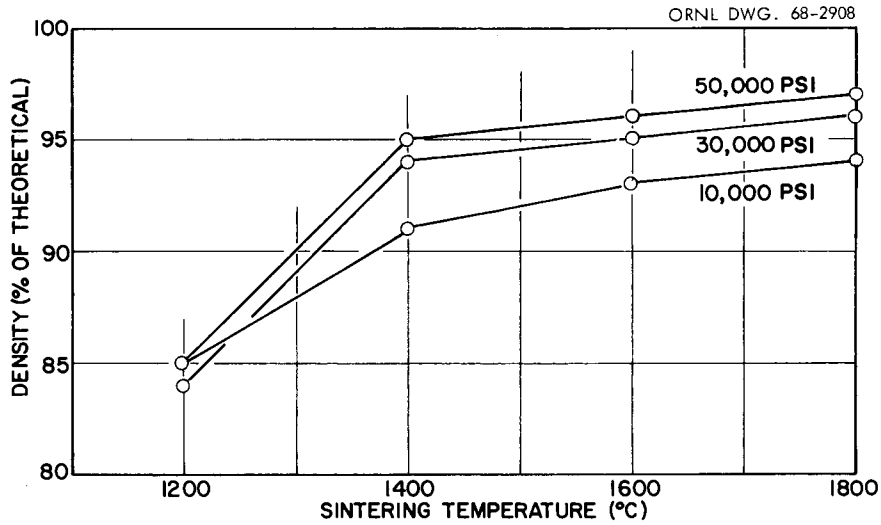


Fig. 1.3. Density of Flame Reactor Powder as a Function of Pressing Pressure and Sintering Temperature.

## Economic Analysis of the Flame Reaction Process for Converting $UF_6$ to $UO_2$ Powder

R. B. Pratt J. I. Federer

An economic analysis has been made of a flame reaction process for converting $UF_6$ directly to $UO_2$ powder form by reaction with hydrogen, fluorine, and oxygen. This analysis was based on relative weights of consumable and flame-reactor-produced materials shown below for plant sizes ranging from 100 to 3000 kg $UO_2$ per day:

| Materials Consumed | Relative Weight |
|---|---|
| $O_2$ | 0.124 |
| $F_2$ | 0.1915 |
| $UF_6$ | 1.6 |
| $H_2$ | 0.1275 |
| **Materials Produced** | |
| $UO_2$ | 1.0000 |
| HF | 0.7335 |
| $UF_4$ | 0.266 |
| $H_2O$ | 0.1325 |
| $H_2$ excess | 0.0821 |

[redacted]

[redacted]



The consumable material weight percentages are comparable to the percentages used by Smiley and Pashley[6] in their study of flame reactor conversions of fluorinated tungsten and rhenium. The process flowsheet investigated includes the following items: consumable materials and their storage and handling, the flame reactor and product collection and defluorination, HF recovery, recycle and waste-disposal system, and the gaseous effluent disposal system. Preliminary investigation revealed the cost of fluorine to be a significant fraction of the total cost of producing $UO_2$ by this method. Therefore, costs for both truck delivery of liquid fluorine and for building an on-site fluorine-production plant were examined.

This analysis shows that the cost of converting $UF_6$ to $UO_2$ with the flame reactor ranged from \$36.00/kg $UO_2$ at a production rate of 100 kg/day to \$9.04 kg at a 3000 kg/day $UO_2$ production rate for capital costs amortized at the rate of 22% per annum. Comparable costs for producing sol-gel shards over the same range of production rates are \$24.50/kg and \$4.20/kg, respectively.

Obviously, for the flame reaction process to be considered competitive, significant cost reductions must be made. A simple and straightforward method for decreasing these costs is to eliminate the requirement for excess fluorine. Preliminary experiments have shown that through improved nozzle design the fluorine contained in the $UF_6$ is sufficient to produce the required heat for the conversion of $UF_6$ to $UO_2$. Therefore, we calculated new conversion costs from which the cost of excess fluorine has been removed. These conversion costs are \$23.06/kg $UO_2$ at 100 kg/day and \$6.94/kg at 3000 kg/day. The unit cost is less than that of sol-gel powder up to a production rate of approximately 400 kg/day.

---

[6]S. H. Smiley and J. H. Pashley, Economic Analysis of Fluorination Processes for the Recovery and Recycle of Valuable CVD Materials, K-L-6151 (1967).

[redacted]

## Preparation of $PuO_2$ Powder from $PuF_6$ by Chemical Vapor Deposition

W. C. Robinson W. R. Martin

The fluorine regulator proved impossible to operate inside the alpha box. Two consecutive regulators became impaired in the early stages of operation and could not be repaired inside the box. The internal fluorine cylinder and regulator were removed from the box and installed outside the building, and an additional pressure gage was added to the line to indicate the fluorine pressure inside the box. When this assembly was completed, the apparatus was operated in place with $UF_6$ for four experiments. A quantity of $UO_2$ powder was produced, and all portions of the apparatus were tested except for the fluorination assembly, since no fluorination is necessary for $UF_6$ conversion.

A 180-g supply of $PuF_4$ was then divided into 20-g portions and placed inside the fluorination box. The fluorination chamber was loaded with 20 g of $PuF_4$, and 100 $cm^3$/min of fluorine was pumped over the material, which was held at 590°C and 500 torr for 5 hr. The resulting $PuF_6$ was collected in a dry-ice cold trap. The $PuF_6$ was then used in a 1000°C conversion experiment, which produced a small quantity of green powder. The powder is presently being examined by x-ray diffraction and chemical analysis. Plutonium dioxide is normally green. The experiments were repeated except that 175 $cm^3$/min of fluorine was used in the fluorination study. A somewhat larger amount of green powder was obtained. However, the total amount of $PuF_6$ obtained in a 5-hr fluorination is sufficient only to operate the conversion apparatus for about 20 min. It amounts to 5 to 10 g of $PuO_2$ product. The limitation, then, is not the conversion step, of which this investigation was designed to demonstrate feasibility, but the fluorination step. The conversion seems to be quite easily accomplished at 1000°C, if one accepts the premise that the green powder produced is indeed $PuO_2$.

[redacted]



## 2. MECHANICAL PROPERTIES

J. R. Weir, Jr.

One objective of this program is to determine the effect of irradiation on the mechanical properties of alloys of interest as fuel cladding and to find a metallurgical condition for the alloys that produces the least effect of subsequent irradiation on the mechanical properties. To accomplish this, our study concerns the interaction of radiation-induced defects and the substructure of the alloys, the effect of irradiation temperature, postirradiation test variables, and neutron dosimetry in the facilities used in the irradiations. The material selected for initial study is type 304 stainless steel and related compositions containing titanium. Additional materials will be studied including type 316 stainless steel, Incoloy 800, and three vanadium alloys. The Hastelloy N work is not supported by the Fuels and Materials Branch, but is added because of its general interest.

### Effects of Neutron Irradiation on the Elevated-Temperature Mechanical Properties of Type 316 Stainless Steel

E. E. Bloom J. R. Weir, Jr.

An investigation of the effects of neutron irradiation upon the mechanical properties of AISI type 316 stainless steel has been started. The initial experiment was a survey to determine the effect of preirradiation annealing treatment and irradiation temperature upon the postirradiation mechanical properties. The composition of the alloy was as follows: 0.068% C, 17.2% Cr, 12.5% Ni, 1.92% Mn, 0.51% Si, 0.004% S, 0.039% P, 2.06% Mo, and 0.0005% B. Specimens were annealed 1 hr at 950, 1050, and 1150°C and then irradiated at temperatures of 550, 650, and 750°C to neutron doses of approximately $9 \times 10^{20}$ neutrons/cm$^2$ (thermal) and $7 \times 10^{20}$ neutrons/cm$^2$ (> 1 Mev). Both tensile and stress-rupture tests are being used to evaluate the mechanical properties.

[redacted]

[redacted]



Irradiation significantly decreases elevated-temperature tensile ductility. Figure 2.1 compares the ductility of the unirradiated alloy (as annealed) to the ductility after irradiation at 550 and 750°C. A thermal control specimen (1 hr at 1050°C plus 2000 hr at 550°C) tested at 650°C exhibited approximately the same ductility as the annealed material. It thus would appear that the reduced ductility is a consequence of the irradiation and not directly related to thermal effects. The reduction in tensile ductility is apparently independent of irradiation temperature over the range of 550 to 750°C.

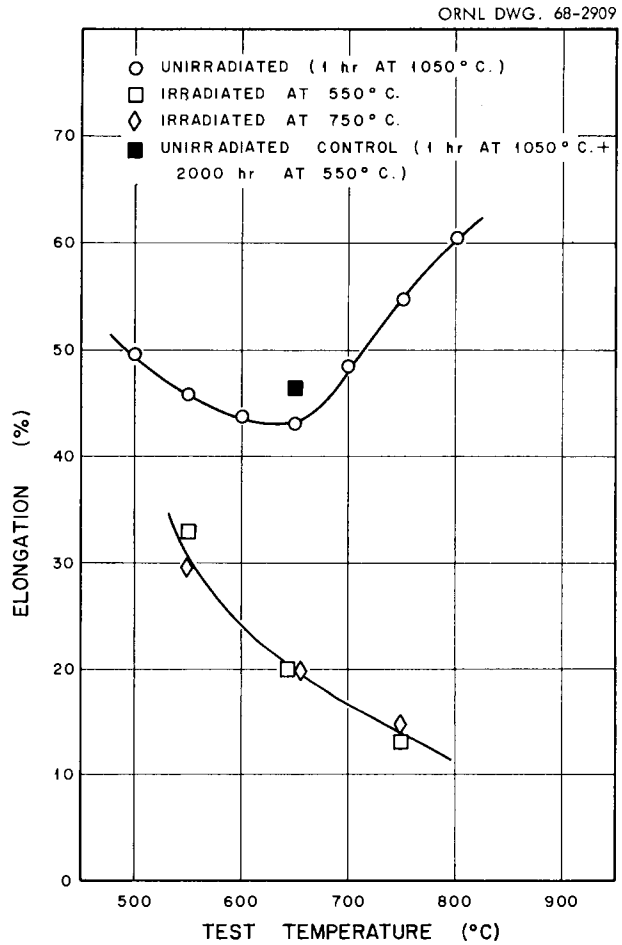


Fig. 2.1. Elevated-Temperature Tensile Ductility of Type 316 Stainless Steel. Strain rate 0.002 $min^{-1}$.

[redacted]

[redacted]



The effect of preirradiation annealing temperature upon the tensile ductility is shown in Fig. 2.2. For test temperatures of 650 and 750°C and for both unirradiated and irradiated specimens, maximum ductility was obtained by annealing 1 hr at 1050°C.

Results of stress-rupture tests completed to date are listed in Table 2.1. Figure 2.3 is a log-stress log-rupture-life plot of these data. It is interesting to note that the ductility of specimens irradiated at 550°C is much lower than that exhibited by specimens irradiated at 750°C, yet with regard to rupture life the opposite is true. Creep rates of the as-annealed specimens and those irradiated at 550°C were approximately the same, while the creep rate of specimens irradiated at

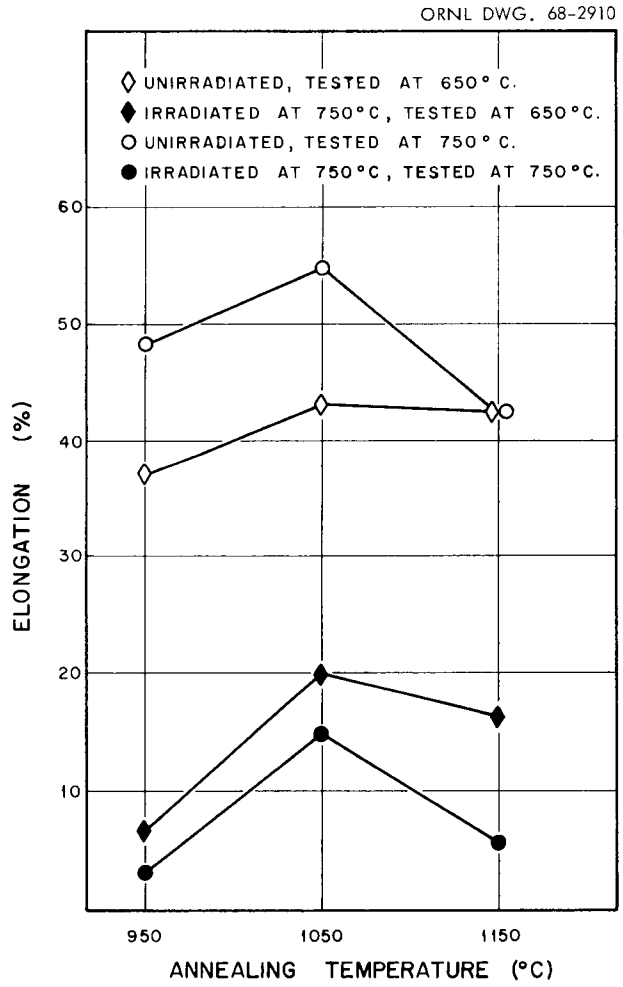


Fig. 2.2. Effect of Annealing Temperature Upon the Ductility of Type 316 Stainless Steel Tested at 650 and 750°C. Strain rate 0.002 $min^{-1}$.

[redacted]

Table 2.1. Stress-Rupture Properties of Type 316 Stainless Steel at 650 °C

| Heat Treatment and/or Irradiation Conditions | Stress (psi) | Rupture Life (hr) | Creep Rate (%/hr) | Elongation (%) | Reduction in Area (%) |
|---|---|---|---|---|---|
| Annealed 1 hr at 1050 °C | 35,000 | 90.8 | 0.14 | 29.6 | 50.4 |
| | 30,000 | 180.1 | 0.024 | 54.5 | 32.9 |
| | 25,000 | 1311.3 | 0.0069 | 30.9 | 57.8 |
| Annealed 1 hr at 1050 °C and irradiated at 550 °C | 30,000 | 15.3 | 0.085 | 3.2 | 9.0 |
| | 25,000 | 252.1 | ~0.005 | 2.7 | 14.3 |
| | 20,000 | >2200 | | >2.3 | |
| Annealed 1 hr at 1050 °C and irradiated at 750 °C | 25,000 | 92.2 | 0.12 | 14.8 | 17.4 |
| | 20,000 | 137.2 | 0.064 | 9.3 | 6.7 |
| | 20,000 | 524.3 | | 16.7 | 22.1 |

[redacted]



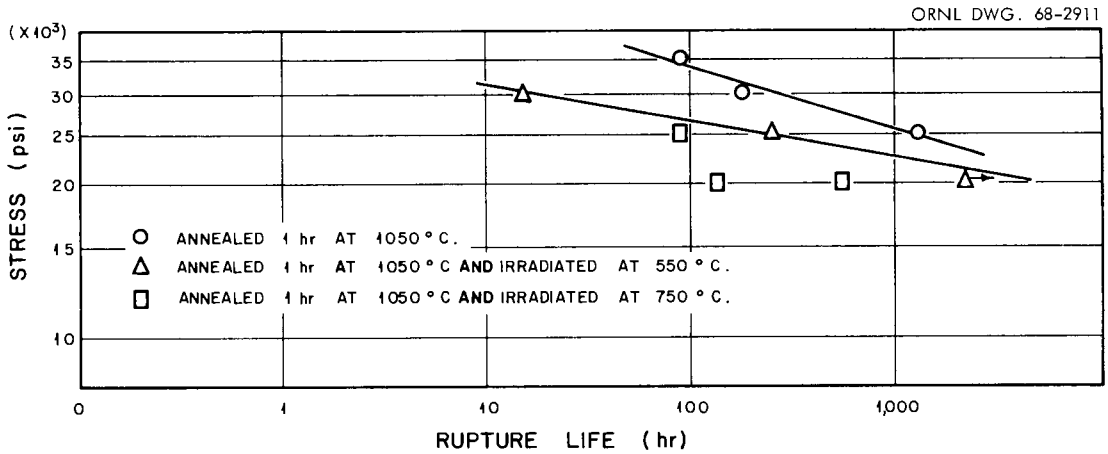


Fig. 2.3. Stress-Rupture Properties of AISI Type 316 Stainless Steel at 650°C in Air.

750°C were significantly higher. Barnby[1] has shown that a considerable portion of the creep resistance of type 316 stainless steel can be attributed to the prevention of dislocation motion by strain aging. When carbon is removed from solution before testing (by an aging treatment) the creep rate is significantly increased. It is thus possible that at the 750°C irradiation temperature (approx 2000 hr) carbide precipitated thus preventing strain-aging and reducing the creep resistance. The higher ductility of the material after irradiation at 750°C as compared to irradiation at 550°C may be a result of the formation of grain boundary carbides.[2] Additional test results and metallographic examination of tested specimens are needed for full understanding of the observed changes in properties.

---

[1]J. T. Barnby, "Effect of Strain Aging on Creep of an AISI 316 Austenitic Stainless Steel," J. Iron Steel Inst. (London) 204, 23 (1966).

[2]W. R. Martin and J. R. Weir, Solutions to the Problems of High-Temperature Irradiation Embrittlement, ORNL-TM-1544 (June 1966).

[redacted]

## Development of Titanium-Modified Type 304L Stainless Steel

E. E. Bloom J. R. Weir

We recently received from the vendor a 2000-lb heat of titanium-modified type 304 stainless steel. The chemical composition of the alloy is given in Table 2.2.

Table 2.2. Chemical Composition of 2000-lb Heat of Titanium-Modified Type 304 Stainless Steel

| Element | Composition, wt % | |
|---|---|---|
| | Vendor's Analysis | ORNL Analysis |
| C | 0.05 | 0.07 |
| Cr | 18.4 | 19.0 |
| Ni | 9.7 | 10.0 |
| Ti | 0.21 | 0.21 |
| Mn | 1.5 | 0.65 |
| Si | 0.7 | 0.8 |
| P | 0.010 | 0.013 |
| S | 0.006 | 0.002 |
| Total N | 0.0075 | 0.009 |
| Soluble N | | 0.003 |
| B | | 0.0027 |

Elevated-temperature tensile and stress-rupture properties are being measured for pretest annealing treatments of 1 hr at 925, 1000, and 1038°C. Specimens having similar heat treatments are being irradiated at 650°C in a poolside position of the ORR. This experiment will be removed from the reactor in December 1967.

The strength and ductility properties of the alloy will be compared to those previously obtained for a 1500-lb heat of titanium-modified type 304L stainless steel to determine optimum mechanical properties and resistance to irradiation damage.

## The Effects of Prestrain on the Tensile and Creep Properties of Irradiated and Unirradiated Type 304L Modified Stainless Steel

D. W. Short G. T. Newman

Under certain conditions of prior prestrain and aging, the creep properties of type 316 stainless steel are improved, the minimum creep rate being decreased and the rupture life increased.[3] The improvement in properties is explained in terms of preferred carbide precipitation on prestrain-induced dislocations, resulting in hindrance to the motion of both these dislocations and those generated during creep.

The presence of small amounts of strain, resulting from material production, may therefore have an influential effect on the subsequent service properties of cladding. Studies are at present being conducted, based on the observations described above, for type 304L stainless steel modified by the addition of titanium. A typical analysis of such material is: 19.5% Cr, 11.16% Ni, 0.012% C, 1.01% Mn, 0.046% Si, 0.006% P, 0.013% S, and 0.19% Ti. Tensile and creep tests are being conducted on both irradiated and unirradiated material.

After an initial heat treatment of 1 hr at 925°C, specimens were deformed in tension to a nominal 1, 2, 5, 10, and 20% prestrain. The prestrains were conducted at 300°C to produce as near a homogeneous dislocation distribution as possible. Electron microscopy of unstrained material revealed a significant increase in the amount of matrix precipitation as a result of aging at 700°C for 100 hr. Specimens were therefore subjected to this heat treatment after prestrain.

The results of tensile tests conducted on unirradiated material at 700°C in air at a strain rate of 0.002 $min^{-1}$ are shown in Table 2.3. Increasing prestrain up to approximately 5% progressively increases the yield stress without any significant changes in elongation, reduction in area, uniform strain, and ultimate tensile stress. While the yield stress continues to increase after prestrains of 10% and above, a decrease in both elongation and uniform strain and an increase in

---

[3] F. Garofalo, F. Von Gemmingen, and W. F. Domis, Trans. Am. Soc. Metals 54, 430 (1961).

Table 2.3. Results of Tensile Tests Conducted on Unirradiated Modified Type 304L Stainless Steel[a]

| Prestrain (%) | Yield Stress[b] (psi) | Elongation (%) | Ultimate Tensile Stress (psi) | Reduction in Area (%) | Uniform Strain (%) |
|---|---|---|---|---|---|
| | $\times 10^3$ | | $\times 10^3$ | | |
| 1.1 | 16.5 | 59.6 | 23.2 | 93.9 | 9.7 |
| 2.0 | 17.5 | 55.0 | 23.6 | 92.1 | 13.2 |
| 4.4 | 20.1 | 56.2 | 24.0 | 93.2 | 11.5 |
| 9.2 | 22.8 | 46.7 | 25.0 | 90.2 | 7.4 |
| 17.3 | 26.9 | 38.9 | 29.1 | 91.8 | 0.6 |
| Nil | 14.7 | 63.1 | 22.1 | 94.5 | 12.4 |

[a]Tested at 700°C and 0.002 $min^{-1}$ strain rate.

[b]0.2% offset.

ultimate tensile stress are observed. The fact that the reduction in area remains essentially constant over the prestrain range studied indicates that the prestrain does not seriously influence the mode of failure of the material. The decrease in elongation at the higher prestrains may therefore be associated with a decrease in the strain before the onset of necking, in agreement with the uniform strain data. Tensile data are not yet available on the irradiated material.

Creep tests have been performed on both irradiated and unirradiated material that had been prestrained at 300°C and subsequently aged at 700°C for 100 hr. The tests were conducted at 700°C under an initial stress of 15,000 psi. The irradiations were performed in the hydraulic facility of the ORR at a temperature of 50°C and approximate doses of $1 \times 10^{20}$ neutrons/$cm^2$ (thermal) and $1 \times 10^{20}$ neutrons/$cm^2$ (> 1 Mev).

The results of these tests are shown in Tables 2.4 and 2.5. The data are not yet complete enough to allow a full comparison between irradiated and unirradiated material; however, several interesting trends are apparent. Both irradiated and unirradiated material exhibit

[redacted]



Table 2.4. Creep of Unirradiated Material Tested at 700°C

| Prestrain (%) | Rupture Life (hr) | Elongation (%) | Reduction in Area (%) | Minimum Creep Rate (%/hr) |
|---|---|---|---|---|
| 0.9 | 36.1 | 80.1 | 77.3 | 1.07 |
| 1.9 | 41.9 | 86.2 | 88.5 | 0.97 |
| 5.0 | 42.6 | 81.4 | 84.5 | 0.97 |
| 8.5 | 62.3 | 63.9 | 79.0 | 0.39 |
| 10.5 | 85.7 | 70.0 | 79.6 | 0.21 |

Table 2.5. Irradiated Material Tested at 700°C

| Prestrain (%) | Rupture Life (hr) | Elongation (%) | Reduction in Area (%) | Minimum Creep Rate (%/hr) |
|---|---|---|---|---|
| Nil | 105.5 | 52.0 | 13.7 | 0.32 |
| Nil | 123.3 | 53.4 | 15.8 | 0.28 |
| 4.6 | 72.7 | 41.5 | 19.2 | 0.22 |
| 4.7 | 91.4 | 51.9 | 22.2 | 0.29 |
| 7.0 | 129.2 | 52.4 | 19.2 | 0.10 |
| 7.4 | 123.6 | 35.8 | 15.8 | 0.07 |
| 14.7 | 139.1 | 37.1 | 17.1 | 0.05 |

decreased minimum creep rate with increasing amounts of prior prestrain. This effect might be expected in view of the work described on type 316 stainless steel,[3] but what might not be expected is the lower minimum creep rate and longer rupture life of the irradiated material compared to that of unirradiated material subjected to similar amounts of prestrain. At the irradiation temperature used displacement damage will occur and will undoubtedly affect the subsequent properties of the material. Interpretation is tentative because optical and electron microscopy are not yet complete. The enhanced reduction in minimum

[redacted]

creep rate in irradiated material may be due to radiation-damage-induced precipitation, although at the temperature of testing, much of the damage will have annealed out and the stability of such precipitation is open to question. The influence of radiation damage on the dislocation structure resulting from prestrain may also be of importance. We hope that electron microscopy on the creep specimens will reveal a more definite understanding of the data.

## Comparison of Postirradiation Properties of Six High-Temperature Alloys at 760°C

D. G. Harman

In a survey experiment we are comparing the properties of several irradiated high-temperature alloys. Hastelloy X, Hastelloy N, titanium-modified Hastelloy N (0.5% Ti), type 304 stainless steel, titanium-modified type 304L stainless steel (0.2% Ti), and several heats of Incoloy 800 containing varying amounts of titanium and carbon are being investigated.

The irradiation was conducted at a poolside facility of the ORR at 760°C to a thermal dose of 2 to $3 \times 10^{20}$ neutrons/cm$^2$. The rod specimens are of the buttonhead design used in previous ORNL experiments, and they are being tested at 760°C.

The compositions of the alloys being tested are included as Table 2.6. Two carbon levels are being investigated in Incoloy 800; low carbon (approx 0.03%) with titanium from 0.21 to 0.41% and high carbon (approx 0.12%) with titanium from < 0.02 to 0.26%.

Eight specimens of each alloy were irradiated; four as annealed and four annealed followed by 100-hr aging. Hastelloy N was aged at 871°C, while all other preirradiation aging was at 800°C. To study the effect of strain rate, two tensile tests and two creep rupture tests were performed on each of the two metallurgical conditions for each alloy. Identical tests are being performed on control specimens that have experienced the same thermal history as those irradiated.

Table 2.6. Chemical Composition of High-Temperature Alloys Used (Survey Experiment ORR-182)

| Alloy | Heat | Chemical Composition (wt %) | | | | | | | | B (ppm) |
|---|---|---|---|---|---|---|---|---|---|---|
| | | Ni | Fe | Cr | Mo | W | C | Ti | Al | |
| Hastelloy N | 5911 | Bal | 0.03 | 6.1 | 17.0 | 0.01 | 0.06 | 0.07 | 0.15 | 10 |
| Titanium-Modified Hastelloy N | 21545 | Bal | | 7.2 | 12.0 | | 0.05 | 0.5 | | 2 |
| Hastelloy X-280 | E-9518 | Bal (~ 47) | 17.5 | 22.8 | 9.2 | 0.6 | 0.10 | | 0.26 | |
| Type 304 Stainless Steel | 33107 | 8.9 | Bal (~ 70) | 19.0 | | | 0.06 | < 0.02 | | 2 |
| Type 304L Stainless Steel | 3756 | 11.2 | Bal (~ 69) | 19.5 | | | 0.012 | 0.2 | | 3 |
| Incoloy 800 | 154M | 30 | Bal (~ 46) | 19 | 0.1 | | 0.03 | 0.15 | 0.11 | 2.0 |
| Incoloy 800 | 25B | 30 | Bal (~ 46) | 20 | | | 0.03 | 0.21 | 0.22 | 2 |
| Incoloy 800 | 33D | 29 | Bal (~ 46) | 18 | | | 0.02 | 0.31 | 0.21 | 2 |
| Incoloy 800 | N | 31.5 | Bal (~ 46) | 20.5 | | | 0.04 | 0.41 | 0.22 | (?) |
| Incoloy 800 | 45G | 32 | Bal (~ 46) | 19 | | | 0.10 | < 0.02 | 0.21 | 3 |
| Incoloy 800 | 93H | 31 | Bal (~ 46) | 21 | | | 0.12 | 0.10 | 0.24 | 5 |
| Incoloy 800 | 41L | 28 | Bal (~ 46) | 19 | | | 0.14 | 0.17 | 0.22 | 5 |
| Incoloy 800 | 54J | 30 | Bal (~ 46) | 20 | | | 0.12 | 0.26 | 0.21 | 4 |

The test results are listed in Table 2.7. The control data are shown in parentheses. The data are preliminary and may be changed slightly as the tests are completely analyzed. As can be seen from the table many of the control creep tests are yet to be run.

As might be expected, all of the alloys suffered irradiation damage but to different degrees. Aging before the irradiation had very little effect at the test temperature of 760°C except to improve the short-time tensile ductility of modified type 304L stainless steel.

A most important parameter for nearly all of these alloys after irradiation is strain rate. Figure 2.4 shows the elongation as a function of strain rate for the three nickel-base alloys. All three alloys exhibit a critical strain rate (or stress level) for minimum postirradiation ductility. Hastelloy N is the most affected, with the elongation falling below 0.2% and recovering to only 1.5% at the lower strain rates. The addition of 0.5% Ti increases the postirradiation ductility of this alloy significantly. Although the ductility of the modified alloy falls below 1% at intermediate strain rates, improved recovery of ductility is noted at the lower strain rates (7% elongation at the lowest creep stress).

Hastelloy X has better postirradiation ductility than does the modified Hastelloy N at this temperature. The minimum elongation for this alloy was about 7%, and it increased to 11% at the lower stresses.

The postirradiation ductilities of type 304 stainless steel, modified type 304L stainless steel, and Incoloy 800 in the annealed condition are shown as a function of strain rate in Fig. 2.5. Type 304 stainless steel is the only alloy that showed continuously decreasing ductility with decreasing strain rate. The elongation at the lowest stress was only about 7% as compared to 25% for the 0.05 $min^{-1}$ tensile test.

Both modified type 304L stainless steel and Incoloy 800 showed increasing ductility at the lower strain rates. Incoloy 800 with 0.12% C and 0.10% Ti (heat 93H) is outstanding in this respect, exhibiting a creep ductility of 45% at 10,000 psi stress. This particular heat of Incoloy 800 creep tested at low stresses suffered essentially no loss in ductility due to the irradiation. Examination of the effect

Table 2.7. Preliminary Report on Testing Status ORR-182. Materials Survey Experiment[a]

| Preirradiation Condition | Strain Rate (%/hr) | Strength (psi) | | Creep Stress (psi) | Time to Rupture (hr) | Strain (%) | |
|---|---|---|---|---|---|---|---|
| | | 0.2% Yield | Ultimate Tensile | | | Uniform | Total |
| | | $\times 10^3$ | $\times 10^3$ | $\times 10^3$ | | | |
| | | Incoloy 800 (Heat 25B, 0.21% Ti, 0.03% C) | | | | | |
| Annealed | $3 \times 10^2$ | 12.50 (17.52) | 35.65 (34.71) | | | 10.1 (16.7) | 11.5 (52.1) |
| Annealed | $1.2 \times 10^1$ | 12.80 (20.97) | 22.49 (22.28) | | | 5.2 (6.2) | 8.2 (57.7) |
| Annealed | $1.5 \times 10^{-1}$ | | | 10.0 | 91 | | 16.0 |
| Annealed | $2.8 \times 10^{-2}$ | | | 8.5 | 481 | | 17.0 |
| Aged | $3 \times 10^2$ | 12.56 (24.73) | 32.00 (36.24) | | | 7.4 (11.9) | 7.9 (51.0) |
| Aged | $1.2 \times 10^1$ | 13.65 (13.15) | 21.91 (22.19) | | | 2.1 (8.6) | 5.8 (71.0) |
| Aged | $9.3 \times 10^{-2}$ | | | 10.0 | 119 | | 14.8 |
| Aged | $4.3 \times 10^{-2}$ | | | 8.5 | 307 | | 18.6 |
| | | Incoloy 800 (Heat 154M, 0.15% Ti, 0.03% C) | | | | | |
| Annealed | $3 \times 10^2$ | 14.15 (11.63) | 32.90 (33.01) | | | 7.7 (15.7) | 8.9 (46.0) |
| Annealed | $1.2 \times 10^1$ | 17.02 (17.31) | 19.04 (22.67) | | | 3.9 (7.7) | 6.7 (63.3) |
| Annealed | $9.0 \times 10^{-2}$ | | | 10.0 | 157 | | 17.6 |
| Annealed | $4.4 \times 10^{-2}$ | | | 8.5 | 274 | | 15.1 |
| Aged | $3 \times 10^2$ | 14.94 (18.69) | 30.25 (33.80) | | | 6.4 (13.7) | 7.1 (44.7) |
| Aged | $1.2 \times 10^1$ | 12.27 (11.84) | 21.69 (20.00) | | | 4.2 (9.8) | 5.5 (55.9) |
| Aged | $9.4 \times 10^{-2}$ | | | 10.00 | 125 | | 15.0 |
| Aged | $3.8 \times 10^{-2}$ | | | 8.5 | 259 | | 13.4 |
| | | Incoloy 800 (Heat 33D, 0.31% Ti, 0.02% C) | | | | | |
| Annealed | $3 \times 10^2$ | 8.02 (18.64) | 38.02 (37.61) | | | 9.7 (13.0) | 11.5 (51.5) |
| Annealed | $1.2 \times 10^1$ | 13.49 (17.25) | 23.71 (22.24) | | | 6.2 (6.9) | 13.5 (61.0) |
| Annealed | $1.1 \times 10^{-1}$ | | | 10.00 | 179 | | 14.8 |
| Annealed | $4.4$ (3.9) $\times 10^{-1}$ | | | 12.5 | 33 (113) | | 13.9 (63.9) |

Table 2.7 (continued)

| Preirradiation Condition | Strain Rate (%/hr) | Strength (psi) | | Creep Stress (psi) | Time to Rupture (hr) | Strain (%) | |
|---|---|---|---|---|---|---|---|
| | | 0.2% Yield | Ultimate Tensile | | | Uniform | Total |
| | | $\times 10^3$ | $\times 10^3$ | $\times 10^3$ | | | |
| | | Incoloy 800 (Heat 33D, 0.31% Ti, 0.02% C) (continued) | | | | | |
| Aged | $3 \times 10^2$ | 13.30 (16.82) | 35.41 (37.22) | | | 10.0 (12.7) | 11.4 (54.8) |
| Aged | $1.2 \times 10^1$ | 8.76 (12.55) | 25.12 (21.49) | | | 6.9 (7.3) | 10.5 (57.8) |
| Aged | $3.4 \times 10^{-1}$ | | | 12.4 | 37 | | 17.0 |
| Aged | 4.8 (3.7) $\times 10^{-1}$ | | | 12.5 | 24 (101) | | 14.5 (39.2) |
| | | Incoloy 800 (Heat N, 0.41% Ti, 0.04% C) | | | | | |
| Annealed | $3 \times 10^2$ | 15.15 (13.23) | 33.42 (34.51) | | | 10.1 (15.2) | 12.4 (55.0) |
| Annealed | $1.2 \times 10^1$ | 8.76 (16.13) | 16.37 (20.23) | | | 6.6 (5.0) | 13.5 (68.1) |
| Annealed | $1.5 \times 10^{-1}$ | | | 10.0 | 96 | | 18.3 |
| Annealed | 5.4 (8.1) $\times 10^{-1}$ | | | 12.5 | 23 (61.5) | | 15.8 (74.5) |
| Aged | $3 \times 10^2$ | 13.65 (12.94) | 33.77 (32.84) | | | 10.3 (12.7) | 12.1 (51.4) |
| Aged | $1.2 \times 10^1$ | 13.57 (16.35) | 21.50 (19.38) | | | 5.2 (4.3) | 9.5 (64.6) |
| Aged | 1.4 (1.4) $\times 10^{-1}$ | | | 10.0 | 95 (294) | | 17.0 (74.5) |
| Aged | 4.6 (6.0) $\times 10^{-1}$ | | | 12.5 | 22 (71) | | 11.0 (53.7) |
| | | Incoloy 800 (Heat 45G, <0.02% Ti, 0.10% C) | | | | | |
| Annealed | $3 \times 10^2$ | 17.66 (18.93) | 37.40 (39.51) | | | 8.3 (13.4) | 11.6 (38.9) |
| Annealed | $1.2 \times 10^1$ | 18.44 (18.90) | 23.03 (24.65) | | | 8.0 (6.5) | 10.2 (41.7) |
| Annealed | $4.3 \times 10^{-2}$ | | | 10.0 | 189 | | 12.9 |
| Aged | $3 \times 10^2$ | 22.10 (28.70) | 36.85 (39.17) | | | 7.7 (9.2) | 11.1 (34.7) |
| Aged | $1.2 \times 10^1$ | 18.52 (15.34) | 23.34 (23.54) | | | 6.5 (7.1) | 9.5 (37.5) |
| Aged | $4.0 \times 10^{-2}$ | | | 10.0 | 260 | | 15.2 |

Table 2.7 (continued)

| Preirradiation Condition | Strain Rate (%/hr) | Strength (psi) | | Creep Stress (psi) | Time to Rupture (hr) | Strain (%) | |
|---|---|---|---|---|---|---|---|
| | | 0.2% Yield | Ultimate Tensile | | | Uniform | Total |
| | | $\times 10^3$ | $\times 10^3$ | $\times 10^3$ | | | |
| | | Incoloy 800 (Heat 93H, 0.10% Ti, 0.12% C) | | | | | |
| Annealed | $3 \times 10^2$ | 19.60 (18.02) | 35.50 (36.94) | | | 9.9 (14.2) | 12.8 (45.2) |
| Annealed | $1.2 \times 10^1$ | 17.38 (17.88) | 23.11 (24.94) | | | 7.4 (7.6) | 11.6 (55.9) |
| Annealed | $6.6 \times 10^{-2}$ | | | 10.0 | 401 | | 45.4 |
| Annealed | 6.1 (2.3) $\times 10^{-1}$ | | | 12.5 | 42 (132) | | 34.2 (41.3) |
| Aged | $3 \times 10^2$ | 21.75 (18.27) | 35.60 (38.44) | | | 7.0 (10.8) | 8.7 (47.7) |
| Aged | $1.2 \times 10^1$ | 17.17 (17.84) | 22.08 (24.53) | | | 8.4 (10.0) | 12.8 (~53) |
| Aged | $9.1 \times 10^{-2}$ | | | 10.0 | 300 | | 37 |
| Aged | 3.4 (1.8) $\times 10^{-1}$ | | | 12.5 | 79 (199) | | 37 (60) |
| | | Incoloy 800 (Heat 54J, 0.26% Ti, 0.12% C) | | | | | |
| Annealed | $3 \times 10^2$ | 19.60 (14.91) | 35.95 (34.64) | | | 8.9 (12.1) | 13.2 (54.1) |
| Annealed | $1.2 \times 10^1$ | 17.51 (17.26) | 23.32 (23.42) | | | 6.9 (8.3) | 11.2 (62.9) |
| Annealed | $2.6 \times 10^{-1}$ | | | 12.5 | 53.1 (181) | | 19.5 (55.7) |
| Annealed | $9.8 \times 10^{-2}$ | | | 10.0 | 141 | | 18.5 |
| Aged | $3 \times 10^2$ | 16.89 (20.08) | 35.95 (37.61) | | | 7.7 (13.2) | 10.2 (50.7) |
| Aged | $1.2 \times 10^1$ | 19.75 (14.87) | 23.11 (21.69) | | | 5.7 (6.4) | 9.2 (61.2) |
| Aged | 2.3 (1.5) $\times 10^{-1}$ | | | 12.5 | 46 (223.4) | | 13.6 (57.2) |
| Aged | $10.0 \times 10^{-2}$ | | | 10.0 | 120 | | 17.1 |

Table 2.7 (continued)

| Preirradiation Condition | Strain Rate (%/hr) | Strength (psi) | | Creep Stress (psi) | Time to Rupture (psi) | Strain (%) | |
|---|---|---|---|---|---|---|---|
| | | 0.2% Yield | Ultimate Tensile | | | Uniform | Total |
| | | $\times 10^3$ | $\times 10^3$ | $\times 10^3$ | | | |
| | | Incoloy 800 (Heat 41L, 0.17% Ti, 0.14% C) | | | | | |
| Annealed | $3 \times 10^2$ | 17.59 (14.83) | 37.30 (36.67) | | | 8.1 (13.5) | 10.3 (50.2) |
| Annealed | $1.2 \times 10^1$ | 21.76 (25.59) | 23.48 (25.84) | | | 5.0 (2.3) | 9.9 (50.4) |
| Annealed | 2.7 (1.6) $\times 10^{-1}$ | | | 12.5 | 50 (200) | | 16.1 (69.8) |
| Annealed | $5.0 \times 10^{-2}$ | | | 10.0 | 184 | | 13.2 |
| Aged | $3 \times 10^2$ | 15.80 (16.35) | 35.95 (39.25) | | | 7.8 (7.0) | 9.3 (50.0) |
| Aged | $1.2 \times 10^1$ | 19.07 (21.75) | 23.00 (23.71) | | | 5.2 (6.5) | 9.3 (41.7) |
| Aged | 2.0 (1.8) $\times 10^{-1}$ | | | 12.5 | 32(188) | | 8.7 (52.3) |
| Aged | $6.9 \times 10^{-2}$ | | | 10.0 | 191 | | 17.5 |
| | | Type 304 Stainless Steel (Heat 33107) | | | | | |
| Annealed | $3 \times 10^2$ | 12.24 (11.43) | 29.33 (30.07) | | | 15.9 (19.7) | 24.8 (55.7) |
| Annealed | $1.2 \times 10^1$ | 15.19 (13.01) | 20.69 (20.46) | | | 8.0 (13.0) | 14.8 (52.2) |
| Annealed | $1.8 \times 10^{-1}$ | | | 10.0 | 35 | | 8.8 |
| Annealed | $7.8 \times 10^{-2}$ | | | 9.0 | 64 | | 7.4 |
| Aged | $3 \times 10^2$ | 11.67 (13.67) | 29.09 (30.99) | | | 13.6 (20.0) | 17.2 (56.9) |
| Aged | $1.2 \times 10^1$ | 12.07 (18.03) | 19.46 (28.46) | | | 7.8 (10.8) | 11.4 (45.9) |
| Aged | $1.4 \times 10^{-1}$ | | | 10.0 | 44 (231) | | 9.0 (38.3) |
| Aged | 8.8 (10.8) $\times 10^{-2}$ | | | 9.0 | 64 (344) | | 7.8 (30.0) |

Table 2.7 (continued)

| Preirradiation Condition | Strain Rate (%/hr) | Strength (psi) | | Creep Stress (psi) | Time to Rupture (hr) | Strain (%) | |
|---|---|---|---|---|---|---|---|
| | | 0.2% Yield | Ultimate Tensile | | | Uniform | Total |
| | | $\times 10^3$ | $\times 10^3$ | $\times 10^3$ | | | |
| | | Modified 304L Stainless Steel (Heat 3756, 0.2% Ti) | | | | | |
| Annealed | $3 \times 10^2$ | 9.76 (9.53) | 21.61 (25.23) | | | 12.1 (24.5) | 16.6 (57.5) |
| Annealed | $1.2 \times 10^1$ | 8.05 (9.34) | 15.76 (17.60) | | | 10.6 (18.0) | 17.4 (60.5) |
| Annealed | $2.8 \times 10^{-1}$ | | | 10.0 | 67 | | 25.0 |
| Annealed | $2.4 \times 10^{-1}$ | | | 9.0 | 72 | | 25.7 |
| Aged | $3 \times 10^2$ | 10.85 (13.36) | 23.99 (26.71) | | | 16.7 (23.2) | 26.0 (54.2) |
| Aged | $1.2 \times 10^1$ | 9.93 (8.84) | 16.67 (15.94) | | | 11.7 (19.6) | 23.7 (72.3) |
| Aged | $3.4 \times 10^{-1}$ | | | 10.0 | 53 | | 25.3 |
| Aged | $1.4 \times 10^{-1}$ | | | 9.0 | 112 | | 25.3 |
| | | Hastelloy X | | | | | |
| Annealed | $3 \times 10^2$ | 35.05 (37.57) | 58.24 (59.45) | | | 7.6 (9.3) | 10.5 (41.3) |
| Annealed | $1.2 \times 10^1$ | 33.00 (30.67) | 38.31 (38.50) | | | 4.0 (4.2) | 7.0 (49.2) |
| Annealed | $8.4 \times 10^{-1}$ | | | 25.0 | 7 | | 8.2 |
| Annealed | $2.4 \times 10^{-1}$ | | | 20.0 | 26 | | 8.7 |
| Aged | $3 \times 10^2$ | 40.63 (29.89) | 58.46 (57.72) | | | 7.2 (10.3) | 10.1 (40.7) |
| Aged | $1.2 \times 10^1$ | 37.55 (34.41) | 40.33 (38.57) | | | 3.6 (4.7) | 7.2 (42.3) |
| Aged | $1.6 \times 10^{-2}$ | | | 13.0 | 460 | | 10.1 |
| Aged | $4.8 \times 10^{-2}$ | | | 15.0 | 184 | | 11.2 |

Table 2.7 (continued)

| Preirradiation Condition | Strain Rate (%/hr) | Strength (psi) | | Creep Stress (psi) | Time to Rupture (hr) | Strain (%) | |
|---|---|---|---|---|---|---|---|
| | | 0.2% Yield | Ultimate Tensile | | | Uniform | Total |
| | | $\times 10^3$ | $\times 10^3$ | $\times 10^3$ | | | |
| | | | Hastelloy N, Heat 5911 | | | | |
| Annealed | $3 \times 10^2$ | 30.07 | 35.76 | | | 2.8 | 2.9 |
| Annealed | $1.2 \times 10^1$ | | 29.92 | | | | <0.1 |
| Annealed | $3.7 \times 10^{-1}$ | | | 25.0 | 0.7 | | 0.3 |
| Annealed | $2.2 \times 10^{-2}$ | | | 12.0 | 27 | | 0.95 |
| Aged | $3 \times 10^2$ | 32.50 | 40.00 | | | 3.2 | 3.3 |
| Aged | $1.2 \times 10^1$ | | | | | | 0.2 |
| Aged | $9.2 \times 10^{-3}$ | | | 10.0 | 104 | | 1.2 |
| Aged | $5 \times 10^{-3}$ | | | 8.0 | 219 | | 1.5 |
| | | | Hastelloy N, Heat 21545, 0.5% Ti | | | | |
| Annealed | $3 \times 10^2$ | 31.67 | 39.20 | | | 6.0 | 6.0 |
| Annealed | $3.4 \times 10^{-2}$ | | | 11.0 | 94 | | 4.7 |
| Annealed | $5.0 \times 10^{-1}$ | | | 25.0 | 0.5 | | 0.66 |
| Annealed | $4.2 \times 10^{-1}$ | | | 20.0 | 1.5 | | 1.0 |
| Aged | $3 \times 10^2$ | 25.80 | 39.51 | | | 7.2 | 7.6 |
| Aged | $1.2 \times 10^1$ | 26.63 | 28.94 | | | 1.4 | 1.8 |
| Aged | $2.0 \times 10^{-2}$ | | | 11.0 | 296 | | 7.0 |
| Aged | $4 \times 10^{-2}$ | | | 12.0 | 101 | | 5.2 |

[a]Irradiated at 760°C, tested at 760°C. Control data in parentheses.

[redacted]



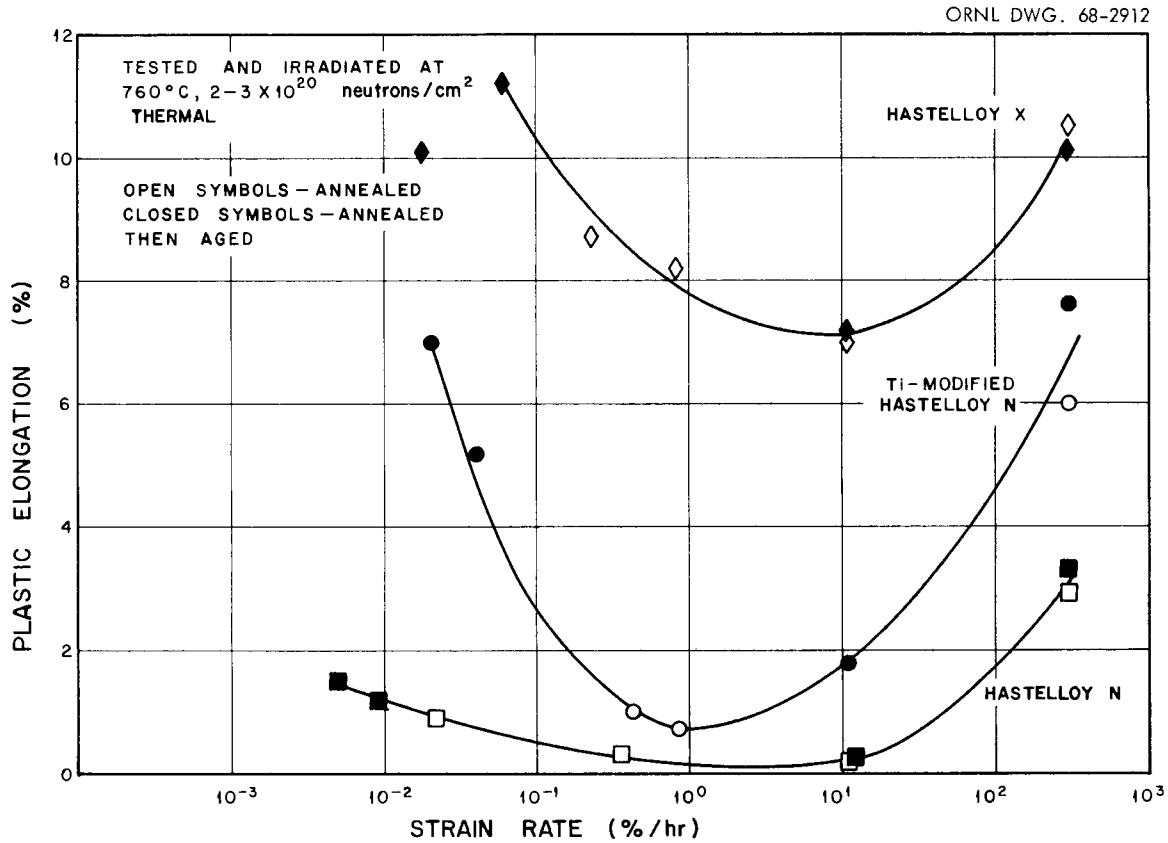


Fig. 2.4. The Effect of Strain Rate on the Postirradiation Ductility of Three Nickel-Base Alloys.

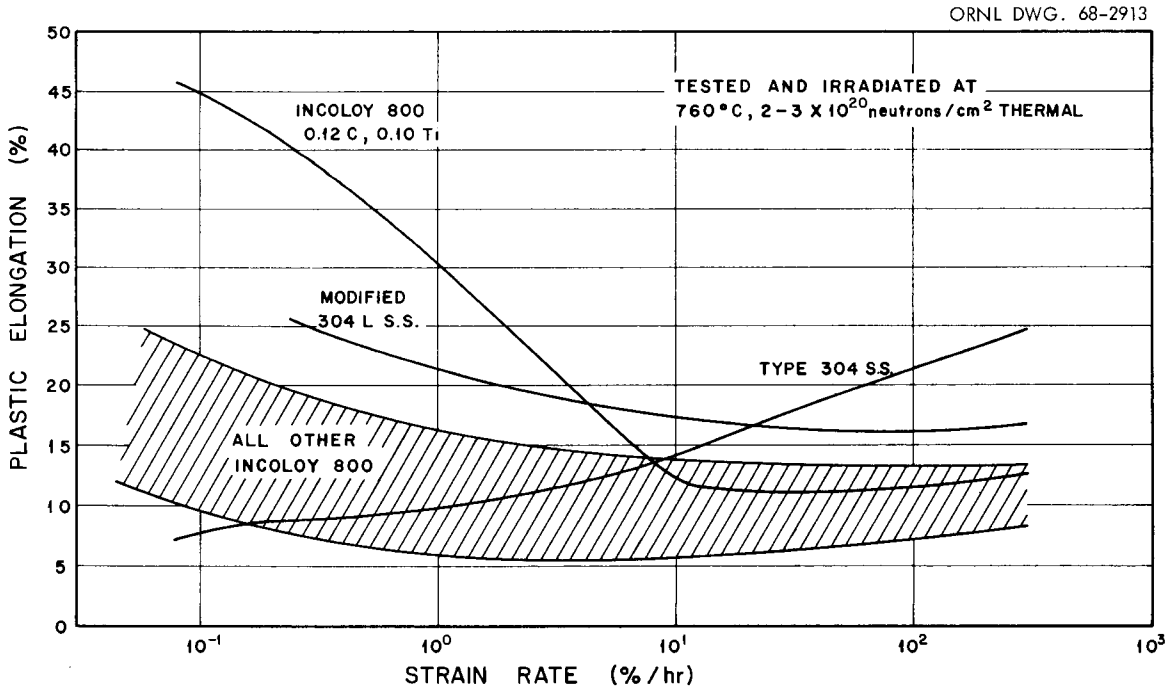


Fig. 2.5. The Effect of Strain Rate on the Postirradiation Ductility of Incoloy 800 and Stainless Steel.

[redacted]

of titanium content in the other high-carbon heats of Incoloy 800 reveals that this increased ductility occurs only at about 0.1% Ti. No beneficial effect, for example, results from 0.17% Ti in the high-carbon heat 41L.

One explanation of the beneficial effect of titanium has been that it ties up carbon as TiC and thus prevents harmful carbide precipitation (e.g., $M_{23}C_6$, $M_6C$) at grain boundaries. The amount of titanium necessary to tie up all of the carbon would be about four times the weight percent of carbon present. We should then expect to see a ductility peak at 0.4 to 0.5% Ti for the high-carbon Incoloy 800 rather than the observed peak at 0.1% Ti.

A recent irradiation experiment at 700°C is showing the same ductility peak for both the high-carbon and low-carbon Incoloy 800 at 0.1% Ti. Ductility seems to be independent of carbon content but sensitive to grain size, with the finer grained material being more ductile.

Electron transmission and fractographic studies have been initiated to help explain this phenomenon.

## Development of a Modified Hastelloy N with Improved Resistance to Radiation Damage

H. E. McCoy, Jr. J. R. Weir

The creep-rupture properties of Hastelloy N are degraded seriously when the material is irradiated. Both the rupture life at a given stress and the rupture ductility are reduced. It is reasonably well established that these property changes arise from the formation of helium in the alloy from the $^{10}B(n,\alpha)$ transmutation. Following the reasoning that helium is most detrimental when present in the grain boundaries, we chose alloying additions that were strong boride formers so that the $^{10}B$ would be distributed uniformly as a stable compound. We have investigated small additions of Ti, Zr, and Hf.

In looking at the composition of Hastelloy N, several other modifications seemed desirable. The microstructure of this alloy normally contains stringers of massive $M_6C$ carbide particles. These stringers

are too coarse to cause any strengthening and are difficult to dissolve, thus making grain-size control a problem. As shown in Fig. 2.6, this precipitate does not form if the molybdenum content is 12% or lower, rather than the normal 16%. The 0.5% Si present in the standard alloy was found to segregate in the carbide with local concentrations of about 3%. We reasoned that this segregation may be associated with the tendency for this alloy to form cracks during welding. The specifications were changed to 0.1% maximum for silicon. The 4% Fe was present in the original alloy to allow the chromium addition to be made with ferrochrome. Since this practice is not normally used, we reduced the iron concentration to 0.1% maximum to obtain as simple an alloy as possible. We retained a specification of 0.2% on manganese to reduce the possibility of sulfur embrittlement. Thus, the composition of the modified alloy is Ni–12% Mo–7% Cr–0.2% Mn–0.05% C with small additions of Ti, Hf, or Zr.

We have spent most of our effort on the titanium-modified alloy. The results of postirradiation creep tests on several laboratory melts with different titanium levels are shown in Fig. 2.7. The specimens were irradiated at 650°C to a thermal dose of $2.5 \times 10^{20}$ neutrons/cm$^2$. They were tested at 650°C and a stress of 32,400 psi. Note that the rupture life and strain continue to improve as the titanium level is increased.

The next stage of development for the titanium-modified alloy was to obtain several 100-lb commercial melts with 0.5% Ti present. Figure 2.8 shows some creep results on one of these alloys, both in-reactor and postirradiation. All irradiations and tests were done at 650°C. The in-reactor creep specimens were exposed to a thermal flux of $6 \times 10^{13}$ neutrons cm$^{-2}$ sec$^{-1}$ and the specimens for postirradiation tests saw a total thermal dose of $2.5 \times 10^{20}$ neutrons/cm$^2$. We thought initially that Hastelloy N behavior might parallel that of type 304 stainless steel, with improved properties being obtained as the grain size was reduced. However, the results in Fig. 2.8 show that the rupture life of the titanium-modified Hastelloy N was less when annealed at 871°C than when annealed at 1177°C. The reduction in rupture life

PHOTO 87192

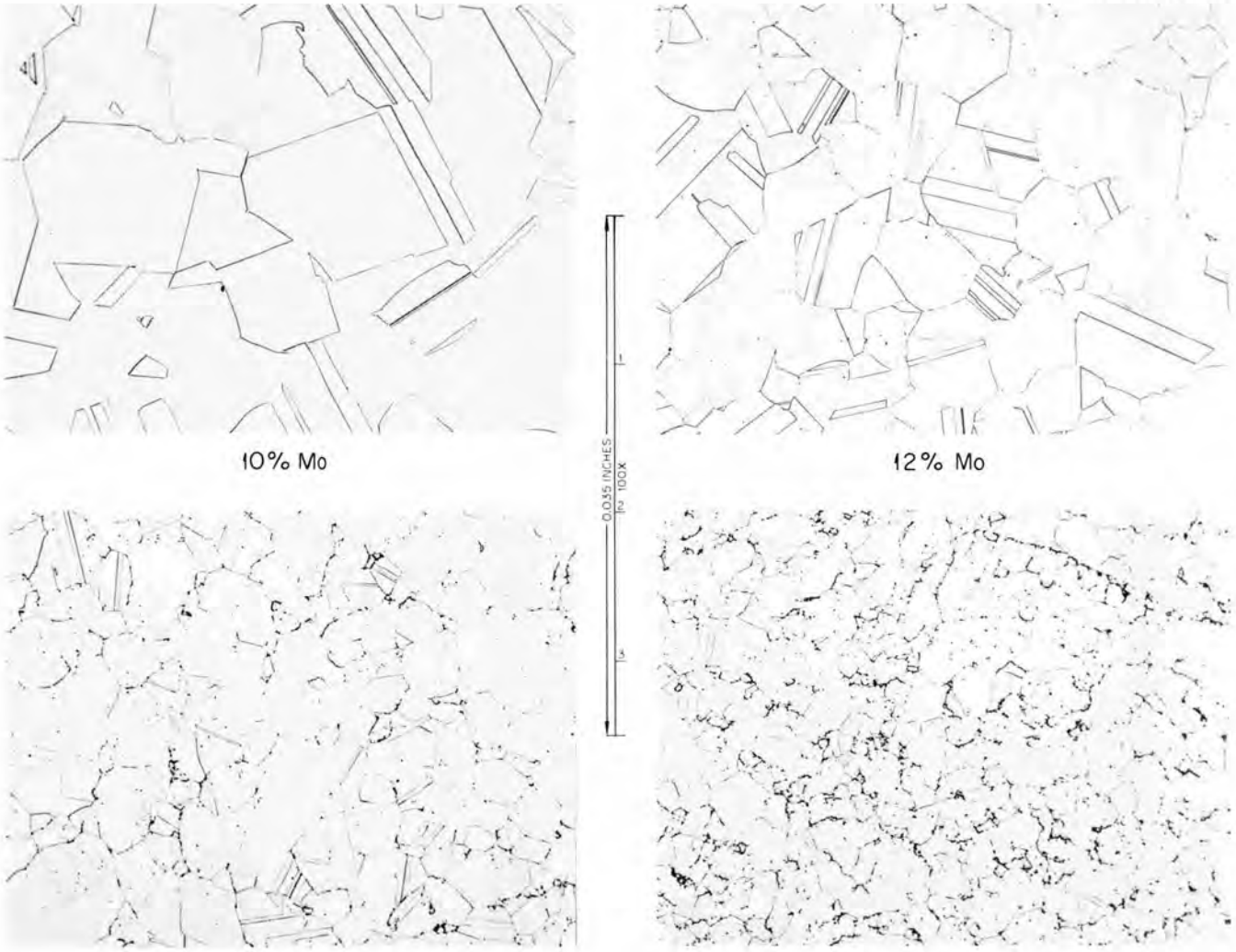


Fig. 2.6. Effect of Molybdenum Content on the Microstructure of Ni–7% Cr–0.2% Mn–0.005% C Alloys After Annealing 1 hr at 1177°C.

[redacted]



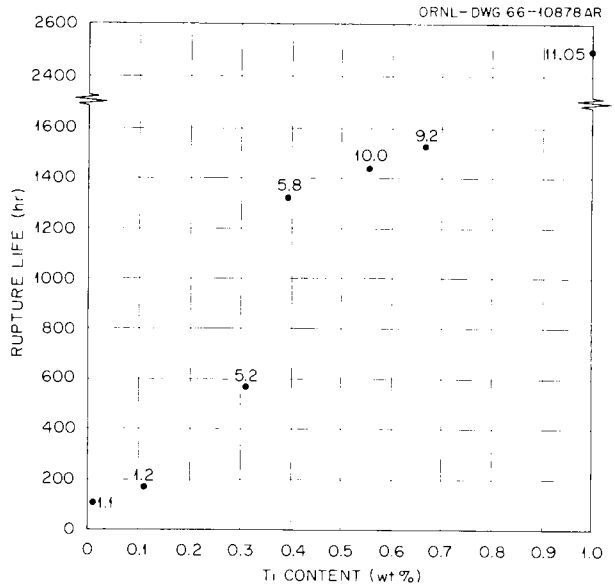


Fig. 2.7. Influence of Titanium on the Postirradiation Creep Properties of Ni–12% Mo–7% Cr–0.05% C. Tested at 650°C and 32,400 psi. The numbers by the individual data points are the fracture strains (% elongation).

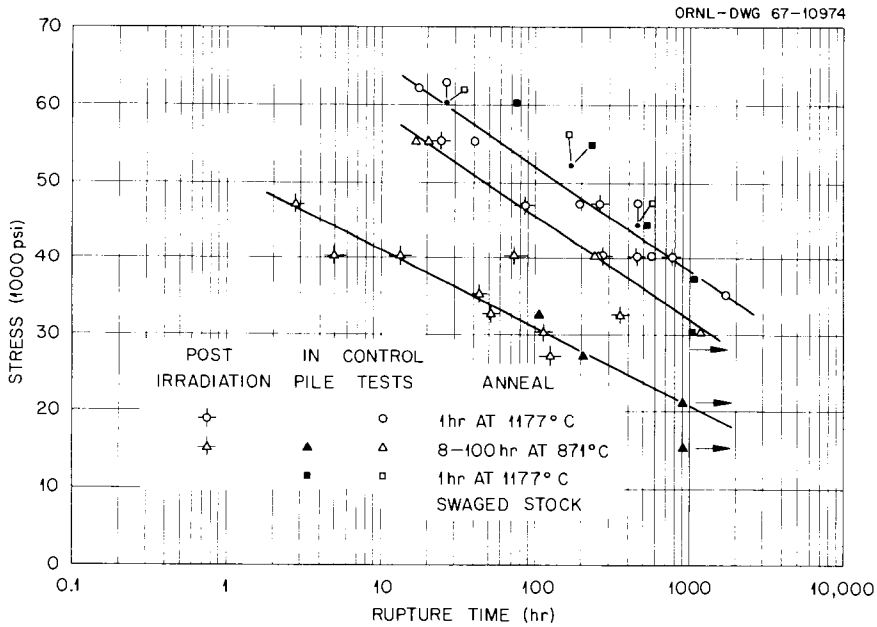


Fig. 2.8. Stress-Rupture Properties of Titanium-Modified Hastelloy N at 650°C.

[redacted]

due to irradiation is also greater for the material annealed at the lower temperature. Note also that the agreement between postirradiation and in-reactor tests is excellent. Figure 2.9 shows the rupture ductilities for the same specimens shown in Fig. 2.8. Although these data exhibit considerable scatter, they indicate the following trends. (1) The ductility decreases with decreasing rupture life. (The curve must exhibit a minimum ductility at a rupture life of about 1 hr, since tensile tests of a few tenths of an hour duration have rupture ductilities of about 15%.) (2) The rupture ductility corresponding to a certain rupture life is greater for the material annealed at 1177°C than for that annealed at 871°C. The rupture strain for irradiated standard Hastelloy N under these conditions ranges from 0.5 to 2.5%. Hence, the titanium-modified alloy offers considerable improvement.

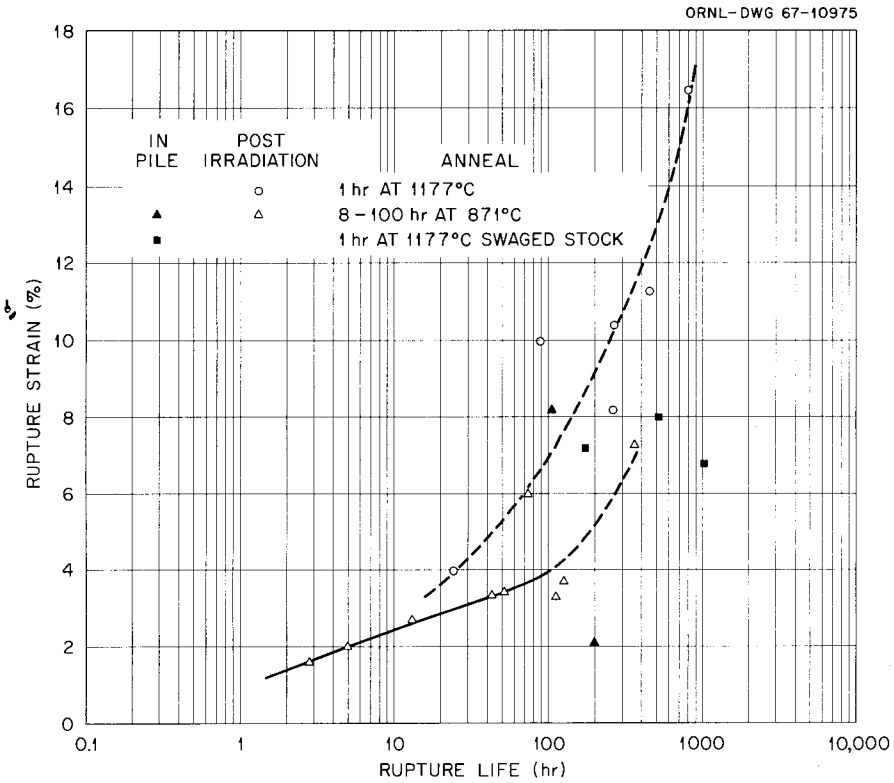


Fig. 2.9. Effects of Irradiation on the Fracture Strains of Titanium-Modified Hastelloy N at 650°C.

[redacted]



Study of the titanium-modified alloy is continuing. Alloys with titanium levels up to 1% and various carbon concentrations have been procured for aging studies. Our work on the 0.5% Ti composition indicates that the alloy has excellent weldability, and we will extend these studies to higher titanium levels to determine whether problems are encountered. A 5000-lb heat of the modified composition with 0.5% Ti is being processed by a commercial vendor.

Our work with the zirconium-modified alloy has proceeded through several small laboratory melts and two 100-lb commercial melts. This alloy with about 0.5% Zr exhibits excellent postirradiation properties. However, it tends to be hot-short, and we have encountered problems in both fabrication and welding. The fabrication problems seem to be handled adequately by reducing the working temperatures, but the weld-metal cracking has not been overcome. We do not plan to proceed further with the development of the zirconium-bearing alloy until we have developed a suitable filler metal.

The hafnium-modified Hastelloy N has been studied only briefly. The results of postirradiation creep tests at 650°C are shown in Fig. 2.10. The excellent ductility and rupture life of this laboratory

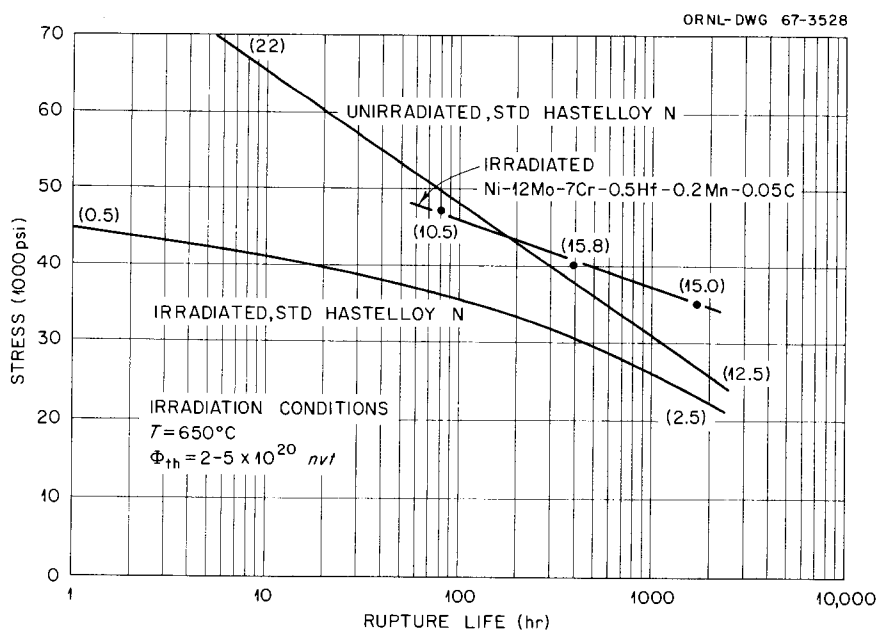


Fig. 2.10. Creep-Rupture Properties of Several Materials at 650°C. Numbers in parentheses are rupture strains in percent.

[redacted]

melt with 0.5% Hf are apparent. We have procured a 100-lb commercial melt containing 0.5% Hf for evaluation. The material has good weldability, and specimens of this material are being irradiated. However, we do not plan a large development program on the hafnium-modified alloy.

## EBR-II Gamma Heat Experiment

E. E. Bloom A. F. Zulliger[4]
J. R. Weir, Jr.

An experiment to measure the axial distribution of nuclear heating in rows 2 and 7 positions of EBR-II has been removed from the reactor and is presently being examined. Briefly, the nuclear heat susceptors (gold-plated stainless steel cylinders) were placed in the central pins of Mark B-7 subassemblies and then irradiated in position in rows 2 and 7. A gas gap was provided between the susceptor surface and the inner wall of the pin. The gas composition and gap size were selected on the basis of published heating rates to produce susceptor centerline temperatures between 500 and 800°C. Each susceptor contained melt wires having melting points both above and below the design temperature. Postirradiation examination of the susceptors placed the actual operating temperature between a lower value (determined by the highest melting point of a melt wire that had melted) and an upper value (determined by the lowest melting point of a melt wire that had not melted).

The experiment was designed to measure the nuclear heating rate (in stainless steel) over the range of 0.5 to 1.5 times the published heating rates (4.8 w/g peak row 2 and 1 w/g peak row 7 in stainless steel at a reactor power level of 45 Mw). Before the experiment was inserted into the reactor, we were informed by EBR-II personnel that the heating rates were approximately double our design values. We thus requested that the experiment be conducted at a reactor power level of 30 Mw to bring the heating rates into the range of our experimental capability.

---

[4]General Engineering Division.

[redacted]



Subassemblies X-023 and X-024 were placed in rows 2 and 7 positions 2B1 and 7D4, respectively. Figure 2.11 shows the power history of the reactor during the experiment. Outlet sodium temperatures were monitored and were 384 and 375°C for rows 2 and 7, respectively, at 30 Mw. In row 2 the melt wires having the lowest melting points showed no signs of melting. In row 7 melt wires at several locations had melted. Nuclear heating rates have been calculated, based upon the temperatures as determined from the melt wires and upon a sodium temperature of 385°C. These data (corrected to 45-Mw reactor power) are shown in Fig. 2.12. In this figure the best fit has been drawn through the row 7 data. For row 2 the curve represents the nuclear heat values that would have caused melting of the lowest temperature melt wires. The actual values are thus somewhat less. Figure 2.13 shows the row 7 data corrected for actual sodium temperature (371°C inlet, 376°C outlet).

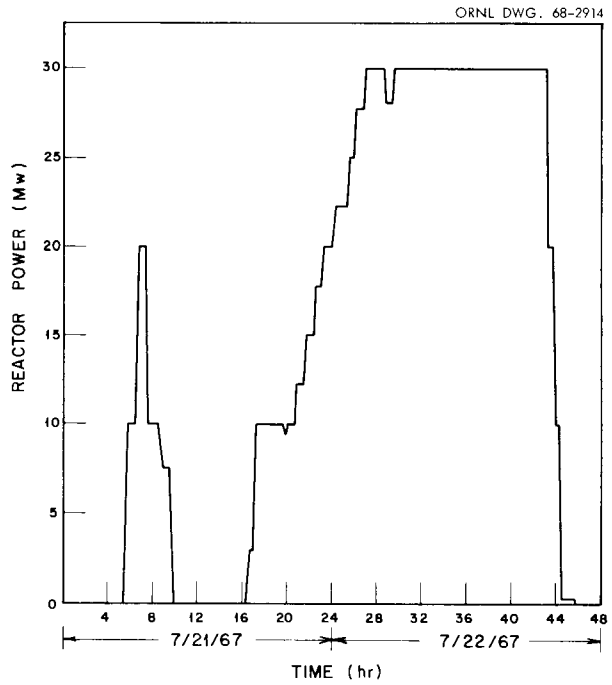


Fig. 2.11. Power History of Subassemblies X-023 and X-024.

[redacted]

[redacted]



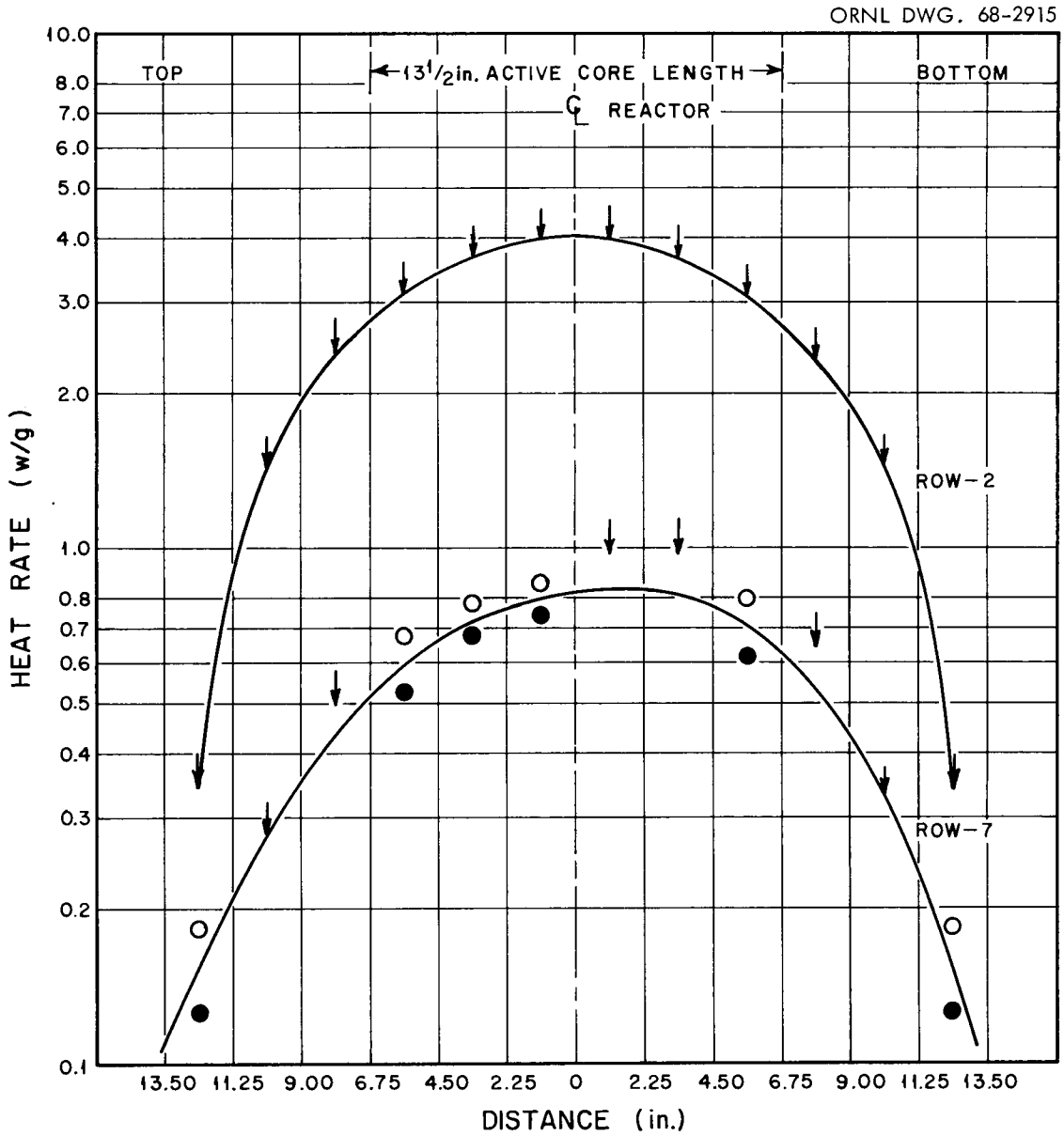


↓ Lowest temperature melt wire had not melted, position corresponds to heating rate which would just cause melting.

● Heating rate required to cause melting of the melt wire having highest melting point which had melted.

○ Heating rate which would just cause melting of melt wire having lowest melting point which had not melted.

Fig. 2.12. Results of EBR-II Gamma Heat Experiment.

[redacted]

[redacted]



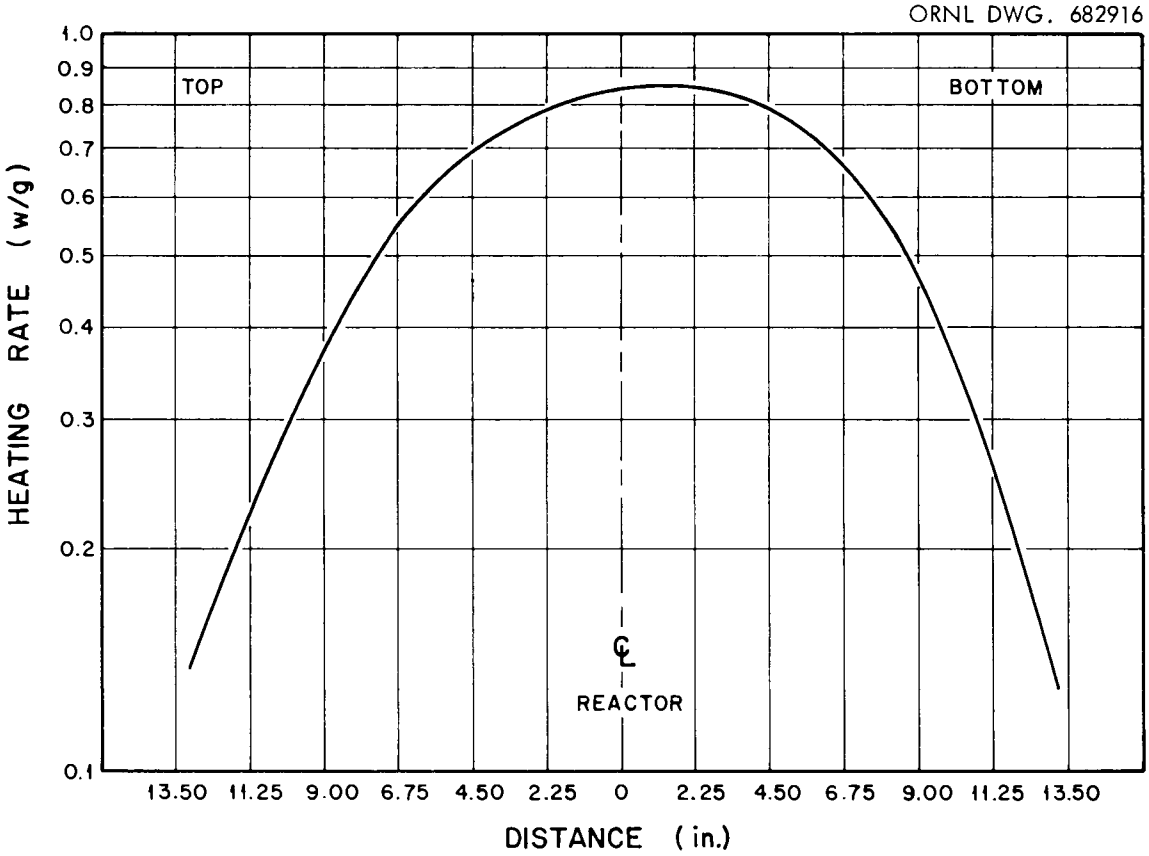


Fig. 2.13. Nuclear Heating Rates in Row 7 of EBR-II. Values are for stainless steel at a reactor power of 45 Mw.

At the present time we are evaluating the possible errors and determining their effect on the calculated nuclear heating rate. For example, in row 7, position 13, the melt wire having a 629°C melting point had melted and the melt wire having a 660°C melting point had not melted. Calculations based upon handbook properties for the density of stainless steel ($\rho_{ss}$), thermal conductivity of stainless steel ($K_{ss}$), thermal conductivity of argon ($K_{Ar}$), and emissivity of gold surfaces at these temperatures give nuclear heating rates of 0.75 and 0.86 w/g for the 629 and 660°C temperatures, respectively. In these calculations the bulk sodium temperature was taken as 374°C and the actual hot gas gap was used. To obtain a value for the maximum possible nuclear heating rate at this position, we assumed that the temperature was 660°C (lowest melting point of an unmelted melt wire), $\rho_{ss}$ was decreased by 5%, $K_{ss}$ increased by 10%, $K_{Ar}$ increased by 10%, and emissivity values

[redacted]

were increased from 0.036 to 0.5. Deviations in geometry, thermal expansion, and sodium film coefficient were not considered since their effect on maximizing nuclear heat rate was determined to be negligible. The result of this calculation gives a nuclear heating rate of 1.02 w/g (extrapolated to reactor power level of 45 Mw). To determine the minimum possible nuclear heating rate (at position 13, row 7) the temperature was taken as 629°C (highest melting point of a melt wire that had melted), $\rho_{ss}$ was increased 5%, $K_{ss}$ decreased 10%, and $K_{Ar}$ decreased 10%, and we assumed that no heat was transferred by radiation. The result was a nuclear heating rate of 0.63 w/g (extrapolated to 45-Mw power level).

This type of calculation gives an unrealistically large spread in the nuclear heat values since the probability of all errors being in the same direction is quite small. We are presently working on a least-square analysis to obtain more realistic deviations.

It is important to note that these data are preliminary and are subject to further analysis.

## 3. MIXED NITRIDE FUELS DEVELOPMENT

J. L. Scott

Mixed (U,Pu)N continues to look attractive as fuel for advanced liquid-metal-cooled fast-breeder reactors. As discussed previously[1] this fuel has a very high theoretical density and good thermal conductivity. Stoichiometry control is easier than in the mixed carbide, a competitive fuel. Thus, compatibility problems should be less severe with the mixed nitride than with the mixed carbide.

Our program for developing the mixed nitride includes fabrication studies, physical property determinations, compatibility work, and irradiation testing. Since our experimental facility for working with plutonium nitride is not yet available, our efforts are directed toward equipment and procedural checkouts with uranium nitride as a stand-in. We expect to have our plutonium facility in operation within the next quarter. Since irradiation testing requires long lead times, preliminary work is already under way on this phase of the program.

Work is continuing on mixed UC-UN. This fuel has the advantages of both UC and UN. Our work will establish practical impurity limits of UC in UN or UN in UC depending on the application. In addition, the carbonitride appears to have a very attractive fuel cycle, since it can be produced readily from the oxide. Furthermore, basic data on the UC-UN system will enrich our understanding of these rock-salt type compounds.

A large program of basic research on UN and U(C,N) at ORNL is relevant to our nitride development program. Although the basic work is funded by the Research Division of AEC, a summary of the results to date is included for information in this report.

---

[1] J. L. Scott, Fuels and Materials Development Program Quart. Progr. Rept. Sept. 30, 1967, ORNL-TM-2020, p. 46.

[redacted]



# Fabrication of Mixed Nitrides

Ji Young Chang

We designed a hot press to fit a small glove box (32 × 43 × 32 in.) to produce high-density mixed nitride fuel. We also surveyed the existing theories of hot pressing, so that we could effectively plan densification experiments and analyze the data. An analog computer circuit was formulated to predict the end-point density of nitride fuel.

## Hot-Press Design

Our high-frequency induction hot press was designed with emphasis on a number of aspects, as follows:

1. elimination of the need for disassembling the furnace body after each hot pressing cycle,
2. reproducibility of the operation, such as automatic sample positioning in the center of the furnace,
3. enough distance between the induction coil and the structural frame,
4. no greater voltage across the induction coil than needed,
5. elimination of sharp corners and provision of enough working space to permit the safe handling of plutonium with gloves,
6. prevention of argon gas leakage from attached parts in a glove box,
7. furnace design that eliminates the difficulty of repair and maintenance in a small glove box.

A schematic drawing of the design is shown in Fig. 3.1. The advantage of this furnace compared with conventional design is that the furnace need not be disassembled after each operation. A sample can be removed remotely from outside the glove box to avoid difficult handling through the gloves. It will also increase the efficiency of fuel fabrication because the furnace need not cool to room temperature for the next operation. Design data are as follows.

[redacted]

[redacted]



ORNL-DWG 68-1343

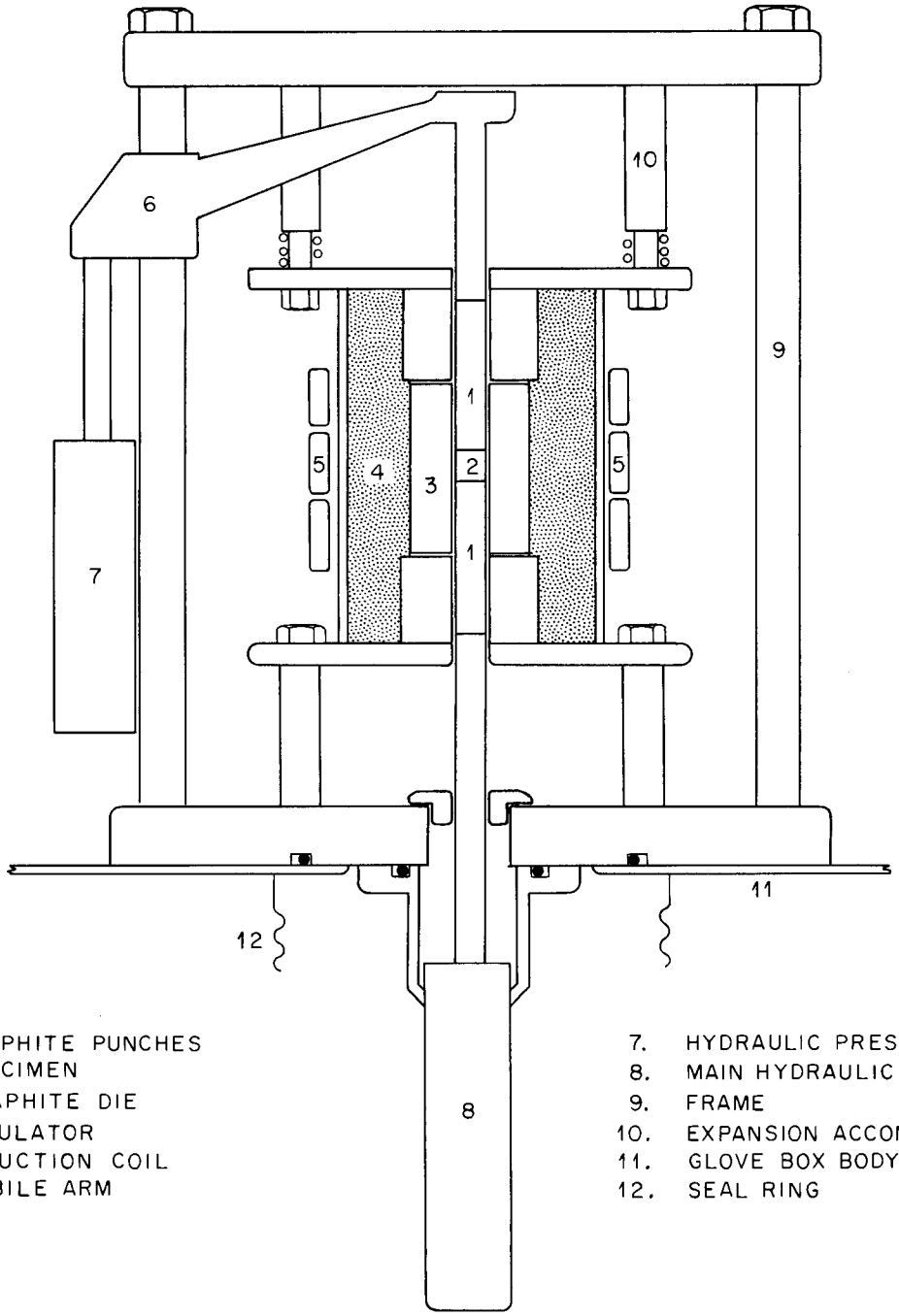


1. GRAPHITE PUNCHES
2. SPECIMEN
3. GRAPHITE DIE
4. INSULATOR
5. INDUCTION COIL
6. MOBILE ARM
7. HYDRAULIC PRESS
8. MAIN HYDRAULIC PRESS
9. FRAME
10. EXPANSION ACCOMMODATOR
11. GLOVE BOX BODY
12. SEAL RING

Fig. 3.1. Hot Press.

[redacted]

| | |
|---|---|
| Available space in glove box, in. | 30 × 30 × 30 |
| Diameter of die (ATJ or POCO graphite), in. | |
| Inside diameter | 0.5 to 1 |
| Outside diameter | 2 to 4 |
| Fracture strength of die, psi | 3000 to 4000 |
| Maximum pressure applicable to the punch, psi | 3000 to 20,000 |
| Induction coil dimensions, in. | |
| Diameter | 5 to 7 |
| Length | 6 to 7 |
| Coupling efficiency, % (induction coil to die) | 94 |
| Power required to heat to 1850°C, kw | 12 to 25 |

Survey on Theory of Hot Pressing

This subject has been reviewed recently by F. Thümmler and W. Thoma[2] and previously by Lars Ramqvist.[3] Densification during hot pressing can be described by three general mechanisms: (a) plastic flow,[4–10] (b) particle rearrangement, sliding, and fragmentation,[11,12] and (c) stress-enhanced diffusion.[13–16] The more important equations that may be used to fit the experimental data of mixed nitride fuels are listed below.

---

[2]F. Thümmler and W. Thoma, "The Sintering Process," Met. Rev. 12, 69–108 (1967).

[3]L. Ramqvist, "Theories of Hot Pressing," Powder Met. 9(17), 1–25 (1966).

[4]J. K. Mackenzie and R. Shuttleworth, "A Phenomenological Theory of Sintering," Proc. Phys. Soc. (London) 62, 833–852 (1949).

[5]P. Murray, E. P. Rodgers, and A. E. Williams, Practical and Theoretical Aspects of the Hot Pressing of Refractory Oxides, AERE-M/R-893 (July 30, 1952).

[6]J. D. McClelland, "Kinetics of Hot Pressing," pp. 157–171 in Powder Met. Proc. Intern. Conf., New York, 1960 (1961).

[7]M. S. Kovalchenko and G. V. Samsonov, "Application of Viscous Flow Theory to Densification of Powders by Hot Pressing," Poroshkovaya Met. Akad. Nauk Ukr. SSR 1961(2), 3–13.

[8]S. Scholz and B. Lersmacher, "The Densification Rate During Hot Pressing," Arch. Eisenhüttenw. 41, 98–108 (1964).

1. Mackenzie and Shuttleworth[4] sintering mechanism:

$$\left(\frac{d\rho}{dt}\right)_s = \frac{3}{2}\left(\frac{4\pi}{3}\right)^{1/3} \frac{\gamma n_0^{1/3}}{\eta^\infty} (1-\rho)^{2/3} \rho^{1/3} \left[1 - a\left(\frac{1}{\rho} - 1\right)^{1/3} \ell n \frac{1}{1-\rho}\right] . \quad (1)$$

where

$$a = \sqrt{2}\left(\frac{3}{4\pi}\right)^{1/3} \frac{\tau_c}{2\gamma n_0^{1/3}} .$$

2. Murray, Rodgers, and Williams[5] modification of Eq. (1) for hot pressing:

$$\frac{d\rho}{dt} = \left(\frac{d\rho}{dt}\right)_s + \frac{3P}{4\eta}(1-\rho) . \quad (2)$$

3. Pressure correction by McClelland[6] from Eq. (2):

$$\frac{d\rho}{dt} = \frac{3P}{4\eta}(1-\rho)\left[\frac{1}{1-(1-\rho)^{2/3}} + \frac{\sqrt{2}\,\tau_c}{P}\,\ell n(1-\rho)\right] . \quad (3)$$

---

[9]S. Scholz, "Some New Views on the Hot Pressing of Refractory Compounds," Soviet Powder Met. Metal Ceram. (English Transl.) 1963(3), 170–175.

[10]G. E. Mangsen, W. A. Lambertson, and B. Best, "Hot Pressing of Aluminum Oxide," J. Am. Ceram. Soc. 43, 55–58 (1960).

[11]E. J. Felton, "Hot-Pressing of Alumina Powders at Low Temperature," J. Am. Ceram. Soc. 44, 381–385 (1961).

[12]R. Chang and G. G. Rhodes, "High-Pressure Hot-Pressing of Uranium Carbide Powders and Mechanisms of Sintering of Refractory Bodies," J. Am. Ceram. Soc. 45, 379–832 (1962).

[13]R. L. Coble and J. S. Ellis, "Hot-Pressing Alumina — Mechanisms of Material Transport," J. Am. Ceram. Soc. 46, 438–441 (1963).

[14]T. Vasilos and R. M. Spriggs, "Pressure Sintering: Mechanisms and Microstructures for Alumina and Magnesia," J. Am. Ceram. Soc. 46, 493–496 (1963).

[15]R. C. Rossi and R. M. Fulrath, "Final Stage Densification in Vacuum Hot-Pressing," J. Am. Ceram. Soc. 48, 558–564 (1965).

[16]G. M. Fryer, "Hot Pressing of Alumina, a New Treatment of Final Densification," Trans. Brit. Ceram. Soc. 66, 127–134 (1967).

[redacted]



4. Viscosity correction as a function of porosity and grain growth [Eq. (4)] by Kovalchenko and Samsonov[7] from Eq. (2), using the diffusional creep models of Nabarro[17] and Herring:[18]

$$\frac{d\rho}{dt} = \frac{P(1-\rho)\ (2+\rho)}{4\eta_o(1+bt)\ (2\rho-1)} \ . \tag{4}$$

5. New viscosity correction as a function of porosity by Scholz and Lersmacher[8] using Eq. (4):

$$\frac{d\rho}{dt} = \frac{3P}{4\eta_0}\ \frac{(1-\rho)}{(1+bt)} \ . \tag{5}$$

6. Empirical formula established by Carlson and Westermann;[19] log (1 − D) is linear in log t. Then

$$\frac{d\rho}{dt} = \frac{K}{t}\ (1-\rho) \ , \tag{6}$$

where

$K = f(\rho,t)$.

7. Empirical equation by Scholz[9]

$$\rho = 1 - (1-\rho_0)\ (1+bt)^{-n} \ , \tag{7}$$

where

$$n = \frac{15\Omega}{2kR_0^2}\ \frac{PD}{bt} \ .$$

8. Rossi and Fulrath[15] stress enhanced diffusion:

$$\frac{d\rho}{dt} = \frac{10D\Omega}{kT}\ bP\ (1-\rho) \qquad b \approx 3 \text{ to } 4. \tag{8}$$

---

[17]R.F.N. Nabarro, "Deformation of Crystals by the Motions of Single Ions," pp. 75–90 in Report of a Conference on Strength of Solids, Held at the H. H. Wills Physical Laboratory, University of Bristol on 7–9 July 1947, Physical Society of London, 1948.

[18]C. Herring, "Diffusional Viscosity of a Polycrystalline Solid," J. Appl. Phys. 21, 437–445 (1950).

[19]R. G. Carlson and F. E. Westermann, "Hot Pressing of Lead Spheres," Planseeber. Pulvermet. 10, 15–23 (1962); Trans. Met. Soc. AIME 221, 649–650 (1961).

[redacted]

9. Fryer[16] vacancy diffusion:

$$\frac{1}{V_s}\frac{dV}{dt} = -z\,\frac{P}{\ell^2}\,\frac{D\Omega}{kT}\left(\frac{P}{\rho}\right)^{5/3} . \qquad (9)$$

The symbols used in these and subsequent equations are listed below.

$b$ = constant

$D$ = diffusion coefficient, $cm^2/sec$

$k$ = Boltzmann constant, $1.38 \times 10^{-6}$ ergs/°C

$\ell$ = mean pore separation

$n_0$ = number of voids

$P$ = pressure, $dyne/cm^2$

$R$ = grain radius, cm

$R_0$ = original grain radius, cm

$t$ = time, sec

$T$ = temperature, °K

$V$ = volume of compact

$V_s$ = volume of solid material

$z$ = numerical constant depending mainly on the pore geometry

$\left(\frac{d\rho}{dt}\right)_s$ = densification rate in the absence of pressure (normal sintering)

$\beta$ = constant

$\gamma$ = surface tension, $g/cm^2$

$\eta$ = viscosity, dyne sec $cm^{-2}$

$\eta_\infty$ = viscosity in infinite shear rate, dyne sec $cm^{-2}$

$\eta_0$ = viscosity before grain growth

$\Omega$ = vacancy volume, $cm^3$

$\rho$ = density, %

$\rho_0$ = density before hot pressing, %

$\tau_c$ = critical shear stress, $dyne/cm^2$

We believe on the basis of all the experimental work that either these mechanisms are operating simultaneously or one mechanism is predominantly operating, depending upon the hot-pressing conditions and the material. The theory of hot pressing requires further development

to solve the discrepancies among the existing equations and also to better interrelate the competing mechanisms to describe their relative importance under varying hot-pressing parameters.

At present, even though the assumptions and mechanisms proposed are not perfectly applicable to all cases, each of these theoretical or phenomenological equations has in many cases proved very useful for the practical purpose of prediction and analysis of hot pressing.

Analog Computer Simulation of Hot Pressing

We rearranged Eq. (3) for the unit correction and computer circuit.

$$\frac{d\rho}{dt} = \frac{5.40}{\beta}\frac{P}{\eta}\left[\frac{1-\rho}{1-(1-\rho)^{2/3}}\right] + \frac{2.198}{\beta}\frac{\tau_c}{\eta}(1-\rho)\left[0.40\log(1-\rho)\right], \qquad (10)$$

and the circuit was formulated as shown in Fig. 3.2. Figure 3.3 shows the simulation of hot pressing using the values

$\eta = 30 \times 10^{10}$ poise, $P = 3000$ psi, $\tau_c = 1500$ psi

and multiples of these values as listed in Table 3.1. According to results of the simulator (Fig. 3.3) we could conclude the following:

1. The densification is very sensitive to pressure for the high-viscosity material (D and G) but not for the low-viscosity case (A and E).

2. High pressure with low viscosity will result in maximum density (B), and low pressure with high viscosity will show minimum density (G), as expected.

3. The higher the shear stress the lower is the density (F and H).

4. Limited densities can be obtained after 4 hr of hot-pressing time (C, D, F, H, and G). Thus if we want to obtain 100% of theoretical density within favorable time such as for B, A, and E, we could estimate from preliminary data and Fig. 3.3 the minimum pressure and temperature needed.

5. One could predict the minimum pressure required to get high density in reasonable hot-pressing time (compare B and E). Application of unnecessarily high pressure could be avoided to extend die life.

6. The final density is very sensitive to viscosity at high pressures (A and C). Thus, raising the pressing temperature may be more effective than raising the pressure.

$$\frac{dD}{d\tau} = \frac{5.40}{\beta}\,\frac{p}{\eta}\left[\frac{1-D}{1-(1-D)^{2/3}}\right] + \frac{2.198}{\beta}\,\frac{T}{\eta}\,(1-D)\left[0.40\,\mathrm{LOG}(1-D)\right]$$

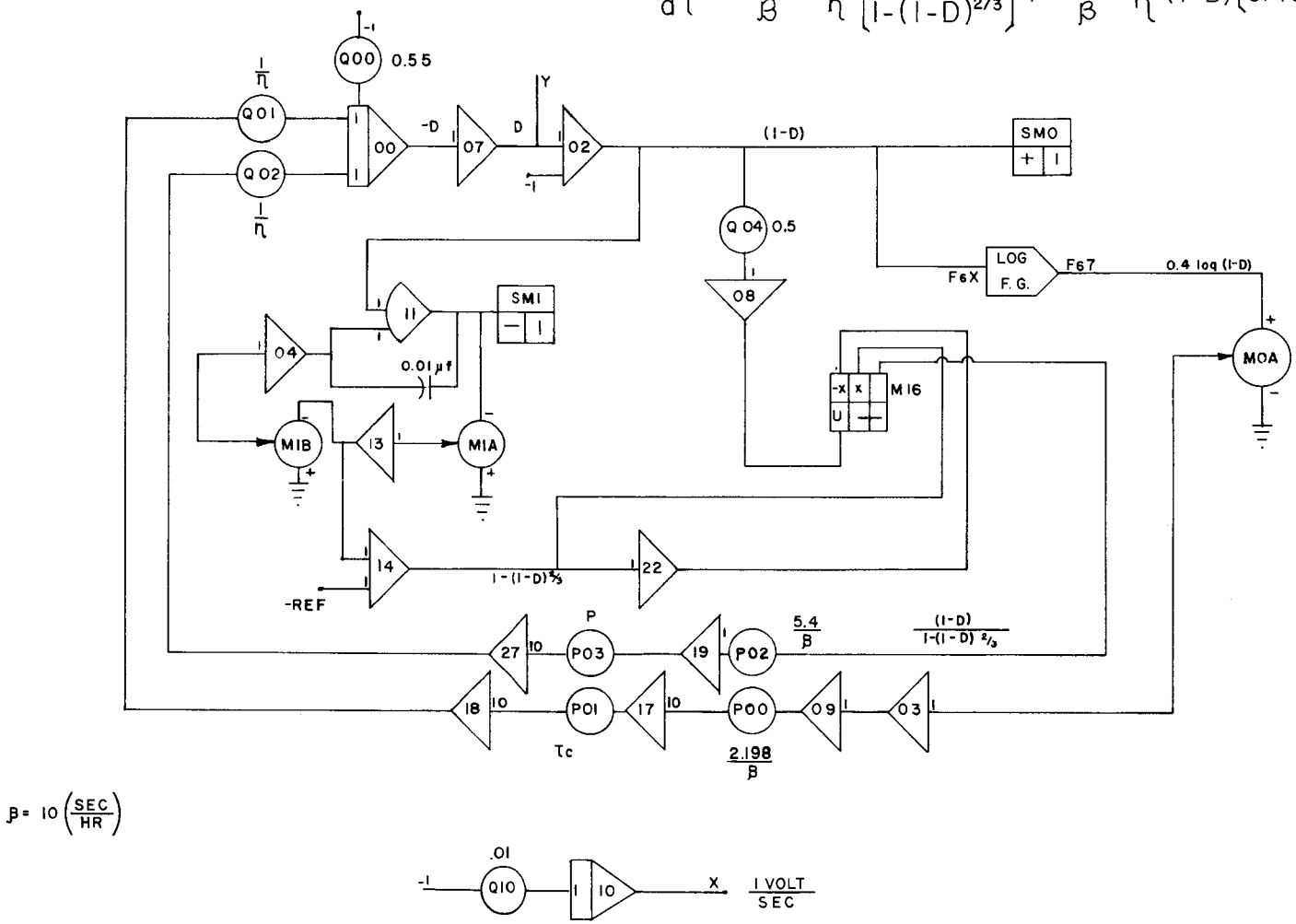


Fig. 3.2. Analog Simulation of Densification During Hot Pressing.

[redacted]



ORNL-DWG 68-1424

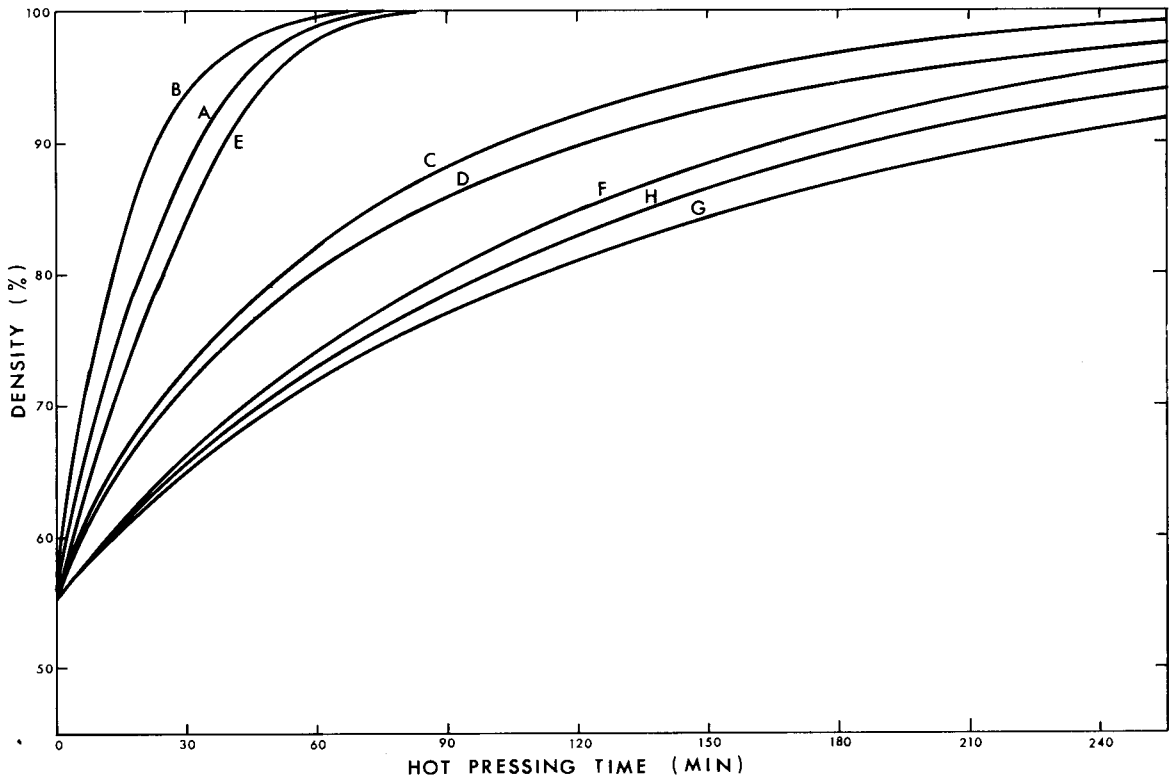


Fig. 3.3. Calculated Densification During Hot Pressing

Table 3.1. Numerical Values Used for Computer Simulation[a]

| Curve | Pressure (psi) | Viscosity (poise) | Shear Stress (psi) |
|---|---|---|---|
| | | $\times 10^{10}$ | |
| A | 3000 | 3 | 1500 |
| B | 6000 | 3 | 1500 |
| C | 3000 | 30 | 1500 |
| D | 3000 | 300 | 1500 |
| E | 1500 | 3 | 1500 |
| F | 1500 | 30 | 1500 |
| G | 1500 | 300 | 1500 |
| H | 1500 | 30 | 3000 |

[a]Values shown are for curves in Fig. 3.3.

[redacted]

# Phase Behavior and Thermodynamic Properties of the Plutonium-Nitrogen System

K. E. Spear J. M. Leitnaker

Plutonium mononitride is being actively considered for use as a fast-breeder fuel. The development of high-density stable fast-reactor fuels with high thermal conductivities requires an understanding of the chemical and thermodynamic properties of possible fuel materials. We have therefore undertaken a review and analysis of these properties for the plutonium-nitrogen system. A complete report of this endeavor is published elsewhere.[20] In this report, we summarize existing phase data and our analysis of the thermodynamic properties for the plutonium-nitrogen system.

## Phase Behavior

The phase behavior of the plutonium-nitrogen system as a function of composition, temperature, and pressure has not been studied. The face-centered cubic mononitride of the NaCl type is the only intermediate phase reported for the system. The composition range of this phase has not been systematically studied. No solid-state transition of PuN has been observed in studies covering a temperature range from 20 to 2200°C.

Plutonium mononitride vaporizes congruently to the elements at temperatures below about 2400 ± 200°C and decomposes to liquid plutonium and nitrogen gas at higher temperatures. It decomposes at 2570 ± 30°C and 1 atm $N_2$. We estimate that PuN melts congruently at 2830 ± 50°C and a minimum nitrogen pressure of 50 ± 20 atm.

The lattice parameter value for pure PuN is still fairly uncertain. Many values in the range 4.9025 to 4.9055 A have been reported. Oxygen increases the parameter, but a systematic study of this effect is needed. The PuN lattice constant increases about 0.0001 A/week due to self-irradiation damage.

---

[20] K. E. Spear and J. M. Leitnaker, A Consistent Set of Thermodynamic Values for Plutonium Mononitride, ORNL-TM-2106 (in press).

## Thermodynamic Properties

Plutonium mononitride's decomposition to metal and gas, congruent vaporization, free energy of formation, and heats of combustion and formation have been investigated by four separate research groups, each working independently. The temperature range over which measurements were made extends from 298 to 3043°K. Heat of formation values for PuN reported with these data range from −70 to −76 kcal/mole. However, all of the experimental data can be reasonably explained and can be combined into a consistent set of thermodynamic values for plutonium mononitride.

High-temperature equilibrium experiments over temperatures from 695 to 3043°K give an internally consistent set of data. If reasonable estimates of entropy and high-temperature heat capacity are made, excellent agreement among these data is obtained by the third-law technique. Moreover, a second-law treatment of these data is also in agreement. The combustion measurements give a value of −70.2 ± 1.5 kcal/mole, which appears to be in disagreement with the equilibrium results of −76.0 ± 1.0 kcal/mole. However, this apparent disagreement can be resolved if one assumes that the PuN stoichiometry considered in the equilibrium measurements differs from that studied in the calorimetric measurements.

## Conclusions

Additional data are needed for a complete thermodynamic description of the PuN phase. Primarily these data are: (1) the composition range of PuN as a function of nitrogen pressure and temperature, (2) heat content (or heat capacity) data at high temperatures, and (3) low-temperature heat capacity data. The self-heating of plutonium, however, will make reliable low-temperature data exceedingly difficult to obtain.

Ternary or more complex systems involving plutonium and nitrogen are not considered in this analysis. A working description of such systems will, however, be necessary before PuN can be used as a fuel.

[redacted]



## Fuel Cycle Sol Gel

T. B. Lindemer

The kinetics of the synthesis of uranium carbides, nitrides, and carbonitrides from sol-gel $UO_2$ is being considered in an effort to determine factors that control the conversion reactions. This knowledge is fundamental to the eventual design of a fuel cycle for the production of the desired reactor fuel material.

We started two new studies in the last quarter. In one we are reacting microspheres of "$UC_2$" with nitrogen in a fluidized bed to determine the interrelation of time, temperature, and particle size in the production of uranium carbonitrides. This study complements another, which we have been performing for about nine months, the conversion of microspheres of $UO_2$ to "$UC_2$" by solid-state reaction with carbon.

The second new study involves what may be a new ternary uranium compound. We do not know the composition of the compound at the present time, but it may be analogous to $Th_2N_2O$. We have produced this compound by reacting microspheres of $UO_2$ with nitrogen in the presence of carbon, the concentration of which is controlled so that uranium carbides do not form. The compound may be a promising intermediate between the sol-gel $UO_2$ and the desired uranium compound because it appears that transport of anions is comparatively rapid in this phase. Such behavior would be expected, since in the thorium analog one-third of the anion sites are vacant. The most important application of this compound appears to be the production of UN or U(C,N) microspheres; the use of the compound as an intermediate may permit the production of nitride compounds free of the graphite that forms when uranium carbides are used as an intermediate compound.

[redacted]

[redacted]



## Synthesis and Fabrication of UN and U(C,N)

R. A. Potter

We are continuing to extend our capability for the preparation of high-quality pressed-and-sintered specimens of UN and selected U(C,N) compositions. Our UN synthesis scheme and equipment have been described previously[21] and remain essentially unchanged. We are now concentrating on the fabrication of specimens of various sizes and shapes for the fundamental studies described elsewhere in this chapter.

Our basic fabrication process, developed for small right-circular solid cylinders and bushings, consisted of adding 1% camphor in acetone to the powder and uniaxially pressing in steel dies at about 50 tsi to a green density approximately 58% of theoretical. Small cylindrical specimens (approx 0.25 in. in diameter) with a length-to-diameter ratio of unity were readily fabricated by the method.

The specimens we are currently furnishing for fundamental studies are of more complex configurations and cannot be satisfactorily prepared by uniaxial cold pressing. Therefore, we have adopted a different method of pressing, in which specimens are preformed in steel dies at uniaxial pressures just adequate to form them, transferred to rubber bags that are then evacuated and sealed, and then isostatically pressed at about 30 tsi.

Pressed UN is heated to 1500°C in a vacuum of about $1 \times 10^{-5}$ torr. At 1500°C, the vapor pressure of nitrogen over UN is appreciable, so to prevent dissociation of the material we introduce 1 atm of nitrogen to the furnace before heating to the sintering temperature of about 2250°C. The sintered specimens are cooled to 1500°C, the nitrogen pressure is reduced to about $1 \times 10^{-5}$ torr, and the furnace is allowed to cool to room temperature. Sintered pieces are readily ground to close tolerances by conventional ceramics machining processes.

---

[21] T. G. Godfrey, J. M. Leitnaker, and R. A. Potter, Fuels and Materials Development Program Quart. Progr. Rept. Sept. 30, 1967, ORNL-TM-2020, pp. 53–57.

[redacted]

We are presently developing synthesis and sintering schemes whereby we can prepare specimens of $U(C_xN_{1-x})$, where x ranges from 0.0 to 1.0. To effect the synthesis, we react powdered UN with spectrographic grade carbon. The equilibrium pressure and temperature for a given composition set the conditions for synthesis.

The reacted powders are cooled under a constantly decreasing nitrogen pressure to prevent precipitation of graphite and formation of the sesquinitride. Specimens are then formed from this U(C,N) powder as in the case of pure UN. The sintering conditions are determined from equilibrium pressure calculations for the particular composition. The sensitivity of the equilibrium nitrogen pressure to composition is shown in Fig. 3.4 for two different U(C,N) specimens sintered at 1675°C and $5 \times 10^{-5}$ torr $N_2$. The $U(C_{0.2}N_{0.8})$ [Fig. 3.4(a)] specimen contains a significant quantity of free uranium dispersed throughout the structure, while the $U(C_{0.4}N_{0.6})$ specimen [Fig. 3.4(b)] has only a small amount of uranium very near the free surface. Thus, it is apparent that the sintering conditions must be carefully controlled to prevent compositional changes.

Because of the relative coarseness of the as-reacted powders, we have not been able to fabricate specimens with densities greater than about 90% of theoretical. We have installed a ball mill in a dry box to effect sufficient particle size reduction to permit the fabrication of higher density specimens.

## Fuel-Cladding Thermal Conductance

R. K. Williams T. E. Banks

Our objective is to improve the permissible power generation ratings of fuel elements by finding ways to decrease the thermal contact resistance associated with the fuel-cladding interface. Study of the thermal contact resistance is particularly applicable to carbide and nitride fuels which have relatively high thermal conductivities. In these materials, the interfacial temperature drop represents a very significant portion of the total center-to-edge temperature drop and thus governs the center temperature obtained at a given power generation rate. This is illustrated by the calculations shown in Table 3.2.

[redacted]



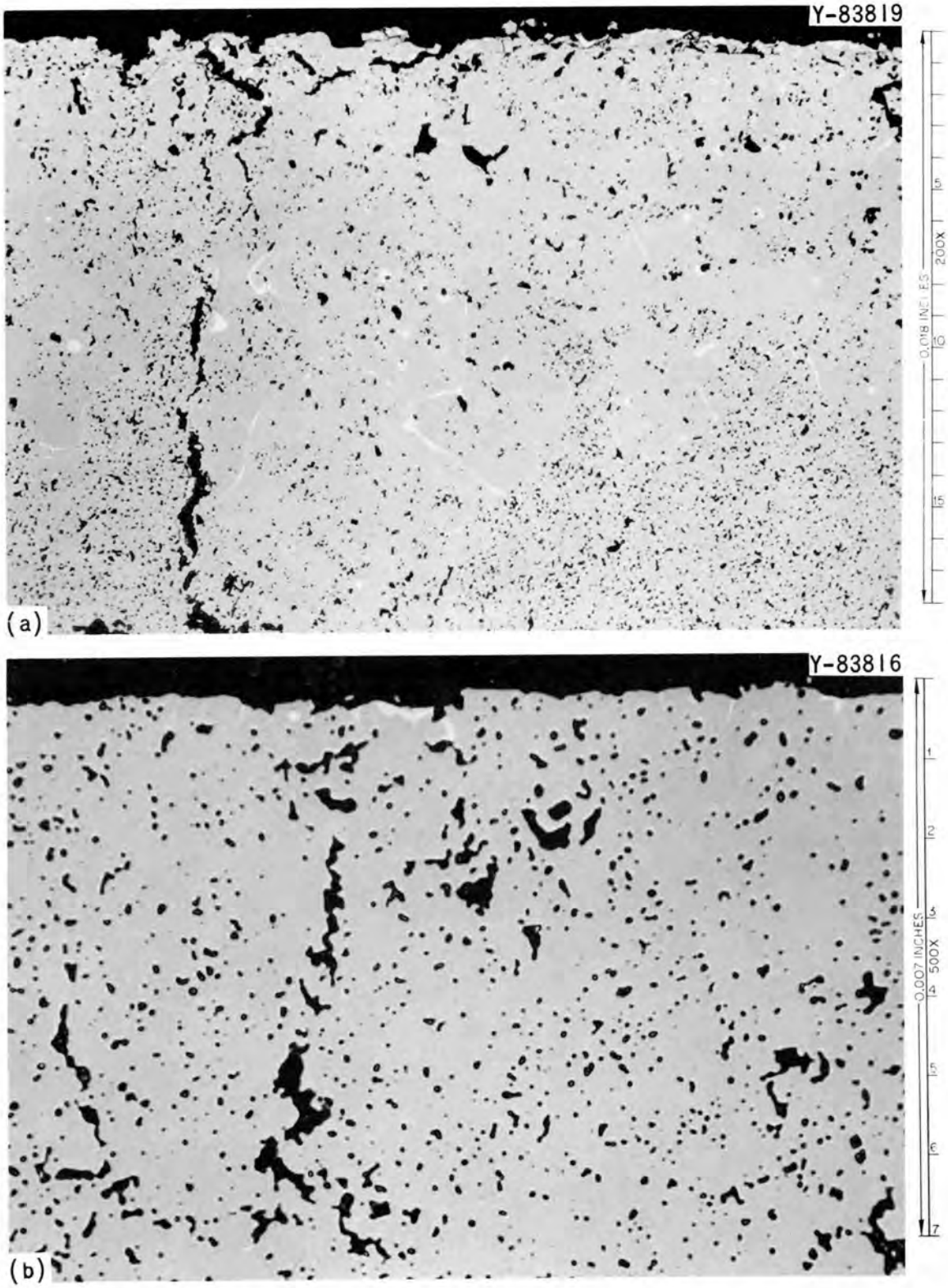


Fig. 3.4. Microstructure of U(C,N) Samples Sintered at 1675°C and $5 \times 10^{-5}$ torr. White phase is metallic uranium. As polished. (a) $U(C_{0.2}N_{0.8})$, (b) $U(C_{0.4}N_{0.6})$.

[redacted]

[redacted]



Table 3.2. Calculated Temperature Drops in 0.200-in.-ID Stainless-Steel-Clad Fuel Rods for Heat Rating of 12 kw/ft (400 w/cm)[a]

| Fuel | Temperature Drops, °C | | | |
|---|---|---|---|---|
| | Fuel | Interface[b] | Cladding[c] | Total |
| $(U,Pu)O_2$ | 1590 | 250 | 50 | 1890 |
| (U,Pu)N | 175 | 250 | 50 | 475 |

[a]J. W. Prados, private communication.

[b]1-mil gap filled with helium.

[c]0.015 in. thick.

The thermal contact resistance is defined as the interfacial temperature drop produced by unit heat flux:

$$R_c = \Delta T_i / q \ , \tag{11}$$

where

$R_c$ = thermal contact resistivity in °C $cm^2$ $w^{-1}$,

$\Delta T_i$ = interfacial temperature drop in °C, and

$q$ = heat flux in $w/cm^2$.

In general, heat can be conducted across an interface by thermal radiation, by conduction and convection due to gases present in areas that are not in intimate contact, and by conduction across the areas of solid-solid contact. The resistance to heat flow due to the solid-solid contacts seems to be the most likely place to seek improvements, so that the initial phase of this study has been concentrated in this area.

Available literature[22] indicates that the solid-solid contact resistance is sensitive to many variables and cannot be reliably predicted. This is especially true when the solid-solid contact involves two dissimilar materials. Previous studies have shown that thermal contact resistance varies with compressive stress, temperature, surface topography, the mechanical properties and thermal conductivities of the two contacting materials, and the presence of corrosion films. These

[22]M. L. Minges, Thermal Contact Resistance, Volume 1 — A Review of the Literature, AFML-TR-65-375, Vol. 1 (April 1966).

[redacted]

facts have led to the adoption of a semiempirical approach in this study. The objectives of this approach are to determine the relative importance of the variables for systems of interest and to show which are the most likely avenues to pursue for minimizing the contact resistance.

Thermal contact resistance measurements are now being obtained in vacuum at temperatures around 50°C to study solid-solid contact resistance without the additional complications of gas conduction and convection or thermal radiation transfer. Data are being obtained in an apparatus that was originally designed for thermal conductivity measurements near room temperature. This apparatus, which has been described by Moore *et al.*,[23] uses two Armco iron heat meter bars to determine the heat flux and temperature difference across a sample sandwiched between the two bars. Previous work showed that compressed indium foil was useful for reducing the thermal contact resistance at the sample—meter bar interfaces, so a system for compressing the test column was included.

For the contact resistance experiments, the single uninstrumented sample and its two indium foils were replaced by two instrumented samples and three foils. The top and bottom foils, at the specimen—meter bar interfaces, are 0.020-in.-thick lead and are used to compensate for misalignment in the test column. The third foil, located between the two 1-in.-long samples, simulates the cladding material. The two samples, which are each instrumented with three Chromel vs Constantan thermocouples, simulate the fuel material. The thermal conductivity of these two specimens is determined in a separate experiment, and with these data four values for the heat flux q are obtained at different positions along the test column. The variation in q indicates the uniformity of the heat flow pattern and the importance of heat losses. The temperature drop across the two simulated fuel-cladding interfaces, $2\Delta T_i$, is obtained by extrapolating the three temperatures measured on each

[23] J. P. Moore, T G. Kollie, R. S. Graves, and D. L. McElroy, Thermal Conductivity Measurements on Solids Between 20 and 159°C Using a Comparative-Longitudinal Apparatus: Results on MgO, BeO, $ThO_2$, $Th_xU_{1-x}O_{2+y}$, and Al-$UO_2$ Cermets, ORNL-4121 (June 1967).

sample to the two interfaces, subtracting, and making a correction for the relatively small temperature drop across the cladding material. This temperature drop and its corresponding heat flux are then used to calculate the thermal contact resistivity [Eq. (11)].

A significant effort was required to convert the thermal conductivity apparatus for thermal contact resistance experiments. The loading mechanism was rebuilt and calibrated to provide much more reproducible compressive loads on the test column. The total load is now obtained from readings on a Baldwin load cell, and the calibration was obtained by replacing the test column with a second load cell. The results of several calibrations indicate that the compressive load is known to about ±10 psi.

Several runs were made to determine the best axial positions for the specimen thermocouples. These experiments indicated that uniform contact pressures are not easily obtained and showed the importance of having multiple temperature sensors for detecting these difficulties. Further modification of the experimental setup to minimize these difficulties and increase the accuracy of the measurements is now being planned.

Some characteristics of the materials obtained for these tests are shown in Table 3.3. The hardened, high-speed tool steel samples were obtained because the hardness and thermal conductivity of this material match those of uranium nitride fairly well at room temperature. These samples are being used for the apparatus check-out and were required because the UN samples were not available when the work was initiated. Microstructural examination and hardness traverse indicated that these samples were quite homogeneous. The ends of these sampled were lapped optically flat before the tests, and the surface roughness values were determined with a profilometer. The pressed-and-sintered UN specimens described in Table 3.3 are now available and will be used in future tests. Details of the procedure used for fabricating these specimens are presented in another section of this chapter. The simulated cladding materials, copper and type 302 stainless steel, are commercial materials and were obtained from laboratory stores.

[redacted]



Table 3.3. Characteristics of Materials for Thermal Contact Resistance Study

| Material | Condition | Hardness (DPH kg/cm$^2$) | Surface Roughness (RMS μin.) | Thermal Conductivity at 25°C (w cm$^{-2}$ °C$^{-1}$) |
|---|---|---|---|---|
| 0.005-in. copper foil | Annealed 2 hr, 250°C in hydrogen | 58 (50-g load) | 14–15 | 4.01 |
| 0.005-in. type 302 stainless steel foil | "half hard" | 368 (50-g load) | 10–12 | 0.12 |
| T-1 tool steel[a] | Quenched and drawn | 836 (1-kg load) | 3–4 | 0.157 |
| UN[b] | Pressed and sintered | 525[c] | 6–8 | 0.137 |

[a]Carpenter Steel Company startenith grade.

[b]95% of theoretical density, some oxide inclusions.

[c]E. Speidel and D. L. Keller, Fabrication and Properties of Hot-Pressed Uranium Mononitride, BMI-1633 (1963).

An extensive set of measurements on the interface between tool steel and annealed copper was obtained and is shown in Fig. 3.5. These data show that the thermal contact resistance at 47°C decreases approximately linearly with increasing compressive stress and may show a further slight decrease on cycling from low to high stresses. This stress dependence is in agreement with the results of several other studies[22] but does not agree with the stress dependence previously obtained for other foils in this apparatus.[23] The maximum determinate error bands shown were computed by assuming that $\delta q = \pm 0.05\ q$, $\delta T_i = \pm 0.1°C$, $\delta x_i = \pm 6.35 \times 10^{-3}$ cm, $\delta K_f = \pm 0.06$ w cm$^{-2}$ °C$^{-1}$, $\delta \Delta x_f = 2.54 \times 10^{-4}$ cm, where

$T_i$ = temperature at axial position $x_i$,

$K_f$ = thermal conductivity of the foil, and

$\Delta x_f$ = thickness of the foil.

[redacted]

[redacted]



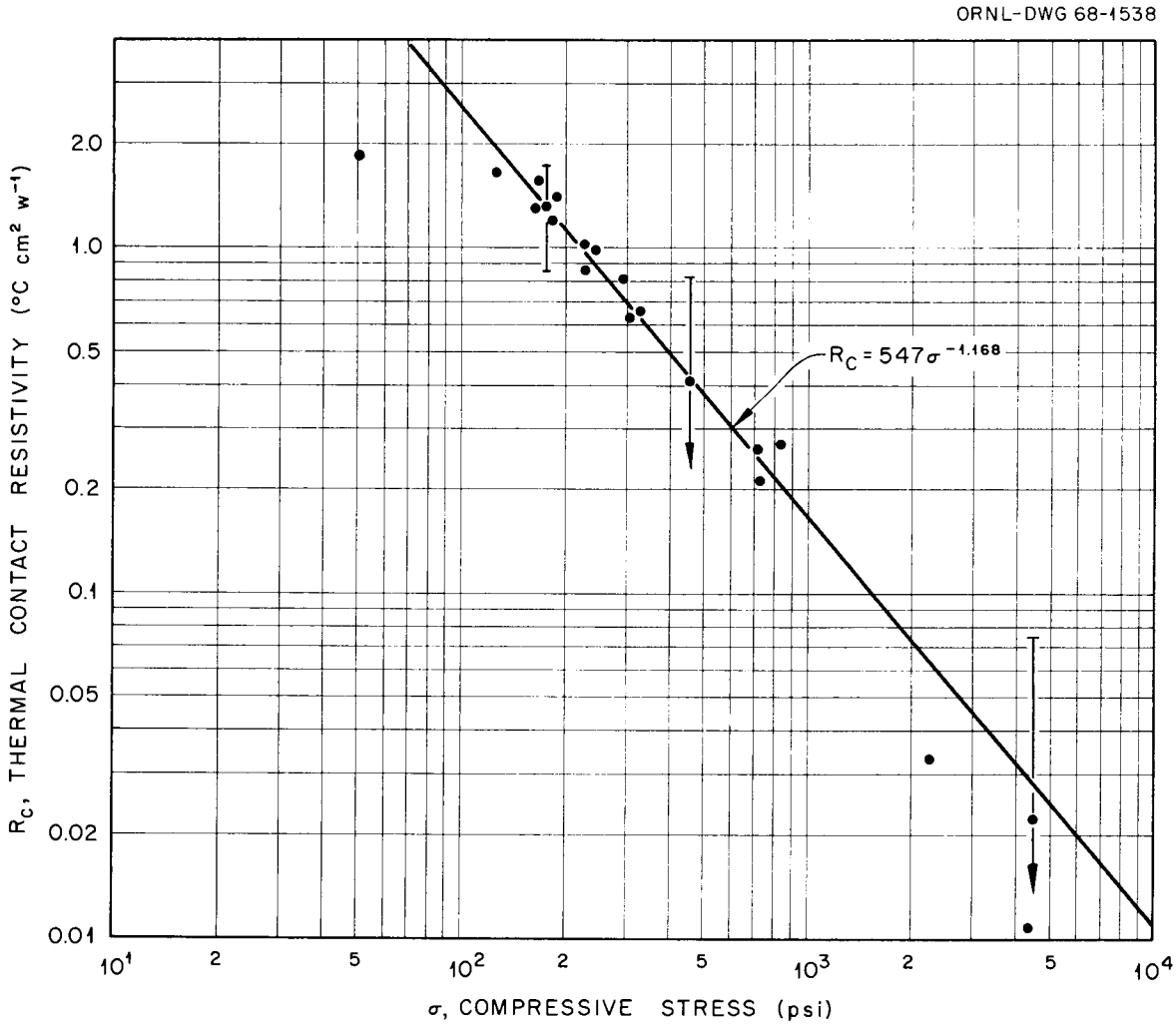


Fig. 3.5. Effect of Compressive Stress on the Thermal Contact Resistivity of the Interface Between Tool Steel and Copper. Interface temperatures vary from 43.8 to 47.5°C.

These calculations show that the temperature uncertainty is critical and thus suggest methods for improving the measurements.

Attempts to determine the temperature variation of $R_c$ at constant stress were inconclusive because the measured effects were slightly smaller than the above calculated maximum uncertainties. The data did indicate that the contact resistance decreases with increasing temperature, and this point will be investigated further.

The effect of helium on the contact resistance was also investigated, but these experiments were also inconclusive and were discontinued. In the experiments, the test column was insulated with alumina wool,

[redacted]

but the insulation would not eliminate heat losses from the test column by gas conduction and convection. These losses could probably be reduced to acceptable levels by installing guard heaters, but the considerable effort required to produce effective thermal guarding would not be justified at this stage of the investigation.

The properties of the annealed copper foil were determined before and after the contact resistance test, and no changes could be detected. Microhardness tests (50 g DPH) showed no change in the foil and uniformity across the contact area. Surface roughness tests gave an indication that the RMS roughness of the copper surface may have decreased from 14 to 15 μin. to about 10 μin., but these results were obtained on two different profilometers and may not be significantly different.

The interface between the tool steel and stainless steel is now being tested. Preliminary results indicate that this interface affords a much poorer thermal contact than tool steel to copper, the difference amounting to a factor of about 11 at a stress of 4200 psi. This effect could be due to differences in surface topography, thermal conductivity, and foil hardness. Further tests will be required to determine the relative importance of these factors.

## Fundamental Studies on Uranium Nitride

W. Fulkerson

We have initiated an intergroup program of basic research on uranium nitride, which will include single-crystal fabrication, band-theory calculations, physical property measurements, deformation mechanism studies, solid-state diffusion studies, low-temperature specific heat measurements, helium bubble migration in a thermal gradient, and surface reaction studies. Hopefully, the results of this coordinated effort will be a better understanding of this important nuclear ceramic.

### Band-Theory Calculations (H. L. Davis, J. S. Faulkner)

The first step to understanding uranium nitride from a fundamental standpoint is to identify the electronic structure. We have initiated first-principle band-theory calculations using the Korringa-Kohn-

Rostoker method and our computer program[24,25] suitably modified to handle the two-atoms-per-primitive-cell case of UN. We have derived a first-guess potential that could be used for a first-generation band structure calculation, but we feel that at present it may be more practical and expedient to obtain a suitable potential from low-temperature electronic specific heat measurements through comparison of theory and experiment. (These measurements are reported in a subsequent section.) If high-quality single crystals of UN become available, Fermiology measurements such as deHaas–van Alphen or magnetoresistance will allow us to establish the potential with much more confidence.

The usefulness of the band calculation is that it provides a unified theory for interpreting and predicting such material behavior as transport properties, magnetic properties, and bonding. Even an unrefined estimate of the potential should yield a band structure that is qualitatively correct and which would tell us the relative distribution of the bonding electrons and how the electronic charge is shared between the two atomic species.

Low-Temperature Specific Heat (J. O. Scarbrough, J. O. Betterton, Jr.)

The specific heat of UN has been measured from 5.7 to 300°K by Westrum and Barber[26] and from 10 to 320°K by Counsell, Dell, and Martin.[27] The derived electronic specific heats vary considerably, being 0.046T and 0.034T j $mole^{-1}$ $deg^{-1}$, respectively. Since UN is antiferromagnetic below 53°K, there will be a magnetic contribution to the

---

[24] J. S. Faulkner, H. L. Davis, and H. W. Joy, "The Calculation of Constant Energy Surfaces for Copper by the Korringa-Kohn-Rostoker Method," Phys. Rev. 161, 656 (1967).

[25] H. L. Davis, J. S. Faulkner, and H. W. Joy, "Calculation of the Band Structure for Copper as a Function of Lattice Spacing," The Physical Review, in press.

[26] E. F. Westrum, Jr., and C. M. Barber, "Uranium Mononitride: Heat Capacity and Thermodynamic Properties from 5 to 350°K," J. Chem. Phys. 45, 635–639 (1966).

[27] J. F. Counsell, R. M. Dell, and J. F. Martin, "Thermodynamic Properties of Uranium Compounds; Part 2, Low-Temperature Heat Capacity and Entropy of Three Uranium Nitrides," Trans. Faraday Soc. 62, 1 (1966).

specific heat added to the lattice and electric portions. We have measured the specific heat of a pressed-and-sintered UN pellet from 1.3 to 4.7°K to unambiguously separate these different components.

The first set of measurements when plotted in the usual $C_p/T$ vs $T^2$ fashion yielded a straight line with an intercept of 48.14 mj $deg^{-2}$ $mole^{-1}$, which is about 5% higher than the value by Westrum and Barber.[26] The value of the density of states calculated from the intercept is 20.5 $(ev)^{-1}$ $molecule^{-1}$, which is an extremely high value, some 70 times that of copper. From the slope of the line through the data, we calculated a Debye temperature of 322.2°K, which is somewhat higher than the values of 293 and 280°K by Westrum and Barber[26] and Counsell, Dell, and Martin,[27] respectively. The scatter of our data is less than 1% from the line, which leads to confidence in our values.

We reduced the size of the specimen and gave it an extended heat treatment at 2250°C in nitrogen in an attempt to reduce the oxygen content significantly from its original 1000 to 2000 ppm level. The smaller specimen was required for a calorimeter equipped with a magnet so we could measure the specific heat as a function of the magnetic field strength. We felt that the magnetic contribution to the specific heat might be changed by a field and could therefore be identified.

Results obtained at magnetic fields from 0 to 35 kilogauss showed no field effect, which indicates that the magnetic contribution is probably negligible. All of the data lay on a straight line parallel to the first but shifted some 2% higher, which results in a 2% higher density of states. The calculated Debye temperatures ranged from 322.2 to 328°K. The differences in the density of states obtained between the first series of measurements and the second probably reflect a real change in the specimen composition resulting from the heat treatment.

From the elastic constant measurements to be described later and a formula described by Herbstein[28] we calculated a Debye temperature of 344°K for a similar UN specimen, which is in good agreement with the

---

[28]F. H. Herbstein, "Methods of Measuring Debye Temperatures and Comparison of Results for Some Cubic Crystals," Advan. Phys. 10, 313 (1961).

322 to 328°K from our specific heat measurements. Similar good comparisons have been obtained for UC: Graham and Chang[29] obtained 330°K from elastic constants, while low-temperature specific heat measurements[30] yielded 320°K.

Elastic Constants (H. L. Whaley)

Longitudinal and shear ultrasonic velocity measurements were made on a pressed-and-sintered rod of UN prepared from the same material and at the same time as the specific heat specimen described above. The technique measured the delay between successive echoes from the end of the rod. The longitudinal measurements were made at 5 MHz with both an immersion and an oil-coupled contact transducer. Both yielded the same result, $V_\ell = 4.52 \times 10^5$ cm/sec ± 0.5%. The shear velocity, $V_s = 2.57 \times 10^5$ cm/sec ± 0.5%, was obtained with a 5-MHz PZT crystal[31] bonded to the specimen. These values were used to calculate the elastic constants of UN and the results are compared with those of other investigators in Table 3.4.

It should be mentioned, in connection with the previous section, that 5 MHz is $10^{-6}$ times the Debye frequency of UN. Therefore, the measurements should be indicative of the harmonic long-wavelength portion of the phonon spectrum, and the derived Debye temperature should correspond to the values derived from the specific heat measurements, which are also indicative of the harmonic part of the phonon spectrum.

Uranium Self-Diffusion in UN (D. K. Reimann)

We are determining the self-diffusion of uranium in UN as a function of temperature and nitrogen pressure, using specimens of BMI arc-melted, large-grained, essentially theoretically dense material. The

---

[29] L. J. Graham and R. Chang, "The Elastic Constants of Uranium Carbide Between 4.2 and 300°K," pp. 409–422 in International Symposium on Compounds of Interest in Nuclear Reactor Technology, ed. by J. T. Waber, P. Chiotti, and W. N. Miner, AIME Metallurgical Society, New York, 1964.

[30] De M. M. Andre de Combarien, P. Costa, and J. Michel, Compt. Rend. 256, 5518 (1963).

[31] PZT denotes a lead zirconate titanate crystal from the Clevite Company.

Table 3.4. Elastic Constants of UN

| Constant | ORNL[a] | Speidel and Keller[b] | Taylor and McMurtry[c] |
|---|---|---|---|
| Density, % of theoretical | 95 | 96 | 88 |
| Poisson's ratio | 0.260 | 0.1 | 0.26 |
| Young's modulus, dynes/cm$^2$ | $2.39 \times 10^{12}$ | $2.1 \times 10^{12}$ | $1.9 \times 10^{12}$ |
| Shear modulus, dynes/cm$^2$ | $9.45 \times 10^{11}$ | $9.6 \times 10^{11}$ | $6.8 \times 10^{11}$ |
| Bulk modulus, dynes/cm$^2$ | $1.68 \times 10^{12}$ | $0.87 \times 10^{12}$ | $1.32 \times 10^{12}$ |

[a]Elastic constants calculated from velocity of sound and the theoretical density of UN.

[b]E. Speidel and D. R. Keller, Fabrication and Properties of Hot-Pressed Uranium Mononitride, BMI-1633 (1963).

[c]K. Taylor and C. McMurtry, Synthesis and Fabrication of Uranium Compounds, Summary Report, May 1959–December 1960, ORO-400 (1961).

nitrogen pressures are being varied with temperature in a manner calculated to yield a constant composition in the single-phase UN field. Although we do not know precisely the stoichiometry range across the single-phase region, we do know that we are operating nearer the UN + U($\ell$) boundary than the UN + $U_2N_3$ boundary. Later we will make measurements on samples more hyperstoichiometric.

The method[32] being used is a sensitive nondestructive technique in which the energy spectrum of alpha radiation of initially deposited $^{233}U$ tracer is measured as a function of annealing time. The energy of the alpha radiation is indicative of the depth of penetration of the tracer, and the intensity is proportional to the concentration at that depth. Therefore, the energy-intensity spectrum of the tracer before and after annealing, or after successive anneals, is sufficient to determine the diffusion coefficient.

Before the tracer is applied, the specimen is given two heat treatments. The first is at 2250 to 2300°C in nitrogen for several hours to homogenize the specimen and relieve stresses. The specimen is then

[32]F. Schmitz and M. Fock, J. Nucl. Mater. 21, 317 (1967).

[redacted]



equilibrated at the temperature and pressure of interest for the experiment and cooled rapidly to room temperature. The tracer is applied and the specimen is quickly reheated to the test temperature.

Our results for the first series of experiments are shown in Fig. 3.6 and are indicative of typical Arrhenius behavior, with the diffusion coefficient given by the equation

$$D = 3.2 \times 10^{-8} \exp(-59{,}400/RT) \text{ cm}^2/\text{sec} . \quad (12)$$

Also plotted in Fig. 3.6 are data for the self-diffusion of uranium in UC by various investigators. Our results are in the range of the recent results of Lindner et al.,[33] although our calculated activation energy, 59.4 kcal/mole, is smaller than those reported for UC, which range

[33]R. Lindner, G. Riemer, and H. L. Scherff, "Self Diffusion of Uranium in Uranium Monocarbide," J. Nucl. Mater. 23, 222 (1967).

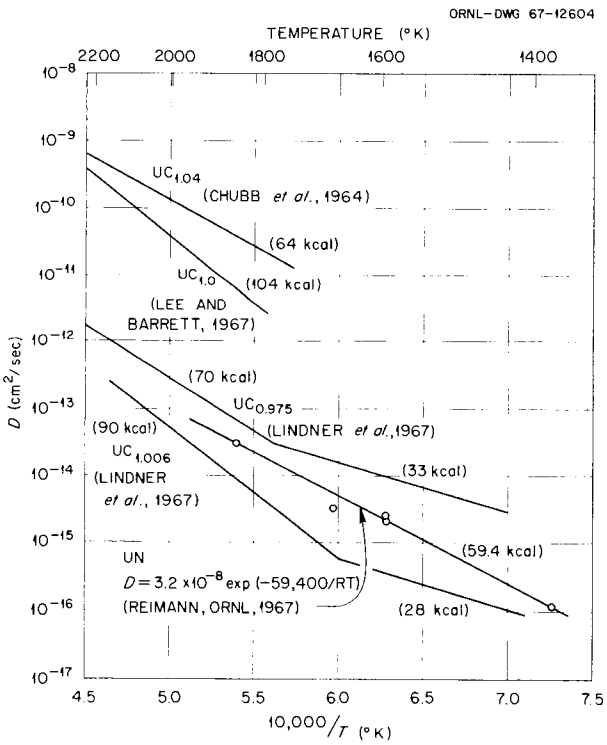


Fig. 3.6. Self-Diffusion of Uranium in UN and UC. [Refs. W. Chubb et al., J. Nucl. Mater. 13, 63 (1964); R. Lindner et al., J. Nucl. Mater. 23, 222 (1967); H. M. Lee and L. R. Barrett, Proc. Brit. Ceram. Soc., No. 7, 159 (1967).

[redacted]

from 64 to 104 kcal/mole. It is in good agreement with a value of about 60 kcal/mole obtained from compressive creep measurements on UN in vacuum.[34] Compressive creep has also been measured[35] on UN at high temperatures (1500 to 1800°C) under 200 mm of nitrogen, yielding activation energies ranging from 70 to 80 kcal/mole. Our experimental conditions more nearly resemble the vacuum environment. It will be interesting to see how our results change as we alter the stoichiometry of the specimen in future experiments.

Ternary Systems Containing Thorium and Uranium[36] (J. T. Venard)

Potential advantages of thermal-breeder fuels having a metallic thorium matrix with a dispersion of either (Th,U)C or (Th,U)N led to an investigation of the Th-U-C and Th-U-N ternary systems. This investigation was limited to the 1000°C isotherm at 50 at.% C or N and below. Alloys in the Th-U-C system were arc-melted, while those in the Th-U-N system were prepared by powder metallurgy. Equilibration times for cast alloys in the Th-U-C system were 240 to 350 hr at 1000°C and greater than 1000 hr at 600 and 800°C. In the Th-U-N system the 1000°C equilibration time was 80 to 100 hr. Lattice parameters across the UC-ThC pseudobinary showed a slight negative deviation from Vegard's law and excellent agreement with published data. Across the UN-ThN pseudobinary, lattice parameters obeyed Vegard's law. The most uranium-rich compounds in equilibrium with metallic thorium were found to be $(Th_{0.906},U_{0.094})C_{0.712}$ and $(Th_{0.944},U_{0.056})N_{0.869}$, respectively. A thermodynamic analysis was shown to be consistent with the experimental results and yielded an estimate of 51.9 kcal/mole as the 1000°C free energy of formation of ThN.

---

[34]M. H. Fassler, H. J. Huegel, and M. A. DeCrescente, Compressive Creep of UC and UN, Part I, PWAC-482 (Pt. I), (October 1965).

[35]R. R. Vandervoort, W. L. Barmore, and C. F. Cline, Compressive Creep of Polycrystalline Uranium Mononitride in Nitrogen, UCRL-70709 (October 1967).

[36]Abstracted from J. T. Venard, Investigation of Certain Ternary Systems Containing Thorium and Uranium, ORNL-TM-2015 (January 1968), M.S. Thesis, the University of Tennessee.

Helium Bubble Migration in UN in a Temperature Gradient[37] (S. C. Weaver)

Helium bubble migration in uranium mononitride was studied in the temperature range of 985 to 1585°C with temperature gradients ranging from 75 to 880°C/cm. The UN specimens were inoculated with 250-kev helium ions from a Cockcroft-Walton accelerator. Both the temperature and temperature gradients were known accurately and could be controlled. The migration distances and bubble sizes were examined by replication electron microscopy applied to longitudinal sections (parallel to the temperature gradient) through the UN specimens. Thin-film transmission and replicas of fractured surfaces were used to support the results obtained from the longitudinal sections. The bubbles were observed to migrate by surface diffusion up the temperature gradient at velocities ranging from 300 A/sec at 985°C to greater than 11,000 A/sec at 1585°C.

From measurements of the migration distances, an approximate surface diffusion coefficient $D_s$ for UN was calculated to be:

$$D_s = 1.92 \times 10^3 \exp(-42,200/RT) \text{ cm}^2/\text{sec} . \quad (13)$$

Although the bubbles migrated large distances, they did not coalesce during the heat treatments. We suggest that this behavior was caused by the existence of large stress fields in the UN matrix surrounding the bubbles. These fields caused the bubbles to repel each other. These stress fields were presumably caused by high nonequilibrium internal pressures in the gas bubbles.

Transport Properties (D. L. McElroy, J. P. Moore, C. V. Dodd, R. K. Williams, T. E. Banks, R. S. Graves)

The electrical and thermal transport properties of uranium nitride are of both fundamental and practical interest. We plan to determine these properties over a wide temperature range for both pure and alloyed polycrystalline specimens and for single crystals as they become available. These data are also needed to afford valid comparisons with other candidate fuel materials.

---

[37]Abstracted from S. C. Weaver, Helium Gas Bubble Migration in Uranium Mononitride in a Temperature Gradient, ORNL-TM-2016 (December 1967), M.S. Thesis, the University of Tennessee.

Density Corrections. Electrical resistivity data obtained on pressed-and-sintered specimens of UN depend on the specimen density. The room-temperature electrical resistivity obtained by various workers[38–41] and from recent ORNL studies is given in Fig. 3.7 as a function of the

[38]B. A. Hayes and M. A. DeCrescente, Thermal Conductivity and Electrical Resistivity of Uranium Mononitride, PWAC-481 (October 1965) ("CANEL" data).

[39]P. Costa et al., "Magnetic Transitions in Uranium and Plutonium Mononitrides, Monocarbides, and Sesquicarbides," p. 83 in International Symposium on Compounds of Interest in Nuclear Reactor Technology, ed. by J. T. Waber, P. Chiotti, and W. N. Miner, AIME Metallurgical Society, New York, 1964 (French data).

[40]R. W. Endebrook, E. L. Foster, Jr., and D. L. Keller, Preparation and Properties of Cast UN, BMI-1690 (EURAEC-1206), (Aug. 28, 1964).

[41]I. H. Warren and C. F. Price, "Thermoelectric Properties of Cubic Uranium Monocompounds," Can. Met. Quart. 3, 183 (1964).

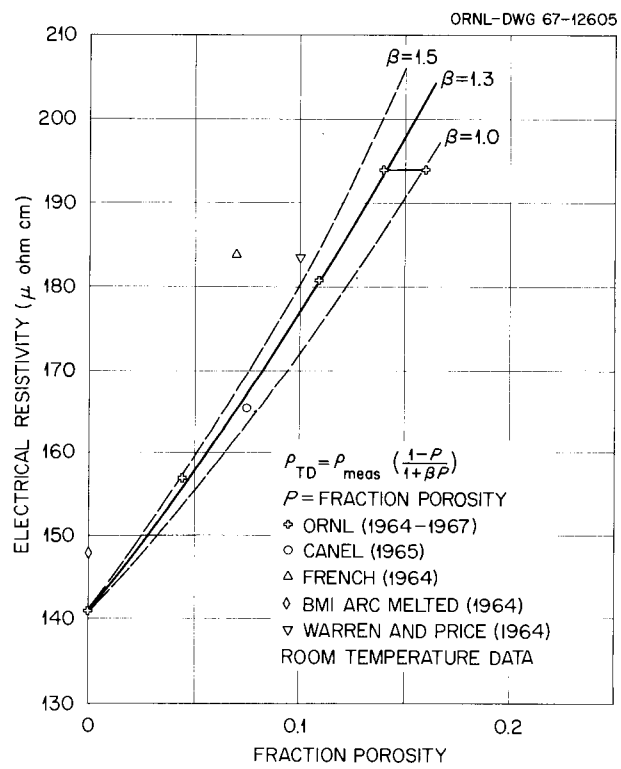


Fig. 3.7. Variation of Room-Temperature Electrical Resistivity of UN with Porosity.

fraction porosity P, using 14.32 g/cm$^3$ for the theoretical density of UN. Except for the French data[39] all of these results agree reasonably well. The ORNL results can be fitted by the equation

$$\rho_{T.D.} = \rho_{measured}\left(\frac{1 - P}{1 + \beta P}\right) \tag{14}$$

where

$\rho_{T.D.}$ is the electrical resistivity of theoretically dense UN,

$\rho_{measured}$ is the measured electrical resistivity of the specimen having a fractional porosity P, and

$\beta$ is a correction constant with a value of 1.3 for the ORNL results.

Equation (14) is a modified Eucken[42] type equation, and a theoretical value of $\beta = 0.5$ is expected for well-isolated spherical pores. The empirical value of 1.3 is an indication of nonspherical pores and the lack of isolation of these pores. The method of specimen preparation may influence the density correction, and this may explain the deviation of the French data. The ORNL values extrapolate to an electrical resistivity of 141 μohm-cm for theoretically dense UN at room temperature. This compares to a range of values from 140.3 to 145.3 μohm-cm found for various small pellets of theoretically dense arc-melted UN obtained from BMI. These values were obtained by a comparative eddy-current technique, which requires a specimen only 0.1 in. in diameter × 0.030 in. thick. These values are lower than the value of 148 μohm-cm obtained by extrapolating to room temperature the electrical resistivity results reported[40] by BMI for their arc-melted material.

Electrical Resistivity and Resistivity Ratio. The electrical resistivity of UN as a function of temperature is given in Fig. 3.8, where all data were corrected to theoretical density with Eq. (14) and $\beta = 1.3$. This correction places the ORNL, CANEL,[38] and Warren and Price[42] data below the BMI data[40] for theoretically dense arc-melted

---

[42]A. Eucken, Forsch. Gebiete Ingenieurw. VDI (Ver. Deut. Ingr.) Forschungsh. 353 (1932).

[redacted]



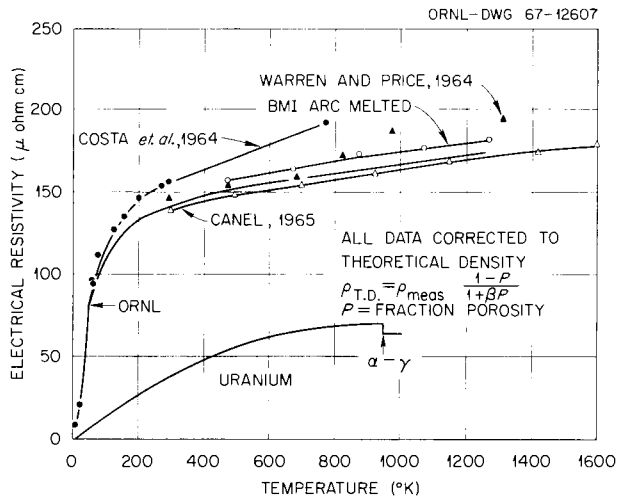


Fig. 3.8. Electrical Resistivity as a Function of Temperature for Theoretically Dense UN and Uranium Metal.

material. This agrees with the eddy-current results on arc-melted material cited above. Above 400°K the resistivity increases approximately linearly with temperature, and the magnitude of this increase is similar to that of an alloy.

The behavior of the electrical resistivity below room temperature is most interesting, and our results are shown in Fig. 3.9. The measurements were made on a rod of UN, which had been used several years ago to obtain electrical resistivity results at high temperatures.[43] This rod was heat treated at 2250°C in 1 atm of nitrogen for 6.5 hr to remove most of the oxygen contamination. The room-temperature resistivity of this rod, uncorrected for porosity, was 194 μohm-cm before heat treatment. The density of the rod was increased from 86 to 89% of theoretical by the heat treatment, and the resistivity decreased to 181 μohm-cm. This change in resistivity is approximately that predicted by the density change.

The electrical resistivity increases extremely rapidly from 4.2°K to the Néel temperature of 53°K. The magnitude of this increase is

[43] T. G. Kollie, D. L. McElroy, R. S. Graves, and W. Fulkerson, "A Thermal Comparator Apparatus for Thermal Conductivity Measurements from 50 to 400°C," pp. 651–676 in International Symposium on Compounds of Interest in Nuclear Reactor Technology, ed. by J. T. Waber, P. Chiotti, and W. N. Miner, AIME Metallurgical Society, New York, 1964.

[redacted]

[redacted]



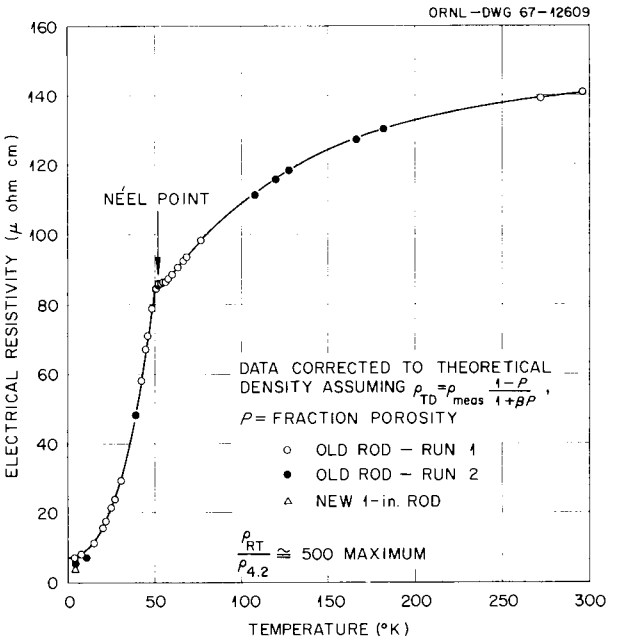


Fig. 3.9. Low-Temperature Electrical Resistivity of UN.

indicative of effective spin wave scattering of the current carriers. The resistivity below about 30°K increases very nearly as $T^2$. Even above the Néel temperature the resistivity continued to increase rapidly, indicating that spin disorder continues to increase 100 to 200° above the Néel point. The shape of the curve in the vicinity of the Néel point is not well defined by these experiments due to a temperature gradient on the specimen between the voltage taps, and these measurements will be repeated under isothermal conditions.

The resistivity ratio (the ratio of the electrical resistivity at room temperature to that at the helium boiling point) varied from 19 to 25 for this rod, depending on the position of the voltage taps. For a rod made from the same batch of material as the specific heat specimens, described in a previous section, the resistivity ratio increased from 26 to 35 upon heat treatment similar to that given the earlier specimen. This is another indication that the increase in the density of states due to heat treatment, also described previously, was because of an improvement in the quality of the specimen.

The resistivity ratio should be a very useful tool for judging the purity and perfection of UN specimens just as it is for metals. However,

[redacted]

[redacted]



the shape of the resistivity curves at 4.2°K indicates the presence of an intrinsic magnetic resistivity of about 0.28 μohm-cm. Thus, 500 is the estimated maximum resistivity ratio for a pure, defect-free, stoichiometric sample of UN.

Thermal Conductivity of UN. A comparative longitudinal heat flow method[44] was used to measure the thermal conductivity between 30 and 150°C of two pressed-and-sintered, approximately 95%-dense UN pellets and of a small arc-melted, theoretically dense UN pellet. The results are plotted in Fig. 3.10 and agree to ±4% after the data are corrected to theoretical density by the inverse of Eq. (14):

$$k_{T.D.} = k_{measured}\left(\frac{1 + \beta P}{1 - P}\right) \tag{15}$$

where

$\beta$ is 1.3.

---

[44]J. P. Moore, T. G. Kollie, R. S. Graves, and D. L. McElroy, Thermal Conductivity Measurements on Solids Between 20 and 150°C Using a Comparative-Longitudinal Apparatus: Results on MgO, BeO, $ThO_2$, $Th_xU_{1-x}O_{2+y}$, and Al-$UO_2$ Cermets, ORNL-4121 (June 1967).

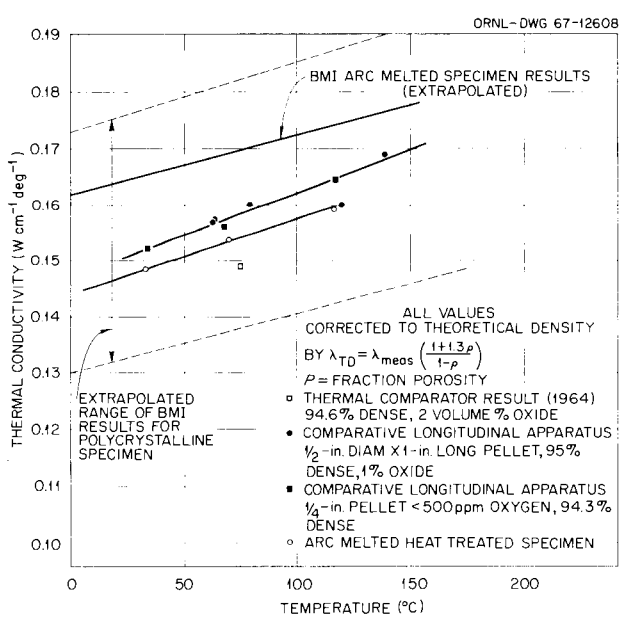


Fig. 3.10. Thermal Conductivity of Arc-Melted UN and Pressed-and-Sintered UN as a Function of Temperature.

[redacted]

The results are in reasonable agreement with the extrapolation of the BMI data.[45,46] The measurements will be extended to low temperatures on rod-shaped specimens with an absolute longitudinal heat flow apparatus.[47] The results should be extremely useful for separating the lattice and electronic contributions to the thermal conductivity and for prediction of high-temperature thermal conductivity values from high-temperature electrical resistivity measurements.

Seebeck Coefficient. Figure 3.11 shows the absolute Seebeck coefficient of UN measured for the same specimen used to measure the low-temperature electrical resistivity. Our results agree well with

---

[45]E. O. Speidel and D. L. Keller, Fabrication and Properties of Hot-Pressed Uranium Mononitride, BMI-1633 (May 1963).

[46]R. W. Endebrook, E. L. Foster, Jr., and D. L. Keller, Preparation and Properties of Cast UN, BMI-1690 (EURAEC-1206), (Aug. 28, 1964).

[47]J. P. Moore, D. L. McElroy, and R. S. Graves, "Thermal Conductivity and Electrical Resistivity of High-Purity Copper from 78 to 400°K," Can. J. Phys. 45(12), 3849–3865 (December 1967).

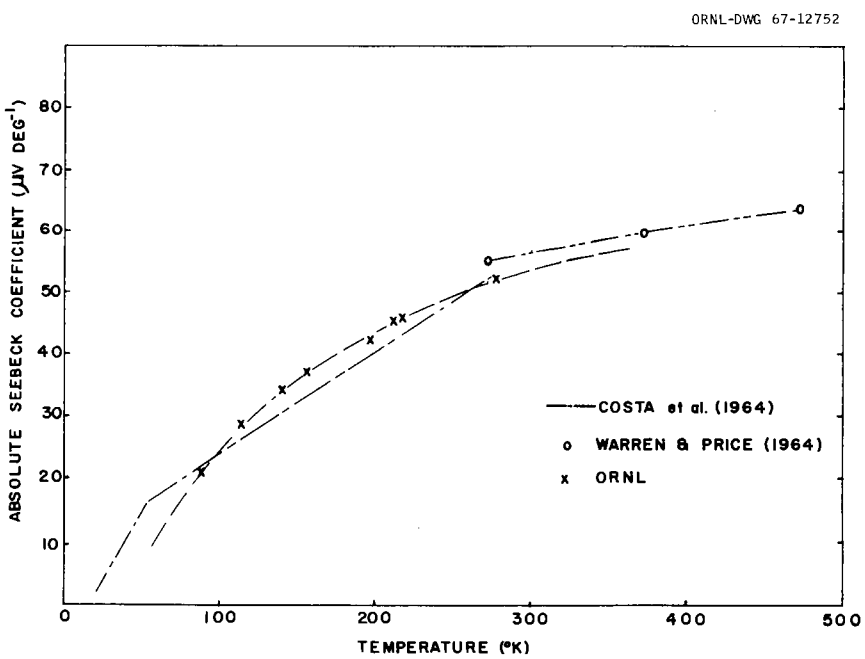


Fig. 3.11. Absolute Seebeck Coefficient of Pressed-and-Sintered UN as a Function of Absolute Temperature.

those of Costa et al.[48] and also tie in well at high temperatures with the results of Warren and Price.[49] The Seebeck coefficient is positive and larger than found for metals.

Electrical Resistivity and Thermal Conductivity of U(C,N). The electrical resistivity at room temperature of 83%-dense and 89.5%-dense pellets of U(C,N), each approximately $U(C_{0.45}N_{0.55})$, was 112.5 and 92 μohm-cm, respectively. If this difference is due entirely to the difference in density, one obtains a β value of 2.59 and 65 μohm-cm for theoretically dense material of this composition. These results are plotted in Fig. 3.12 and compared to values for UC and UN. For normal alloying behavior we would expect the electrical resistivity to be above the straight line drawn between pure UN and UC in Fig. 3.12. The predicted 65 μohm-cm value is below the line, and this could be due to ordering. However, Ohmichi and Kikuchi[50] have reported similar negative deviation for all compositions across the pseudobinary diagram, so that ordering is probably not the explanation. The substitution of carbon for nitrogen in UN may shift the Fermi energy in such a way as to either reduce scattering of the current carriers or to increase the number of carriers. A third alternative is that the magnetic scattering, so preponderant in UN, is reduced by the addition of carbon, and this hypothesis is reinforced by the nonmagnetic character of UC. However, Ohmichi and Nasu[51] measured the magnetic susceptibility of U(C,N) solid solutions and found an approximate Curie-Weiss law behavior above 400°K near our composition. Further work is required before these solid solutions will be understood.

---

[48]P. Costa et al., "Magnetic Transitions in Uranium and Plutonium Mononitrides, Monocarbides, and Sesquicarbides," p. 83 in International Symposium on Compounds of Interest in Nuclear Reactor Technology, ed. by J. T. Waber, P. Chiotti, and W. N. Miner, AIME Metallurgical Society, New York, 1964 (French data).

[49]I. H. Warren and C. F. Price, "Thermoelectric Properties of Cubic Uranium Monocompounds," Can. Met. Quart. 3, 183 (1964).

[50]T. Ohmichi and T. Kikuchi, Japan Atomic Energy Research Institute, Tokai Establishment, private communication, October 18, 1967.

[51]T. Ohmichi and S. Nasu, Magnetic Susceptibility of U-C-N System, JAERI-Memo-2702 (1967).

[redacted]



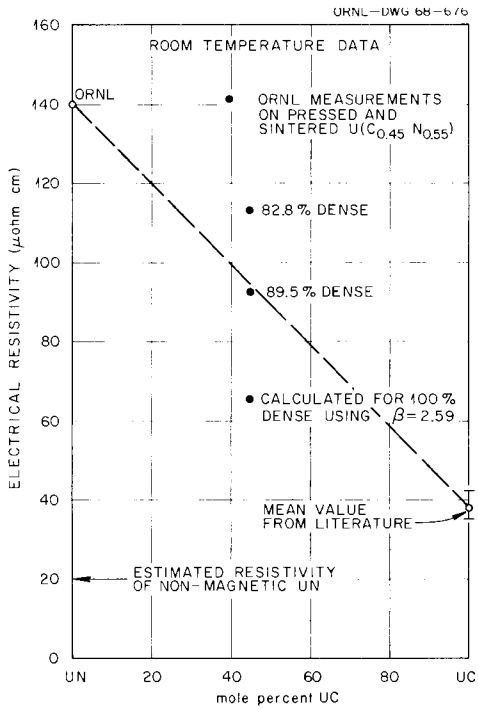


Fig. 3.12. Measured and Predicted Values of the Electrical Resistivity of Pressed-and-Sintered $U(C_{0.45}N_{0.55})$ of Different Densities Compared to Those of Pure UN and UC at Room Temperature.

Since U(C,N) is a potentially important fast reactor fuel, the lower-than-usual electrical resistivity is of considerable importance, since it means that the electronic portion of the thermal conductivity will be unusually high. We measured the thermal conductivity of these pellets, and the results are shown in Fig. 3.13. If the difference between the measured values is ascribed to density, a β of 2.49 results, and this agrees with the value of 2.59 derived from electrical resistivity. The thermal conductivity calculated for the theoretically dense material lies below the straight line between UN and UC (value for UC from Moser and Kruger[52]). This result does not disagree with the

[52] J. B. Moser and O. L. Kruger, "Thermal Conductivity and Heat Capacity of the Monocarbide, Monophosphide, and Monosulfide of Uranium," J. Appl. Phys. 38, 3215–3222 (1967).

[redacted]

[redacted]



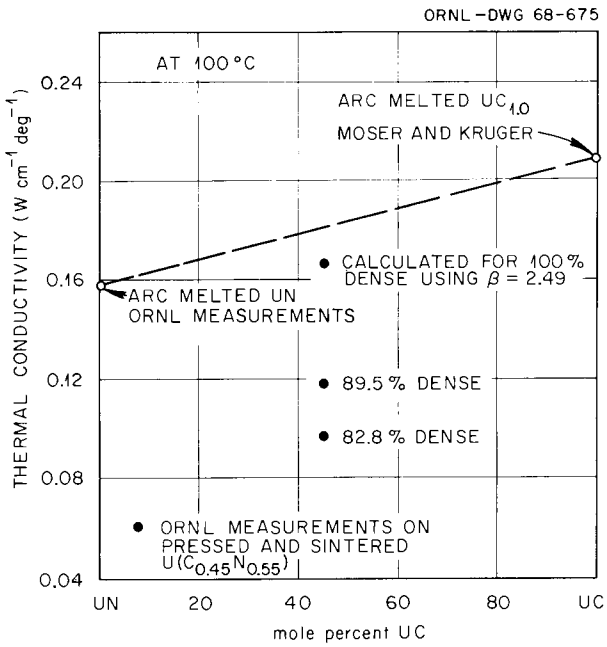


Fig. 3.13. Measured and Predicted Thermal Conductivity of Pressed- and Sintered $U(C_{0.45}N_{0.55})$ of Different Densities Compared to that of Pure UN and UC at 100°C.

electrical resistivity results, since 50% or more of the thermal conductivity at 100°C is due to phonon transport, and this part of the conductivity will be reduced by alloying. It is interesting to note that the predicted thermal conductivity of U(C,N) is greater than that of UN. Furthermore, the Seebeck coefficient of these alloys should be measured to establish the thermoelectric figure of merit as a function of composition.

## Studies in the U-C-N System

J. M. Leitnaker R. A. Potter
K. E. Spear

A solid solution of UC and UN may have practical importance as a nuclear fuel, since both components are under active consideration for such use. The large-scale production of a carbonitride should be easier than that of either a pure carbide or nitride. Thermal conductivity and irradiation stability should lie intermediate to the end members of the system. Compatibility problems are not expected to be

[redacted]

any more serious than those of either end member and may be less difficult. Thus, additional information on the solid solution is of potential practical importance. In addition to the intrinsic interest in U(C,N) the information may also be a valuable guide to experiments with other carbonitride fuels, notably (Pu,U)(C,N) as well as Cm(C,N).

We previously[53] reported a study of the thermodynamic properties of the solid solution. Two important questions about the system were left unanswered: (1) we were never able to analyze successfully for free carbon in the samples, and (2) other analytical procedures seemed to give less precision than desirable. As a result of these two problems, we were forced to depend on lattice parameter determinations and the assumption of Vegard's law to interpret the data obtained.

Further work was done to attempt to resolve the analytical problems and establish whether or not U(C,N) in equilibrium with graphite does indeed obey Vegard's law. In this endeavor we have cooperated with W. R. Laing, whose group in the Analytical Chemistry Division performed a number of the analyses reported herein.

Problems associated with the free carbon analysis are well illustrated in Fig. 3.14. (Since one can analyze for total carbon by combustion, determination of percent of free carbon allows one to compute bound carbon by difference.) Values of total carbon in the samples illustrated are approximately correct, but the values for combined carbon are inconsistent with each other and with x-ray data. Clearly, the results vary widely.

Problems with nitrogen determinations are illustrated in Table 3.5, which compares four methods for determination of nitrogen content. We see that three methods are internally consistent, but the chemical analysis gives results that are consistently high by about 10%.

Since no standard samples for nitrides or carbonitrides exist, we need to obtain analyses for all constituents to surmise that if 100% of the material is found all analyses are correct. Since earlier

---

[53]J. M. Leitnaker, "The Ideality of the UC-UN Solid Solution," to be published as a part of the proceedings of the International Atomic Energy Agency Symposium on Thermodynamics of Nuclear Materials with Emphasis on Solution Systems, Vienna, Austria, September 4–8, 1967.

[redacted]



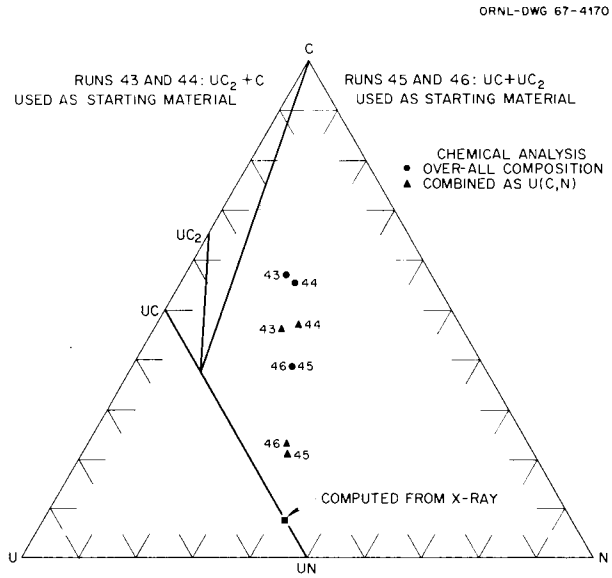


Fig. 3.14. Data Illustrating Uncertainty Associated with Free Carbon Determination.

Table 3.5. Alternative Determinations of Nitrogen in U-C-N Samples

| Nitrogen Content, wt % | | | |
|---|---|---|---|
| Calculated[a] | Weight Change[b] | Difference[c] | Chemical Analysis |
| 4.6 | 4.5 | 4.6 | 4.9 |
| 3.3 | 3.2 | 3.4 | 3.6 |
| 4.8 | 4.6 | 4.7 | 5.3 |
| 3.8 | 3.8 | 4.0 | 4.3 |
| 4.6 | 4.6 | 4.6 | 5.0 |
| 2.3 | | 2.6 | 2.9 |

[a]Calculated from lattice constant of U(C,N) assuming Vegard's law is obeyed.

[b]Obtained by weighing sample before and after reaction to form U(C,N).

[c]Uranium and carbon percentages subtracted from 100.

[redacted]

observations led to some suspicion that uranium carbonitride was not susceptible to the same analytical procedures as were uranium nitride and carbide separately (as described above), samples were obtained either by heating uranium carbides in nitrogen or by heating a mixture of UN and graphite. The procedure used has been described.[53]

Solution to the nitrogen analysis appears to have been resolved in the Analytical Chemistry group of W. R. Laing. Samples are now analyzed for nitrogen by first dissolving the sample in acid in a sealed tube and then completing the usual modified Kjeldahl procedure. Samples are also now analyzed in triplicate, a procedure which gives more confidence in the results. In Table 3.6 we show that the nitrogen analyses agree,

Table 3.6. Nitrogen Contents for U-C-N Samples Obtained by Various Routes[a]

| Sample | Nitrogen Pressure (torr) | Nitrogen Content, wt % | | | |
|---|---|---|---|---|---|
| | | Difference[b] | Weight Change[c] | X-Ray Analysis[d] | Chemical Analysis[e] |
| | | UC + $N_2$ Starting Material | | | |
| 5077-60 | 400 | 4.27 | 4.20 | 4.39 | 4.09 |
| 5077-62 | 600 | 4.52 | 4.33 | 4.52 | 4.40 |
| 5077-64 | 200 | 4.17 | 3.95 | 4.24 | 4.16 |
| | | UN + C Starting Material | | | |
| 5077-52 | 600 | 4.98 | | 4.88 | 4.96 |
| 5077-54 | 600 | 4.93 | | 4.79 | 4.78 |
| 5077-56 | 400 | 4.08 | | 4.62 | 4.04 |

[a]Samples were run at 1500°C in the equipment described by J. M. Leitnaker, "The Ideality of the UC-UN Solid Solution," to be published as a part of the proceedings of the International Atomic Energy Agency Symposium on Thermodynamics of Nuclear Materials with Emphasis on Solution Systems, Vienna, Austria, September 4–8, 1967.

[b]Obtained by subtracting our determinations of carbon and uranium from 100%.

[c]Obtained by weighing the sample before and after reaction.

[d]Calculated from the lattice constant, assuming Vegard's law.

[e]Direct analysis by modified Kjeldahl by Analytical Chemistry. A sealed-tube technique is used to dissolve the sample.

within a reasonable experimental error, with results obtained by other means (with the exception of sample 5077-56, which we cannot explain). Further, there appears to be no significant trend in the experimental errors.

In addition to the analytical agreement, two other observations are noteworthy. First, we get good agreement, not only among the various methods, but also regardless of whether we start with UC and nitrogen or with UN and graphite. That is, we have approached equilibrium from two directions. Second, since the calculated amount of nitrogen present agrees with that found by other means, one can reasonably conclude that in the composition range shown (produced by equilibration at 1500°C) the UC-UN solid solution is ideal. We conclude this because the calculated nitrogen results of Table 3.6, which agree with other determinations, depend on the x-ray lattice parameter and the assumption that this system obeys Vegard's law; our previous work showed if the system obeys Vegard's law, then it is ideal in the thermodynamic sense.

In addition to these data on nitrogen determinations we have credible results for free carbon. The demonstration that the free carbon analyses are reasonable involves several steps, as follows:

1. demonstrating that precise, accurate percentages can be determined for spectrographic grade graphite,
2. demonstrating that accurate values can be obtained for spectrographic grade graphite mixed with $U_3O_8$,
3. from these, concluding that accurate values can be obtained for total carbon in uranium carbides,
4. obtaining values for total carbon in U(C,N) samples in which no free carbon is present,
5. inferring that if the bound carbon in U(C,N) samples that have excess carbon approximates the results shown for item 4, the results will be deemed "reasonable." Further confirmation will, of course, be desirable.

[redacted]



The demonstration that precise, accurate percentages can be obtained for spectrographic grade graphite is shown in Table 3.7. The apparatus built to determine this quantity is shown in Fig. 3.15. The technique is a standard one: passing purified oxygen over the sample, catalytically oxidizing any CO to $CO_2$, absorbing the $CO_2$ on Ascarite, and weighing.

The demonstration that graphite can be determined correctly when mixed with $U_3O_8$ was somewhat more difficult. When samples of $U_3O_8$ and graphite were mixed in a bottle and then sampled for combustion, the amount of graphite found differed from the amount taken by 1 to 2%, which is considerably less precise than our results shown in Table 3.7. If, however, a layer of $U_3O_8$ was weighed into a platinum boat, followed by a layer of graphite and then another layer of $U_3O_8$, the results were quite good, as seen in Table 3.8. We concluded that segregation in the samples was an important possible source of error.

The data reported above indicate that the total amount of carbon in uranium carbides or carbonitrides can be determined. The next step was to obtain the lattice parameter of the UC-UN solid solution as a function of composition in the absence of free carbon. Our data are

Table 3.7. Results for Calibration of Carbon Analysis Train[a]

| Graphite,[b] mg | | Difference |
|---|---|---|
| Taken | Found | (%) |
| 39.8 | 39.87 | 0.2 |
| 37.6 | 37.72 | 0.3 |
| 60.0 | 60.12 | 0.2 |
| 0.0 | 0.08 | |

[a] If the blank were subtracted, the percent difference in each of the three samples would be better than the precision of weighing. This kind of agreement is surely fortuitous.

[b] −50 mesh spectrographic grade.

[redacted]

[redacted]



ORNL-DWG 67-8197

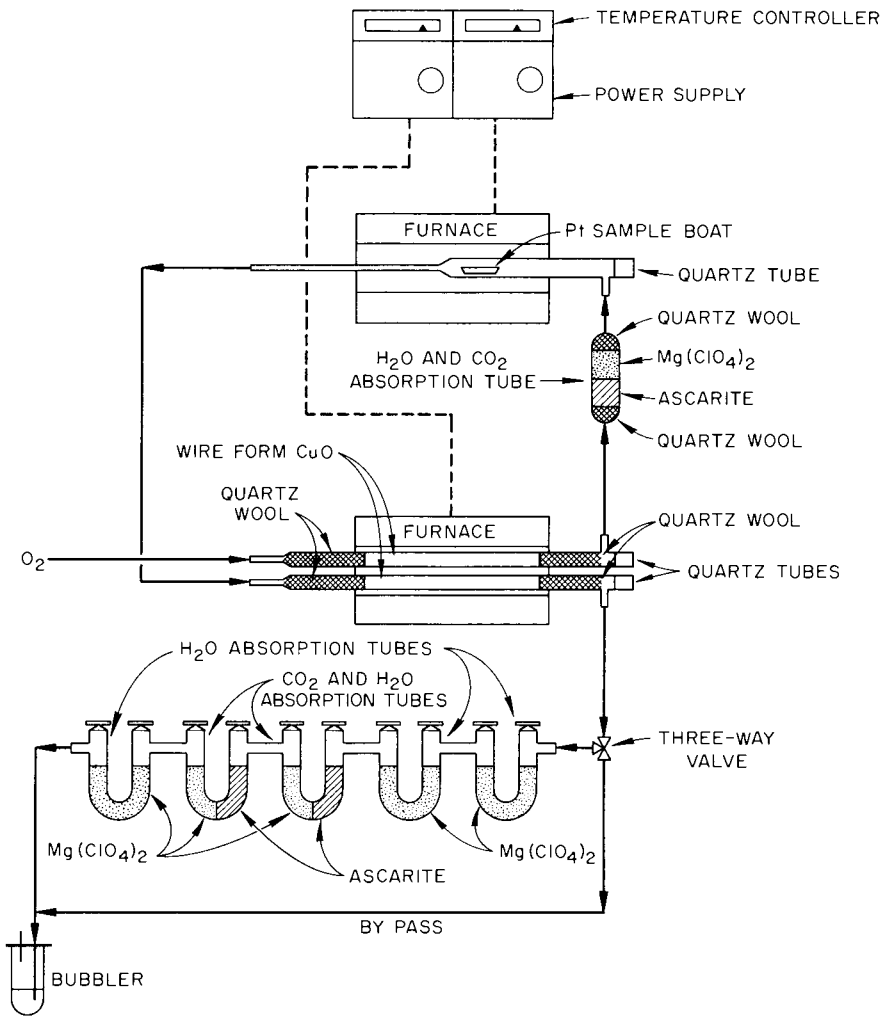


Fig. 3.15. Apparatus for the Determination of Uranium and Carbon.

Table 3.8. Determination of Carbon Embedded in $U_3O_8$

| Weight of $U_3O_8$, g | | Weight of Graphite, g | |
|---|---|---|---|
| Taken[a] | Found | Taken | Found |
| 0.1878<br>0.2141 | 0.4017 | 0.0536 | 0.05376 |
| 0.0831<br>0.2702 | 0.3530 | 0.0400 | 0.04023 |

[a]Some $U_3O_8$ was weighed into the boat, the graphite was then placed on top of it, and finally the graphite was covered with additional $U_3O_8$.

[redacted]

listed in Table 3.9 and compared with literature data[54–56] in Fig. 3.16. From Fig. 3.16 it is clear that agreement with Anselin is quite good; in most instances it appears that earlier workers are in disagreement over a portion of the system. An interesting calculation that can be made from data in Table 3.9 is the comparison of the total numbers of gram-atoms of carbon plus nitrogen with that of uranium. We show this calculation in Table 3.10. The values are remarkably constant, and, with few exceptions, the U(C,N) samples are slightly substoichiometric with respect to carbon and nitrogen. However, if all analyses by the authors are considered, the average value of the combined carbon plus nitrogen almost exactly equals the average value of the uranium. When we compare the same quantities based on Analytical Chemistry results, the average of total carbon plus nitrogen is clearly less than the uranium. If two high results are omitted from the average in the first part of Table 3.10 and if 0.0033 mole of oxygen (average from Analytical Chemistry results) is also subtracted, one obtains 0.393 for the total carbon plus nitrogen, which is nearly the same average obtained in the lower part of Table 3.10. We conclude that U(C,N) is slightly substoichiometric.

The observation that the carbonitrides contain approximately the same number of gram-atoms of nitrogen plus bound carbon as of uranium offers an important guide to establishing whether or not our analysis for free carbon is satisfactory. In Table 3.11 we show the results of equilibrating U(C,N) with graphite. The bound carbon is obtained by subtracting free carbon from total carbon. We determine free carbon by dissolving about 0.5 g of the carbonitride in 8 M $HNO_3$, filtering hot through a quartz frit, washing with hot nitric acid, and igniting in

---

[54] F. Anselin, Préparation et Étude des Nitrures et Carbonitrures d'Uranium et de Plutonium, CEA-R-2988 (June 1966).

[55] A. E. Austin and A. F. Gerds, The Uranium-Nitrogen-Carbon System, BMI-1272 (1958).

[56] J. William and R.A.J. Sambell, "The Uranium Monocarbide-Uranium Mononitride System," J. Less-Common Metals 1, 217 (1959).

[redacted]



Table 3.9. Analysis of U-C-N Samples with no Free Carbon

| Sample | Content,[a] wt % | | | | Lattice Parameter (A) |
|---|---|---|---|---|---|
| | Uranium | Carbon | Nitrogen | Oxygen | |
| 365A | 94.78[b] | 1.85[b] | 3.37[c] | | 4.91054 ± 8 |
| 365B | 94.78[b] | 2.17 | 3.05[c] | | 4.92642 ± 17 |
| 366 | | [2.33] | [2.85] | [0.05] | 4.93459 ± 16 |
| 367 | 94.74[b]<br>[94.8] | 2.18[b]<br>[2.10] | 3.08[c]<br>[3.00] | <br>[0.06] | 4.92968 ± 21 |
| 368 | 94.795[b]<br>[94.6] | 1.985[b]<br>[1.98] | 3.22[c]<br>[3.30] | <br>[0.06] | 4.92682 ± 18 |
| 369 | 94.815[b]<br>[94.9] | 2.160[b]<br>[2.13] | 3.025[c]<br>[2.97] | <br>[0.08] | 4.92727 ± 10 |
| 370 | 94.81[b]<br>[94.4] | 2.06[b]<br>[2.39] | 3.13[c]<br>[3.10] | <br>[0.06] | 4.92595 ± 11 |
| 372 | 94.82[b]<br>[94.9] | 2.12[b]<br>[2.10] | 3.06[c]<br>[3.04] | <br>[0.03] | 4.92704 ± 16 |
| 373 | 94.75[d]<br>[94.6] | 2.14[d]<br>[2.14] | 3.11[c]<br>[2.94] | <br>[0.03] | 4.92699 ± 12 |
| 374 | | | | | 4.95147 ± 14 |
| 376 | 94.85[d] | 3.19[b] | 1.96[c] | | 4.94037 ± 14 |
| 377 | 94.93[b] | 3.08[b] | 1.99[c] | | 4.94237 ± 26 |
| 378 | 94.85[b] | 3.15[b] | 2.00[c] | | 4.94102 ± 14 |
| 379 | 94.90[b] | 3.07[b] | 2.03[c] | | 4.94110 ± 20 |
| 380 | | | | | 4.94198 ± 14 |
| 382 | 94.62[b] | 1.02[b] | 4.36[c] | | 4.90699 ± 12 |
| 383 | 94.65[b] | 0.97[b] | 4.38[c] | | 4.90640 ± 12 |

[a]Results in brackets were obtained from Analytical Chemistry; other results were determined by the authors.

[b]Average of two results.

[c]Obtained by difference: 100% − wt % U − wt % C.

[d]Average of three results.

[redacted]

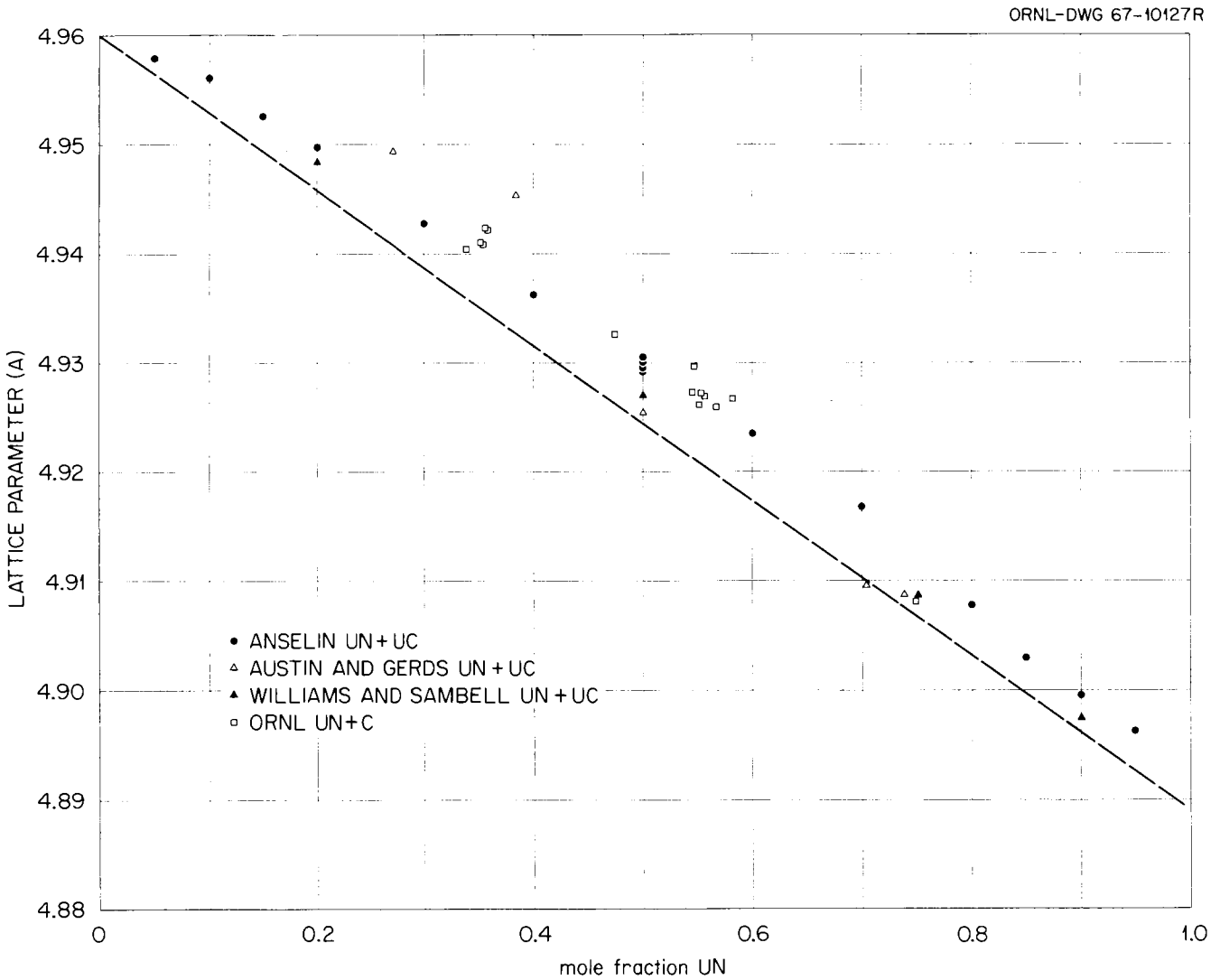


Fig. 3.16. Variation of Lattice Parameter with Composition for UC-UN System.

[redacted]



Table 3.10. Comparison of Total Metalloid Content with Metal Content in Uranium Carbonitride Samples

| Sample[a] | Content, gram-atoms per 100 g | | | |
|---|---|---|---|---|
| | Carbon | Nitrogen | Carbon plus Nitrogen | Uranium |
| | Based on Analysis by the Authors | | | |
| 365A | 0.1540 | 0.2406 | 0.3946 | 0.3981 |
| 365B | 0.1807 | 0.2177 | 0.3984 | 0.3981 |
| 367 | 0.1815 | 0.2199 | 0.4014 | 0.3979 |
| 368 | 0.1653 | 0.2299 | 0.3952 | 0.3981 |
| 369 | 0.1798 | 0.2160 | 0.3958 | 0.3982 |
| 370 | 0.1715 | 0.2235 | 0.3950 | 0.3982 |
| 372 | 0.1765 | 0.2185 | 0.3950 | 0.3982 |
| 376 | 0.2656 | 0.1399 | 0.4055 | 0.3984 |
| 377 | 0.2564 | 0.1421 | 0.3985 | 0.3987 |
| 378 | 0.2622 | 0.1428 | 0.4050 | 0.3984 |
| 379 | 0.2556 | 0.1449 | 0.4005 | 0.3986 |
| 382 | 0.0849 | 0.3113 | 0.3962 | 0.3974 |
| 383 | 0.0808 | 0.3127 | 0.3935 | 0.3975 |
| Average | | | 0.3980 | 0.3982 |
| | Based on Analysis by Analytical Chemistry[b] | | | |
| 367 | 0.1748 | 0.2142 | 0.3890 | 0.3982 |
| 368 | 0.1648 | 0.2356 | 0.4004 | 0.3973 |
| 369 | 0.1773 | 0.2120 | 0.3893 | 0.3986 |
| 370[c] | 0.1990 | 0.2213 | 0.4203 | 0.3965 |
| 372 | 0.1748 | 0.2170 | 0.3918 | 0.3986 |
| 373 | 0.1782 | 0.2099 | 0.3881 | 0.3973 |
| Average | | | 0.3917 | 0.3980 |

[a]Identified in Table 3.9.

[b]Average number of moles of oxygen: 0.0033.

[c]Sample 370 is clearly in error and was not included in average.

the apparatus shown in Fig. 3.15. However, some of the values in Table 3.11 are based on free carbon results reported by Analytical Chemistry and performed before we developed our own procedure.

The results shown in Table 3.11 do not appear to be greatly in error, but the precision is clearly not as good as that in Table 3.9. Some difficulty has been experienced with the carbon apparatus in recent weeks; the Ascarite is a finer grade than available previously and the

[redacted]

[redacted]



Table 3.11. Analysis of U(C,N) Samples with Excess Carbon

| Sample | Carbon Content, wt % | | Content, moles/100 g | |
|---|---|---|---|---|
| | Total | Bound | Uranium | Carbon plus Nitrogen |
| | | From UN + C | | |
| 34 | 4.05 | 1.09 | 0.3847 | 0.3491 |
| 36 | 7.48 | 1.11 | 0.3738 | 0.3537 |
| 38 | 7.42 | 1.12 | 0.3742 | 0.3559 |
| 40 | 4.05 | 1.79 | 0.3894 | 0.3703 |
| 44 | 5.80 | 1.84 | 0.3819 | 0.3809 |
| 46 | 3.93 | 1.97 | 0.3902 | 0.3717 |
| 48 | 5.60 | 2.13 | 0.3841 | 0.3836 |
| 50 | 4.82 | 2.03 | 0.3867 | 0.3817 |
| 52 | 2.97 | 0.27 | 0.3866 | 0.3766 |
| 54 | 4.54 | 0.41 | 0.3802 | 0.3753 |
| 56 | 4.98 | 1.11 | 0.3819 | 0.3808 |
| | | From UC + $N_2$ | | |
| 58 | 4.55 | 0.39 | 0.3801 | 0.3711 |
| 62 | 9.50 | 0.42 | 0.3611 | 0.3490 |
| 64 | 9.56 | 0.964 | 0.3623 | 0.3773 |

U-tube sections tend to plug up. This problem appears to have been overcome by designing a special diffusing device for our U-tubes. Nevertheless, it appears that we can successfully analyze for free carbon in U(C,N) samples.

The remaining question to be answered concerning the UC-UN solid solution is: does the solid solution in equilibrium with carbon follow the same lattice constant—composition relationship followed by the solid solution in equilibrium with uranium. A start has been made on this problem but the answers are not yet clear.

[redacted]

[redacted]



# 4. NONDESTRUCTIVE TEST DEVELOPMENT

R. W. McClung

This program is intended to develop new and improved methods of nondestructively examining reactor materials and components. To achieve this we are studying various physical phenomena, developing instrumentation and other equipment, devising application techniques, and designing and fabricating reference standards. Among the methods being actively pursued are electromagnetics (with major emphasis on eddy currents), ultrasonics, and penetrating radiation. These and other methods are being evaluated for both normal and remote inspection.

## Electromagnetic Test Methods

C. V. Dodd

### Analytical Studies

We continued[1] research and development on both analytical and empirical bases and wrote a report[2] describing the calculation of various eddy-current phenomena using the newly derived equations for a closed form solution. The abstract is presented below.

> Solutions have been obtained for axially symmetric eddy-current problems in two configurations of wide applicability. In both cases the eddy currents are assumed to be produced by a circular coil of rectangular cross section, driven by a constant amplitude alternating current. One solution is for a coil above a semi-infinite conducting slab with a plane surface, covered with a uniform layer of another conductor. This solution includes the special cases of a coil above a single infinite plane conductor or above a sheet of finite thickness, as well as the case of one metal clad on another. The other solution is for a coil surrounding an infinitely long circular conducting rod with a uniformly thick coating of another conductor. This includes the special cases of a

[1] C. V. Dodd, Fuels and Materials Development Program Quart. Progr. Rept. Sept. 30, 1967, ORNL-TM-2020, pp. 58–59.

[2] C. V. Dodd and W. E. Deeds, Analytical Solutions to Eddy-Current Probe Coil Problems, ORNL-TM-1987 (November 1967).

[redacted]

[redacted]



coil around a conducting tube or rod, as well as one metal clad on a rod of another metal. The solutions are in the form of integrals of first-order Bessel functions giving the vector potential from which the other electromagnetic quantities of interest can be obtained. The coil impedance has been calculated for the case of a coil above a two-conductor plane. The agreement between the calculated and experimental values is excellent.

Figure 4.1 shows the excellent agreement between values of calculated and measured coil impedance. We have written computer programs to calculate:

1. the impedance of a coil above a two-conductor plane,
2. the impedance of a coil encircling a two-conductor rod,

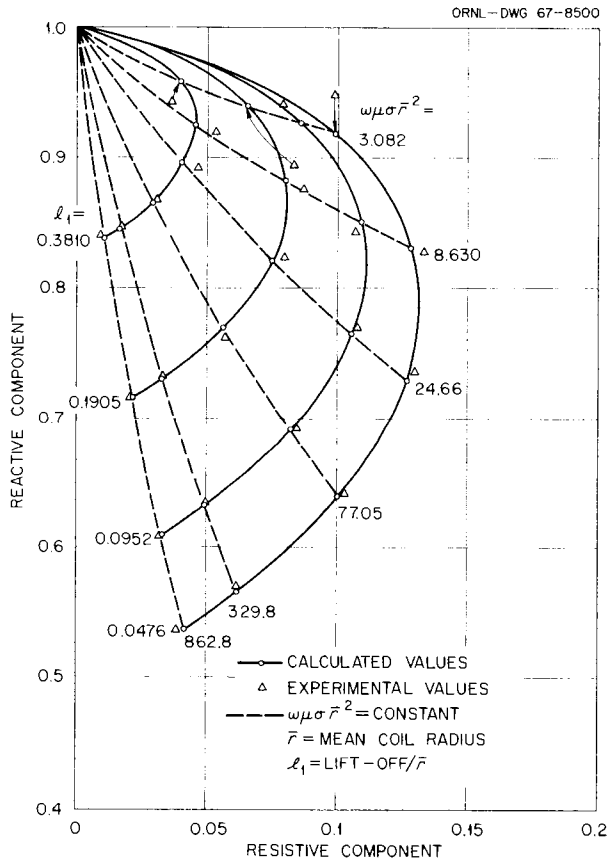


Fig. 4.1. Variation of Experimental and Calculated Values of Normalized Impedance with Frequency and Lift-Off.

[redacted]

3. the phase and amplitude of the voltage induced in a pickup coil by a coaxial transmitter coil on the opposite side of a conducting plane,
4. the phase and amplitude of the voltage of two pickup coils coaxial to the driver coil on the same side of a two-conductor plate.

These programs are being used to aid the design of eddy-current tests for both impedance-bridge and phase-sensitive instruments.

In addition, we have derived the integral equations for a coil between two conducting planes and for a coil inside one conducting cylinder clad on another.

## Phase-Sensitive Eddy-Current Instrument

A paper on the portable phase-sensitive eddy-current instrument was presented at the National Fall Conference of the American Society for Nondestructive Testing in Cleveland and submitted for publication in Materials Evaluation. The abstract is given below.[3]

> A new portable phase-sensitive eddy-current instrument has been developed at the Oak Ridge National Laboratory. The instrument operates on either alternating current or its own rechargeable batteries. Its frequencies for operation are 50 and 500 kilohertz. The instrument can be used for a wide range of metal or cladding thickness measurements and also for sorting and identifying metals according to their conductivity. It is insensitive to lift-off over a wide range of measurements. The instrument features ease of setup and operation along with good stability.

## Temperature-Compensated Probes

We are attempting to reduce the effect of temperature variations on eddy-current coils used with bridge-type instruments. One of the major contributions to thermal drifts (change of response with temperature) of a coil is the change of direct-current resistance with temperature. We are testing over a range of temperatures coils wound from copper wire, manganin wire, and a nickel-base alloy containing

[3] C. V. Dodd, "A Portable Phase-Sensitive Eddy-Current Instrument," to be published in Materials Evaluation.

20% Cr, 3% Al, and smaller amounts of copper or iron. Copper has a resistivity of 1.73 microhm-cm with a temperature coefficient of about 0.39%/°C, manganin has a resistivity of 48 microhm-cm with a coefficient of ±0.001%/°C from 20 to 35°C, and the nickel-base alloy has a resistivity of 133 microhm-cm with a coefficient of ±0.002%/°C from −55 to 100°C. While the overall test sensitivity is reduced by using the higher resistivity wire, there is a net gain in temperature stability. The manganin wire has the smallest temperature coefficient, but the nickel-base alloy has the greatest range.

## Ultrasonic Test Methods

K. V. Cook

### Fabrication of Reference Notches

We are continuing to work on the problems encountered in inspecting tubing by ultrasonic methods. A major problem is the establishment of realistic ultrasonic notch standards for calibration. Since electrical discharge machining (EDM) appears to be a reliable method for making both inner- and outer-surface notches, we are continuing our notch fabrication studies.

We have developed techniques and procedures that allow us to machine longitudinal and transverse notches reproducibly in tubing with bores as small as 0.050 and 0.180 in., respectively. However, we are experiencing some difficulty in machining good notches in tungsten- and molybdenum-base alloys. The machining operation in these two materials apparently introduces microcracking in the bottom of the reference notches. If the cracking becomes excessive the true notch depth cannot be determined and, thus, the EDM notch is not a reproducible, accurate reference. This condition was noted particularly in unalloyed tungsten, in which cracks propagated from the machined notch in all directions. We are not sure if the problem is related to the specific metallurgical condition or if this can be expected in all

conditions of unalloyed tungsten. Further studies will be made (depending on material availability) to determine the severity of the problem.

We are continuing to produce reference curves for both longitudinal and transverse notches as materials are available. It appears that the calibration curves for short transverse notches (1/32 and 1/16 in. long) are almost identical to those for longitudinal notches. This observation is based on data for stainless steel, Hastelloy C, Zircaloy, and W–26% Re and may or may not be true for other materials.

We also demonstrated the making of silicone rubber replicas of the complete inner surface of tube standards by spinning the tube in a small jeweler's lathe while the rubber hardens. The amount of rubber is limited to avoid formation of a solid plug, which is very difficult to remove from the tube and usually necessitates destroying the replicas for removal. A vacuum applied to a hollow replica causes collapse and ready retrieval from the tube inner surface. This method of replicating is necessary for rapid accurate measurement of transverse notch standards. A side benefit is the ability to examine the entire inner surface of the tube. This work has been partially funded by the High-Temperature Materials Program.

## Ultrasonic Frequency Analysis

With our recently developed frequency analysis system,[4] we further confirmed that commercial transducers are relatively broad banded in frequency response and do not always give the maximum response at the nominal frequency. The spectral responses from a number of commercial transducers have been observed (and duplicated at later dates), indicating that a frequency analysis system might be used to advantage as part of a specification for the purchase of high-performance transducers.

There are frequently anomalies in response characteristics of apparently identical testing systems. As we have indicated, the transducer is one possible source of these anomalies, since a labeled

[4]K. V. Cook, Fuels and Materials Development Program Quart. Progr. Rept. Sept. 30, 1967, ORNL-TM-2020, pp. 60–62.

frequency response on a transducer can differ considerably from the actual output. However, since the instrument is also a variable, a method is needed for checking the integrated transducer and instrument response from one system to another. Our recent studies indicate that the frequency analysis system might accomplish much along these lines. For instance, we have monitored the combined transducer and pulser output spectra generated by five of our basic ultrasonic test instruments. All were commercial instruments and included three Immerscopes,[5] one Attenuation Comparator,[6] and one Reflectoscope.[6]

The Immerscope delivers an untuned fast-rise voltage shock to excite the transducer, which in turn produces a relatively wide-band frequency response. We noted that the transducer response spectra did not depend upon the particular Immerscope being used but was essentially constant for a common transducer. However, an instrument with improper pulser excitation could change the transducer response.

Both the Reflectoscope and Attenuation Comparator excite the transducer with a pulse that can be tuned over a range of frequencies. We noted that these instruments essentially tune the transducer output response. Thus, varying the pulser frequency varies the output frequency and amplitude. This amplitude variation depends on the particular frequency and on the transducer sensitivity at that frequency. We plan to continue these studies, as well as other promising uses, for the frequency analysis system.

Optical Visualization of Ultrasound (H. L. Whaley, K. V. Cook)

Several 3- × 4- × 2-in. blocks of optical glass, Plexiglas, and polystyrene have been received for our visual study of ultrasound inside transparent solids. We were able to introduce and observe pulses of 2.25 MHz ultrasound in both the Plexiglas and polystyrene. However, local imperfections in the polystyrene reduced the visibility for the pulse, and another piece of better quality has been ordered. We have not yet been able to get positive results with the glass because of

[5]Budd Company, Phoenixville, Pa.

[6]Automation Industries, Inc., Sperry Division, Danbury, Conn.

its high acoustical impedance at the surface. Results with the glass will be quite beneficial, however, because of its low attenuation and acoustical similarity to steel.

## Penetrating Radiation Methods

B. E. Foster S. D. Snyder

### Holography

We are studying the technique of making high-quality reflection holograms using a 2-mw helium-neon gas laser. The purpose is to enable us to become familiar with the associated problems in holography as well as the appropriate technical requirements for good holograms. Upon completion of these studies, we plan to develop techniques that will allow holography to be used as a powerful tool for nondestructive testing for surface as well as subsurface discontinuities in metals and ceramics. These techniques will not necessarily involve the use of laser light.

### Fuel Homogeneity

For several years we have successfully used an x-ray attenuation technique for measuring the inhomogeneity of fuel and total fuel content in reactor fuel plates. The method consisted of passing an x-ray beam through the fuel plate, monitoring the attenuated transmitted radiation beam with a sodium-iodide (thallium-activated) crystal with associated electronics and displaying the resultant signal on a strip-chart recorder.

The fuel content determination involves the averaging of each 20-in.-long scan (approx 45 scans per plate) and relating this strip-chart average to mass of uranium with a previously determined calibration curve. The present chart averaging technique is quite laborious and time consuming. Circuitry has been developed and installed to obtain this chart average electronically and give a digital print-out at the conclusion of this scan. Initial but incomplete checkout of the system is quite promising.

[redacted]



## 5. SINTERED ALUMINUM PRODUCTS DEVELOPMENT

W. R. Martin

Sintered aluminum products are powder-metallurgy-produced alloys that consist of aluminum oxide dispersed within an aluminum matrix. These alloys have a high strength-to-weight ratio, and this beneficial effect is stable up to temperatures approaching the melting point of aluminum.

Although this alloy is attractive for applications in several reactor systems, commercial SAP products lack the reproducibility of properties needed for many nuclear components. Our program was initiated to investigate the problems and parameters related to primary billet fabrication of SAP for HWOCR fuel rods and pressure tubes. General process steps involve feed-powder characterization, dispersion preparation, and consolidation.

### Dispersion Preparation

G. L. Copeland

A topical report summarizing the investigation is in preparation.

### Powder Consolidation

G. L. Copeland M. M. Martin

Our concluding series of experiments involves:

1. the maximum permissible levels of impurities Fe, C, and H,
2. the duration of time required during vacuum hot pressing and vacuum annealing of the billet to stabilize the material,
3. comparison of two consolidation processes on material produced by these processes in larger billet sizes,
4. establishing the reproducibility of mechanical properties of material consolidated by process B procedures.

[redacted]

In the two processes under consideration, the powder is consolidated by hot pressing at 600°C and less than $10^{-2}$ torr. In process B the pressed billet is vacuum annealed at 600°C; in process D the powder is vacuum annealed at 600°C before pressing and the pressed billet is not vacuum annealed. Our conclusions from these experiments will be based on the tensile properties at 450°C and 0.002 $min^{-1}$ strain rate and the chemical composition of the extruded products. The work on permissible hydrogen impurity level, duration of vacuum treatments for the billet, and comparison of processes B and D is complete. Our remaining tasks lack only a few mechanical property tests and interpretation of data.

Since the last reporting period, we have extended our previous relationship[1] between ultimate tensile strength and initial billet density to include 70%-dense process B billets. As reported previously,[2] we prepared billets of various initial densities by both process B and D techniques for testing of mechanical properties. The results are presented in Table 5.1. The data for SAP 239 and 240 are in agreement with our previous conclusion that the strength of extruded SAP is essentially independent of initial billet density. Please note in Table 5.1 that the extrusions from the 70%-dense billets contain approximately 20% more oxide than the billets of higher density. This additional oxide is undoubtedly formed from the water of hydration during thermal treatments to stabilize the materials. We believe that this oxide only increases the thickness of the oxide layer around the aluminum flake and does not significantly change the strength level of the material, since the interparticle oxide spacing is virtually unaffected.

The billet is vacuum annealed to convert the hydrated oxide formed at low temperature to a form stable at high temperature and to remove the released hydrogen and water along with any organic materials still in the billet. We processed three 4-in.-diam billets by heating the powder to 600°C in vacuum and immediately applying pressure until the

---

[1]G. L. Copeland and M. M. Martin, Fuels and Materials Development Program Quart. Progr. Rept. June 30, 1967, ORNL-TM-1941, pp. 44–49; note especially Fig. 4.7, p. 48.

[2]M. M. Martin and D. H. Turner, Fuels and Materials Development Program Quart. Progr. Rept. Mar. 31, 1967, ORNL-TM-1825, pp. 26–33.

Table 5.1. Strength of SAP Rods Extruded from 2- and 4-in.-diam Billets of Various Densities

| Identification (SAP Rod) | Consolidation Process (in.) | Billet Diameter (in.) | Oxide Content[a] (wt %) | Ultimate Tensile Strength,[b] psi | | | |
|---|---|---|---|---|---|---|---|
| | | | | Number of Determinations | Average Value | Expected Statistical Deviation[c] | Billet Density (% of theoretical) |
| 230 | D | 2 | 5.9 | 6 | 11,840 | ±1420 | 95.5 |
| 231 | D | 2 | 5.9 | 6 | 12,760 | ±1420 | 95.7 |
| 232 | D | 2 | 6.0 | 6 | 11,930 | ±1420 | 89.5 |
| 233 | D | 2 | 6.1 | 6 | 13,080 | ±1420 | 88.3 |
| 234 | D | 2 | 6.2 | 6 | 12,700 | ±1420 | 79.8 |
| 235 | D | 2 | 6.8 | 6 | 13,380 | ±1420 | 80.7 |
| 239 | B | 4 | 8.0 | 18 | 11,010 | ±370 | 71.5 |
| 240 | B | 4 | 8.2 | 18 | 10,860 | ±370 | 70.6 |
| 241 | B | 4 | 6.5 | 18 | 10,490 | ±570 | 80.6 |
| 242 | B | 4 | 6.7 | 18 | 10,650 | ±570 | 80.4 |
| 243 | B | 4 | 6.5 | 18 | 10,450 | ±780 | 86.7 |
| 244 | B | 4 | 6.5 | 18 | 10,520 | ±780 | 86.8 |
| 245 | D | 4 | 5.4 | 18 | 10,320 | ±850 | 79.8 |
| 246 | D | 4 | 5.4 | 18 | 10,140 | ±340 | 81.6 |
| 247 | D | 4 | 5.3 | 18 | 10,250 | ±625 | 91.8 |
| 248 | D | 4 | 5.3 | 16 | 9,950 | ±625 | 92.8 |
| 249 | D | 4 | 5.9 | 12 | 10,160 | ±620 | 98.2 |
| 250 | D | 4 | 5.4 | 18 | 9,760 | ±620 | 97.3 |

[a]After primary extrusions.

[b]Test conditions: 450°C and a strain rate of 0.002 $min^{-1}$.

[c]Tolerance limits calculated at the 95% confidence level to include 99% of a normal distribution.

density reached 80% of theoretical. The previous process B billets had been held for 2.5 hr under vacuum at 600°C during compaction. The billets were then stored in sealed plastic bags until they could be (1) annealed in vacuum for 10, 17.5, or 25 hr at 600°C and (2) immediately placed in the 600°C holding furnace for primary extrusion without an intermediate cooling. The total reduction ratio during primary and secondary extrusion was 156.

The completeness of conversion to a stable form was determined by annealing part of the samples for 40 hr at 600°C in an atmosphere of less than $10^{-3}$ torr of air and then comparing the tensile strengths before and after annealing. As shown in Table 5.2, the changes observed were small and are not significant for normal process variations. The effect of eliminating the 2.5-hr holding time is also seen to be small by comparing these results with a previous process B extrusion (SAP 257-4). We conclude that a 10-hr anneal is sufficient and shorter annealing times should be investigated for process optimization.

Table 5.2. Effect of Billet Vacuum Anneal Duration on Thermal Stability of Process B Extrusions

| Identification (SAP Rod) | Rod Characterization | | Vacuum Anneal Duration,[a] hr | | Ultimate Tensile Strength[b] (psi) | |
|---|---|---|---|---|---|---|
| | Oxide Content (wt %) | Hydrogen Content (ppm) | Hot Pressing of Powder | Consolidated Billet | As Extruded | Change upon Stability Test |
| 260-2 | 7.5 | 4.4 | 0.2 | 10.0 | 11,220 | −320 |
| 261-2 | 7.5 | 3.4 | 0.2 | 17.5 | 10,640 | −130 |
| 257-4 | 12.5 | 2.2 | 2.5 | 17.5 | 15,100 | +120 |
| 262-2 | 7.5 | 3.0 | 0.2 | 25.0 | 10,760 | −240 |

[a]Billets heated at 600°C for the indicated time in an atmosphere of less than $10^{-3}$ torr of air.

[b]Test conditions: 450°C and a strain rate of 0.002 $min^{-1}$; values represent the average of 5 or 6 determinations.

The presence of hydrogen at high concentrations in SAP has been shown to cause structural instability at high temperature.[3,4] Hydrogen contents of approximately 20 ppm and higher generated fissures, voids, and external evidence of blistering when the materials were exposed to temperatures of 600°C and above for several hours. To examine the effect of hydrogen at lower concentrations, we compared the strengths of extruded rods to those of rods annealed for 40 hr at 600°C in vacuum and in air. Table 5.3 shows the results.

In general, as shown in Table 5.3, the secondary extrusion step appears to lower the hydrogen content of primary rods that contain more than 4 ppm H. The vacuum annealing treatment performed on the extruded rods tends to lower the ultimate tensile strength and, in all cases, reduces the hydrogen content to less than 3 ppm without evidence of blistering. However, the air annealing treatment increases the hydrogen content. We observed blistering and also a significant decrease in strength for SAP 258-4 rod that contained 5.3 ppm H before the high-temperature exposure in air. Although vacuum annealing SAP 233 rod reduced the hydrogen content from 25 to 2.5 ppm, the strength level was also lowered markedly. We note that the annealed strength corresponds to that of material of similar oxide content but with initial lower concentrations of hydrogen. Thus, in vacuum-annealed SAP products with less than 20 ppm H, the extruded strength value is decreased and appears to approach that value for materials of less than 5 ppm H.

On the basis of the testing of 2-in.-diam extrusions, process D, in which the powder is given a stabilizing vacuum anneal, was selected as our reference process for scale-up to larger billets.[5] Process B,

---

[3]G. L. Copeland, Fuels and Materials Development Program Quart. Progr. Rept. Dec. 31, 1966, ORNL-TM-1720, pp. 39–41.

[4]N. Hansen and E. Adolph, The Effect of Heat Treatment on the Structural Stability of Sintered Aluminum Products, Risö-25 (May 1961).

[5]M. M. Martin and D. H. Turner, Fuels and Materials Development Program Quart. Progr. Rept. Dec. 31, 1966, ORNL-TM-1720, pp. 34–39.

Table 5.3. Effect of Hydrogen on the Thermal Stability of Extruded SAP Materials

| Identification (SAP Rod) | Oxide Content (wt %) | Hydrogen Content, ppm | | | Heat Treatment Atmosphere | Average Ultimate Tensile Strength,[c] psi | | Consolidation Process | Billet Diameter (in.) |
|---|---|---|---|---|---|---|---|---|---|
| | | After Extrusion | | After Annealing[a,b] | | As Secondary Extrusion | Change upon Annealing[b] | | |
| | | Primary | Secondary | | | | | | |
| 241-1 | 6.5 | 2 | 3.6 | 1.8 | Vacuum | 10,440 | −40 | B | 4 |
| 255 | 11.4 | 3 | 3.6 | 1.5 | Vacuum | 12,870 | −70 | Commercial | SAP 895 |
| 262-2 | 7.0 | 3 | 3.0 | 1.6 | Vacuum | 10,760 | −240 | B | 4 |
| 260-2 | 7.1 | 4 | 4.4 | 1.3 | Vacuum | 11,220 | −320 | B | 4 |
| 261-2 | 8.1 | 5 | 3.4 | 2.0 | Vacuum | 10,640 | −130 | B | 4 |
| 247-3 | 5.3 | 5 | 3.2 | 1.1 | Vacuum | 10,330 | −610 | D | 4 |
| 257-2 | 12.6 | 6 | 1.8 | 5.0 | Air | 15,180 | −370 | B | 4 |
| 257-4 | 12.5 | 6 | 2.1 | 1.5 | Vacuum | 15,100 | +120 | B | 4 |
| 245-3 | 5.4 | 10 | 3.8 | 2.9 | Vacuum | 10,540 | −760 | D | 4 |
| 258-3 | 11.8 | 20 | 5.5 | 3.0 | Vacuum | 13,880 | −110 | D | 4 |
| 258-4 | 12.0 | 20 | 5.3 | 7.7 | Air | 14,770 | −1330 | D | 4 |
| 233 | 6.1 | 25 | 25.0 | 2.5 | Vacuum | 13,080 | −1990 | D | 2 |

[a]Content is average of 2 to 3 determinations from actual tensile specimens.

[b]Rods annealed at 600°C for 40 hr in an atmosphere of less than $10^{-3}$ torr of air or 1 atm of air.

[c]Test conditions: 450°C and a strain rate of 0.002 $min^{-1}$. Values represent the average of 4, 5, or 6 determinations.

[redacted]



in which the billet is vacuum annealed immediately before extrusion, was considered equivalent to process D except for undesirable variations of mechanical properties along the extrusion. This effect is notably absent in products prepared from 4-in.-diam process B billets that are extruded twice to a total reduction in area of ratio 156.

Since process B is more amenable to production in that a solid billet rather than powder is vacuum annealed, we again compared the two processes using ORNL-milled flake containing 10% oxide. The fabrication parameters and properties of rods made by the two routes and also those for commercial SAP 895 are given in Table 5.4. The oxide content of the rods reflects the differences in primary extrusion conditions between the two processes in that higher temperature and longer holding time before extrusion increased the oxide content. The strengths of the materials produced by processes B and D are equivalent, since the additional oxide formed during consolidation and extrusion contributes little to the strength of the product. However, the hydrogen content, which may affect thermal stability, and the variations in mechanical

Table 5.4. Effect of Consolidation Route on Experimental SAP Rods

| Variables | SAP Rods | | | | |
|---|---|---|---|---|---|
| | 256 | 257 | 258 | 259 | 255 (SAP 895) |
| Consolidation route | B | B | D | D | |
| Primary extrusion condition | | | | | |
| Preheat temperature, °C | 600 | 600 | 500 | 500 | |
| Preheat duration, hr | 2.7 | 2.7 | 2.1 | 2.2 | |
| Oxide content, wt % | 12.1–12.3 | 12.5–12.6 | 11.3–12.0 | 11.3–11.6 | 11.3–11.5 |
| Hydrogen content, ppm | 4–9 | 5–8 | 10–39 | 11–19 | 2–3 |
| Mechanical properties[a] | | | | | |
| Strength, psi | | | | | |
| Ultimate tensile | 14,800 | 15,140 | 14,580 | 15,480 | 12,870 |
| 0.2% yield | 14,210 | 14,650 | 14,080 | 14,920 | 12,450 |
| Elongation, % | | | | | |
| Total | 0.90 | 0.79 | 0.87 | 1.16 | 1.74 |
| Uniform | 0.60 | 0.62 | 0.57 | 0.61 | 0.69 |

[a]Test conditions: 450°C, 0.002 $min^{-1}$ strain rate.

[redacted]

properties are less for process B. For equivalent oxide contents, our material is 20% stronger than commercial SAP 895 and has similar values for uniform elongation. Thus, we conclude that process B is the more desirable technique for consolidating SAP powder for subsequent extrusion.

## Effects of Reduction During Extrusion

T. M. Nilsson

To study the effects of extrusion ratio on the mechanical properties of extruded SAP alloys, a series of experiments was carried out. We used MD 3100 aluminum powder, ball-milled at ORNL. The powder was first compacted according to the procedure that after extrusion gives optimum mechanical properties, as found at ORNL. This procedure involves vacuum hot pressing the powder at 600°C to a density of 80%, followed by vacuum annealing for 17 hr at the same temperature. The billet is then extruded at about 500°C to various diameters through conical dies. Since not enough dies are available to allow a direct extrusion from the initial 4 in. to the desired diameter, it is necessary to perform the extrusions with greater reduction ratios in several steps as shown below. The average analysis of the extruded material is 6.6 wt % $Al_2O_3$, 0.2 wt % Fe, 0.2 wt % C, and 2 ppm H.

| Final Extrusion Ratio | Steps |
|---|---|
| 1 | As compacted |
| 10 | 4 to 1.25 in. |
| 32 | 4 to 1.75 in.; 1.25 to 0.52 in. |
| 130 | 4 to 1.75 in.; 1.25 to 0.25 in. |
| 156 | 4 to 1.75 in. to 0.32 in. |
| 256 | 4 to 1.75 in. to 1.25 to 0.25 in. |

[redacted]



The extruded products were tensile tested at 450°C with a strain rate of 0.002 $min^{-1}$. The results are presented in Figs. 5.1 and 5.2. In Fig. 5.1 only ultimate tensile strength is shown, since the yield stress follows ultimate tensile strength closely, being about 2% lower. Figure 5.1 shows that the high-temperature strength increases with increasing working during extrusion. Also, ductility seems to increase with increasing extrusion ratio, as shown in Fig. 5.2, but the scatter is quite large.

To confirm the beneficial effect of increasing extrusion ratio on 10 wt % oxide material and especially to examine whether the increase continues at very high reductions, SAP 895 extruded at Montecatini to a reduction ratio of 20 and further extruded to a final ratio of 1740 will be tested in the near future.

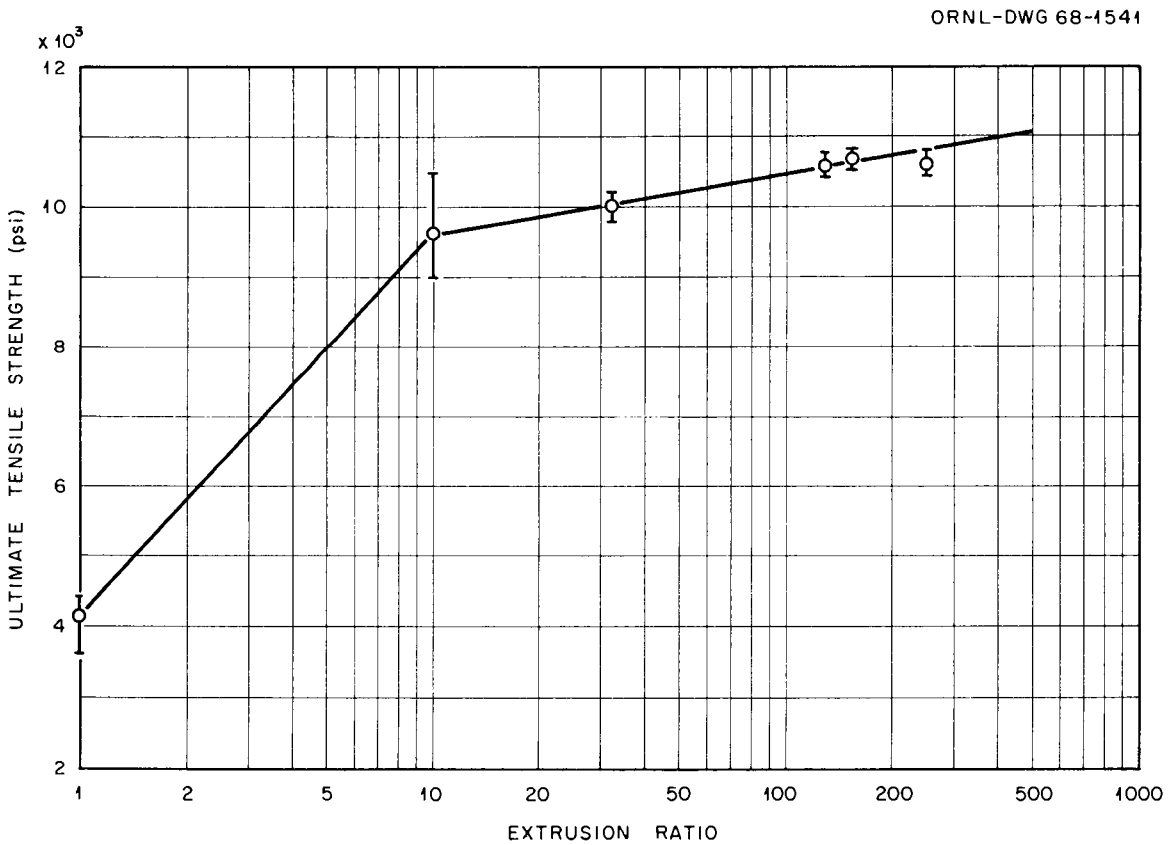


Fig. 5.1. Ultimate Tensile Strength as a Function of Extrusion Ratio Tested at 450°C and a Strain Rate of 0.002 $min^{-1}$.

[redacted]

[redacted]



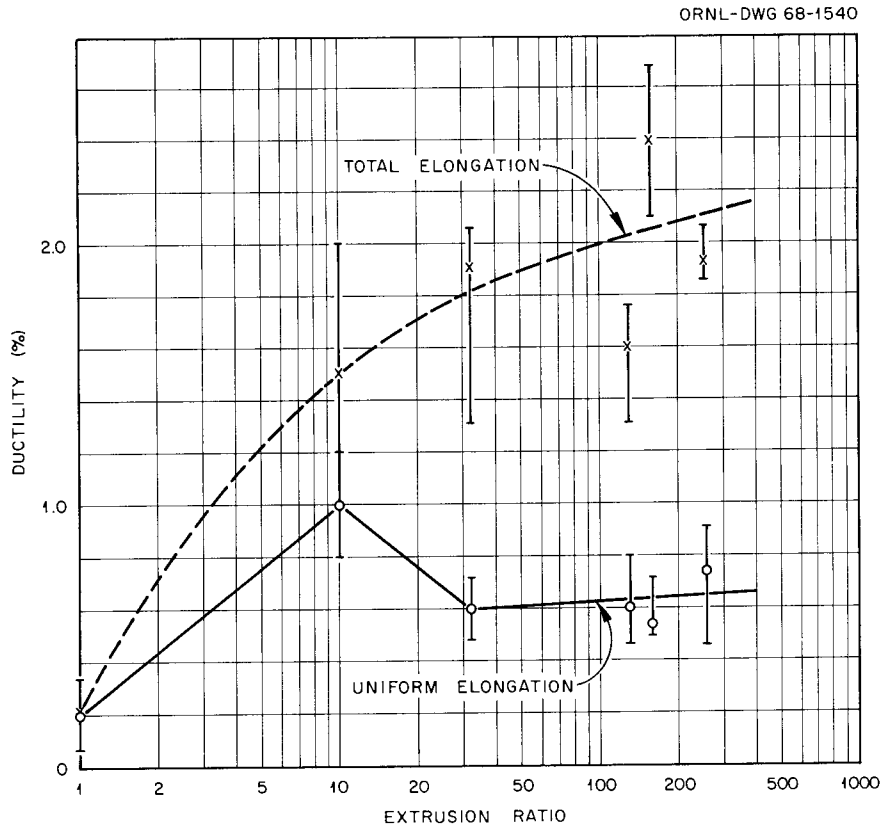


Fig. 5.2. Ductility as a Function of Extrusion Ratio after Tensile Testing at 450°C and a Strain Rate of 0.002 $min^{-1}$. Total elongation is for specimens with gage length ten times diameter.

## Effects of Transverse Extrusion

T. M. Nilsson

The distribution of the oxide phase is very important for the mechanical properties of SAP materials. One way to improve the distribution, and thus the mechanical properties, may be to work the material in a direction different from the extrusion direction, since further working in the extrusion direction seems to have very little effect.[6] Therefore, cylindrical samples were cut out of SAP 895 bar material extruded at Montecatini to a ratio of 20. The samples were further

[6]E. G. Hess, Influence of Various Cold-Working Processes on the Mechanical Properties and Degree of Dispersion of Sintered Aluminum Products, EUR-433d (1963).

[redacted]

extruded in a direction perpendicular to the original extrusion direction; the transverse extrusion ratios ranged between 1.5 and 30. The extrusion temperature was about 500°C, and both shear dies and 45° conical dies were used.

Mechanical properties from tensile testing at 450°C are shown in Table 5.5. Since the properties do not depend on the type of extrusion dies used, only the mean values are plotted in Fig. 5.3. The figure shows that the strength increased rapidly with increasing transverse extrusion ratio and surpassed the initial longitudinal stress (11,000 psi) at a reduction ratio of about 8. The ductility was also about restored at this amount of transverse working after an initial decrease. At further extrusion, both strength and ductility increased. Transverse extrusion seems to be a more effective way of improving properties than further longitudinal extrusion. Harman[7] found very little difference in strength of SAP 895 after increasing the extrusion ratio from 25 to 750. For the same amount of work applied in the transverse direction, strength properties changed 50% and exceeded the original longitudinal strength by about 10%.

This large variation in mechanical properties is understandable when the microstructure is examined. Figure 5.4 shows the microstructure of SAP 895 after transverse extrusion, with transverse reduction of ratio of 4. Considering the anisotropy of extruded SAP alloys, lower mechanical properties must be expected if the structure is altered from the usual extruded structure. That ductility decreases below the original transverse properties is probably due to localized yielding and failure. The transverse properties improve over the original longitudinal properties because a very much improved distribution of oxide occurs during transverse working. Figure 5.5 shows the structure in the longitudinal direction after a transverse extrusion ratio of 15. Not only has the distribution been improved by breaking up of many of the original oxide agglomerates, but it has also been improved by the

---

[7]D. G. Harman and D. H. Turner, Fuels and Materials Development Program Quart. Progr. Rept. Dec. 31, 1966, ORNL-TM-1720, pp. 42–48.

Table 5.5. Mechanical Properties of SAP 895 after Transverse Extrusion at about 500°C[a]

| Reduction Ratio | Die Type | Uniform Elongation (%) | Standard Error (%) | Extension (10d) (%) | Standard Error (%) | Strength, psi | | | |
|---|---|---|---|---|---|---|---|---|---|
| | | | | | | Ultimate Tensile | Standard Error | Yield | Standard Error |
| | | | | | | $\times 10^3$ | $\times 10^3$ | $\times 10^3$ | $\times 10^3$ |
| 1.5 | Conical | 0.30 | ±0.02 | 0.64 | ±0.03 | 8.6 | ±0.05 | 8.5 | ±0.05 |
| 1.5 | Shear | 0.36 | ±0.02 | 0.54 | ±0.03 | 8.5 | ±0.05 | 8.45 | ±0.05 |
| 2 | Conical | 0.34 | ±0.02 | 0.59 | ±0.04 | 9.2 | ±0.1 | 9.05 | ±0.1 |
| 2 | Shear | 0.38 | ±0.01 | 0.64 | ±0.05 | 9.0 | ±0.05 | 8.9 | ±0.05 |
| 4 | Conical | 0.31 | ±0.03 | 0.67 | ±0.05 | 10.15 | ±0.05 | 10.1 | ±0.05 |
| 4 | Shear | 0.38 | ±0.02 | 0.57 | ±0.02 | 9.8 | | 9.7 | ±0.1 |
| 8 | Conical | 0.45 | ±0.05 | 1.0 | ±0.1 | 11.2 | ±0.05 | 11.1 | ±0.05 |
| 8 | Shear | 0.44 | ±0.03 | 1.2 | ±0.1 | 11.2 | ±0.1 | 11.1 | ±0.1 |
| 15 | Conical | 0.50 | ±0.02 | 1.4 | ±0.05 | 11.8 | ±0.05 | 11.7 | ±0.05 |
| 15 | Shear | 0.48 | ±0.05 | 1.6 | ±0.05 | 11.8 | ±0.1 | 11.55 | ±0.05 |
| 30 | Conical | 0.49 | ±0.04 | 1.3 | ±0.1 | 12.2 | ±0.05 | 12.05 | ±0.05 |
| 30 | Shear | 0.52 | ±0.03 | 2.0 | ±0.2 | 12.2 | ±0.05 | 12.0 | ±0.05 |

[a]Tensile tested at 450°C at a strain rate of 0.002 $min^{-1}$. The direction of tension was parallel to the new extrusion direction. The values given are means and standard errors from five or six tests. Note that the type of extrusion die does not seem to affect mechanical properties.

[redacted]



ORNL-DWG 68-1543

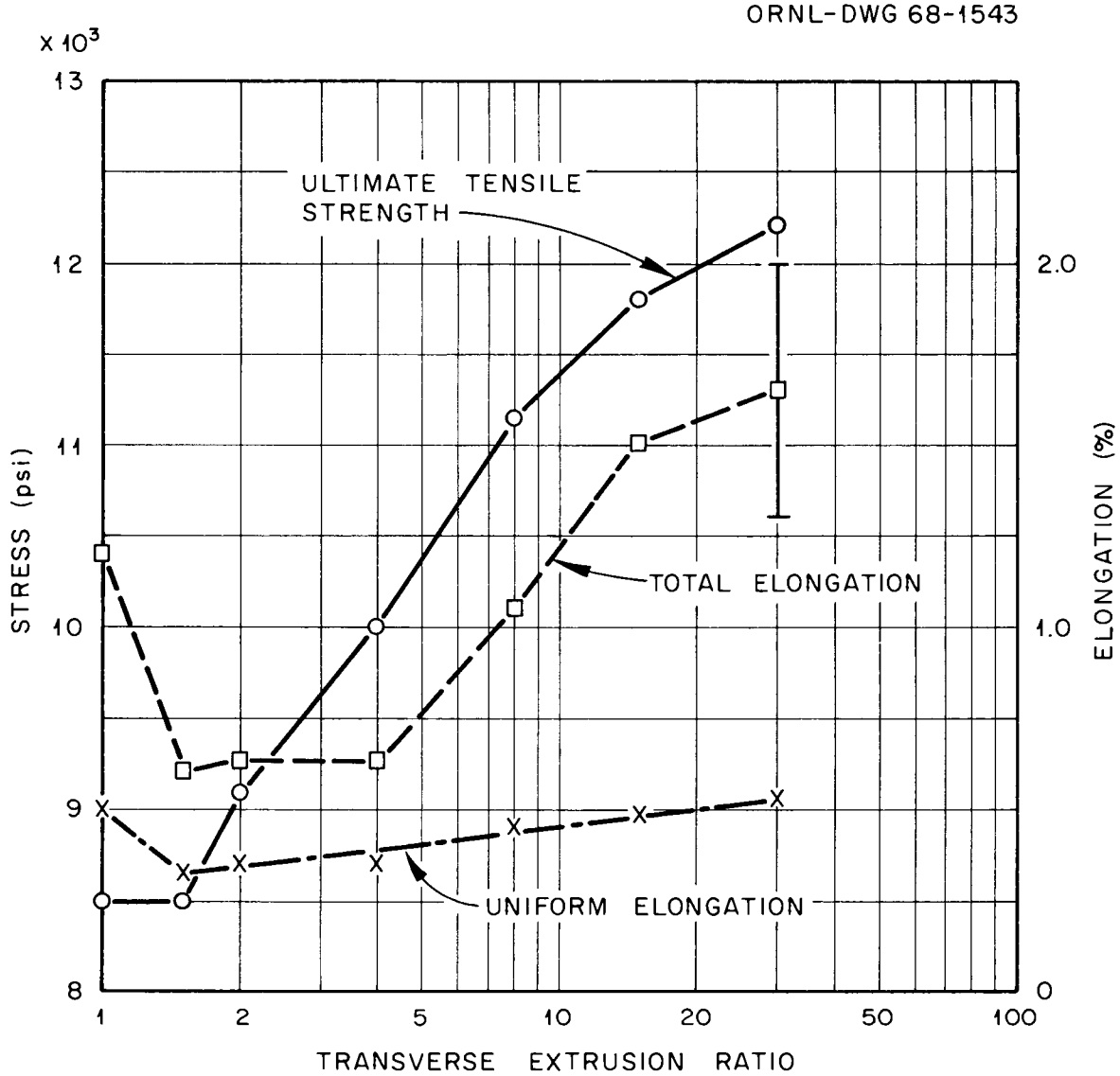


Fig. 5.3. Tensile Properties of SAP 895 After Transverse Extrusion at About 500°C. The longitudinal properties of the initially extruded bar (primary extrusion ratio 20) are ultimate tensile strength: 11,000 psi; total elongation 1.45%; uniform elongation 0.43%; transverse properties of the initial bar are shown as properties corresponding to an extrusion ratio of 1. Total elongation is for specimens with gage length ten times diameter.

breaking of the individual particles, since measurements of oxide particle dimensions give decreased values after transverse extrusion. The oxide-free zones seem to have diminished in number and area by the transverse working.

[redacted]

[redacted]



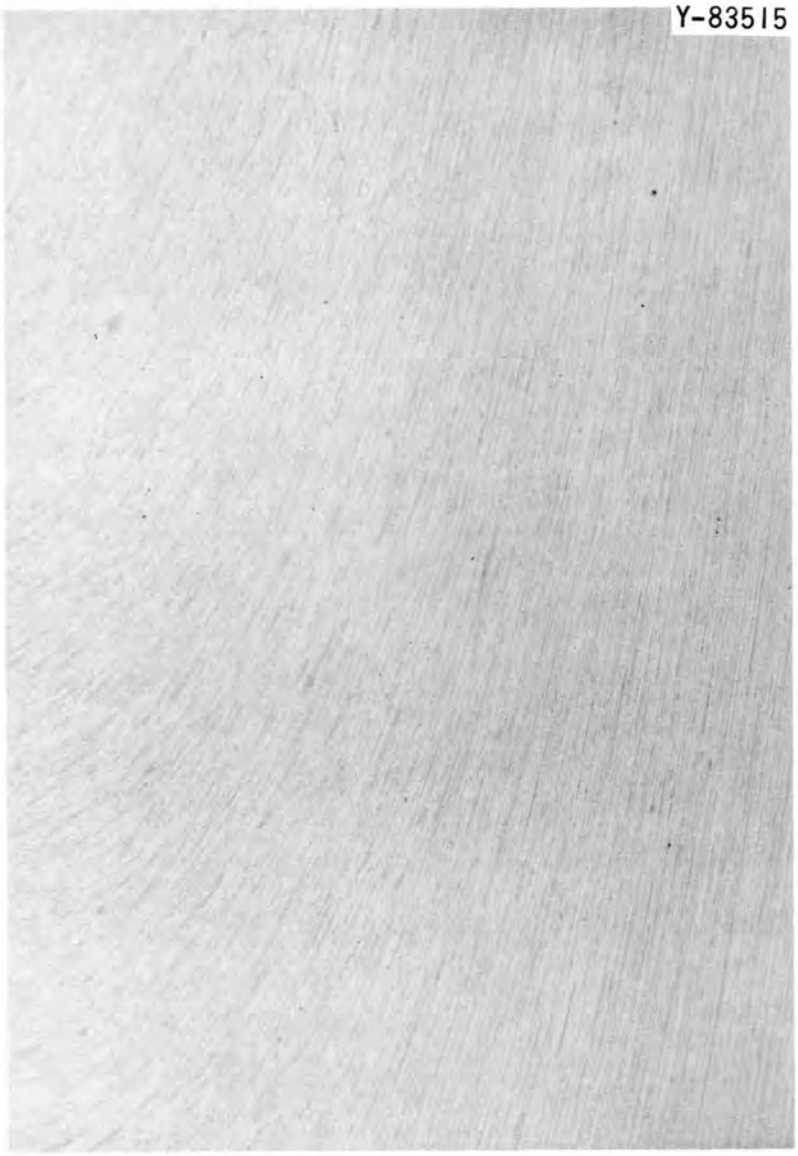


Fig. 5.4. Microstructure of SAP 895 After Transverse Extrusion to a Ratio of 4. The picture shows a section from the center of the bar (left) to the outer edge (right). The structure is seen to realign from the original (horizontal) extrusion direction to the new (vertical downward). 12×.

[redacted]

Fig. 5.5. Microstructure of SAP 895 After Transverse Extrusion to a Ratio of 15. The section is parallel to the new extrusion direction. The distribution of the oxide particles is very much improved compared with that of the same material before transverse extrusion (see later section, "Anisotropy of Extruded SAP 895").

## Thin Foil Preparation of High-Oxide SAP

T. M. Nilsson J. T. Houston

Techniques used at ORNL for preparation of electron-transparent foils of low-oxide SAP are not effective for use on high-oxide material. When large amounts of oxide are present, the material is not adequately polished during the initial jet dimpling, leaving the dimple surface very rough and irregular with black oxide deposits. This surface results in an unacceptable sample after penetration by the second electropolishing. To overcome this, we now use a chemical polish step between the usual dimpling and final electropolishing techniques described elsewhere.[8] The solution, which is maintained at 95 to 100°C during polishing, consists of 70 vol % concd phosphoric acid, 12 vol % concd acetic acid, 3 vol % concd nitric acid, and 15 vol % distilled water and is used at Risö[9] in the preparation of thin foils of SAP. Usually a 2- to 3-min immersion of the dimpled specimen provides for sufficient oxide dissolution and surface smoothening and results in a bright, flat, smooth dimple. After the final electropolishing step, suitable thin foils are obtained.

## Development of Advanced SAP Materials

G. L. Copeland

The objective of this phase of the program is to improve the ductility of SAP products through alloy modifications. Development of the atomizing conditions to provide a satisfactory yield of −100 mesh alloyed aluminum powders is progressing according to schedule at IIT Research Institute. Five small batches of Al–5 wt % Mg and Al–10 wt % Mg have been atomized and are listed in Table 5.6. The first three runs

---

[8]C.K.H. DuBose and J. O. Stiegler, Semiautomatic Preparation of Specimens for Transmission Electron Microscopy, ORNL-4066 (February 1967).

[9]T. M. Nilsson, Investigation of the Ductility of Dispersion-Strengthened Aluminum–$Al_2O_3$ Alloys, Thesis, Danish Technical University, 1965.

Table 5.6. Atomizing Data for 100-gal Chamber[a]

| Run | Alloy | Melt Weight (g) | Tundish Outlet Diameter (in.) | Air Pressure (psi) | Screen Size (mesh) | Powder Yield, wt % | | Remarks |
|---|---|---|---|---|---|---|---|---|
| | | | | | | Based on Melt | Based on Recovered Powder | |
| 1,2[b] | Al–5 wt % Mg | 1380 | 0.1875 | 350 | +100 | 14.8 | 23.0 | Freeze-up in nozzle during second pouring |
| | | | | | –100 +200 | 15.0 | 23.0 | |
| | | | | | –200 | | | |
| 3 | Al–5 wt % Mg | 699 | 0.1875 | 200 | +100 | 51.9 | 58.5 | No freeze-up |
| | | | | | –100 +200 | 18.9 | 21.2 | |
| | | | | | –200 | 18.0 | 20.3 | |
| 4 | Al–5 wt % Mg | 1000 | 0.25 | 350 | +100 | 28.9 | 35.2 | No freeze-up |
| | | | | | –100 +200 | 22.0 | 26.8 | |
| | | | | | –200 | 31.1 | 38.0 | |
| 5 | Al–10 wt % Mg | 1170 | 0.25 | 350 | +100 | 14.1 | 15.9 | No freeze-up |
| | | | | | –100 +200 | 20.4 | 23.6 | |
| | | | | | –200 | 52.5 | 60.5 | |

[a]Runs 1 through 3 made with modified USAF nozzle assembly; runs 4 and 5 made with new ORNL nozzle assembly; all runs were atomized into 60 gal of water (16 in. below nozzle).

[b]Two melts poured before powders were removed.

were made with an existing nozzle, and freeze-up occurred at the higher pressures necessary for increasing the yield of fine powder. A redesigned nozzle constructed for ORNL was used for runs 4 and 5 and allowed the use of higher atomizing pressures without freeze-up. The nozzle is presently being installed on a larger chamber capable of producing 10-lb melts. The 82 and 87% recoveries of runs 4 and 5 are considered good for the small melt sizes. Improved yields should be obtained as the melt and chamber sizes are scaled up.

Oxidation and hydration of very fine powders could be a problem with the air atomization into a water bath. We separated the −325 mesh fraction of runs 1 and 2 into three size fractions with a sonic sifter to determine the distribution of fines and analyzed each fraction for oxide content. As shown in Table 5.7, oxidation and hydration of the powder are low, resulting in about the same oxide content as in aluminum powders air atomized in a dry environment.

Aluminum powders containing 2, 4, and 6 wt % Mg have been received from Whittaker Corporation. These powders are made by a spinning-electrode arc-melting technique and their size range is −42 +200 mesh. These powders, along with those from the initial atomizing runs and an aluminum standard, have each been ball-milled to three different oxide contents and consolidated. The compacts will be vacuum annealed, extruded at a reduction ratio of 30 in area, and tested.

Table 5.7. Size Distribution and Oxide Content of Fines from Atomized Al–5 wt % Mg Alloy[a]

| Size (μ) | Weight Fraction (%) | Oxide Content (wt %) |
|---|---|---|
| 30 to 44 | 53.4 | 0.40 |
| 10 to 30 | 42.9 | 0.75 |
| less than 10 | 3.7 | 0.94 |

[a]This powder is the −325 mesh fraction of runs 1 and 2 from Table 5.6.

[redacted]



## Anisotropy of Extruded SAP 895

T. M. Nilsson

To examine more thoroughly the anisotropy in mechanical properties of extruded SAP products, we cut specimens from the center of a bar of commercial SAP 895 at angles of 0, 30, 45, 60, and 90° to the extrusion direction. The SAP bar, manufactured by Montecatini, had been extruded at a ratio of about 20. The average composition of the material is 10.3 wt % $Al_2O_3$, 0.07 wt % Fe, 0.3 wt % C, and 4 ppm H.

The results of tensile testing at 450°C are shown in Fig. 5.6. Usually, when the anisotropy of SAP materials has been examined (i.e., to find out how bad properties can become if the structure is unfavorably oriented), transverse properties have been measured. Figure 5.6 shows, however, that the strength properties are not only low in the transverse direction but also in directions close to longitudinal. In fact, transverse properties may not be the lowest; properties around 30° orientation may very well be lower. The effect of a 100-fold increase in strain rate seems to be to raise the strength by about 20% for all orientations, meaning that the ratio between properties in the longitudinal and different directions is relatively unaffected by the variation in strain rate from 0.2 to 0.002 $min^{-1}$. Concerning ductility, Fig. 5.6 shows that the orientations 0 and 60° show favorable elongation at rupture and that the orientations of 30 and 45° show a more brittle behavior than does the transverse direction. The important property, uniform elongation, seems to be the lowest in the longitudinal direction. In addition to showing the anisotropy of extruded SAP bars, Fig. 5.6 is also of interest with respect to working of these alloys. If some of the material during secondary working gets aligned just slightly away from the usual extruded structure, lower strength properties and especially lower ductility must be expected because of possible localized yielding and failure in the altered structure.

The mechanical properties illustrated in Fig. 5.6 are to a certain extent reflected in the fracture appearance as shown in Fig. 5.7. The 0° specimens usually fractured perpendicular to the tension direction,

[redacted]

[redacted]



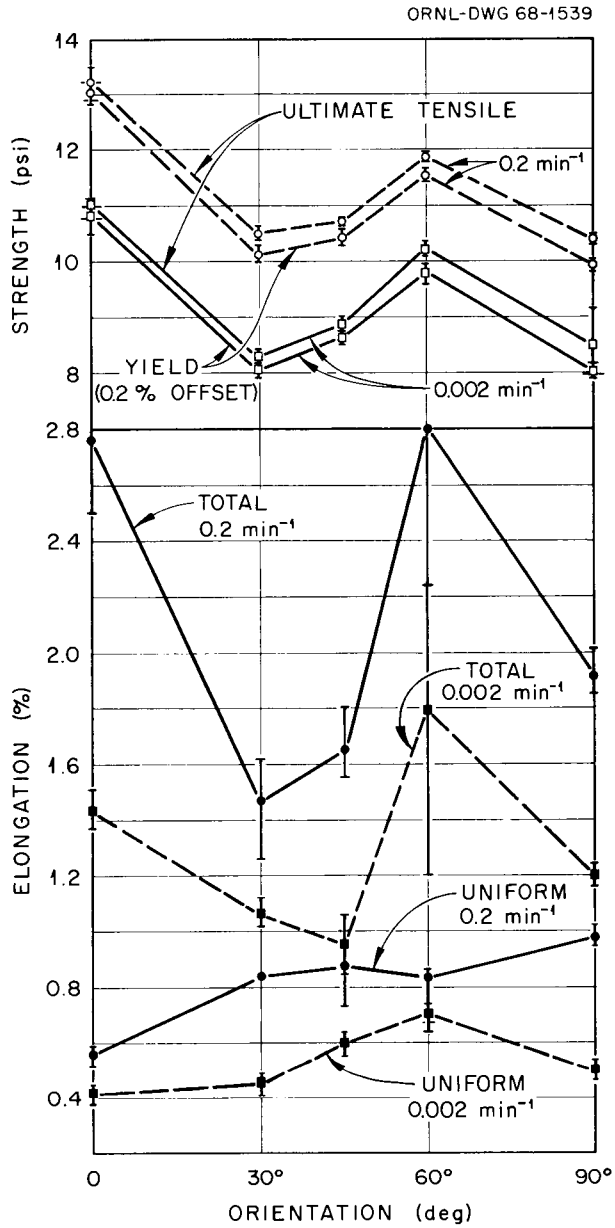


Fig. 5.6. Tensile Properties at 450°C of SAP 895 as a Function of Orientation Relative to the Extrusion Direction. 0° corresponds to longitudinal properties and 90° to properties transverse to the extrusion direction. Six specimens of each orientation were tested at 450°C, three at a strain rate of 0.2 $min^{-1}$ and three at 0.002 $min^{-1}$. Total elongation is for gage length ten times diameter.

[redacted]

[redacted]



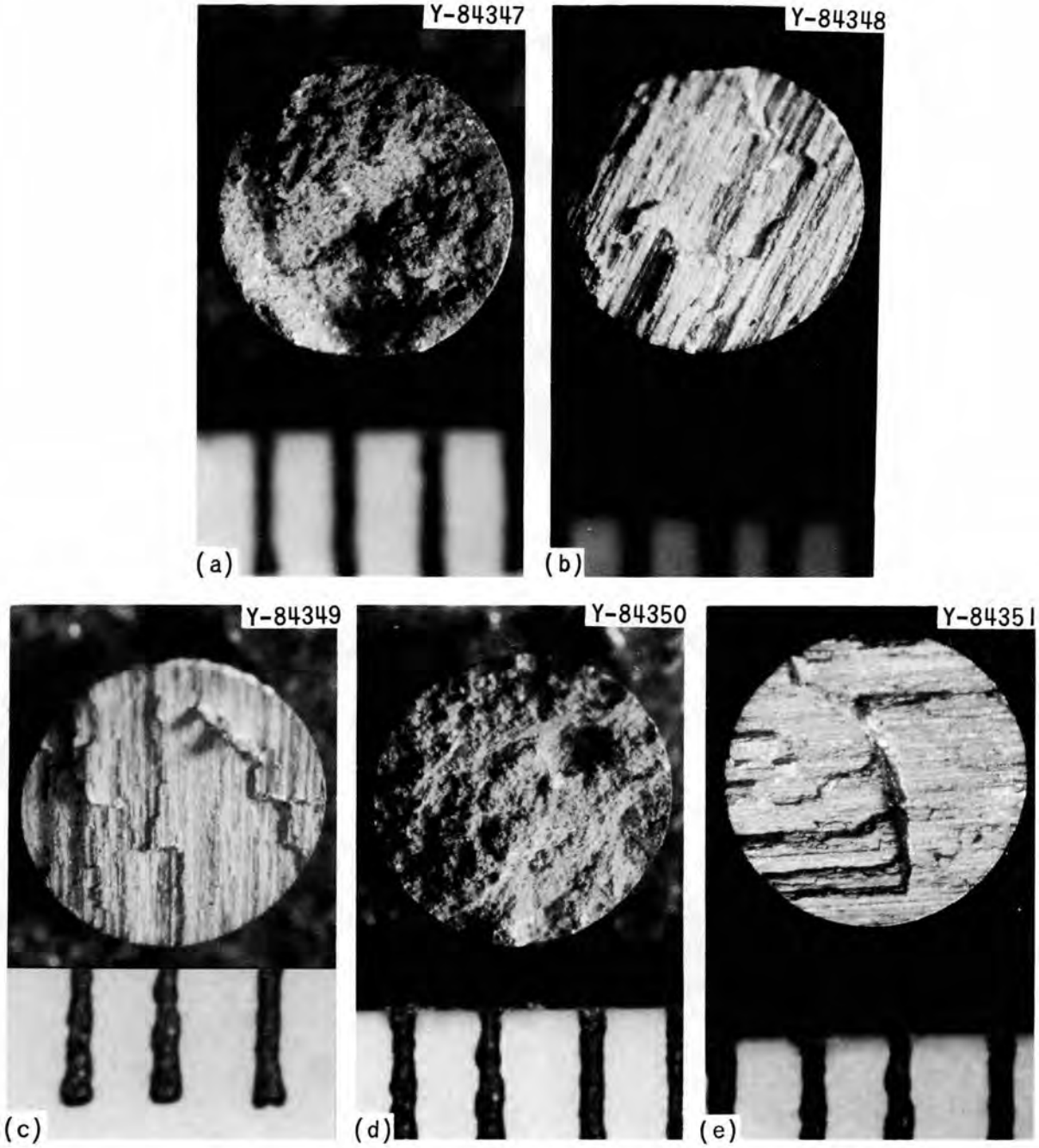


Fig. 5.7. Fractures of Specimens Tensile Tested at 450°C at a Strain Rate of 0.002 $min^{-1}$. (a) Tested 0° from the extrusion direction; (b) 30°; (c) 45°; (d) 60°; (e) 90°. The overall fracture surface is at 45° to the direction of tension in the case of the 30, 45, 60, and 90° orientations, and the longest axis of the elliptic fracture surface is maintained vertical. Notice the change in direction of the striated pattern as the orientation relative to extrusion direction changes. The scale markers are 1 mm apart and in the direction of tension.

[redacted]

[redacted]



whereas specimens with other orientations usually fractured along a 45° plane relative to the direction of tension. The 30, 45, and 90° fracture surfaces have a striated appearance, and it is noteworthy how the direction of the striation changes with orientation. Considering the alignment of the structure after extrusion, the fracture seems to occur along that 45° plane that contains the direction of extrusion. The fracture surface of the 60° specimen does not look striated; in fact, the surface looks more like the fracture of the 0° specimen. The striated fracture appearance was always connected with a brittle fracture, as seen from Fig. 5.6.

The microstructure of the bar is shown in Figs. 5.8 and 5.9. Although the oxide particles are quite uniformly distributed, the transverse view shows that the concentration of oxide particles is greater in the grain boundaries than in the interior and that the greater agglomerations nearly always lie in the boundaries. This uneven distribution

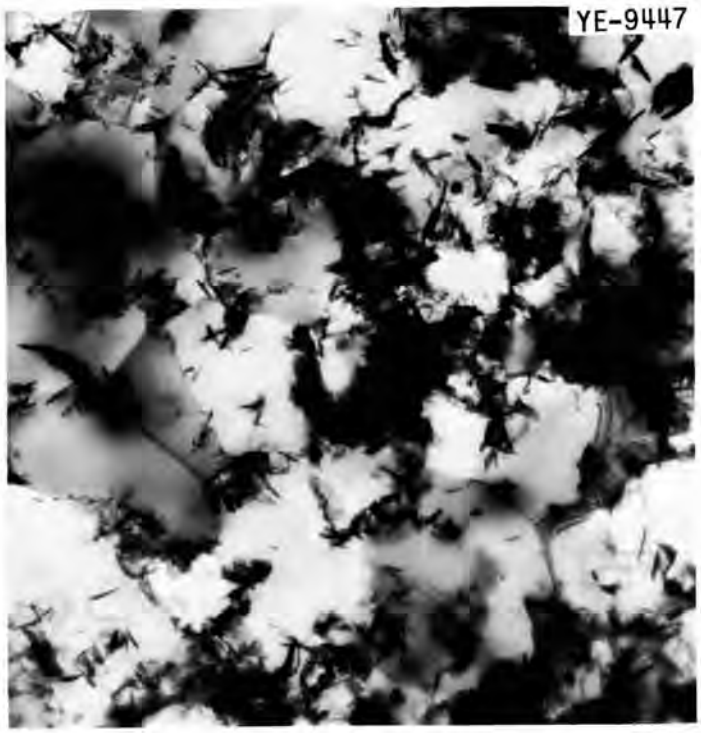


Fig. 5.8. Transverse Microstructure of SAP 895 Bar After a Reduction Ratio of 20 During Extrusion. 20,000×.

[redacted]

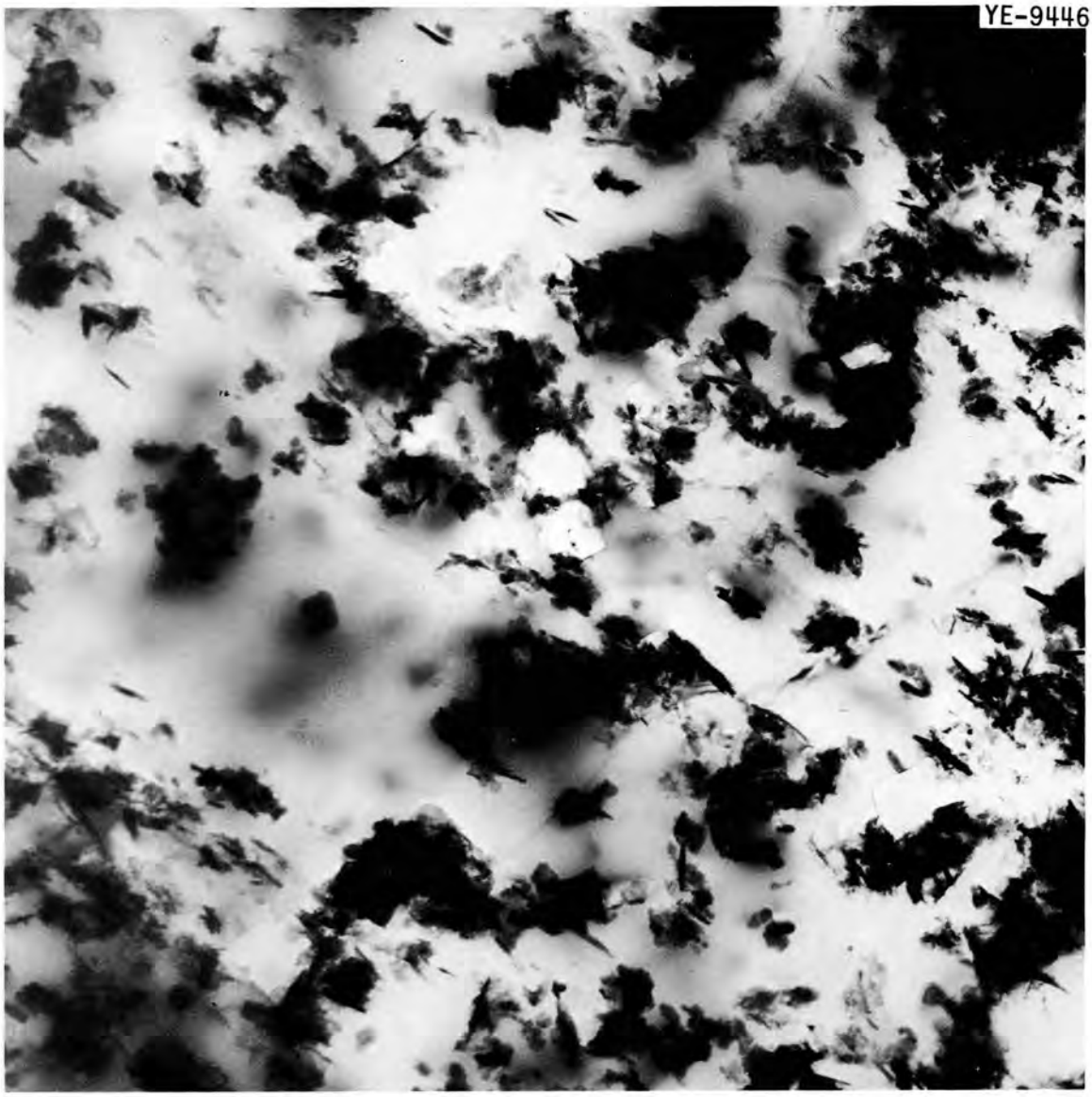


Fig. 5.9. Longitudinal Microstructure of SAP 895 Bar After Reduction Ratio of 20 During Extrusion. 20,000×.

of the oxide particles, "oxide stringers," arises during extrusion and probably explains the mechanical behavior of samples tested in directions different from the extrusion direction. The fracture of longitudinal SAP specimens, examined by Harman,[10] may also to a certain

[10]D. G. Harman and T. A. Nolan, Fracture of Aluminum-$Al_2O_3$ Alloys: Fracture Analysis of the Commercial SAP-Type Alloy XAP-001, ORNL-TM-1826 (July 1967).

[redacted]



extent be explained by the presence of oxide stringers, positioned in the grain boundaries. The reason for the different behavior of the 60° specimens is not immediately obvious, and we have not yet been able to satisfactorily explain this phenomenon.

The mechanical properties at room temperature as a function of orientation are shown in Fig. 5.10. The trend is the same as at 450°C; both strength and ductility show high values at 0 and 60° orientations, whereas the material is weaker and more brittle when tested in the three other directions.

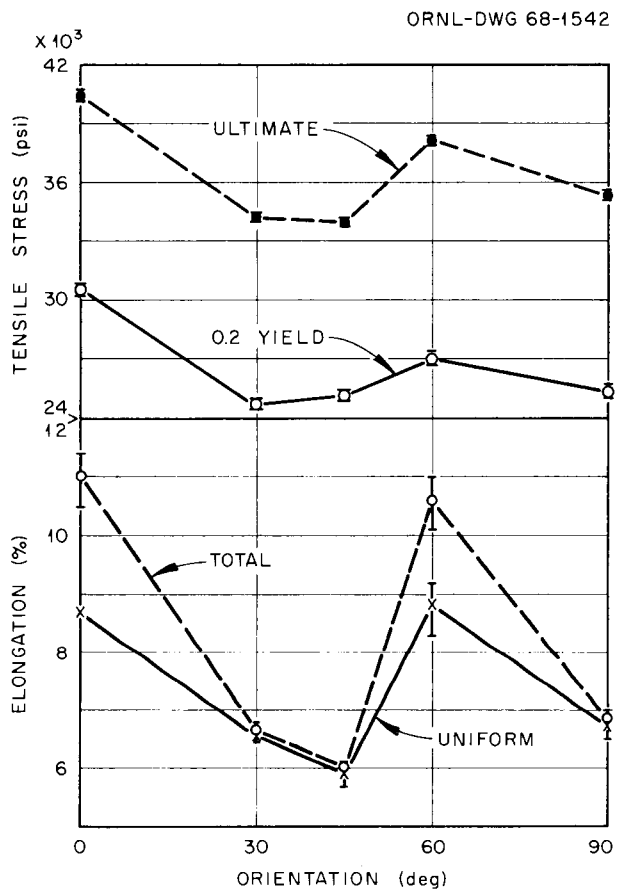


Fig. 5.10. Mechanical Properties of SAP 895 at Room Temperature as a Function of Orientation Relative to the Extrusion Direction; Strain Rate 0.02 $min^{-1}$. Two specimens were tested at each orientation, and the figure shows the means and the scatter around the means. Total elongation is for gage length ten times diameter.

[redacted]

[redacted]



# 6. SOL-GEL FAST REACTOR FUELS

A. L. Lotts

We are developing and testing sol-gel-derived $(U,Pu)O_2$ fuel to assess the potential of the fuel for use in primarily the liquid metal-cooled fast breeder reactors and the Fast Flux Test Facility. The effort involves

1. the preparation of $(U,Pu)O_2$ fuel by the sol-gel process,
2. out-of-reactor testing to characterize the sol-gel product,
3. the development of fabrication procedures for incorporating the mixed oxide fuel into a suitable fuel rod component,
4. the irradiation testing of the fuel.

The program was initiated in late fiscal year 1967; accordingly, our activities have necessarily emphasized those tasks that provide the facilities, experimental design, and equipment to accomplish a broad spectrum of work. The activities now include (1) the preparation of a variety of $(U,Pu)O_2$ products by the sol-gel method; (2) the addition of equipment to the plutonium laboratories for out-of-reactor characterization of material and for additional fabrication methods; (3) the development of procedures for packing of $(U,Pu)O_2$ microspheres and a method for making $UO_2$ and $(U,Pu)O_2$ pellets from sol-gel-derived material; and (4) the irradiation of noninstrumented capsules in the ETR to test the Sphere-Pac $(U,Pu)O_2$, the design and construction of instrumented capsules for the ORR, and the design of experiments for transient testing, for short-term rabbit tests, and for testing of sol-gel materials in the EBR-II. Also, we are developing calculation techniques for experimental design and for interpretation of the results of our irradiation experiments, and we are accumulating and classifying cladding and fuel data required for design of fast breeder fuel elements.

[redacted]

[redacted]



# Plutonium Ceramic Facilities

J. D. Sease E. S. Bomar W. H. Pechin
M. K. Preston[1] C. F. Sanders

Our plutonium ceramic facilities are being equipped to examine and prepare ceramic nuclear fuels that contain alpha-active materials. Glove-box facilities are being provided for fuel preparation and characterization and for fabrication of fuel rods and irradiation test capsules.

The facilities, which are in two locations due to the scarcity of available alpha laboratory space, are being developed to complement each other. The equipment in Building 3019 is to contain most of the equipment for developing sol-gel mixed oxide fabrication processes, facilities for assembling and welding irradiation capsules and fuel elements, and a complete alpha metallography facility. The equipment in Building 4508 is directed mainly toward developing preparation techniques for reactive materials such as mixed uranium-plutonium nitrides and the characterization of fuels with respect to structure, composition, and thermal characteristics. Because of the possible presence of reactive materials, all of the boxes for 4508 will be designed for high-purity inert-atmosphere operation. This inert atmosphere will be supplied initially by a one-pass purge system, but this will be replaced eventually with a closed loop and purifier. In Building 3019, the metallography boxes and a few of the other boxes will be supplied with inert-atmosphere purge capabilities. We have received all of the glove boxes and equipment that were ordered, and we are currently either operating or installing this equipment. The status of the work in the two buildings follows.

## Building 3019 Facilities

The layout of the 3019 Interim Alpha Laboratory and the principal equipment associated with the glove boxes are shown in Fig. 6.1. The two rooms, which are approximately 24 × 24 ft each, will contain 23 glove boxes when installation is complete. Glove boxes 1 through 4

[1]General Engineering Division.

[redacted]

[redacted]



ORNL-DWG 67-13261R

PRINCIPAL EQUIPMENT IN GLOVE BOXES

1. SCALES-BLENDER-DISPENSER
2. HYDRAULIC PRESS-VACUUM PUMP
3. TUBE FURNACE
4. SINTERING FURNACES-REACTION FURNACE
5. WELDING FIXTURE-COLLAPSE CHAMBER
6. WELDING FIXTURE-NaK BACKFILL RIG
7. PARTICLE COATER SERVICE EQUIPMENT
8. PARTICLE COATER FURNACE
9. MICRORADIOGRAPHY EQUIPMENT
10. POWDER CONDITIONING EQUIPMENT
11. CENTERLESS GRINDER
12. ULTRASONIC DRILL
13. VACUUM PUMP-COLD TRAPS
14. VAPOR DEPOSIT FURNACE
15. TUBE FURNACE-CONVERSION EQUIP.
16. LAPPING MACHINE-CUT-OFF SAW
17. POLISHING WHEELS-ULTRASONIC CLEANER
18. INSPECTION MICROSCOPE
19. ELECTROLYTIC POLISHER-CATHODE ETCHER
20. TRANSFER BOX
21. METALLOGRAPH
22. MACRO CAMERA
23. MICRO HARDNESS TESTER

ORNL-DWG 67-13262R

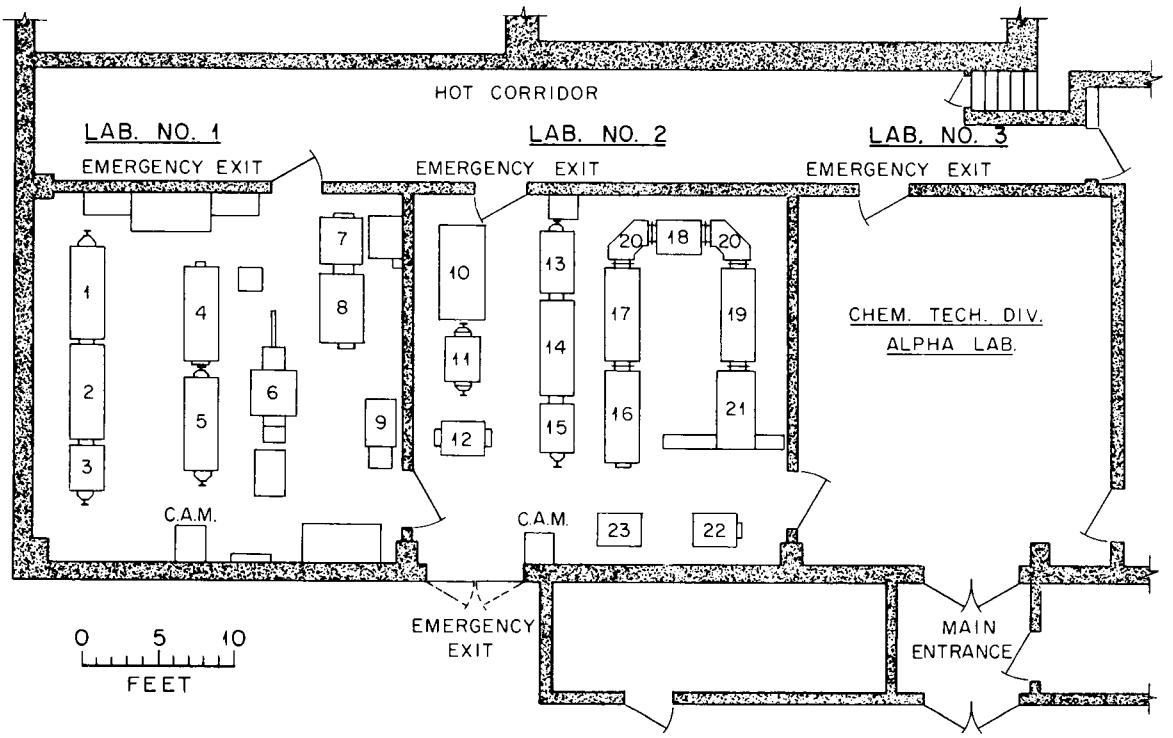


Fig. 6.1. Interim Alpha Laboratory Equipment Layout, Bldg. 3019.

and 10 through 12 are primarily for oxide fabrication; glove boxes 5 and 6 are for irradiation capsule assembly and welding; boxes 7 and 8 are for pyrolytic carbon coating of plutonium-bearing microspheres; box 9 is for microsphere microradiography; boxes 13, 14, and 15 are for deposition of mixed $(U,Pu)O_2$ from the fluoride vapors, and boxes 16 through 23 are for metallographic preparation and examination. With the exception of boxes 12, 22, and 23 all of the glove boxes shown on the layout are installed and are either operating or in the final stages of check-out. The principal work this quarter has involved the

[redacted]

[redacted]



substitution of two inert-atmosphere boxes for boxes 1 and 2, the installation and check-out of the centerless grinder glove box in the oxide fabrication equipment, and the installation and check-out of the metallographic equipment. In addition an argon distribution system for the laboratory was started.

Oxide Fabrication. Two 6-ft inert-atmosphere glove boxes were substituted for the original TRU pellet preparation boxes (boxes 1 and 2) to permit controlling the valance state in mixed uranium-plutonium sols. Most of the original equipment, such as the pellet press and balances, are being utilized in the new boxes, and in addition an extrusion press is being fabricated and will be installed. These boxes will be operative before the end of January.

The powder preparation box (10), which contains equipment for tray and freeze drying of mixed sol, fluid energy grinding, and sigma mixing of sol pastes, was completed; the equipment was checked out; the hazards analysis was prepared and approved; and the box was placed in operation.

The centerless grinding glove box was installed in the laboratory, a hazards analysis was prepared, and a tentative approval for operation was obtained. Installation of the ultrasonic drill in its glove box has just begun.

Metallography. Seven of the nine metallography glove boxes were moved to the 3019 Alpha Laboratory and were connected into their operating line. We are making the final service connections and equipment installation. Leak testing and cold check-out should be started during the last half of January. Installation of the hardness testing and macrocamera glove boxes (22 and 23) will not begin until the other seven boxes are placed in hot operation. In the place to be occupied by these two boxes we are currently operating the two old TRU-type metallography boxes to maintain plutonium metallography capabilities during the installation of the new line. Both the hardness tester and macrocamera have been installed and are currently being checked out in 4500-S.

[redacted]

[redacted]



Building 4508 Facilities

The layout of the 1700 $ft^2$ 4508 Interim Plutonium Laboratory and the principal equipment associated with each glove box are shown in Fig. 6.2. The boxes are grouped according to purpose:

| Group | Purpose |
|---|---|
| 1, 19, 20, 21 | Fuel characterization |
| 2, 3, 4, 5, 8 | Nitride synthesis and fabrication |
| 6, 7 | Pellet examination |
| 9, 10 | Short-term compatibility studies |
| 11, 12, 13 | Thermal conductivity measurement |
| 14 | Fuel rod density scan |
| 15, 16, 17 | X-ray diffraction studies |
| 18 | Vapor pressure measurement |
| 22 | Arc melting |
| 23 | Isothermal grain growth |
| 24 | Creep measurement |

Only 14 of the boxes will be set up initially; these boxes are 1 through 4, 6, 8 through 10, 14 through 17, 19, and 20. These boxes are now essentially completely installed and ready for initial cold check-out. A hazards review for this area has been prepared, and we hope to be ready for a formal hazards review by the middle of February and for hot operations in March. Much effort has been expended during the last quarter preparing this laboratory. A brief summary and status of each major equipment group follows.

Box Argon Purge-Exhaust System. The boxes are all being equipped to operate with a high-purity (< 50 ppm total impurities) argon atmosphere, initially with a once-through purge and later with an argon purification-recirculation system. Developing a system that is compatible with both the purge and recirculating modes of operation and capable of compensating for pressure fluctuation caused by glove movement has been a most difficult task in time allotted. A schematic diagram of the system we developed is shown in Fig. 6.3.

[redacted]

ORNL-DWG 67-13259R

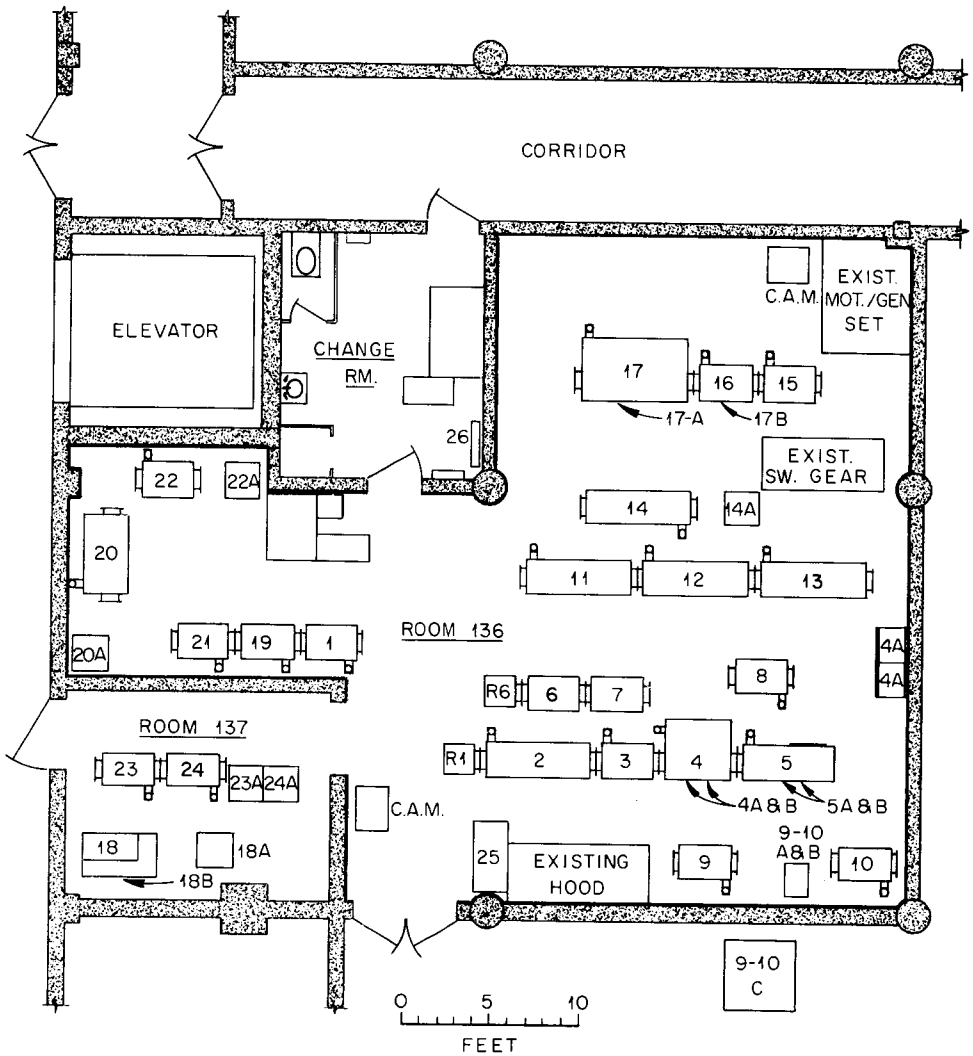


## PRINCIPAL EQUIPMENT

| | |
|---|---|
| 1 | WEIGHING STATION |
| R-1 | TRANSFER BOX |
| 2 | POWDER CONDITIONING EQUIP. |
| 3 | PELLET HOT PRESSING EQUIP. |
| 4 | SINTERING & SYNTHESIS EQUIP. |
| 4-A | POWER SUPPLY, 4-B TEMP. CONTROL |
| 5 | VACUUM TUNGSTEN FURNACE |
| 5-A | FURNACE TEMP. CONTROL |
| 5-B | FURNACE POWER SUPPLY |
| 6 | PELLET EXAM. & LOADING EQUIP. |
| R-6 | TRANSFER BOX |
| 7 | PROFILOMETER |
| 8 | SHATTER BOX, GRINDER |
| 9 | COMPATIBILITY EQUIPMENT |
| 10 | COMPATIBILITY EQUIPMENT |
| 9-10A | VACUUM INSTRUMENTS |
| 9-10B | INDUCTION POWER SUPPLY CONTROL |
| 9-10C | 25 KW INDUCTION HEATING UNIT |
| 11 | ELECTRICAL RESISTIVITY EQUIP. |
| 12 | COMPARATIVE & ABSOLUTE LONG. APPAR. |
| 13 | RADIAL HEAT FLOW & FUEL ELEMENT SIM. |
| 14 | GAMMA SCANNER APPARATUS |
| 14-A | GAMMA SCANNER CONTROL CABINET |
| 15 | X-RAY DIFF. PREPARATION EQUIP. |
| 16 | X-RAY DIFF. DECONTAMINATION EQUIP. |
| 17 | X-RAY DIFFRACTOMETER |
| 17-A | X-RAY DIFF. COUNTING CABINET AND POWER CONTROLS |
| 17-B | X-RAY DIFF. G.E. POWER SUPPLY TRANS. |
| 18 | VAPOR PRESSURE EQUIPMENT |
| 18-A | VAPOR PRESSURE POWER SUPPLY |
| 18-B | VAPOR PRESSURE CONTROL CABINET |
| 19 | DTA & TGA EQUIPMENT |
| 20 | HOT STAGE MICROSCOPE |
| 20-A | HOT STAGE MICROSCOPE PROGRAMMER |
| 21 | PARTICLE SIZING EQUIPMENT |
| 22 | ARC MELTING FURNACE |
| 22-A | FURNACE CONTROL CABINET |
| 23 | ISOTHERMAL GRAIN GROWTH EQUIP. |
| 23-A | ISOTH. GRAIN GROWTH CONTROL CAB. |
| 24 | CREEP MEASURING EQUIPMENT |
| 24-A | CREEP MEAS. EQUIP. CONTROL CAB. |
| 25 | STORAGE CABINET |
| 26 | ANNUNCIATING PANEL |

Fig. 6.2. Interim Plutonium Laboratory Equipment Layout, Bldg. 4508.

[redacted]



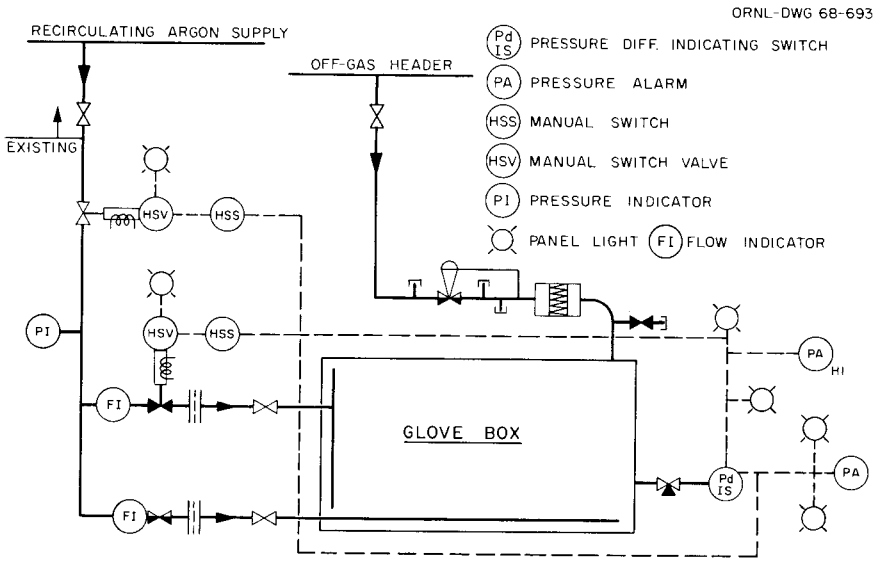


Fig. 6.3. Glove-Box Argon Purge System Flow Diagram.

The system is based on a "Photohelic" gage working through two solenoid valves and a high-capacity regulating valve. The Photohelic controls a normal purge flow and a high-rate purge flow based on two preset pressures. At normal operating pressure the normal purge (1/2 to 1 cfm) flow is on. If a glove is withdrawn the pressure in the box is lowered, and the Photohelic turns on the fast purge (approx 5 cfm) in addition to the normal flow; at the same time the regulating valve throttles the exhaust flow. If a glove is inserted, the pressure rises and the Photohelic turns off all flow to the box; at the same time the regulating valve opens further to increase exhaust flow. The principle of the supply portion of this system is used for the 3019 purge system; however, due to the existing exhaust system in 3019, a simple back-flow preventer is used instead of a regulating valve.

Fuel Characterization. The group of boxes includes the analytical balance box, DTA-TGA box, hot-stage microscope box, and particle-size analysis equipment. All of this equipment except the particle-size analysis equipment has been initially checked out, and we are in the final stages of the installation of these glove boxes. Some difficulties

[redacted]

with the control circuit supplied with the hot-stage microscope have not been resolved; however, we hope this will be resolved in the near future.

Nitride Synthesis and Fabrication. All of the equipment except the high-temperature tungsten furnace has been installed or is in fabrication. Revised purchase specifications for the tungsten furnace were prepared and circulated to the vendors for bids. Detailed design of the hot press was completed and the press is currently being fabricated in the local shops. The power lead from the induction power supply has been installed for the hot press. The sintering and synthesis glove box contains two 1 5/8-in.-diam Marshall tube furnaces capable of operating up to 1750°C in a vacuum or with an oxidizing, neutral, or reducing gas purge. Both furnaces have a temperature controller; however, only one furnace is equipped with a programmer and temperature chart recorder. The installation of this box and all its equipment is essentially completed, except gas services and the two mechanical pumps for the furnace vacuum systems. Check-out of this box should begin in late January.

The "Shatterbox" grinder has been installed in its glove box and initial check-out completed. The pellet press and other related equipment are installed.

Compatibility. Installation of the induction power supply was completed and initial check-out made. The circuits for controlling the power supply and vacuum system with required safety interlocks were designed, fabricated, and installed. The unit is now ready for cold check-out.

X-Ray Diffraction. The three boxes for x-ray diffraction have been set up in their operating positions, and the x-ray power supply and counting circuits were installed under the box. The high-voltage power lead into the box was designed, fabricated, and installed. The equipment is now ready for the installation of the x-ray tube and initial check-out alignment.

## Preparation of $(U,Pu)O_2$ Sol-Gel Material

W. T. McDuffie[2]

The work reported in this section is part of a larger program on sol-gel process development and demonstration at ORNL. It is that being carried out in the Chemical Technology Division Pilot Plant. During the past quarter about 1 kg of $UO_2$–25% $PuO_2$ microspheres was prepared for use in fabrication studies and irradiation test capsules. Approximately 500 g was delivered to Battelle Northwest Laboratory. The remainder was used at ORNL.

Recently work has been directed toward preparation of $(U,Pu)O_2$ gel shards for use in pellet formation studies. About 280 g of $PuO_2$ sol was prepared to be mixed with about 850 g of $UO_2$ sol for these studies.

## Development of $(U,Pu)O_2$ Fabrication Techniques

J. D. Sease R. A. Bradley R. B. Fitts
R. L. Hamner A. R. Olsen

Various techniques are being investigated for fabricating sol-gel-derived urania-plutonia into fuel for LMFBR applications. Current activities are directed toward developing a process for pressing and sintering pellets for loading into fuel rods for irradiation tests. Pellets with controlled densities at various levels between 86 and 96% of theoretical and with oxygen-to-metal ratios slightly less than 2.00 are required for the irradiation tests.

Sphere-Pac, a method for loading fuel rods directly with dense microspheres by low-energy vibratory compaction, is also being investigated.

### Sphere-Pac Development (R. B. Fitts, J. Komatsu, A. R. Olsen)

The Sphere-Pac process combines sequential loading of sol-gel microspheres with compaction by low-energy vibration. The initially

[2]Chemical Technology Division.

developed process using two size fractions produces fuel loadings of 83 to 85% volume packing. This development work has been reported elsewhere.[3–6] Our current program is aimed at achieving higher volume packing densities. The alternate approaches to this process were discussed previously.[6] We have continued to investigate the blended-bed single-infiltration technique. We have determined that a blended coarse size fraction can be obtained by mechanically mixing microspheres of two size fractions in size ratios up to approximately 4 without subsequent gross segregation under vibration. Coarse bed densities can be raised from the normal 62.5% up to 72.5% by this blending. Subsequent infiltration of the blended coarse bed with a single fine size fraction has produced volume packing densities of greater than 88%. Although the process has not been optimized, a blend of approximately 65% 775-μ-diam (–20 +25 mesh) microspheres and 35% 163-μ-diam (–80 +100 mesh) microspheres infiltrated with less than 37-μ-diam (–400 mesh) microspheres will produce these higher loadings.

Present efforts are concentrated in three areas of interest for the formation of blended binary Sphere-Pac beds.

1. Studies are under way to define the best approaches to blending the coarse bed. Techniques for control of segregation of different-size spheres during blending may be required.

2. Methods of separating subsieve-size spheres (< 37 μ) into size fractions are being investigated.

---

[3]A. R. Olsen and J. D. Sease, Metals and Ceramics Div. Ann. Progr. Rept. June 30, 1966, ORNL-3970, p. 220.

[4]A. R. Olsen, J. D. Sease, R. B. Fitts, and A. L. Lotts, "Fabrication and Irradiation Testing of Sol-Gel Fuels at Oak Ridge National Laboratory," paper presented at Symposium on Sol-Gel Processes for Production of Ceramic Nuclear Fuels, Turin, Italy, Oct. 2–3, 1967, to be printed in the Transactions (also available as ORNL-TM-1971).

[5]F. G. Kitts, R. B. Fitts, and A. R. Olsen, "Sol-Gel Urania-Plutonia Microsphere Preparation and Fabrication into Fuel Rods," paper presented at the AIME 1967 Nuclear Metallurgy Symposium, Plutonium Fuels Technology, Phoenix, Arizona, Oct. 4–6, 1967 (to be published in Transactions).

[6]R. B. Fitts and A. R. Olsen, Fuels and Materials Development Program Quart. Progr. Rept. Sept. 30, 1967, ORNL-TM-2020, pp. 8–9.

3. The vibratory equipment is being instrumented to better define the mode and amount of energy input during sphere packing.

Pellet Development (R. A. Bradley, R. L. Hamner)

Summary of Experience in Pelletizing Sol-Gel $UO_2$. Hamner and Robbins[7] conducted a preliminary investigation of the pelletization of sol-gel-derived urania. They demonstrated that pellets with densities in the range of 70 to 92% of theoretical could be produced from various forms of sol-gel-derived material, with the density depending on the powder preparation, the pressure used in forming the pellet, and the sintering conditions.

The sintering schedule and atmosphere selected[7] were based upon sintering studies of urania microspheres by differential thermal analyses, chemical analyses, and x-ray crystallite size measurements. A mixture of Ar–4% $H_2$ was used as the primary gas for safety and to keep the oxygen-to-metal ratio low. The gas used between room temperature and 900°C was bubbled through deoxygenated water at 95°C to introduce steam, which had been found effective in the removal of carbon.[8] Dry gas was used during heating from 900 to 1450°C and during cooling to room temperature. A soak period at 150°C subdued an intense exotherm that occurs just above this temperature because of a nitrate-organic reaction, and another soak at 450°C removed as much of the volatile material as possible before sintering began just above this temperature.

The same general procedure was used in our preliminary studies on pelletizing sol-gel urania-plutonia.

Urania-Plutonia Preparation. Approximately 1.5 kg of microspheres was formed from a mixed urania-plutonia sol. The sol was dried in argon at 90°C for 1 to 2 hr and at 170°C for 16 hr. After sieving through a screen with an 810-μ opening to remove clusters, the microspheres were blended by tumbling. Three samples were withdrawn for

---

[7]R. L. Hamner and J. M. Robbins, Fuels and Materials Development Program Quart. Progr. Rept. Sept. 30, 1967, ORNL-TM-2020, pp. 9–16.

[8]H. Beutler and R. L. Hamner, Metals and Ceramics Div. Ann. Progr. Rept. June 30, 1967, ORNL-4170, pp. 223–226.

[redacted]



uranium and plutonium analyses. The remainder was divided into two batches, one to be sent to Battelle Northwest Laboratory and the other to be used for fabrication studies at ORNL. The results of chemical and spectrographic analyses and measurements of crystallite size, bulk density, and surface area of this material are given below:

| Analysis | Value |
|---|---|
| Chemical, wt % | |
| Pu | 20.1 |
| U | 62.3 |
| C | 3.3 |
| O + $NO_3^-$ (by difference) | 14.3 |
| Semiquantitative Spectrographic, wt % | |
| Al | 0.15 |
| Cr | 0.02 |
| Cu | 0.03 |
| Fe | 0.08 |
| Mn | 0.003 |
| Ni | 0.01 |
| Pb | Very faint trace |
| Mo, Ti, Zr | Sought, not detected |
| BET surface area, $m^2/g$ | 68 |
| Crystallite size, A | 60 |
| Bulk density (Mercury porosimeter) % of theoretical | 34 |

Pelletization. We determined the effects of starting material and compacting pressure on the density of urania-plutonia pellets. Pellets 0.25 in. in diameter were pressed at pressures ranging from 15,000 to 60,000 psi from as-received microspheres and from −100- and −325-mesh powder obtained by grinding microspheres in a mortar and pestle and sieving. The green density of the pellets ranged from 31 to 44% of theoretical, depending on the starting material and compacting pressure. The pellets were sintered with the cycle shown below, which had been previously established for urania pellets.

[redacted]

[redacted]



| | |
|---|---|
| Room temperature to 150°C | 50°C/hr |
| Hold at 150°C for 2 hr | |
| 150 to 450°C | 50°C/hr |
| Hold at 450°C for 12 hr | |
| 450 to 1000°C | 100°C/hr |
| 1000 to 1450°C | 200°C/hr |
| Hold at 1450°C for 1 hr | |
| Atmosphere | Ar–4% $H_2$ with steam from room temperature to 900°C; dry Ar–4% $H_2$ from 900 to 1450°C |

The densities obtained from various starting materials and pressing conditions are shown in Table 6.1. The highest density was obtained from –325 mesh powder pressed at 30,000 or 40,000 psi. Pellets pressed at higher pressures laminated either in the green state or during sintering. Pellets pressed from unground microspheres had densities up to 88% of theoretical, but their surfaces were pitted and contained numerous cracks encircling the microspheres.

Conclusion. With this first batch of microspheres we achieved a density of 93% of theoretical by grinding to –325 mesh, pressing at 30,000 psi, and sintering at 1450°C. Although we have demonstrated that pellets within the acceptable density range can be achieved by grinding microspheres to a fine powder, we recognize that the process

Table 6.1. Density of Urania-Plutonia Pellets Pressed from Various Materials at Different Pressures

| Material | Density,[a] % of theoretical, at pressure, psi | | | | |
|---|---|---|---|---|---|
| | 15,000 | 30,000 | 40,000 | 45,000 | 60,000 |
| –325 mesh | 88.5 | 93.3 | 92.3 | 86.0[b] | |
| –325 mesh[c] | 86.1 | 91.8 | | b,d | b,d |
| –100 mesh | 81.8 | 90.8 | | d | b,d |
| Microspheres | 79.3 | 83.8 | | 87.8 | 87.6 |

[a]Value reported is average for three pellets, calculated from weights and measurements.

[b]5 wt % Carbowax used as binder.

[c]Second sintering batch.

[d]Pellets laminated.

[redacted]

can be shortened by tray drying the sol directly, producing angular particles that can be ground directly. We now have facilities for tray drying urania-plutonia sols and have conducted two preliminary drying experiments with urania sol.

Future efforts will be directed toward establishing a process that will reproducibly yield pellets of the required density and oxygen-to-metal ratios.

## Irradiation Testing of Sol-Gel $(U,Pu)O_2$ Fuels

A. R. Olsen

The final evaluation of the sol-gel-derived $(U,Pu)O_2$ fuels will be based upon their irradiation performance. The irradiation testing program includes comparative tests of all the fabrication forms, Sphere-Pac, Vi-Pac, extrusions, and pellets under a variety of irradiation conditions. The program includes both thermal reactor and fast reactor irradiation tests. Thermal flux irradiations permit the use of instrumented capsules and the achievement of high burnup levels in relatively short periods of time for screening-type irradiations. These are being used to supplement the fast-flux irradiations where the fission rate distribution and fuel temperature profiles are more typical of the anticipated LMFBR operating conditions. The development of mathematical models of fuel behavior and the necessary computer programs for doing the manifold calculations are an integral part of the irradiation test program.

### Uninstrumented Screening Irradiation Tests (A. R. Olsen, R. B. Fitts, J. Komatsu)

Uninstrumented capsules designed for screening-type irradiations are being exposed in the Engineering Test Reactor. The capsule design, described previously,[9] permits the simultaneous irradiation of four fuel rods.

---

[9]R. B. Fitts and A. R. Olsen, Fuels and Materials Development Program Quart. Progr. Rept. Sept. 30, 1967, ORNL-TM-2020, pp. 19–24.

[redacted]



Examination of the first two capsules in this series, ORNL 43-99 and 43-100, is continuing. Although overpower operation caused failures in these capsules, the postirradiation examination and analysis have helped to establish operating limits for the fuel and improve our mathematical models.

The relative power of the fuel rods in capsules 43-99 and 43-100 is indicated in Fig. 6.4. The fuel rod locations are superimposed upon the plot of time-averaged unperturbed flux for the ETR facility used for 43-99. The flux distribution for 43-100 was similar, but all fluxes were about 10% lower. The results of radiochemical burnup analyses are compared in Table 6.2 with the values calculated by the ANISN computer code reported last quarter. Burnup calculations based upon isotopic analyses are not yet available.

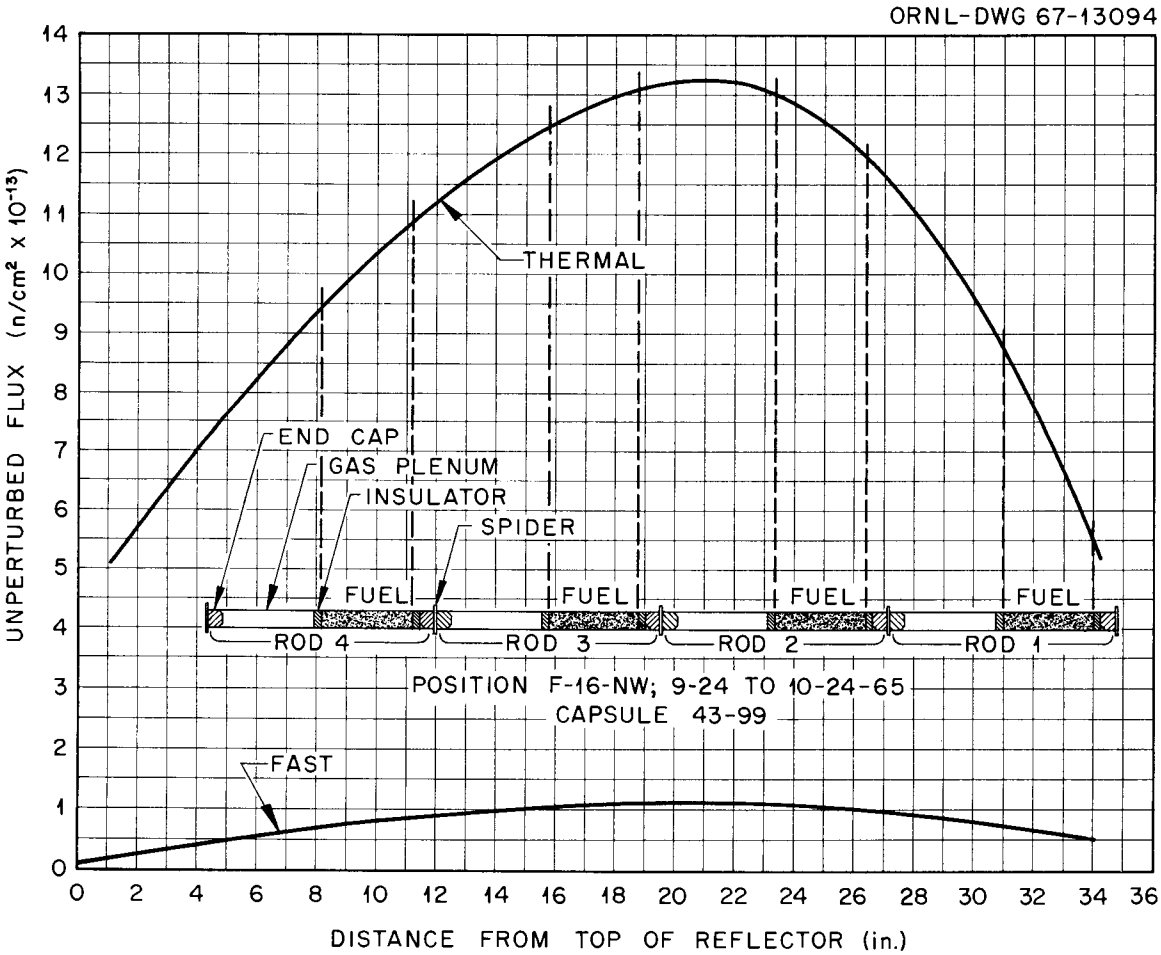


Fig. 6.4. Variation of Unperturbed Flux with Distance. Flux is in neutrons $cm^{-2}$ $sec^{-1}$.

[redacted]

Table 6.2. Fuel Operating Conditions for Capsules 43-99 and 43-100

| Fuel Rod | Calculated Heat Rating (kw/ft) | Temperature,[a] °C | | Burnup, % FIMA[b,c] | | | |
|---|---|---|---|---|---|---|---|
| | | Cladding | Fuel | ANISN | $^{137}Cs$ | $^{144}Ce$ | Average |
| | | | $(U,Pu)O_2$ Fuel | | | | |
| 43-99-3 | 49.90 | 925 | Molten | 1.5 | d | d | d |
| 43-100-3 | 44.89 | 845 | Molten | 1.4 | 0.92 | 2.5 | 1.7 |
| 43-99-1 | 32.59 (34.65) | 645 | Molten | 0.9 | 1.0 | 1.4 | 1.2 |
| 43-100-1 | 29.33 | 590 | Molten | 0.8 | 0.22 | 1.2 | 0.7 |
| | | | $(Th,Pu)O_2$ Fuel | | | | |
| 43-99-2 | 13.11 | 325 | 2165 | 0.4 | 0.54 | 0.50 | 0.52 |
| 43-100-2 | 11.81 | 305 | 2025 | 0.4 | 0.41 | 0.41 | 0.41 |
| 43-99-4 | 10.94 | 280 | 1930 | 0.3 | 0.36 | 0.23 | 0.30 |
| 43-100-4 | 9.85 | 270 | 1815 | 0.3 | 0.34 | 0.28 | 0.31 |

[a]Calculated for section 0.25 in. below maximum power end of rod. Fuel value is for center line.

[b]Percent fissions per initial metal atom.

[c]Isotopic analyses are expected to yield more reliable information for the high-heat-rating rods.

[d]Not available.

[redacted]



Three of these rods failed under thermal transient at unplanned overpower conditions. However, successful operation was apparently obtained at continuous power levels of 50 kw/ft to a peak burnup of approximately 2% FIMA, and fuel rod 43-99-1 survived continuous operation at a peak linear heat rating of approximately 29 kw/ft to a burnup of approximately 1% FIMA.

Experiment 43-112 was removed from the reactor after one cycle of irradiation to confirm the ANISN heat generation calculation and to obtain some information on the behavior of Sphere-Pac fuels at moderate heat ratings and low burnup. Postirradiation gamma scans indicated no change in fuel column heights. All rods were found intact on disassembly. Fission gas samples have been obtained and sections removed for burnup analysis. When the burnup samples were cut the fuel was found to be essentially unchanged, although there was incipient sintering of the microspheres in the peak flux positions. Metallographic examination of these rods is scheduled to begin next quarter. To date we have burnup analyses based on radiochemical analyses of fission products, shown in Table 6.3 with the comparable ANISN burnup level predictions. Although these radiochemical analyses are less reliable than isotopic analyses, the agreement between the ANISN predictions and the $^{144}Ce$ analyses is

Table 6.3. Comparison of ANISN Burnup Predictions with Radiochemical Fission Product Analyses for Experiment ORNL 43-112[a]

| Fuel Rod | Fuel Material | Fuel Burnup, % FIMA | | | | |
|---|---|---|---|---|---|---|
| | | ANISN[b] | $^{144}Ce$ | $^{137}Cs$ | $^{89}Sr$ | Average |
| 43-112-1 | $(U_{0.85}Pu_{0.15})O_2$ | 0.49 | 0.47 | 0.33 | 0.59 | 0.46 |
| 43-112-2 | $UO_2$ (20% $^{235}U$) | 0.71 | 0.72 | 0.49 | 0.77 | 0.66 |
| 43-112-3 | $(U_{0.85}Pu_{0.15})O_2$ | 0.69 | 0.67 | 0.44 | 0.83 | 0.65 |
| 43-112-4 | $(U_{0.85}Pu_{0.15})O_2$ | 0.54 | 0.39 | 0.43 | 0.72 | 0.51 |

[a]Experiment ORNL-43-112 operated for 27.8 effective full-power days.
[b]Predicted for the fuel at the location of the burnup sample.
[c]For the three radiochemical values.

[redacted]

remarkably good. Both cesium and strontium are subject to redistribution in the thermal gradients of the fuel, so they are the least reliable burnup analyses. Isotopic analyses are being obtained.

Using the available burnup analyses we have obtained the following fission-gas-release values for the four rods in this experiment: 43-112-1, 1.7%; 43-112-4, 4.4%; 43-112-3, 31.1%; and the $UO_2$ rod 43-112-2, 38.5%. Final determination of these gas-release rates will depend on a more thorough review of the temperature distribution and the metallographic findings, but the values appear to be higher than would be anticipated for pellets of similar density.

A duplicate replacement capsule for ORNL 43-112, to be designated ORNL 43-115, is being fabricated. This capsule will be irradiated to a peak burnup level of approximately 2% FIMA, while the other duplicate, ORNL 43-113 currently in-reactor, will be irradiated to a burnup level of 10% FIMA.

ORR Instrumented Tests (R. B. Fitts, V. A. DeCarlo[10])

The design of the instrumented ORR capsule has been completed. Figure 6.5 is a schematic drawing of it. It contains two 3-in.-long fuel rods, which are expected to operate at about equal heat generation rates. The rods are instrumented in three ways:

1. A central thermocouple in the top rod measures fuel central temperature. A dummy thermocouple well in the bottom rod preserves the geometry.

2. Three thermocouples are located at top, center, and bottom of the fuel region by each fuel rod in the NaK to monitor cladding temperature.

3. Four sets of calorimeter thermocouples in the outer Zircaloy-2 wall at the midplane of each fuel rod monitor heat generation.

Engineering drawings are complete, all parts are on hand or on order, and a mockup fuel rod of this design has been successfully test loaded by the Sphere-Pac technique.

[10]Reactor Division.

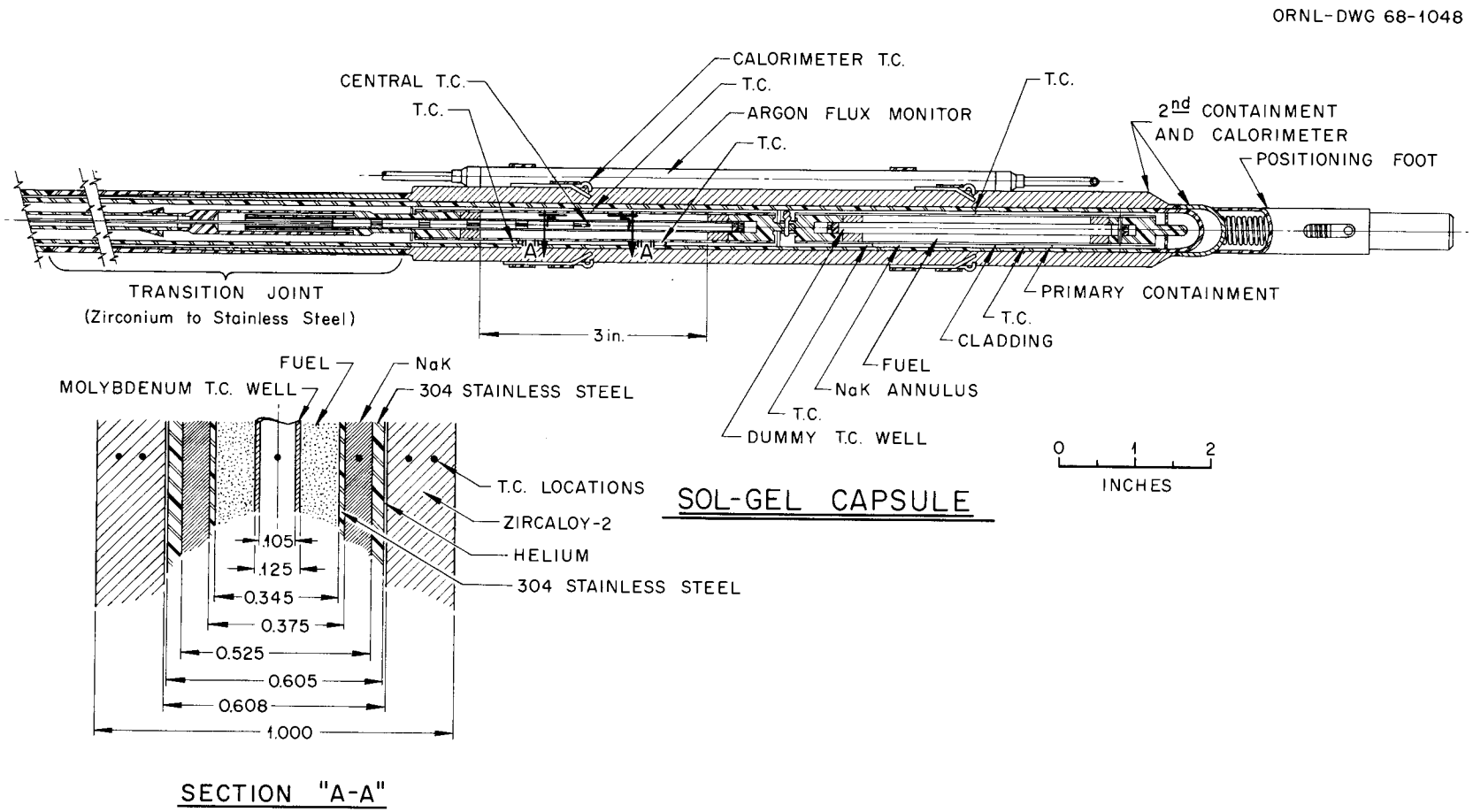


Fig. 6.5. ORR Instrumented Capsule.

A literature search covering in-reactor thermal conductivity for both $UO_2$ and $(U,Pu)O_2$ fuels is under way. It is apparent that despite the generally recognized importance of in-reactor thermal conductivity, there is still no general agreement on all of the operative mechanisms for heat transfer or the proper mathematical formulation for analysis of these mechanisms. We will formulate our initial models for heat transfer based upon this literature survey and refine these models as our experimental program proceeds.

The first capsule in this series will test the design and provide calibration data for future capsules. A preliminary test program has been outlined and is currently being reviewed before final scheduling.

Transient Testing of Sol-Gel-Derived $(U,Pu)O_2$ Fuel (C. M. Cox)

A literature survey of TREAT test results on $UO_2$ and $(U,Pu)O_2$ fuels has been completed, and a program has been formulated to investigate the sol-gel $(U,Pu)O_2$ under conditions simulating accidental power excursions. These will define the fuel and cladding transient performance with respect to:

1. identification of failure mechanisms during transient,
2. establishment of the threshold limits of these failure mechanisms,
3. densification and redistribution of the fuel as a result of transient melting,
4. cladding deformation from high thermal and pressure stresses during the transients.

We reviewed the available facilities for performing these experiments, and the TREAT facility was chosen for its relatively long pulse width, availability of existing capsule designs, approval for testing of plutonium-bearing fuel, and the availability of a neutron radiography facility for interim test capsule examination.

In discussions of this experimental program, one should recognize the limitations imposed by the use of a thermal reactor to simulate transient conditions that might be postulated for a fast reactor fuel element. Because of its long neutron lifetime (approx $9 \times 10^{-4}$ sec)

compared with that of a typical fast reactor (approx $10^{-7}$ sec), TREAT cannot approach the short period produced by prompt excursions in a fast reactor. However, the 40-msec-minimum period of TREAT is much shorter than the periods of the most probable fast reactor accidents leading to meltdown. Such accidents might result from loss of coolant flow without scram or the improper removal of a control rod, which would lead to a reactor period of several tenths of a second.

The other limitation of using a thermal reactor is the nonuniform heat generation rate across the fuel pin due to self-shielding of thermal neutrons. During a transient the temperature will initially peak at the periphery of the fuel, and during a very sharp transient one could conceivably melt the cladding without melting the fuel. However, this effect is minimized by use of the longer transient periods, which would correspond to typical credible hypothetical accidents.

One additional limitation of all transient test programs for plutonium-bearing fuel is that no facility is available at which a transient accident may be simulated with the fuel initially at operating power and temperature conditions. We can, however, use a capsule heater to establish typical cladding operating temperatures; furthermore, the effects of densification, swelling, and fission products on the transient performance can be determined by preirradiating the fuel pins in another facility and reencapsulating for the TREAT tests.

The most significant variables in determining transient performance are expected to be fuel smear density, burnup, and degree of axial restraint.

We have consulted with representatives of ANL, BNWL, GE, and other divisions of ORNL who have been active in transient test programs for $UO_2$ and $(U,Pu)O_2$ fuels in regard to their philosophies of testing, available capsule designs, and available transient heat transfer programs. On the basis of our literature search and the information obtained in these personal contacts, we have planned four series of tests for single-pin geometry in doubly-contained stagnant-NaK-filled capsules using an existing capsule design. The decision as to whether

[redacted]



to progress from this type of experiment to tests with flowing sodium, transparent capsules, or multiple-pin capsules has been deferred, awaiting the results of the initial experiments.

The fuel specimen variables to be studied are:

| | |
|---|---|
| Fuel smear density, fraction theoretical | 0.80 to 0.90 |
| Fuel length, in. | up to 24 |
| Oxygen-to-metal ratio | approx 1.98 |
| Fraction $PuO_2$ | 0.15 to 0.25 |
| Fabrication form | Pellets, Sphere-Pac, Extrusions, Vi-Pac |
| Cladding material | 300 series stainless steel |
| Cladding, outside diameter, in. | approx 0.25 |
| Cladding thickness, in. | approx 0.015 |
| Thermal flux preirradiation, Mwd/MT | 0 to 100,000 |
| Fast flux preirradiation, Mwd/MT | 20,000 to 100,000 |

The four initial series are identified as follows:

1. nonpreirradiated fuel with "standard" fuel pin design,
2. nonpreirradiated fuel with slump suppressors in the fuel pin,
3. thermal flux preirradiated fuel,
4. fast flux preirradiated fuel.

Important variables in these series are listed above.

A letter of intent to use the TREAT facility has been submitted to ANL; and material is being prepared for the preliminary proposal for Series I, which is tentatively scheduled for transient testing in two parts, one in June and another in October.

The capsule loadings planned for Series I are shown in Table 6.4. The results of the tests with capsules 1 through 6 should establish the comparative transient performance of low-density Sphere-Pac fuel and low- and high-density pellets. Capsules 7 through 9 will compare the transient performance of long fuel columns of low-density Sphere-Pac fuel

[redacted]

[redacted]



Table 6.4. Proposed Capsule Loadings for TREAT Series I[a] Experiments with Sol-Gel $(U,Pu)O_2$

| Capsule | Fuel Rod | Nominal Fuel Column Length (in.) | Nominal Fuel Smear Density (fraction theoretical) | Fuel Fabrication Form |
|---|---|---|---|---|
| 1 | A | 8 | 0.81 | Pellets |
| | B | 8 | 0.81 | Sphere-Pac |
| | C | 8 | 0.88 | Pellets |
| 2 | A | 8 | 0.81 | Pellets |
| | B | 8 | 0.81 | Sphere-Pac |
| | C | 8 | 0.88 | Pellets |
| 3 | A | 8 | 0.81 | Pellets |
| | B | 8 | 0.81 | Sphere-Pac |
| | C | 8 | 0.88 | Pellets |
| 4 | A | 8 | 0.81 | Pellets |
| | B | 8 | 0.81 | Pellets |
| | C | 8 | 0.88 | Pellets |
| 5 | A | 8 | 0.81 | Pellets |
| | B | 8 | 0.81 | Pellets |
| | C | 8 | 0.81 | Pellets |
| 6 | A | 8 | 0.88 | Pellets |
| | B | 8 | 0.88 | Pellets |
| | C | 8 | 0.88 | Pellets |
| 7 | A | 24 | 0.81 | Sphere-Pac |
| 8 | A | 24 | 0.81 | Pellets |
| 9 | A | 24 | 0.88 | Pellets |

[a]General fuel specifications for Series I: nominal fraction $(U,Pu)O_2$, 0.25; nominal oxygen-to-metal ratio, 1.98; cladding material, type 304 stainless steel; cladding outside diameter, 0.250 in.; cladding thickness, 0.016 in.; no preirradiation.

with low- and high-density pellets under identical transient conditions, within the limitations of TREAT to duplicate transients. The transients to be specified will be determined from reactor physics and transient heat transfer calculations.

[redacted]

Short-Term Irradiations (Rabbit Tests) (C. M. Cox)

The ORR rabbit facilities provide a relatively inexpensive means of performing short irradiations of controlled duration under essentially constant flux. We plan to perform a series of experiments to be used in conjunction with the instrumented capsule experiments to study the kinetics of grain growth and the effects of diametral gap, density, and a central void on fuel structural changes. We anticipate that approximately 50 rabbits with approximately 1-in. fuel columns will be irradiated next fiscal year.

Fast Flux Irradiation Tests of Sol-Gel $(U,Pu)O_2$ Fuels (A. R. Olsen)

A preliminary program involving two smear densities of 25% Pu fuel fabricated by both pelletizing and Sphere-Pac techniques has been outlined. The initial set of encapsulated fuel rods will provide burnups of 2, 8, and 10% FIMA. Some of these rods will subsequently be exposed to a transient in the TREAT facilities. We plan to operate at 16 kw/ft, the peak linear heat rating anticipated for FFTF driver fuels. This heat rating will provide a reasonable burnup rate.

The initial set will not provide a statistically proven fuel rod performance but will provide comparative performance data for the various fuel fabrication processes.

Gas-Cooled Fast Reactor Program (C. M. Cox)

Further work on the program proposed to obtain cladding compatibility data[11] has been postponed pending a definite funding allocation.

We reviewed the fuel element designs for the GGA reference design[12] (GCFR-4) and the "derated" design[13] (GCFR-4d) for an ORNL study in progress.[14] Steady-state temperature distributions were calculated with

---

[11] C. M. Cox, Fuels and Materials Development Program Quart. Progr. Rept. Sept. 30, 1967, ORNL-TM-2020, p. 26.

[12] A 1000-Mw(e) Gas-Cooled Fast Reactor Study for the Alternate Coolant Task Force, GA-7804 (July 21, 1967).

[13] Preliminary Development Plans for the Gas-Cooled Fast Reactor — General Atomic, GA-8257 (October 1967).

[14] L. L. Bennett, An Evaluation of Gas-Cooled Fast Breeder Reactors, ORNL-4206 (to be published).

the PROF computer program described later in this chapter; from them we concluded for both designs that programmed startups to allow fuel densification would be necessary to avoid central fuel melting. Application of Kennedy and Venard's instantaneous tube collapse curves for type 304 stainless steel[15] predicts instantaneous collapse of the cladding against the fuel for both the reference and derated designs as soon as coolant operating pressure and cladding operating temperature are established. If the collapsed cladding design is to be tolerated, it will be necessary to ascertain that the fuel offers sufficient support to keep the fuel pin distortion within acceptable limits.

Comparison of Neutron Cross Sections of Cladding Materials (C. M. Cox)

Cross-section data on proposed cladding materials for LMFBR and GCFR application are being studied. We are compiling composition, densities, and microscopic and macroscopic epithermal neutron-capture cross sections of types 304, 316, and 347 stainless steels; Inconel 600 and 625; Incoloy 800; Hastelloy X; 19-9 DL; and a number of vanadium, niobium, and iron alloys recently proposed for LMFBR applications.

Although a thorough evaluation for a specific reactor design would require determining the effect of the different cladding materials on the required fissile concentration, neutron energy spectrum, and breeding ratio, a comparative evaluation of the various materials can be based on their macroscopic neutron-capture cross sections in the neutron energy range 100 to 260 kev. This range includes the mean neutron energy and mean fission energy for essentially all fast breeder designs.

The data collection and calculations have been completed, and the final report is being prepared.

Irradiation Test Calculations (W. H. Pechin, C. M. Cox, R. B. Fitts)

A calculation procedure has been developed for irradiation tests. The preirradiation procedure consists of developing a flux-energy

[15] C. R. Kennedy and J. T. Venard, "Collapse of Tubes by External Pressure," pp. 421–422 in Developments in Theoretical and Applied Mechanics, Proceedings of the First Southeastern Conference, Vol. 1, Plenum Press, New York, 1963; ORNL-TM-166 (Apr. 17, 1962).

spectrum for the irradiation facility (unperturbed), solving the Boltzmann transport equation for the particular fuel to be placed in this flux to get fission rate as a function of radius, and calculating radial temperature distribution from the fission rate. Postirradiation procedures include calculation of burnup from analytical data and comparing observed microstructural changes with the calculated temperature profile.

The flux calculation, which is valid only for thermal reactors, is based on a thermal distribution for low energies, a "1/E" distribution for intermediate energies, and an exponential distribution for high energies. The parameters of these equations are adjusted to match the measured values of thermal flux, cadmium ratio, and fast flux.

ANISN is a FORTRAN IV code[16] based on the $S_n$ or angular augmentation solution of the Boltzmann equation for neutron transport. It has the advantages of not being subject to serious errors at material boundaries and it allows the inclusion of detailed cross sections as a function of neutron energy. In addition, a large number of small radial increments can be used in the calculation for a fuel rod, and the flux spectrum for an experimental position can be input directly as the source flux.

The fuel surface temperature is calculated by a BASIC language code,[17] GENGTC, which determines the temperature profile through the cladding and irradiation capsule for a given linear heat rating. The fuel surface temperature is then input to one of two other programs to calculate center-line temperature and temperature as a function of radius.

PETP is a program written in BASIC language to calculate the radial temperature profile for a cylindrical fuel element. The input includes fission rates as a function of radial increments. The heat generation

---

[16]W. W. Engle, Jr., A User's Manual for ANISN: A One-Dimensional Discrete Ordinate Transport Code with Anisotropic Scattering, K-1693 (March 30, 1967).

[17]H. C. Roland, GENGTC, A One-Dimensional CEIR Computer Program for Capsule Temperature Calculations in Cylindrical Geometry, ORNL-TM-1942 (December 1967).

for each increment is calculated by the program. The program calculates the temperature drop across each increment as a function of the heat generation in the increment and the total heat generation inside the inner radius of the increment. The thermal conductivity of the oxide fuels is assumed to be a constant below a given temperature, a linearly increasing value with temperature to a higher temperature B-2, and a constant value at temperatures above B-2. We are using 0.012 w $cm^{-1}$ $°C^{-1}$ below 1450°C and 0.021 w $cm^{-1}$ $°C^{-1}$ above 1750°C for sol-gel Sphere-Pac beds. These values are based upon preliminary out-of-reactor measurements for the low temperatures and available in-reactor data at the higher temperatures.

PROF is a BASIC computer program that uses the thermal conductivity function recently presented by Bailey et al.[18] to calculate the steady-state radial temperature distribution through a long cylindrical $(U,Pu)O_2$ fuel pin. The program first calculates the temperature distribution for as-fabricated fuel and then accounts for densification at operating temperatures by assuming a three-region fuel: columnar grains of 0.99 times theoretical density for temperatures 1900°C and above, equiaxed grains of 0.97 times theoretical density for temperatures 1400°C and above, and initial fuel density for temperatures below 1400°C. Changes in the radial heat generation distribution due to densification are estimated by assuming that the change in heat generation rate varies linearly with the change in fuel density. The central void diameter is predicted by a mass balance, neglecting axial transport of material.

A report outlining the current calculational techniques is in preparation.

---

[18]W. E. Bailey et al., "Thermal Conductivity of U-Pu Oxide Fuels," paper presented at the AIME 1967 Nuclear Metallurgy Symposium, Plutonium Fuels Technology, Phoenix, Arizona, Oct. 4–6, 1967.

# 7. WELDABILITY OF NICKEL-BEARING ALLOYS

G. M. Slaughter

The results of the hot-ductility tests on the experimental Incoloy 800 alloys were reported last quarter.[1] The presence of titanium and aluminum had lowered the zero-strength and zero-ductility temperatures (ZST and ZDT, respectively). We believe that this decrease is associated with a melting point depression. In addition, there was the surprising result that phosphorus and/or sulfur additions to titanium- and aluminum-bearing alloys had no systematic effect on hot ductility.

During the past quarter, we studied the effect of these additions on the microstructures of synthetic weld heat-affected zones. In addition, a sulfur-bearing alloy has been electron-beam microprobe analyzed.

## Metallographic Study

D. A. Canonico W. J. Werner

All of the alloys prepared for the hot-ductility investigation[1] have been studied metallographically; however, because they best illustrate the microstructural effects observed, only alloys Nos. 800-1 through 800-6, -11, -14, and -16 are included in this report. It is important to remember that in the hot-ductility test the specimens are heated by electric resistance. Therefore the fracture surface is heated to the highest temperature, and a slight thermal gradient exists axially along the specimen from this interface. The first six alloys contain only aluminum and titanium. The latter three contain (in addition to aluminum and titanium) sulfur, phosphorus, and combined sulfur and phosphorus, respectively.

---

[1]D. A. Canonico and W. J. Werner, Fuels and Materials Development Program Quart. Progr. Rept. Sept. 30, 1967, ORNL-TM-2020, pp. 98–102.

Aluminum and Titanium

Figure 7.1 illustrates the effect of increasing the amount of titanium and aluminum. It can be seen that titanium and aluminum tend to produce a laminated structure. Figure 7.1(a) (alloy 800-1) is a photomicrograph of the Fe—31.5% Ni—21.5% Cr ternary alloy with no added aluminum or titanium (< 0.05% Al and < 0.01% Ti). The microstructure is uncomplicated, the fracture appeared to be due to liquation, and no secondary cracks are visible. Alloy 800-2 [Fig. 7.1(b)] contained 0.13% Al and 0.095% Ti. Close observation of the microstructure, however, shows traces of laminations. Again no secondary cracks are evident. The remaining two alloys are more heavily laminated. Alloy 800-4 in Fig. 7.1(d) contains the highest percentage of aluminum and titanium (0.52 and 0.51%, respectively) and is by far the most laminated. Both alloys failed intergranularly and both contained secondary intergranular cracks.

A grain-size difference can be seen between the first and last pairs of samples. This is in part due to the temperatures to which they were heated during testing (the first pair had a ZST of about 2450°F, whereas the last had ZST's closer to 2400°F).

The mode of failure in this series of tests appears to be element dependent. Figure 7.2 compares two aluminum-rich and titanium-rich experimental Incoloy 800 alloys that have been heated to their ZST, 2400°C. The aluminum-rich alloy (800-8) in Fig. 7.2(a) appears to be more banded. Liquation within the bands adjacent to the fracture interface is evident. When the alloy is titanium rich, as is the case with alloy 800-6, there is less tendency for laminae to form, and the failures tend to be intergranular (there is evidence of grain-boundary embrittlement).

Influence of Sulfur and Phosphorus

Alloys 800-11, -14, and -16 all contain nominally 0.38% Al and 0.38% Ti. These alloys have all been heated and tested at 2400°F (their ZST) and Fig. 7.3 shows the resulting microstructures. The addition of sulfur resulted in precipitates that tended to align themselves in the

[redacted]



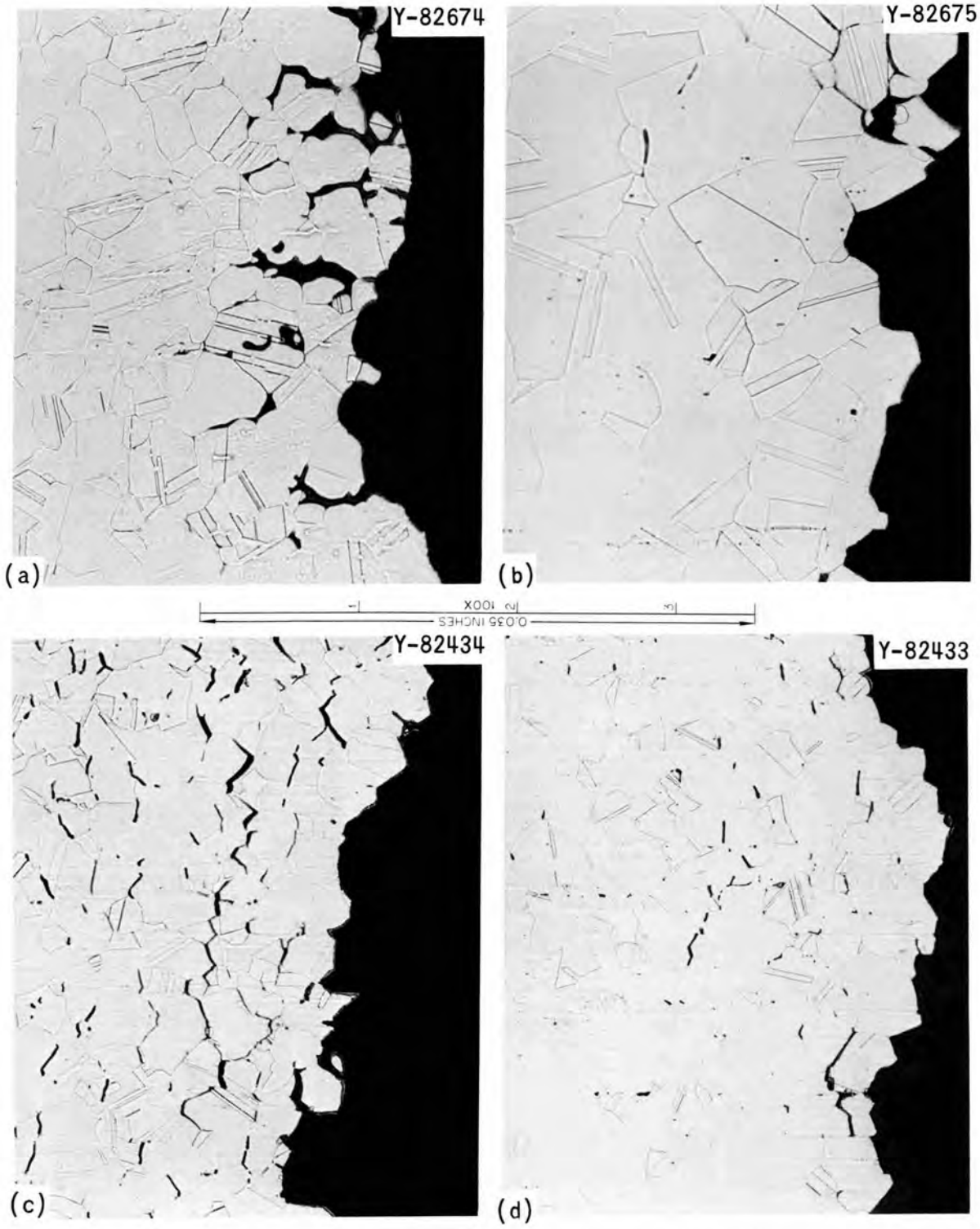


Fig. 7.1. Effect of Titanium and Aluminum on the Microstructure of Simulated Heat-Affected Zones in Experimental Incoloy-800 Alloys. (a) Simple Fe-Ni-Cr ternary. (b) 0.13% Al and 0.095% Ti added. (c) 0.43% Al and 0.44% Ti added. (d) 0.52% Al and 0.51% Ti added.

[redacted]

OFFICIAL USE ONLY



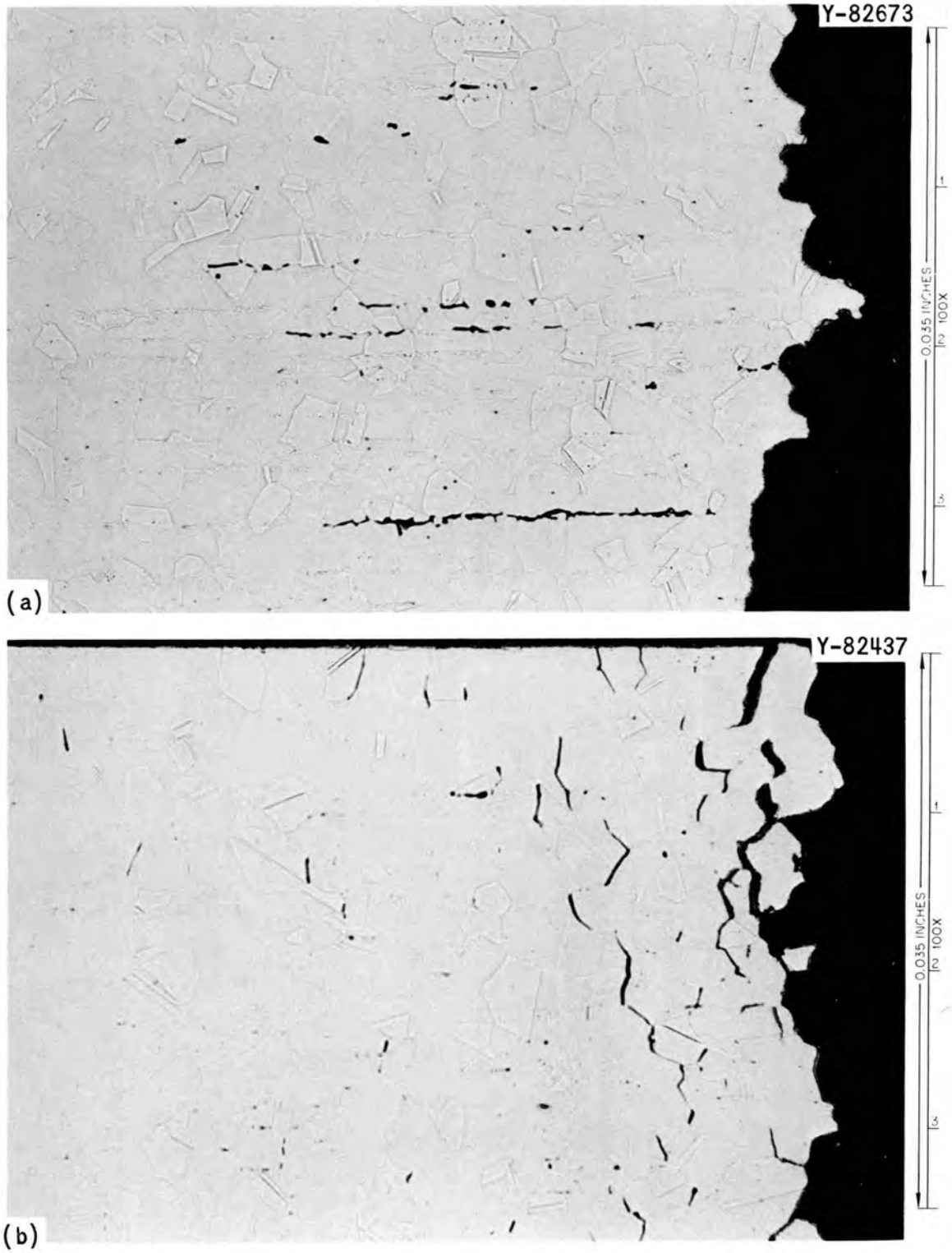


Fig. 7.2. The Effect of Titanium and the Effect of Aluminum on the Simulated Heat-Affected Zone Microstructure of Experimental Incoloy-800 Alloys. (a) Ternary composition with 0.54% Al and 0.35% Ti. (b) Ternary composition with 0.35% Al and 0.54% Ti.

OFFICIAL USE ONLY

[redacted]



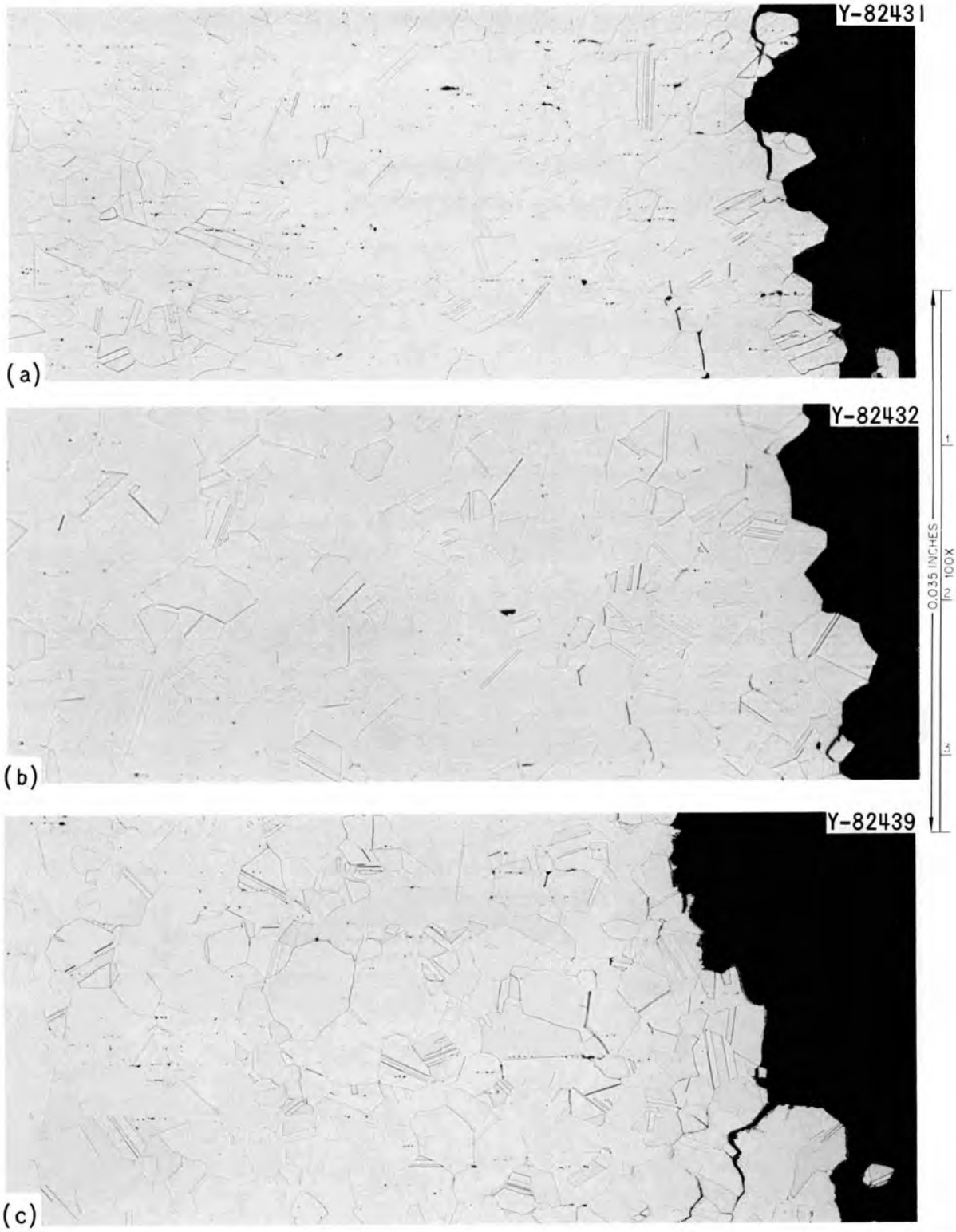


Fig. 7.3. The Effect of Sulfur and/or Phosphorus on the Simulated Heat-Affected Zone Microstructure of Experimental Incoloy-800 Alloys. In addition to the Fe-Ni-Cr ternary, the alloys contained a nominal 0.38% Al, 0.38% Ti, and (a) 0.015% S, (b) 0.002% S, 0.015% P, (c) 0.010% S, 0.013% P.

[redacted]

[redacted]



original rolling direction, as is evident in Fig. 7.3(a). The failure was intergranular; however, when compared to alloy 800-3 [Fig. 7.1(c)], which also contained a nominal 0.38% Al and 0.38% Ti, there is an evident difference. Figure 7.1(c), although exhibiting very slight laminations, does not reveal any precipitate comparable to that seen in Fig. 7.3(a).

Over the ranges studied, the addition of phosphorus to the nominal 0.38% Al and 0.38% Ti alloys does not appear to affect the tendency toward grain-boundary embrittlement. This observation is based on a comparison between Figs. 7.3(b) and 7.1(c). The laminae present in Fig. 7.1(c) are present in 7.3(b) and, indeed, appear to be unaffected by the presence of phosphorus. If the secondary intergranular cracks in Fig. 7.1(c) are ignored, then the two structures are quite similar.

Adding equal amounts (approx 0.01%) of both sulfur and phosphorus to the nominal 0.38% Al and 0.38% Ti alloys resulted in the structure seen in Fig. 7.3(c), which is quite similar to that in Fig. 7.3(a). The laminae seen in both Figs. 7.3(b) and 7.1(c) are not present here; however, an aligned precipitate, less in amount than in Fig. 7.3(a), is evident. The presence of sulfur, either with or without phosphorus, apparently reduces the tendency toward the formation of laminae; however a precipitate aligned in the original rolling direction is present.

Due to the apparently innocuous effect of sulfur and phosphorus on the ZST and ZDT, we suggested[2] that perhaps the sulfur and phosphorus were combining with the titanium and aluminum. A table of free-energy-of-formation values for sulfides was included in support of that argument. The tendency toward precipitation seen in Figs. 7.3(a) and (c) and the minimization (if not elimination) of secondary intergranular cracks in Fig. 7.3(b) add credence to this suggestion.

## Microprobe Studies

To determine the composition of the precipitate seen in the sulfur-containing alloy, an electron-beam microprobe analysis was conducted.

---

[2]D. A. Canonico and W. J. Werner, Fuels and Materials Development Program Quart. Progr. Rept. Sept. 30, 1967, ORNL-TM-2020, pp. 98–102.

[redacted]

[redacted]



Four areas were analyzed: (1) the matrix, (2) large precipitate particles, (3) stringers [such as are seen in Figs. 7.3(a) and (c)], and (4) grain boundaries (both those with and without precipitate). The analysis was for four elements: Al, Ti, P, and S. No phosphorus segregation was detected; however, this was expected because its level was less than 0.001% in the alloy analyzed.

Table 7.1 contains the results of this analysis. It is evident that the precipitate particles in the stringers are enriched in aluminum, titanium, and sulfur. The precipitate in the grain boundaries showed definite titanium and sulfur enrichments; however, because of small particle size in relation to the size of the beam, the actual magnitudes are not precise. The large precipitate particles noted in the table are the pink-colored, angular intermetallics often seen in titanium-containing alloys (these are usually titanium carbonitrides).

Table 7.1. Electron-Beam Microprobe Analysis of an Experimental Incoloy 800 Alloy that Contained Aluminum, Titanium, and Sulfur

| Area | Chemical Composition, wt %[a] | | |
|---|---|---|---|
| | Aluminum | Titanium | Sulfur |
| Matrix | 0.2 | 0.2 | x |
| Large precipitate particles | 0.7 | 80.8 | x |
| Stringers[b] | ≥ 25x | ≥ 36x | > 10x |
| Grain boundaries[c] | | | |
| with precipitates | Same | Increase | Increase |
| without precipitates | Same | Slight increase | Depletion |

[a]x represents nominal content in matrix.

[b]Semiquantitative.

[c]Qualitatively compared to matrix.

The results of the microprobe analysis lends further evidence that the titanium, aluminum, or both, are associated with the sulfur and prevent the usual deterioration that accompanies sulfur additions to nickel-containing alloys.

[redacted]

The S-Ti-Al-P-bearing Incoloy-800 alloys all had ZST's (which in our study coincided with the liquation temperature) in the vicinity of 2400°F. Some recent unpublished work at Rensselaer Polytechnic Institute on 18% Ni maraging steels (which contain titanium and residual sulfur) showed that a precipitate identified as a titanium sulfide began to liquate at about 2400°F. Our findings seem to agree quite well with those results.

## Special Alloy Fabrication

R. E. McDonald W. J. Werner
D. A. Canonico

To obtain more information on the studies reported above, additional alloys are being fabricated. These alloys are:

| Alloy | Additive, wt % |
|---|---|
| 800-17 | 0.38 Al |
| 800-18 | 0.38 Ti |
| 800-19 | 0.015 S |
| 800-20 | 0.015 P |
| 800-21 | 0.015 S, 0.015 P |

These alloys were formulated in order that sulfur and/or phosphorus effects can be investigated without the contributory influences of titanium and/or aluminum. In addition, alloys containing only aluminum or titanium are being fabricated to determine whether or not the microstructural effects seen in Fig. 7.2 are element dependent as indicated or whether there is a synergistic effect due to the presence of the second element.

[redacted]



# 8. ZIRCONIUM METALLURGY

P. L. Rittenhouse

Zirconium-base alloys are used extensively as fuel cladding in nuclear reactors. Although these alloys have relatively low neutron cross sections, economics dictates that we use the minimum amount of material consistent with service requirements. Rather then designing fuel element cladding on the basis of lowest strength values, as is presently done, we are attempting to control texture and thereby match the strongest direction in the material against the highest service stresses. This will permit use of thinner cladding for comparable conditions or allow longer service life and/or higher operating temperature.

## Tubing Test Program

P. L. Rittenhouse

Several Zircaloy tubing specimens have been tested under internal pressure to check the performance of the hydraulic and electronic systems of the biaxial testing machine. Both systems performed satisfactorily, as did the new diametral strain gage. Additional machined specimens have been received from the shops and are now being fitted with pressure closure flanges.

A program has been written for our desk-top computer to speed calculation of test instructions and analysis of the experimental data. In the series of tests planned the tangential-to-axial stress ratio will be varied from infinity to less than one half.

## Knoop Microhardness Analysis of Texture Changes During Tubing Fabrication

P. L. Rittenhouse

In the past we acquired several experimentally produced lots of "tube reduced" Zircaloy tubing. At the same time we obtained tapered

[redacted]

[redacted]



lengths of tubing taken from the reducing dies. These pieces contain the complete reduction history for each tube reduction pass. A wall section of tubing showing the profile of the working dies and the mandrel is presented in the top of Fig. 8.1. Each tapered length was cut at points corresponding to no reduction, total reduction, and at one or more intermediate reductions. These specimens were annealed and then mounted to permit Knoop microhardness to be measured on the surface perpendicular to the tube axis. The reference directions chosen were the radius and the tangent (radial, R, and tangential, $\theta$, directions, — see lower right of Fig. 8.1). Measurements were made with the long axis of the indenter parallel to R ($\phi$ = 90°), parallel to $\theta$ ($\phi$ = 0°), and at two intermediate positions — see Fig. 8.1 lower center. We reported

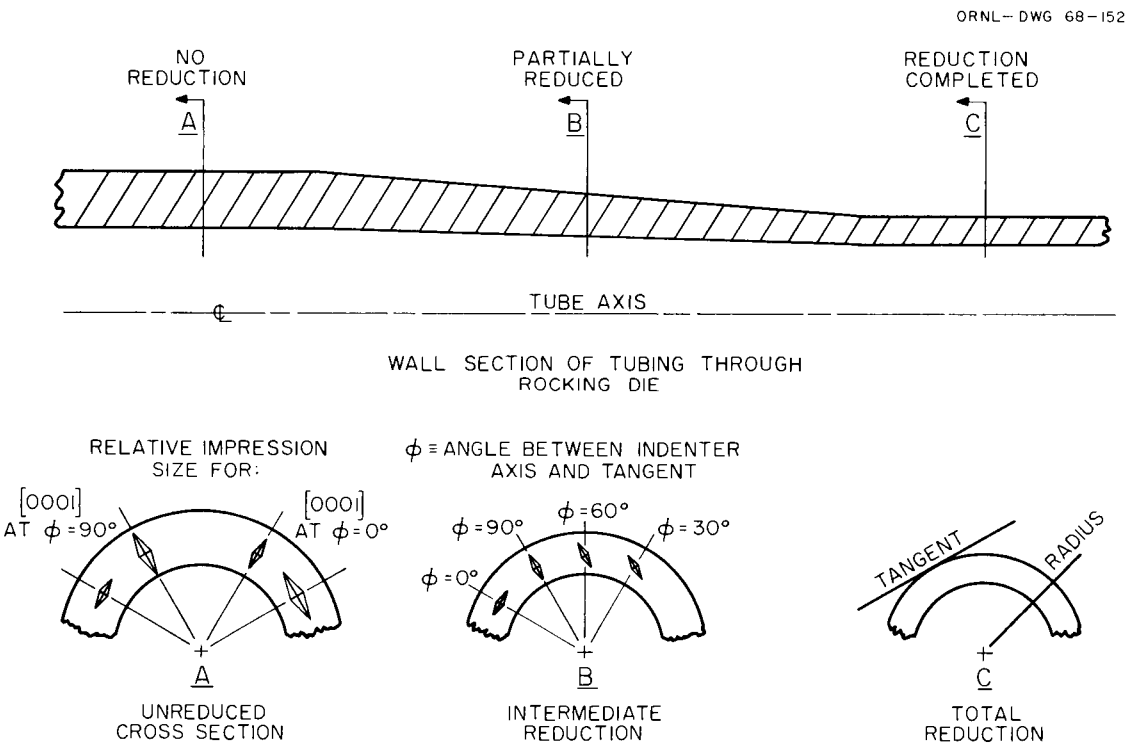


Fig. 8.1. Sections of Tube-Reduced Zircaloy.

[redacted]

previously[1,2] the relationship between the Knoop microhardness number (KHN) and impression size and the orientation of the basal pole. For example, if a greater number of basal pole traces are parallel to R than to $\theta$, the KHN for $\phi = 90°$ will be less than for $\phi = 0°$.

Knoop microhardness is shown as a function of indenter orientation in Fig. 8.2 for five tapered-die lengths. Data are shown for several degrees of reduction in area $R_A$ in each instance. The initial and final outside and inside diameters and the Q number for the reduction are indicated on the individual figures. The Q number, an important fabrication variable, is the ratio of wall-to-diameter reduction.

For the tube reduction pass with Q = 0, Fig. 8.2(a), the KHN of the starting material ($R_A = 0\%$) was essentially constant for all orientations on the surface examined. Notice, however, that the KHN at $\phi = 0°$ ($KHN_\theta$) and $\phi = 30°$ decreases with increasing $R_A$ while that in R ($KHN_R$) and at $\phi = 60°$ increases. This indicates that the number of basal poles inclined toward $\theta$ is increasing at the expense of those originally closer to R as the reduction progresses. This is also true when Q = 1.1, Figs. 8.2(b) and 8.2(c). For Q = 1.7 and 2.6, however, the reverse is true, Figs. 8.2(d) and 8.2(e).

Figures 8.3(a) and 8.3(b) show the changes in KHN at $\theta$ and R, $\Delta[KHN]_\theta$ and $\Delta[KHN]_R$, as a function of $R_A$ for the various Q's. Positive values of $\Delta[KHN]_\theta$ or negative values of $\Delta[KHN]_R$ show that the basal pole intensity in the radial direction is increasing with reduction in area. This method of KHN analysis provides a simple and rapid qualitative method of following the combined effects of Q number and reduction in area on texture during the fabrication process.

---

[1]P. L. Rittenhouse and M. L. Picklesimer, "Comparison of Pole-Figure Data Obtained by X-Ray Diffraction and Microhardness Measurements on Zircaloy-2," Trans. Met. Soc. AIME 236, 496–501 (April 1966).

[2]P. L. Rittenhouse and M. L. Picklesimer, Fuels and Materials Development Program Quart. Progr. Rept. June 30, 1964, ORNL-TM-920, pp. 60–66.

[redacted]



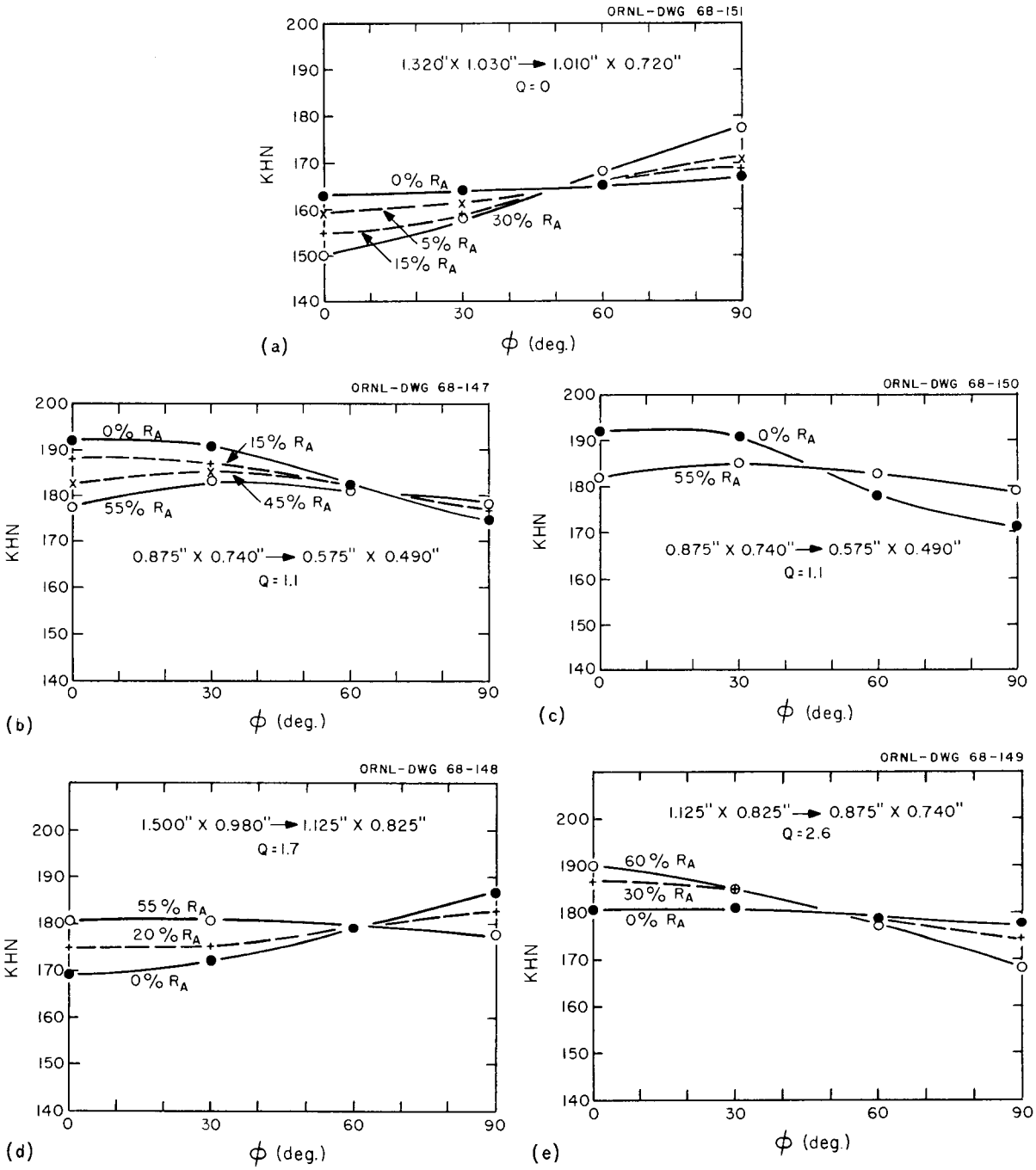


Fig. 8.2. Knoop Hardness Number as a Function of Indenter Orientation for: (a) Q (ratio of wall to diameter reduction) = 0, $R_A$ (reduction in area) = 0, 5, 15, and 30%; (b) Q = 1.1, $R_A$ = 0, 15, 45, and 55%; (c) Q = 1.1, $R_A$ = 0 and 55%; (d) Q = 1.7, $R_A$ = 0, 20, and 55%; (e) Q = 2.6, $R_A$ = 0, 30, and 60%.

[redacted]

[redacted]



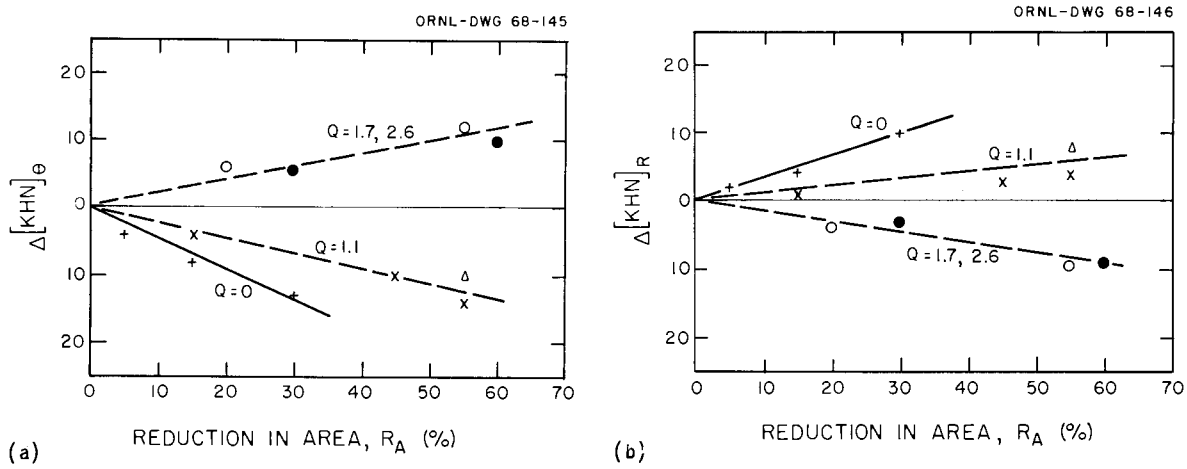


Fig. 8.3. Change in Knoop Hardness Number with Reduction in Area. (a) Parallel to the tangential direction for all Q's. (b) Parallel to the radial direction for all Q's.

## Tubing Fabrication Study

P. L. Rittenhouse

Because the anisotropy of physical and mechanical properties of zirconium and its alloys is highly texture sensitive, it is often desirable to control the texture of products fabricated from these materials. We know that the texture at each intermediate stage of fabrication is a function of all the fabrication steps that have preceded it. To achieve texture control we must know the contribution that each step in the procedure makes to the final texture. In any particular reduction step the texture developed depends on both the texture of the starting material (past history) and the deformation state characteristic of the reduction operation. If one has a final tube size and texture in mind, it should be possible to obtain the desired end product by some definite sequence of fabrication steps.

A typical fabrication procedure for zirconium alloy tubing will consist of the following:

1. melt and cast 14-in.-diam ingot,
2. forge to 6.5 in. square, 1800 to 1900°F,
3. forge to 4.75 in. octagon, 1800 to 1900°F,
4. forge to 4.5 in. round, 1350 to 1500°F,

[redacted]

5. extrude to 1.5 in. diam × 0.25 in. wall, 1200 to 1450°F,
6. tube reduce, draw, or swage to final size (typically 0.5625 in. diam × 0.0312 in. wall for fuel cladding), cold with intermediate anneals.

We started our study by machining extrusion billets from 4-in.-diam forged Zircaloy-4 bar. Extrusion should yield about 55 ft of 1.5-in.-OD × 1-in.-ID tube stock. Fabrication schedules have been designed incorporating tube reduction, drawing, and swaging. At each step in the fabrication schedule specimens will be taken for texture determination by x-ray diffraction. Mechanical property specimens of the final product and the smaller sizes of the intermediate stages will also be taken, and a full range of biaxial tests will be performed to determine yield behavior. In this way we can determine the effect of starting texture and the various fabrication variables on the texture, properties, and quality of the final product, whatever the desired final size.

We should be able to determine the effect of: (1) fabrication technique (e.g. tube reduction vs drawing with their different deformation states); (2) reduction in area per step; (3) total and final Q number and the sequence in which Q is varied; (4) intermediate annealing temperature; and (5) perhaps, lubrication. We will also seek to evaluate the fabrication schemes in terms of mill yield, mill economy, quality (surface and internal defects), and reproducibility of texture and properties.

Combinations of fabrication techniques have been chosen for study because they provide a wider range of variables for examination and because it is entirely possible that a combination of techniques may yield a superior product. For instance, tube reduction might be specified for economy of gross reduction with ball swaging used for final texture control and surface finish. We also plan to examine texture variation (see ref. 3 and next section) in tubing and in the tube shell. We will study how the various fabrication techniques accentuate or eliminate these texture variations.

---

[3]P. L. Rittenhouse and D. O. Hobson, Fuels and Material Development Program Quart. Progr. Rept. Sept. 30, 1967, ORNL-TM-2020, pp. 85–89.

[redacted]



In summary, this program on the fabrication of zirconium alloy tubing will: (1) show in detail how fabrication events affect texture; (2) allow control of texture in the finished product; and (3) demonstrate the most economical and efficient method of tube production.

## Circumferential Texture Variations in Zircaloy Tubing

P. L. Rittenhouse D. O. Hobson

In a previous report of this series[3] we discussed the various cross-section shapes obtained on tensile testing Zircaloy tubes. We showed that these shapes were associated with a circumferential variation in texture and suggested how this variation might result from texture inhomogeneities in the starting material and/or peculiarities of certain fabrication techniques. Before discussing some additional experimental verification for our suggestion it may be profitable to illustrate how these texture variations might influence the behavior of the tubing.

An important consideration in the use of Zircaloy tubing for fuel cladding is the orientation that the hydride will assume relative to the tensile hoop stress that is caused by fission-gas pressure. The ductility of the tubing is reduced drastically if the hydride precipitates perpendicular to the hoop stress direction, that is, parallel to the tubing radius. This is generally the hydride orientation observed when basal poles are oriented parallel to the tangential direction (circumferentially). However, a texture with basal poles parallel to the radius promotes circumferentially oriented hydride, the least harmful orientation. Suppose that the average texture of the tubing, or the texture in the area selected for examination, indicates that circumferential hydride will predominate, but that in certain areas the texture is actually tangential. Although nearly all the hydride may be oriented so as to be innocuous, the hydride in the area of texture variation will be as effective in reducing ductility as if all were oriented radially (i.e., the least ductile point will determine the ductility of the tubing).

Texture is first formed during the solidification of the ingot. Modification of this texture occurs when the ingot is forged to bar.

[redacted]

[redacted]



We have examined a cross section from a forged 4-in.-diam Zircaloy-4 bar to determine the texture at various positions on the cross section. The section was cut into 1-in. × 1-in. specimens as shown in Fig. 8.4. The (0001), $\{10\bar{1}0\}$, and $\{11\bar{2}0\}$ pole figures were determined on each specimen with a Philips pole figure device. All specimens were oriented to the same reference direction relative to themselves and to the pole figure device. The (0001) pole figures were integrated into a single pole figure that approximates the overall or average texture of the cross section. This is shown in Fig. 8.5. The texture is rather mild with only two small texture peaks, one spreading from 2 o'clock and one from 7 o'clock. Notice, however, that the position and intensity of the peaks for the individual sections vary considerably. These sections, except for No. 1 which is removed on machining the tube blank, will subsequently form different parts of the wall of the tube. Therefore, the texture and texture variation around the outer part of the forging are more important considerations than the overall texture.

Another cross section of the 4-in. bar will be mounted on an x-ray diffractometer so that conditions are right for diffraction from an area

ORNL-DWG 68-153

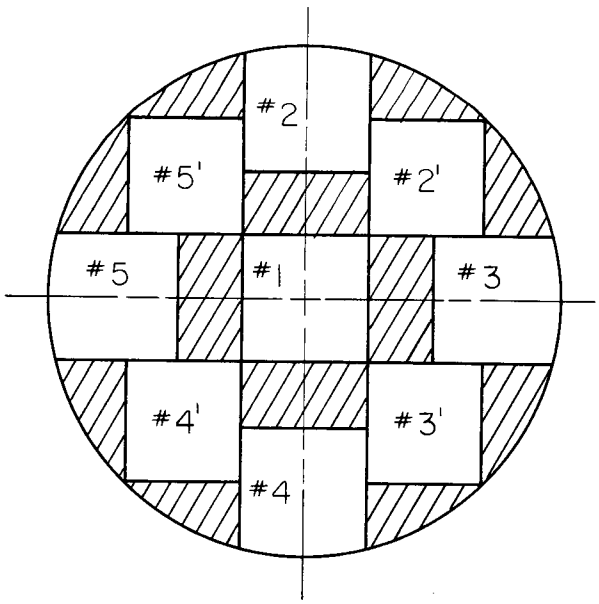


Fig. 8.4. Scheme for Cutting X-Ray Diffraction Specimens from Cross Section of Zircaloy Bar.

[redacted]

[redacted]



ORNL-DWG 68-144

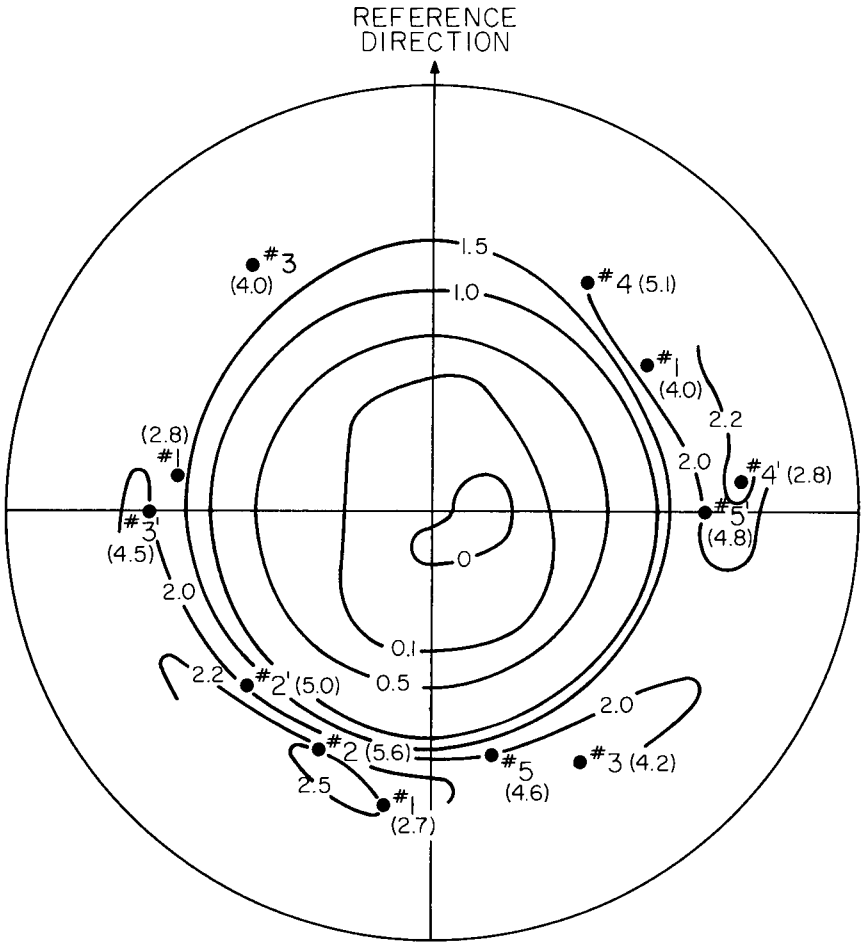


Fig. 8.5. Basal Pole Figure for Zircaloy Bar. The relative basal pole intensity is shown by the numbers associated with the contour lines. The small filled circles are the positions of the peaks for the individual specimens (Nos. 2–5 and 2′–5′). The intensity associated with each peak is shown in parentheses.

on the outer circumference of the bar. This disk will be rotated to give a more accurate description of the distribution of selected crystallographic poles around the circumference. The diameter of the disk will be reduced and the experiment repeated.

[redacted]

## Texture Development in Single-Crystal Zirconium

D. O. Hobson

We reported previously on the effects various fabrication procedures have on the textures of single crystals of zirconium.[4,5] The data were obtained by back-reflection Laue techniques that give only a qualitative idea of the distribution of poles that constitute the texture. A more accurate indication of the textures existing in the rolled specimens has been gained by using a Philips pole figure device that can measure the distribution of a crystallographic pole out to an angle of 75° from the normal to the surface being examined. The more complete data have changed none of the conclusions reached earlier. Rather, they have allowed a more precise determination of the deformation sequences that lead to the final textures.

Figure 8.6, for a single-crystal specimen with the basal plane in the rolling plane and the $[11\bar{2}0]$ direction in the rolling direction, illustrates one sequence of the twinning operations possible under rolling conditions. The figure shows first-, second-, and third-order twinning. Figure 8.7 illustrates all the possible basal pole positions that could result from first- and second-order twinning with all possible sequences operative. Third-order twinning would put additional poles within 10° of the initial pole position. Figure 8.8 shows the texture that resulted from a 20% reduction of this specimen. All pole positions can be explained as resulting from the twinning discussed above. Higher rolling reductions of this specimen gradually shifted basal pole positions toward the ideal rolling texture for zirconium. Specimens of other starting orientations were as easily explained by evoking known deformation systems.

In every case examined rolling was operationally equivalent to simple simultaneous compression in the thickness direction and extension

---

[4] D. O. Hobson, Fuels and Materials Development Program Quart. Progr. Rept. June 30, 1967, ORNL-TM-1941, pp. 57–62.

[5] D. O. Hobson, Fuels and Materials Development Program Quart. Progr. Rept. Sept. 30, 1967, ORNL-TM-2020, pp. 89–92.

[redacted]



ORNL-DWG 67-12047

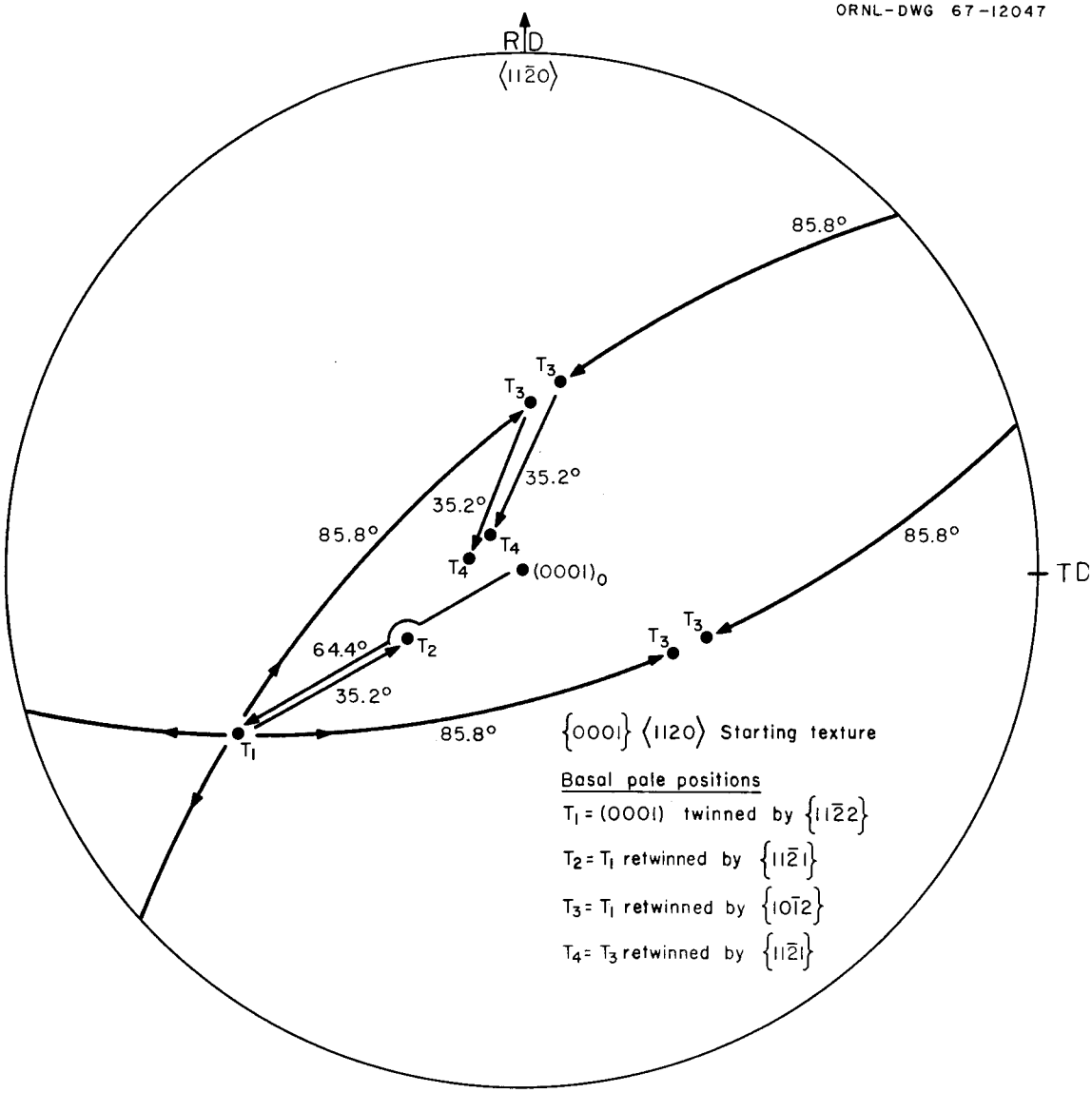


Fig. 8.6. A Typical Sequence of Twinning Operations During the Rolling of a (0001) ⟨11$\bar{2}$0⟩ Specimen.

in the rolling direction. In all likelihood, the ability to twin allowed the deformation to extend completely through the specimen thickness during the initial rolling pass, thus producing the texture change before inhomogeneities in flow could affect the result. Subsequent rolling passes would see a new texture that is relatively stable to deformation by continued rolling. The present work has shown that all major textural changes occur quite rapidly, mainly by twinning, and are

[redacted]

[redacted]



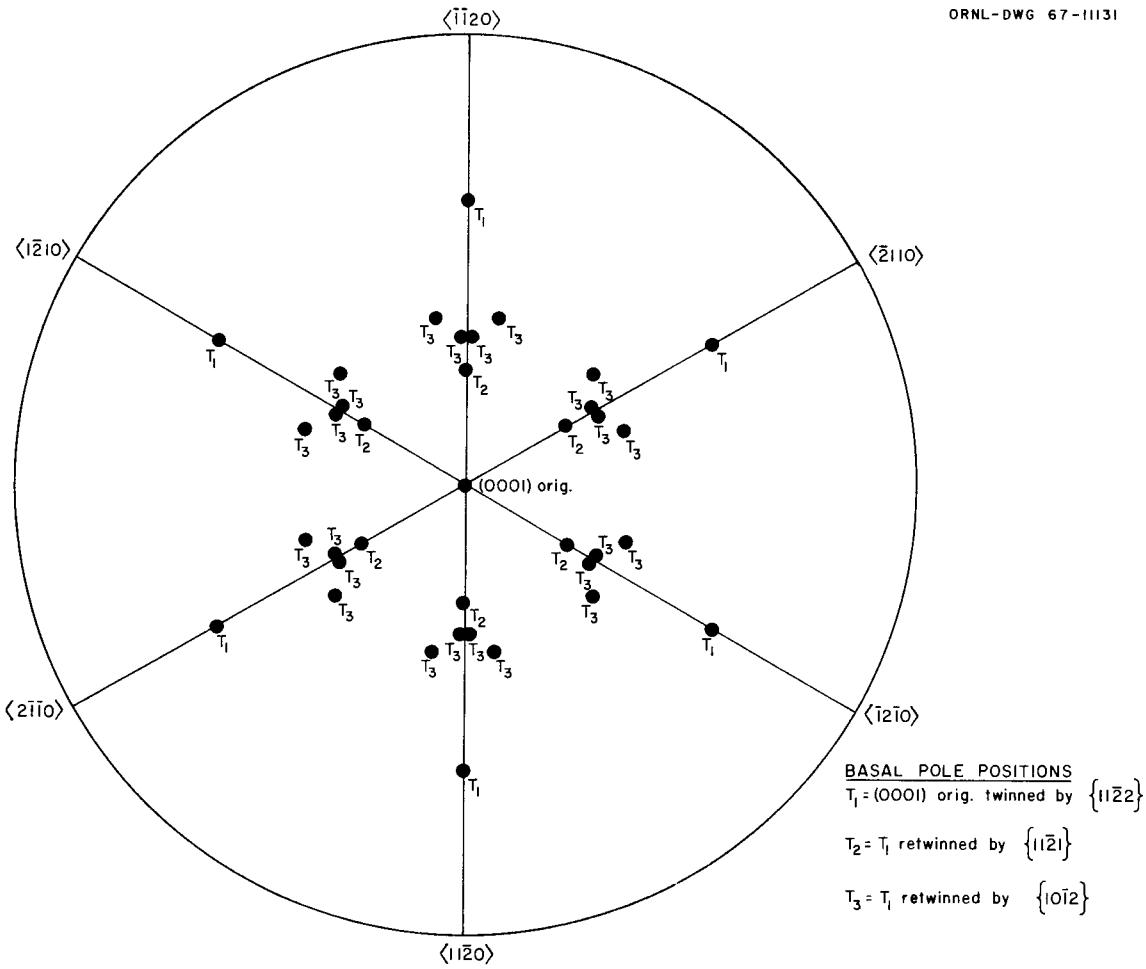


Fig. 8.7. Basal Pole Positions Resulting from First- and Second-Order Twinning in (0001) ⟨11$\bar{2}$0⟩ Rolling Specimen.

completed early in the deformation process. This new texture is generally quite close to the final texture. The final perfecting of the textures occurs rather slowly during the later higher reductions.

Perhaps the chief significance of this work is that it gives a clue to the behavior of polycrystalline materials under similar stress conditions. We infer, from work by Reed-Hill[6] and unpublished work by the author, that polycrystalline zirconium behaves as if each grain were a single crystal, which, under the applied stress, deforms similarly to

[6]R. E. Reed-Hill, "Role of Deformation Twinning in the Plastic Deformation of a Polycrystalline Anisotropic Metal," pp. 295–330 in Deformation Twinning, Gordon and Breach, New York, 1964.

[redacted]

[redacted]



ORNL-DWG 67-11124

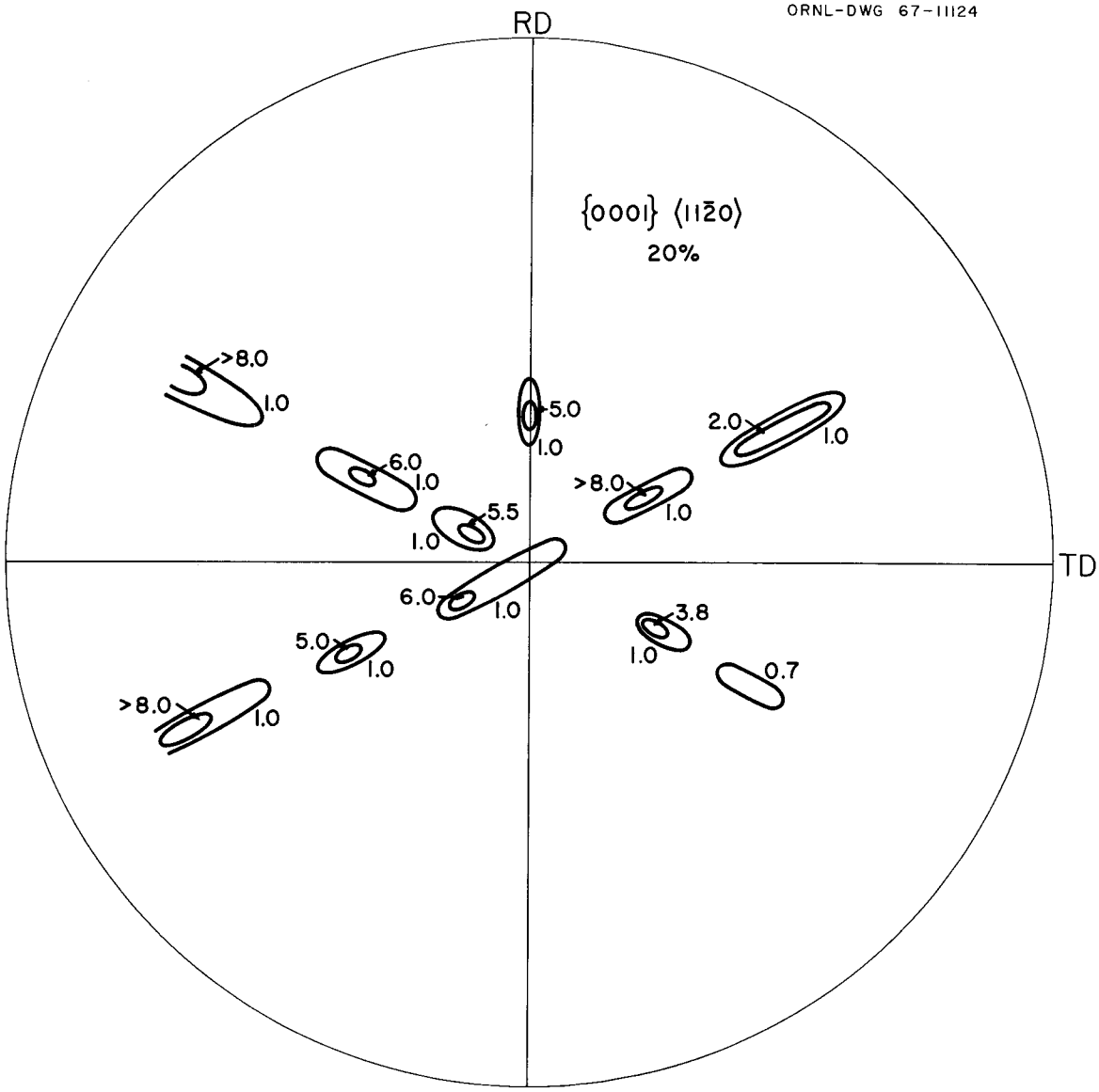


Fig. 8.8. Basal Pole Figure for (0001) ⟨11$\bar{2}$0⟩ Rolling Specimen After 20% Reduction.

the crystals described above. Large-grained material deforms so that grain interactions are confined to regions near the grain boundaries, leaving the main grain volumes to deform according to the applied stress. If these criteria are approximated for fine-grained material, we should be able to predict the texture that will result from any series of fabrication events.

[redacted]

[redacted]



# Corrosion of Zirconium Alloys

J. C. Wilson

All investigation of the oxidation anisotropy and corrosion inhibition of zirconium and its alloys has been terminated. Several topical reports and papers on these subjects are being prepared and will be released during the early part of 1968.

[redacted]

[redacted]

# PART II.

# REACTOR CHEMISTRY DIVISION

[redacted]

[redacted]

[redacted]

[redacted]



# 9. FISSION-GAS RELEASE AND PHYSICAL PROPERTIES OF FUEL MATERIALS DURING IRRADIATION

R. M. Carroll R. B. Perez
G. M. Watson J. G. Morgan
O. Sisman

Fission-gas release from $UO_2$ is being studied in an effort to determine the mechanism by which the gas migrates and escapes from the fuel. From these studies we hope to develop a model to make engineering calculations of noble-gas escape from operating fuel materials. Our experimental method is to irradiate carefully selected and characterized specimens in a facility where the neutron flux and temperature are controlled independently. Fission gas released from the specimen is entrained in a moving stream of sweep gas and carried outside the reactor, where it is analyzed by gamma-ray spectrometry.

A defect-trap model of fission-gas release has been developed, and two methods are used to evaluate the coefficients of the mathematical version of the model. One is the steady-state method, wherein the gas release is measured while irradiation conditions are constant. In the other method, the specimen is oscillated sinusoidally in the reactor so as to oscillate the neutron flux and the specimen temperature. Waves of fission-gas release are produced by the oscillations, and analyses of these waves add an extra degree of freedom for fitting the model to the data.

This perturbation method offers promise of being a good way to measure thermal diffusivity during irradiation, since the time lag between a change of fission heating and the resultant change of temperature depend on the thermal diffusivity of the specimen. For this reason, hollow-cylinder specimens of single-crystal and fine-grain $UO_2$ have been used to develop the instrumentation and techniques for in-reactor thermal diffusivity measurements.

[redacted]

## Steady-State Fission-Gas Release from $UO_2$ at High Temperature

As now formulated, the mathematical equations for the defect-trap model apply only to temperatures at which clusters of defects do not migrate, for $UO_2$ below about 1100°C. To obtain information at higher temperatures, single-crystal (experiment C1-19) and fine-grain (experiment C1-20) specimens were irradiated at temperatures ranging to 1700°C. Both types of specimens showed gas release that was characteristic of small cluster migration in the temperature range 1100 to 1600°C. The fine-grain specimen showed increased gas release at 1700°C, which is interpreted as caused by grain growth.[1] The temperature dependence for gas release from the single-crystal $UO_2$ did not change up to 1700°C.

At temperatures of 1600°C and above, bursts of gas were released by both specimens during steady-state operation. When the fine-grain specimen was cooled by removal from the neutron flux, a large burst of gas resulted (see Fig. 9.1). Iodine was also released in this burst so that more $^{135}Xe$ was being released after withdrawal than just before (because of iodine decay into xenon). We think the spontaneous bursts are caused by the collection of gas into large defect traps near the specimen surface, where enough pressure is eventually generated to cause microcracks.[1] A temperature of about 1600°C appears to be necessary to allow the formation of these large traps. Internal pressures and thermal stresses during cooling caused microcracks, resulting in the large cooling burst. After the initial cooling burst, following the 1600 to 1700°C irradiation, a second spontaneous burst was observed (see Fig. 9.1). This was likely caused by the decay of trapped iodine into xenon, the increased pressure causing a microcrack.

The change in the gas-release mechanism at 1700°C for the fine-grain specimen (C1-20) is shown in Fig. 9.2. The gradual increase of fission-gas release over a five-day period at 1700°C would seem to

---

[1]R. M. Carroll, J. G. Morgan, R. B. Perez, O. Sisman, and G. M. Watson, Fuels and Materials Program Quart. Progr. Rept. Sept. 30, 1967, ORNL-TM-2020, pp. 107–116.

[redacted]



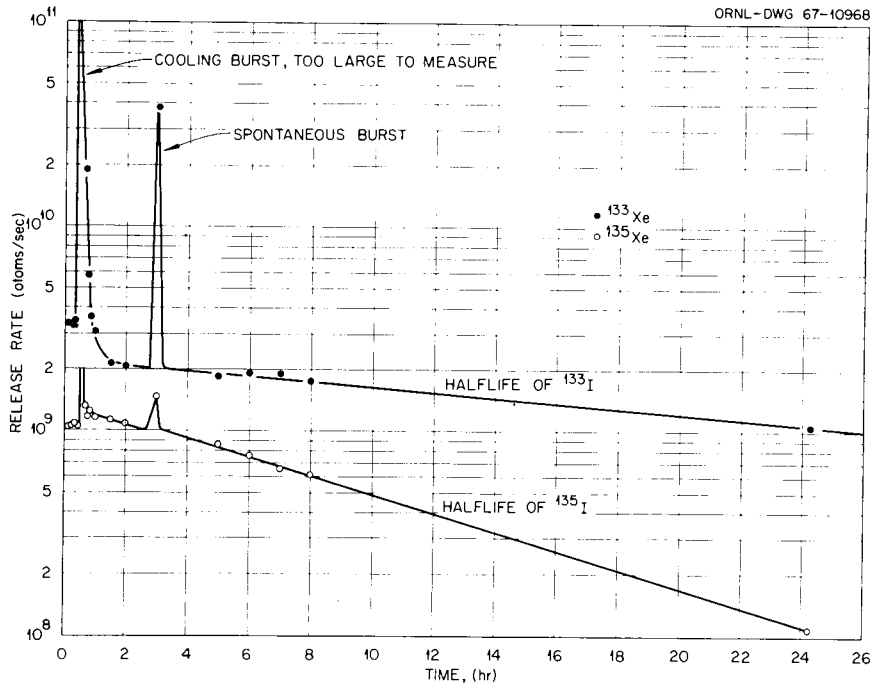


Fig. 9.1. Xenon-133 and Xenon-135 Release When Fine-Grain Specimen (C1-20) Was Withdrawn from Neutron Flux After Five Days Irradiation at 1700°C and a Flux of $6.0 \times 10^{13}$ Neutrons $cm^{-2}$ $sec^{-1}$.

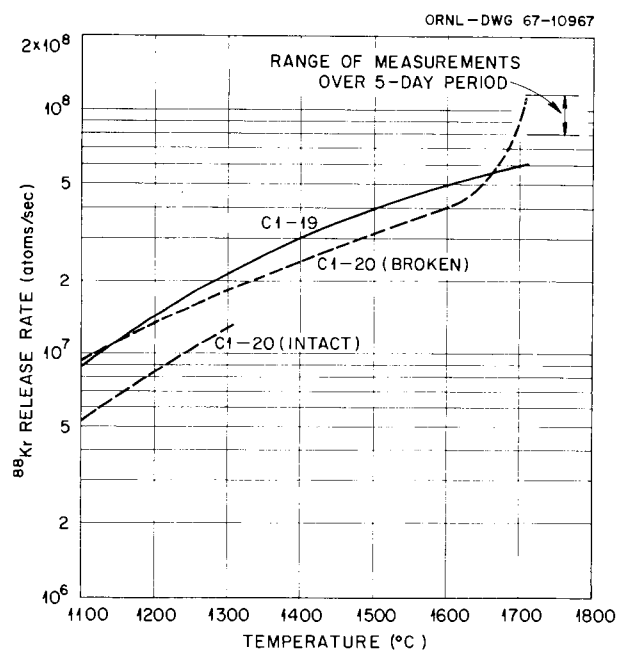


Figure 9.2. Comparison of High-Temperature Release from Single-Crystal (C1-19) and Fine-Grain (C1-20) Specimens of $UO_2$.

[redacted]

indicate grain growth. After the 1700°C run was terminated, resulting in the cooling burst shown in Fig. 9.1, the specimen was irradiated again in the 1100 to 1300°C temperature range. We had expected that the grain growth would affect the subsequent fission-gas release rate, but we were surprised to find that the gas release was lower, corresponding to the "Cl-20 (intact)" section of Fig. 9.2.

After 10 days irradiation at a neutron flux of $3 \times 10^{13}$ the fission-gas release made a sudden step increase so that it corresponded to the portion of Fig. 9.2 marked "Cl-20 (broken)." We suspect that during the period of grain growth the specimen may have healed some cracks and then fractured again at the 1100 to 1300°C temperature irradiation.

The irradiation of specimen Cl-20 was then terminated. In post-irradiation examination the specimen was found to be fractured, as expected. Equiaxed grain growth had occurred (see Figs. 9.3 and 9.4), and gas bubbles were segregated at grain boundaries. The microstructure of the specimen is consistent with the explanation of the spontaneous bursts and the cooling burst.[1]

## Specimens for High-Burnup Studies

The defect-trap model postulates that at low burnup the fission-gas release rate will be lowered by the forming of small cluster traps. The effects of higher burnup are not clear; we have not attained very high burnups because all of our specimens have been of natural enrichment (previous maximum was $9 \times 10^{19}$ fissions/cm$^3$ or 0.37% U burnup). To obtain high enrichment single-crystal specimens of $UO_2$, it was necessary to grow a crystal by a floating zone technique[2] from a comparatively small batch of $UO_2$.

The enriched $UO_2$ crystal was sliced into cubes about 0.15 cm on edge and sent to H. J. Anderson, Pacific Northwest Laboratory, where the cubes were heat treated to remove imperfections. The specimens were then ground into spheres 0.0997 cm in diameter. We placed 36 of

[2]A. T. Chapman and G. W. Clark, "Growth of $UO_2$ Single Crystals Using the Floating-Zone Technique," J. Am. Ceram. Soc. 48, 494–495 (1965).

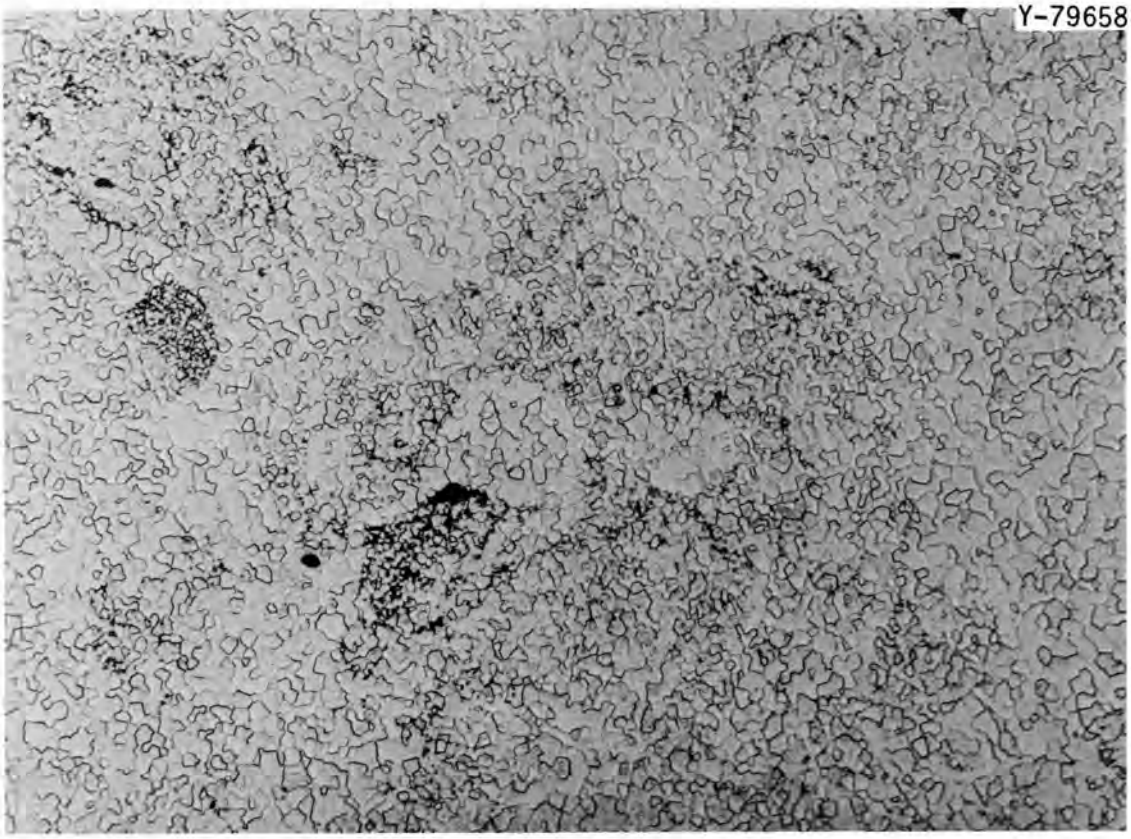


Fig. 9.3. Grain Structure of Unirradiated Control Specimen C1-20. Note: control is 200× whereas the irradiated specimen (Fig. 9.4) is shown at 250×.

the spheres (see Fig. 9.5) into a tungsten holder so they formed a hollow cylinder of 12 spheres in circumference and three spheres deep. Thermocouples measured the inside temperature of the array. The total weight of the spheres is 0.20564 g, and they have a combined geometric surface area of 1.13 $cm^2$. The specimens are enriched to 48.66% $^{235}U$.

These specimens were all cut from the same single crystal. They have a uniform and spherical shape that should allow a postirradiation measurement of swelling. Unfortunately, because of the method of manufacture, the crystals have a higher impurity content than we usually have in the single-crystal specimens (see Table 9.1). However, the impurity level is probably not high enough to have a significant effect on the fission-gas behavior.

[redacted]



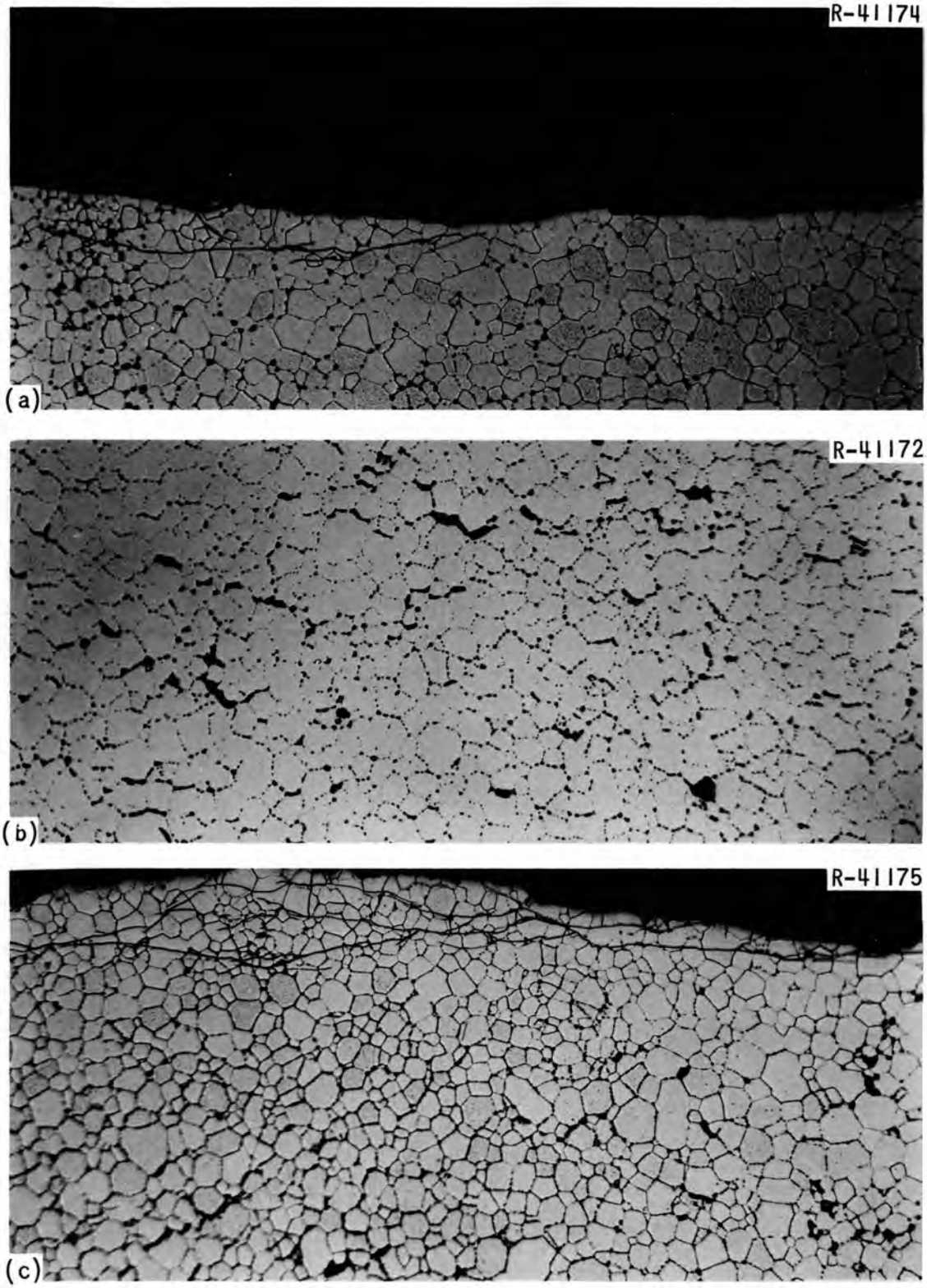


Fig. 9.4. Grain Structure of C1-20 Specimen After Irradiation. 250×. (a) Inner surface. (b) Center. (c) Outer surface.

[redacted]

[redacted]



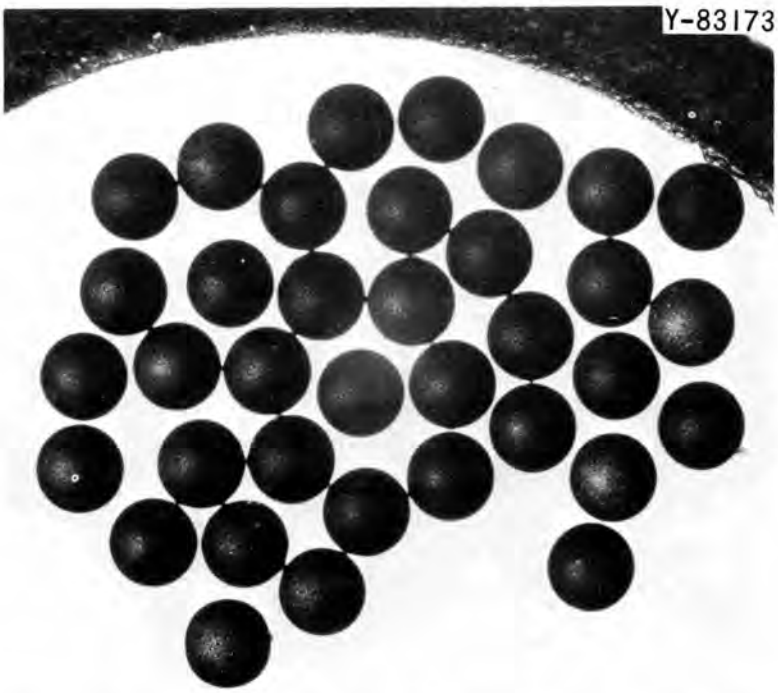


Fig. 9.5. Enriched Single-Crystal 0.0997-cm-diam $UO_2$ Spheres Used in the C1-21 Experiment.

Table 9.1. Impurity Levels in Single-Crystal Spheres

| Element | Concentration, ppm | | |
|---|---|---|---|
| | After Annealing (BNW) | After Grinding (ORNL) | Typical Specimen (BNW) |
| Al | 20 | 27 | < 5 |
| B | < 0.1 | 5 | < 0.1 |
| Ca | 100 | 56 | 20 |
| Cr | < 5 | < 30 | < 5 |
| Cu | 10 | < 10 | 1 |
| Fe | 30 | < 50 | < 10 |
| Mg | 5 | 12 | < 1 |
| Mn | 10 | < 3 | |
| Mo | < 5 | < 100 | |
| Na | < 2 | < 1000 | < 2 |
| Ni | < 10 | < 100 | |
| Pb | 2 | < 500 | |
| Si | 133 | 60 | < 25 |
| Sn | 20 | < 500 | |
| Zn | < 50 | < 500 | |

[redacted]

[redacted]



Fission-Gas Release from Enriched Specimens (C1-21)

The main effect of burnup in the low-enrichment material has been that the fission-gas release rate decreased during the initial stages of the irradiation. This effect has been observed in many specimens and is predicted by the defect-trap model. To date we have obtained a burnup on the enriched specimens of $4.5 \times 10^{20}$ fissions/cm$^3$ or 1.8% U, corresponding to 16,000 Mwd/MT.

The fission-gas release from the enriched spheres has demonstrated an effect that we have not observed before. Namely, when the fission rate in the specimens is increased the fission-gas release rate is increased more than would be predicted by diffusion theory (see Fig. 9.6).

By diffusion theory the equilibrium release rate of an isotope is directly proportional to its concentration, which in turn is directly proportional to the fissioning rate. Thus a doubling of flux at a constant temperature should cause a doubling of fission-gas release. The defect-trap model was developed because we found this did not occur; instead, the gas release was a very weak function of fission rate

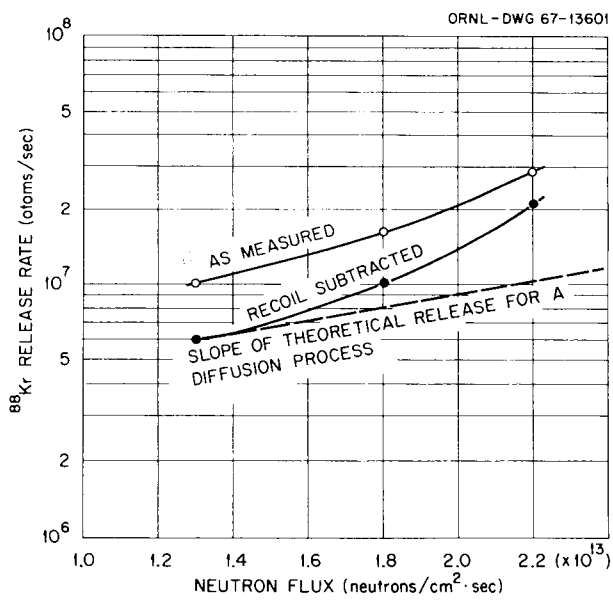


Fig. 9.6. Krypton-88 Release from Enriched Single-Crystal $UO_2$ Specimens (C1-21) at 850°C.

[redacted]

[redacted]



(as example see Fig. 9.7). Thus we postulated that the fissioning process created traps that had a liftime depending on the temperature and fuel conditions.

The defect-trap theory predicted that the fission process retards the migration of fission gas. The new data, on the other hand, show that the fission process accelerates the migration of fission gas. It is important to recognize that these enriched specimens have a fission density 18 times the highest of any of our previous specimens.

We have always recognized that the defect-trap model would have upper and lower bounds to the range of fission density in which it could be applied. It seems that we have now exceeded the upper bound, and the traps are interacting with each other rather than being annealed by the fuel temperatures. We observe that during temperature drops the gas release does not have the characteristics of diffusion release. This supports our belief that the gas release is a function of trap behavior. Since this accelerated release with fission rate has not been observed before, we will study this effect closely.

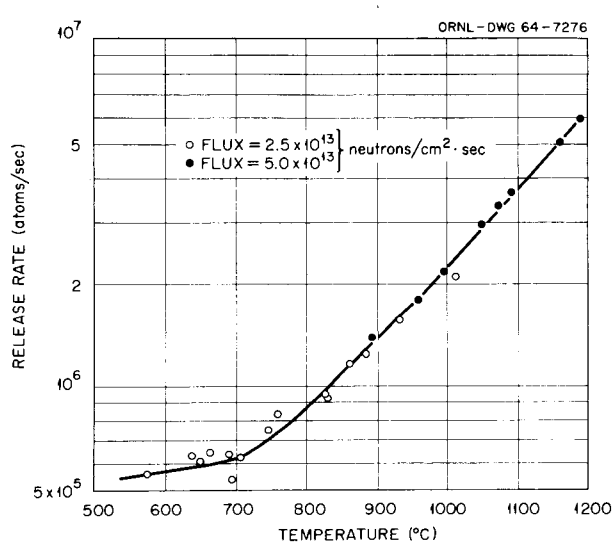


Fig. 9.7. Release Rate of $^{88}Kr$ from Fine-Grain Specimen (C1-12) of $UO_2$.

[redacted]

[redacted]



## In-Reactor Thermal Conductivity of Uranium Dioxide

As a by-product of dynamic fission-gas release experiments,[3] a program to measure the thermal conductivity of single crystals of uranium dioxide under irradiation conditions was started.[4] The essence of the experiment is the heating of the sample by a pulse of fission heat generated by varying the position of the specimen within the flux field of the reactor. The experimental situation was such that the thermal conductivity had to be determined with a single temperature measurement in the sample. The theoretical treatment predicts that the "heating curve" of the specimen is of the form:

$$\Delta T(t) = A_0 - A_1 e^{-r_1 t} - A_2 e^{-r_2 t} , \qquad (1)$$

where

$\Delta T(t)$ = temperature increment at the center of the sample,

$A_0, A_1, A_2$ = constants depending on the properties of the sample and thermal shield (°C),

$r_1, r_2$ = inverse relaxation times.

The form of Eq. (1) arises from the fact that after the fission heat has propagated through the sample it is then transferred to the thermal shield, which in turn dissipates the heat to the surroundings. There must be then two overall relaxation times, $r_1^{-1}$ and $r_2^{-1}$, associated with the heat transport in the sample and insulation, respectively. From the knowledge of the four parameters ($r_1$, $r_2$, $A_1$, and $A_2$) obtained by a numerical fitting to the experimental data, one computes the inverse relaxation time $\lambda_0$ ($sec^{-1}$) and the Laplacian $\alpha_0^2$ ($cm^{-2}$), which are the parameters characterizing the conductive heat transport in the specimen. Then the thermal conductivity K is obtained from the simple relation:

$$K = \rho c \lambda_0 / \alpha_0^2 \ (\text{cal cm}^{-1}\ \text{sec}^{-1}\ {}^\circ\text{C}^{-1}) , \qquad (2)$$

---

[3] R. M. Carroll and O. Sisman, "Fission Gas Release During Fissioning," Nucl. Appl. 2, 142 (April 1966).

[4] R. M. Carroll and J. G. Morgan, Fuels and Materials Development Program Quart. Progr. Rept. June 30, 1966, ORNL-TM-1570, pp. 85–95.

[redacted]

[redacted]



where

$\rho$ = density (g/cm$^3$),

c = specific heat (cal g$^{-1}$ °C$^{-1}$) .

Because it is in general difficult to isolate and determine two exponential functions of relatively close exponents, a numerical program[5] has been developed to compute the Fourier Transforms of Eq. (1). The amplitude of this function shows clearly two break frequencies, in agreement with the theoretical predictions.

These general results are also valid for the case in which the heat transfer between the sample and the shield is controlled by a radiative, rather than purely conductive, process. Data pertinent to a typical run follow.

| | |
|---|---|
| Initial sample temperature, °C | 764.5 |
| Sample constants, °C | |
| Maximum temperature increment | |
| $A_0$ | 84.7 |
| $A_1$ | 47.9 |
| $A_2$ | 37.0 |
| Inverse relaxation times, sec$^{-1}$ | |
| $r_1$ | $7.5 \times 10^{-3}$ |
| $r_2$ | $5.9 \times 10^{-2}$ |
| $\lambda_0$ | $5.2 \times 10^{-2}$ |
| Laplacian $\alpha_0^2$, cm$^{-2}$ | 40 |
| Thermal conductivity, (cal cm$^{-1}$ sec$^{-1}$ °C$^{-1}$) | $1.1 \times 10^{-3}$ |

The resulting thermal conductivity is reduced to about 90% of its out-of-reactor value[6] of $8.1 \times 10^{-3}$ cal cm$^{-1}$ sec$^{-1}$ °C$^{-1}$.

This result, although preliminary, indicates a lowering of the thermal conductivity occurring in irradiated uranium dioxide,[7] which

---

[5]R. K. Adams and R. L. Simpson, Instrumentation and Controls Division, ORNL, private communication, 1967.

[6]J. Belle, ed., Uranium Dioxide: Properties and Nuclear Applications, pp. 180–181, Naval Reactors, Division of Reactor Development, USAEC, Washington, D.C., 1961.

[7]J. Belle and R. M. Berman, Thermal Conductivity of Bulk Oxide Fuels, WAPD-TM-586 (February 1967).

[redacted]

[redacted]



can be attributed to radiation-induced scattering centers. To improve the accuracy of the thermal conductivity measurement, a program has been started to evaluate the nonfission heating of the system and devise corrections for the perturbation introduced by the thermocouple inserted at the center of the specimen.

[redacted]

[redacted]



Previous reports in this series are:

| | |
|---|---|
| ORNL-TM-920 | Period Ending June 30, 1964 |
| ORNL-TM-960 | Period Ending September 30, 1964 |
| ORNL-TM-1000 | Period Ending December 31, 1964 |
| ORNL-TM-1100 | Period Ending March 31, 1965 |
| ORNL-TM-1200 | Period Ending June 30, 1965 |
| ORNL-TM-1270 | Period Ending September 30, 1965 |
| ORNL-TM-1400 | Period Ending December 31, 1965 |
| ORNL-TM-1500 | Period Ending March 31, 1966 |
| ORNL-TM-1570 | Period Ending June 30, 1966 |
| ORNL-TM-1700 | Period Ending September 30, 1966 |
| ORNL-TM-1720 | Period Ending December 31, 1966 |
| ORNL-TM-1825 | Period Ending March 31, 1967 |
| ORNL-TM-1941 | Period Ending June 30, 1967 |
| ORNL-TM-2020 | Period Ending September 30, 1967 |

[redacted]

[redacted]

[redacted]

[redacted]





INTERNAL DISTRIBUTION

1–3. Central Research Library
4–5. ORNL – Y-12 Technical Library Document Reference Section
6–15. Laboratory Records Department
16. Laboratory Records, ORNL R.C.
17. ORNL Patent Office
18. G. M. Adamson, Jr.
19. T. E. Banks
20. J. H. Barrett
21. S. E. Beall
22. R. J. Beaver
23. M. Bender
24. R. G. Berggren
25. J. O. Betterton, Jr.
26. D. S. Billington
27. E. E. Bloom
28. A. L. Boch
29. E. S. Bomar
30. B. S. Borie
31. G. E. Boyd
32. R. A. Bradley
33. R. B. Briggs
34. R. E. Brooksbank
35. W. E. Brundage
36. D. A. Canonico
37. R. M. Carroll
38. J. V. Cathcart
39. A. K. Chakraborty
40. Ji Young Chang
41. G. W. Clark
42. K. V. Cook
43. G. L. Copeland
44. C. M. Cox
45. F. L. Culler
46. J. E. Cunningham
47. H. L. Davis
48. V. A. DeCarlo
49. J. H. DeVan
50. C. V. Dodd
51. R. G. Donnelly
52. K. Farrell
53. J. S. Faulkner
54. J. I. Federer
55. D. E. Ferguson
56. R. B. Fitts
57. B. E. Foster
58. A. P. Fraas
59. J. H Frye, Jr.
60. W. Fulkerson
61. T. G. Godfrey, Jr.
62. R. J. Gray
63. W. R. Grimes
64. H. D. Guberman
65. R. L. Hamner
66. D. G. Harman
67. W. O. Harms
68–70. M. R. Hill
71. N. E. Hinkle
72. D. O. Hobson
73. H. W. Hoffman
74. R. W. Horton
75. W. R. Huntley
76. H. Inouye
77. G. W. Keilholtz
78. B. C. Kelley
79. J. Komatsu
80. J. A. Lane
81. J. M. Leitnaker
82. T. B. Lindemer
83. A. P. Litman
84. R. H. Livesey
85. A. L. Lotts
86. R. N. Lyon
87. H. G. MacPherson
88. R. E. MacPherson
89. M. M. Martin
90. W. R. Martin
91. R. W. McClung
92. H. E. McCoy, Jr.
93. H. C. McCurdy
94. R. E. McDonald
95. W. T. McDuffie
96. D. L. McElroy
97. C. J. McHargue
98. F. R. McQuilkin
99. A. J. Miller
100. E. C. Miller
101. J. P. Moore
102. J. G. Morgan
103. F. H. Neill
104. G. T. Newman
105. T. M. Nilsson
106. T. A. Nolan (K-25)
107. S. M. Ohr

[redacted]

[redacted]



108. A. R. Olsen
109. P. Patriarca
110. W. H. Pechin
111. A. M. Perry
112. S. Peterson
113. R. A. Potter
114. R. B. Pratt
115. M. K. Preston
116. R. E. Reed
117. D. K. Reimann
118. P. L. Rittenhouse
119. W. C. Robinson
120. M. W. Rosenthal
121. C. F. Sanders
122. G. Samuels
123. A. W. Savolainen
124. J. L. Scott
125. J. D. Sease
126. O. Sisman
127. G. M. Slaughter
128. S. D. Snyder
129. K. E. Spear
130. I. Spiewak
131. J. T. Stanley
132. W. J. Stelzman
133. J. O. Stiegler
134. D. B. Trauger
135. R. P. Tucker
136. G. M. Watson
137. M. S. Wechsler
138. A. M. Weinberg
139. J. R. Weir, Jr.
140. W. J. Werner
141. H. L. Whaley
142. G. D. Whitman
143. J. M. Williams
144. R. K. Williams
145. R. O. Williams
146. J. C. Wilson
147. R. G. Wymer
148. F. W. Young, Jr.
149. C. S. Yust
150. A. F. Zulliger

EXTERNAL DISTRIBUTION

151–154. F. W. Albaugh, Battelle, PNL
155–157. R. J. Allio, Westinghouse Atomic Power Division
158. R. D. Baker, Los Alamos Scientific Laboratory
159. C. Baroch, Babcock and Wilcox
160. V. P. Calkins, General Electric, NMPO
161. S. Christopher, Combustion Engineering, Inc.
162. D. B. Coburn, Gulf, General Atomic
163. D. F. Cope, RDT, SSR, AEC, Oak Ridge National Laboratory
164. G. K. Dicker, Division of Reactor Development and Technology, AEC, Washington
165. D. E. Erb, Division of Reactor Development and Technology, AEC, Washington
166. E. A. Evans, General Electric, Vallecitos
167. W. C. Francis, Idaho Nuclear Corporation
168. A. J. Goodjohn, Gulf, General Atomic
169. S. P. Grant, Babcock and Wilcox
170. J. F. Griffo, Division of Space Nuclear Systems, AEC, Washington
171. R. G. Grove, Mound Laboratory
172. D. H. Gurinsky, Brookhaven National Laboratory
173. A. N. Holden, General Electric, APED
174–176. J. S. Kane, Lawrence Radiation Laboratory, Livermore
177. Haruo Kato, Albany Metallurgy Research Center, P.O. Box 70, Albany, Oregon 97321
178. E. A. Kintner, Fuel Fabrication Branch, AEC, Washington
179. J. H. Kittel, Argonne National Laboratory

[redacted]

[redacted]



180. E. J. Kreih, Westinghouse, Bettis Atomic Power Laboratory
181. W. J. Larkin, AEC, Oak Ridge Operations
182. W. L. Larsen, Iowa State University, Ames Laboratory
183. C. F. Leitten, Jr., Linde Division, Union Carbide Corp.
184. P. J. Levine, Westinghouse Advanced Reactor Division, Waltz Mill Site, Box 158, Madison, Pa. 15663
185. J. J. Lombardo, NASA, Lewis Research Center
186. J. H. MacMillan, Babcock and Wilcox
187. C. L. Matthews, RDT, SR, AEC, Oak Ridge National Laboratory
188. M. McGurty, General Electric, NMPO
189. A. Mullunzi, Division of Reactor Development and Technology, AEC, Washington
190. M. Nevitt, Argonne National Laboratory
191. R. E. Pahler, Division of Reactor Development and Technology, AEC, Washington
192. S. Paprocki, Battelle Memorial Institute
193. W. E. Ray, Westinghouse Advanced Reactor Division, Waltz Mill Site, Box 158, Madison, Pa. 15663
194. W.L.R. Rice, AGMR, AEC, Washington
195. B. Rubin, Lawrence Radiation Laboratory, Livermore
196. F. C. Schwenk, Division of Reactor Development and Technology, AEC, Washington
197. W. F. Sheely, Division of Research, AEC, Washington
198. P. G. Shewmon, Argonne National Laboratory
199–201. J. M. Simmons, Division of Reactor Development and Technology, AEC, Washington
202. L. E. Steele, Naval Research Laboratory
203. R. H. Steele, Division of Reactor Development and Technology, AEC, Washington
204–206. D. K. Stevens, Division of Research, AEC, Washington
207. A. Strasser, United Nuclear Corporation
208. A. Taboada, Division of Reactor Development and Technology, AEC, Washington
209. A Van Echo, Division of Reactor Development and Technology, AEC, Washington
210. James Watson, Gulf, General Atomic
211. C. E. Weber, Atomics International
212. J. F. Weissenberg, RDT, OSR, General Electric, NMPO
213. G. W. Wensch, Division of Reactor Development and Technology, AEC, Washington
214. G. A. Whitlow, Westinghouse Advanced Reactor Division, Waltz Mill Site, Box 158, Madison, Pa. 15663
215. E. A. Wright, AEC, Washington
216. Laboratory and University Division, AEC, Oak Ridge Operations
217–231. Division of Technical Information Extension

[redacted]